Preoperative planning and simulation for artificial heart implantation surgery

Sophie Collin

ANNÉE 2018

THÈSE / UNIVERSITÉ DE RENNES 1
sous le sceau de l'Université Bretagne Loire

pour le grade de

DOCTEUR DE L'UNIVERSITÉ DE RENNES 1

Signal, Image, Vision

Ecole doctorale MathSTIC

présentée par

Sophie COLLIN

Préparée à l'unité de recherche LTSI – Inserm U1099
Laboratoire Traitement du Signal et de l'Image – Université de Rennes 1

Preoperative planning and simulation for artificial heart implantation surgery

Thèse soutenue à Rennes
le 29/03/2018

devant le jury composé de :

Alain LALANDE
MCU PH, Université de Bourgogne / *rapporteur*

Gabriele DUBINI
Professeur, Politecnico di Milano / *rapporteur*

Frédérique FROUIN
CR Inserm, Université Paris Sud / *examinateur*

Erwan FLECHER
PU PH, CHU Rennes / *examinateur*

Pascal HAIGRON
Professeur, Université de Rennes 1 / *directeur de thèse*

Michel ROCHETTE
Directeur technique, ANSYS France / *co-directeur de thèse*

Remerciements

Je tiens tout d'abord à remercier les membres du jury de cette thèse : **Alain Lalande** et **Gabriele Dubini** qui ont accepté d'être rapporteurs pour cette thèse, ainsi que **Frédérique Frouin** d'être membre du jury. Je les remercie pour l'intérêt qu'ils ont porté à mon travail, leurs conseils, commentaires et remarques qui ont permis d'améliorer le manuscrit.

Je remercie sincèrement mes deux directeurs de thèse **Pascal Haigron** et **Michel Rochette** de m'avoir donné l'opportunité de travailler sur ce projet. J'ai beaucoup apprécié leur soutien durant ces trois années ainsi que leur confiance dans les travaux de recherches que j'ai pu entreprendre. Je les remercie tout particulièrement pour leurs encouragements, leur générosité, leur patience et pour tout ce qu'ils ont pu m'apprendre au cours de cette thèse.

Je tiens aussi à exprimer ma gratitude aux autres membres de cette équipe merveilleuse qui m'a accompagnée tout au long de cette thèse. Merci pour leur source de motivation et leur enthousiasme. Travailler avec vous a été un réel plaisir et je n'aurais pas pu aboutir à tous ces résultats sans votre aide. Mes sincères remerciements à **Erwan Flecher** pour tout ce qu'il m'a enseigné, sa générosité dans le partage de ses connaissances ainsi que sa disponibilité. J'adresse aussi mes sincères remerciements à **Valery Morgenthaler**. Je lui suis reconnaissante de son implication dans le projet ainsi que pour le temps qu'il a passé à m'expliquer certaines notions dans le domaine des simulations fluides. Je remercie également **Amedeo Anselmi** pour son étroite collaboration au sein de ce projet.

Merci à mes **collègues et amis du LTSI et d'ANSYS**: Karim (qui va devoir trouver une nouvelle secrétaire), Hélène (pour son soutien), Hung (pour son aide durant mes 2 premières années), ainsi que Jeroen et Clémentine qui m'ont fait découvrir Lyon. Je remercie Muriel, Soizic et Patricia pour leur joie de vivre, Christine qui a toujours su répondre à nos questions et Jean qui trouve toujours une solution à nos problèmes malgré la distance. Merci à tous les collègues d'Ansys pour leur accueil lors de mes déplacements à Lyon et leur curiosité scientifique. Merci à tous les collègues du LTSI ainsi que Lotfi Senhadji, directeur du LTSI de m'avoir si bien intégrée au sein du labo et leur intérêt scientifique.

Mes remerciements vont aussi à tous mes **amis de Rennes**. Je leur suis reconnaissante pour leur soutien, leur entraide mais surtout pour leur joie de vivre et ces moments passés ensemble. Un

énorme merci à Auréline (qui me suit toujours dans mes plans sans jamais trop savoir ou ça va aboutir ! Bon promis la prochaine fois j'escaladerai la grille pour récupérer Titine !), Bastien (partenaire de natation, d'escalade, etc… on est d'accord, le sport c'est la vie), Matthieu (« YMCA » = 100% de réussite et on finit par un Top 1. Quelle équipe de choc !) et Maud (qui a supporté mes horaires durant 2 années de colocation et heureusement pour elle, elle a fui avant la dernière année de thèse). Je tiens à remercier Pascal B. ainsi que tous les membres du club qui m'ont fait découvrir le JJB. Merci pour votre combativité, votre respect, votre bonne humeur et surtout votre bon humour.

Je voudrais tout particulièrement remercier **ma famille** pour son soutien et son aide précieuse. Merci à Bérénice (que je rejoins dans la clique des docteurs); à Manon, qui a toujours été présente et m'a toujours soutenue depuis qu'on se connait (20 ans ce n'est pas rien). Un grand merci à mes deux grandes sœurs sur qui j'ai toujours pu compter, Hélène qui a passé des heures au téléphone pour me changer les idées et Mathilde qui, malgré la distance, est toujours là pour nous. Un énorme merci à mes parents : mon papa pour avoir réussi à arrêter le temps afin de venir assister à ma soutenance, ma maman pour sa présence et ce délicieux festin toujours aussi parfait. Je suis sûre que mes sœurs se joindront à moi pour vous dire à quel point vous êtes incroyables et qu'on vous aime. Vous nous avez toujours soutenues dans toutes nos décisions et quelles que soient les épreuves. Vous avez toujours été là pour chacune d'entre nous et ce malgré une année haute en émotion : une naissance, un mariage et un doctorat, Félicitations ! Mille mercis et promis nous serons plus calmes l'année prochaine (enfin peut-être).

Contents table

Remerciements ..... **i**

Acronyms ..... **ix**

List of figures ..... **xi**

List of Tables ..... **xv**

Résumé en français ..... **xvii**

Introduction **1**

Chapter 1 - Clinical Context **5**

1. Cardiovascular system 5

1.1. Blood circulation 5
1.2. The heart 7
1.3. Mechanical and electrical physiology 9

2. Heart failure 10

2.1. Pathology and symptoms 11
2.2. Diagnosis and treatments 12
2.3. End-stage Heart Failure (HF) and heart transplant 14
2.4. Mechanical Circulatory Support (MCS) devices 15
2.5. Total Artificial Heart (TAH) pump 17
2.6. Ventricular Assist Devices (VAD) pump 18

3. Surgical procedure 20

3.1. Patient selection and preoperative exams 20
3.2. Surgical intervention 21
3.3. Medical follow-up and complications – INTERMACS analysis 24

4. Summary 25

References 26

Chapter 2 - Issues related to device implantation **29**

1. Interactions between the MCS implants and anatomical structures 29

2. Mechanical and fluidic issues 33

2.1. Related approaches 33
2.2. Parameters influencing the aorta properties and hemodynamics 34
2.3. Parameters influencing the pump inflow 37
2.4. Computational modelling contributions 40

3. Morphological issues 43

3.1. Aortic calcifications and heart motion 44
3.2. Intrathoracic space 44
3.3. Solutions from the literature 45

4. Work positioning and proposed approach 48

References 50

Chapter 3 - Anatomical structures description **57**

1. Medical imaging and segmentation methods 57
1.1. Medical imaging in MCS context 57
1.2. Classification of segmentation methods 58
2. Evaluation of preoperative CT scans 60
3. Cardiovascular structures 63
3.1. Aorta 63
3.2. Heart segmentation, related works 66
3.3. Heart segmentation, methods and experiments 68
3.3.1. MA based segmentation method 68
3.3.2. Comparison to the results from the literature 69
3.3.3. Modification of the atlas 71
4. Surrounding structures 72
4.1. Lungs segmentation, related works 72
4.2. Lungs segmentation, methods and experiments 74
4.2.1. Thresholding-based methods 75
4.2.2. Region growing method 76
4.2.3. Multi-atlas segmentation 76
4.2.4. Lungs segmentation results 77
4.3. Chest wall segmentation, related works 78
4.3.1. Rib cage segmentation 79
4.3.2. Thoracic cavity segmentation 80
4.4. Rib cage segmentation, methods and experiments 81
4.4.1. Morphological approach 81
4.4.2. Results 84
5. Conclusion 86
References 88
Chapter 4 - Geometrical approach 95
1. Devices and their specificities 95
2. Metrics for LVAD inflow cannula pose 97
2.1. Literature and related issues 97
2.2. Definition of indices characterizing the inflow cannula pose 99
2.3. Retrospective analyses 101
2.3.1. Relation between the device pose and postoperative complications 102
2.3.2. Influence of the surgical process on inflow cannula orientation 104
3. Geometrical constraints 106
3.1. Study assumptions 106
3.2. Retrospective analysis 107
4. Presentation of the planning solution 108
4.1. Device and patients anatomy representation 109
4.2. Collision detection methods and IC positioning 110
4.2.1. Right ventricle and inter-ventricular septum constraint for LVAD 111
4.2.2. Thoracic constraint for MCS device 111
4.2.3. Information about IC positioning for LVAD 111
4.3. Implementation 113

5. Potential and discussion....116
5.1. Postoperative and planning comparison....116
5.2. Evaluation of the semi-automatic MV definition....118
5.3. Discussion....120
References....123
Chapter 5 - Biomechanical approach....125
1. CFD simulations assessing hemodynamic issues related to LVAD IC: a state of the art....125
1.1. CFD simulations elaborations (geometry and parametrization)....126
1.1.1. Geometry....126
1.1.2. Models....127
1.1.3. Materials and boundary conditions....129
1.2. Post-processing and validation....130
2. CFD modelling approach....131
2.1. Geometry....131
2.2. Parametrization of the model....132
2.3. Numerical settings....133
3. Parametrisation and analyses of the coaxial configuration....134
3.1. Stagnation distribution in space....135
3.1.1. Parametrization analyses....135
3.1.2. Interpretation of the results....137
3.2. Quantification of the residence time....139
3.2.1. Parametrization analyses....139
4. LV hemodynamic with an IC oriented toward the septum....142
4.1. Particles trajectories....143
4.2. Velocity magnitude and residence time....144
5. Conclusion and discussion....146
References....149
Conclusion....151
List of publications....155
Annexes....157
Annex 1 Total Artificial Hearts -TAH....157
Annex 2 Ventricular Assist Devices - VAD....159
Annex 3 Four heart cavities and left myocardium segmentation approaches, a state of the art....160
Annex 4 Thoracic cavity and rib cage segmentation, a state of the art....162
Annex 5 Segmentation of bones with high density and costal cartilages, a state of the art....163

Acronyms

Active Shape Model
ASM 59
Aortic Valve
AoV 7, 31
Bi-Ventricular Assist Device
BiVAD 18
Computational Fluid Dynamic
CFD 34, 125
Computer Assisted Medical Intervention Toolkit
CamiTK 113
Computerized Tomography
CT 37
Cone Beam Computed Tomography
CBCT 109
Continuous-flow VAD
CFVAD 20
Deformable Model
DM 59
Dice Score
DSC 68
Food and Drug Administration
FDA 18
Heart Failure
HF 10
Heart Transplant
HTx 14
HeartMate II
HM II 43, 96
HeartWare HVAS
HVAS 96
Hounsfield Unit
HU 58
Inflow Cannula
IC 18, 31, 96
Interagency Registry for Mechanically Assisted Circulatory Support
INTERMACS 12
Inter-Ventricular Septum
IVS 7, 97, 125
Intra-Cardiac Device
ICD 14, 58
Large Eddy Simulation
LES 128
Left Myocardium
LMy 66
Left Ventricle
LV 7, 31
Left Ventricular Assist Device
LVAD 18
Magnetic Resonance Imaging
MRI 12
Mechanical Circulatory Support
MCS 14
Mitral Valve
MV 7, 38, 97
Multi-Atlas
MA 66
New York Heart Association
NYHA 12
Outflow Cannula
OC 18, 29
Probability Density
PD 140
Pulsatile-Flow VAD
PFVAD 19
Right Ventricle
RV 7, 30
Right Ventricular Assist Device
RVAD 18
Total Artificial Hearts
TAH 17
Ventricular Assist Devices
VAD 17
Wall Shear Stress
WSS 32

List of figures

Figure 1 - Composition du cœur artificiel total (TAH - Total Artificial Heart) xvii
Figure 2 - Composition du dispositif monogauche (LVAD- Left Ventricular Assist Device) xviii
Figure 3 – Aide à la décision préopératoire pour la planification d'implantation d'ACM xix
Figure 4 – Représentation du patient virtuel dans le cadre de la planification d'implantation d'ACM xx
Figure 5 – Solution de planification xxi
Figure 6 –Répartition du temps de résidence au sein de la cavité ventriculaire gauche sous assistance xxii
Figure 1.1 - Blood circulation 6
Figure 1.2 - Heart vessels 6
Figure 1.3 - Heart location in the thoracic cavity 7
Figure 1.4 - Intracardiac anatomy and circulation 8
Figure 1.5 - Electrical and mechanical phases during a cardiac cycle 9
Figure 1.6 - Cardiac conduction system 10
Figure 1.7 - Prevalence of heart failure by sex and age (2009–2012) 11
Figure 1.8 - INTERMACS classification system compared to NYHA classification 13
Figure 1.9 - Number of adult and pediatric heart transplants by year (transplants: 1982–2015) and geographic region 15
Figure 1.10 - Number of patients in the waiting list compared to transplanted ones, by year, in France. 15
Figure 1.11 - Mechanical Circulatory Support composition – Example of left ventricular assist device (LVAD) 16
Figure 1.12 - INTERMACS – Implants per year by device strategy, 2006 to 2016. 17
Figure 1.13 - Total Artificial Heart - TAH 18
Figure 1.14 - Ventricular Assist Device pump – VAD - Example of a LVAD (HeartMate III - Thoratec Inc., Pleasanton, CA) 19
Figure 1.15 - Device positioning 19
Figure 1.16 - Conventional incision - Sternotomy 21
Figure 1.17 - Extracorporeal circulation 22
Figure 1.18 - TAH implantation (example of the Syncardia TAH) 23
Figure 1.19 - LVAD implantation with a) the insertion of the inflow cannula ring; b) the insertion of the LVAD within the intrathoracic space. 23

Figure 2.1 - Interactions with the Total Artificial Heart (TAH) 30
Figure 2.2 - Interactions related to the Left Ventricular Assist Device (LVAD) implantation 30
Figure 2.3 - Outflow cannula anastomosis to aorta 32
Figure 2.4 - Azimuthal and inclination angles defining aortic anastomosis direction. 36
Figure 2.5 - Illustration of two configurations of the HM II inflow cannula through postoperative radiographies 39
Figure 2.6 - Two manageable angles for the inflow cannula implantation configuration of the HM II. a) Elbow angle b) Circumferential angle 39
Figure 2.7 - Resume of physiological modifications and potential sources related to LVAD implantation 40
Figure 2.8 - Computerized approaches in the context of MCS. 47
Figure 2.9 - Preoperative decision support for MCS computer-aided planning 49
Figure 3.1 - Illustration of the contrast quality in CT scan 60
Figure 3.2 - 2D segmentations for the evaluation of the CT contrast quality 61
Figure 3.3 - Definition of contrast inhomogeneity in a CT scan 62
Figure 3.4 - Endosize software *(Therenva, Rennes, France)* 63
Figure 3.5 - Illustration of contrast-enhanced CT at the aorta level 64
Figure 3.6 - Results for aortic segmentation with the TAVI module from Endosize software *(Therenva, Rennes, France)* 65
Figure 3.7 - Grade 2 and grade 3 illustration of the aorta segmentation 65
Figure 3.8 - Multi-atlas based heart segmentation from preoperative CT scan 69
Figure 3.9 - Dice results for the whole heart segmentation with the multi-atlas approach $MA_{kirisli}$ 71
Figure 3.10 - Lungs segmentation method based on thresholding 75
Figure 3.11 - Illustration of segmented lungs atlases; a) without opacifications; b) with opacifications 76
Figure 3.12 - Lungs segmentation classification, illustration of grade 3 and failed segmentation 77
Figure 3.13 - Lungs segmentation results for thresholding-based, region-based and shape-based methods 77
Figure 3.14 - Illustration of the rib cage segmentation (a.); Thoracic cavity segmentation (b.); and Thoracic wall delineation (c.) 78
Figure 3.15 - Rib cage segmentation method based on thresholding 82
Figure 3.16 - Identification of tissue regions in the rib cage segmentation method 83
Figure 3.17 - Example of rib cage segmentation results 84

Figure 3.18 - Rib cage segmentation results (32 CTs) 85
Figure 3.19 - Virtual patient for computer-aided planning for MCS device implantation 87
Figure 4.1 - Syncardia TAH 95
Figure 4.2 - LVADs considered in the thesis 96
Figure 4.3 - a. Inflow cannula to mitral valve alignment. Definition of the coronal angle (deviation toward IVS) b. 3D representation of the heart within the thoracic cavity 98
Figure 4.4 - Workflow for retrospective analyses 99
Figure 4.5 - Mitral valve representation and its associated coordinate system 99
Figure 4.6 - φ, θ orientation and D(p,o) distance representation 100
Figure 4.7 - The angle between the inflow cannula and the pump body: **a.** $\alpha < 15°$ - a normal angulation, **b.** $\alpha \in [15°; 30°]$ – medium angulation; **c.** $\alpha > 30°$ - excessive angulation 101
Figure 4.8 - Illustration from postoperative CT scans of collision between the device and the thoracic wall (a) or right ventricle (b) 107
Figure 4.9 - Retrospective evaluation of collision between implanted LVAD and the thoracic wall or right ventricle 108
Figure 4.10 - Overview of the planning approach 109
Figure 4.11 - 3D mesh of the Jarvik 2000 created from a CBCT scan with an active contour method. 110
Figure 4.12 - Overview of the pose planning method 112
Figure 4.13 - CamiTK architecture with several collaborating modules 113
Figure 4.14 - Screenshot of the user interface 114
Figure 4.15 - Representation of the area of LVAD implantation 115
Figure 4.16 - Illustration of thoracic and right ventricular collision with respectively the Syncardia and Heartmate II device 115
Figure 4.17 - LVAD IC orientation and position information 116
Figure 4.18 - Workflow for the evaluation of pose planning benefits 117
Figure 4.19 - Workflow for the evaluation of the automatic mitral valve plane definition within the pose planning solution 119
Figure 4.20 - Angles between the mitral valve plane defined by the heart segmentation and selected points 119
Figure 4.21 - Workflow of methods and studies presented in this chapter 121
Figure 5.1 - Representation of a laminar and turbulent flow 128
Figure 5.2 - Workflow of the left ventricle geometry elaboration for the static CFD model of this thesis 132

Figure 5.3 - Left ventricular CFD geometry with a LVAD inflow cannula 132
Figure 5.4 - CFD simulation settings parametrization.....133
Figure 5.5 – Post-processing variables and settings 134
Figure 5.6 - Residence time with the laminar CFD model.....135
Figure 5.7 - Comparison of the velocity magnitude from the laminar to the LES model 136
Figure 5.8 - Illustration of particles coloured by their residence time from 0.5sec to 3.0sec of simulation time – coaxial configuration.....137
Figure 5.9 - Velocity magnitude flow vectors (LES).....138
Figure 5.10 - Distribution of velocity magnitude within the left cavity (LES).....138
Figure 5.11 - Distribution of residence time within the left cavity with an inflow cannula oriented toward the mitral valve.....139
Figure 5.12 - Probability density of the laminar and LES model for several statistical time values (t_{stat}) 140
Figure 5.13 - Probability density of the laminar model for several simulation time values (T_0)...141
Figure 5.14 - Probability density of the residence time for laminar and LES models 141
Figure 5.15 – Statistical distribution of the residence time for the laminar and LES models.....142
Figure 5.16 - Left ventricle geometry with a coaxial and IVS IC configuration 143
Figure 5.17 - Illustration of particles coloured by their residence time from 0.5sec to 3.0sec of simulation time – IVS configuration 143
Figure 5.18 - 3D distribution of particles velocity magnitude with an inflow cannula toward the inter-ventricular septum 144
Figure 5.19 - Distribution of the residence time.....145
Figure 5.20 – Probability density of the residence time for the IVS configuration.....145
Figure 5.21 – Statistical distribution of the residence time for the IVS configuration 146
Figure 5.22 - Flowchart for the elaboration of heart beating simulation with a LVAD inflow cannula 148

List of Tables

Table 1-I - The New York Heart Association Classification 13
Table 2-I - Factors influencing physiological modifications of the left ventricular hemodynamics 41
Table 2-II - Factors influencing physiological modifications of the aortic hemodynamics related to ascending anastomosis 42
Table 2-III - Factors influencing physiological modifications of the aortic hemodynamics related to descending and subclavian arteria anastomoses 43
Table 3-I - Major classes of segmentation methods with their advantages and disadvantages 59
Table 3-II - Contrast quality in our database (32 CTs) 62
Table 3-III - Results from the literature of three competitive heart segmentation methods 67
Table 3-IV - Results obtained with $MA_{Kirisli}$ heart segmentation approach 70
Table 3-V - Results obtained with MA_{ICD} heart segmentation approach 72
Table 3-VI - Lung segmentation articles 73
Table 3-VII - Effectiveness of class of methods for segmentation of the lung fields and evaluation of the presence of abnormality in the context of MCS implantation 74
Table 3-VIII - Sources of rib cage segmentation failures (12/32 CTs) 85
Table 3-IX - Way of use of anatomical segmentations in the context of MCS 86
Table 4-I - LVADs characteristics 96
Table 4-II - Results of retrospective studies evaluating the influence of the IC orientation on postoperative outcomes 97
Table 4-III - Results for complicated (Group 1) and uncomplicated (Group 2) patients 102
Table 4-IV - Lateral and IVS deviation for complicated and uncomplicated patients 102
Table 4-V - Comparison of φ and θ deviations according to the LVAD 103
Table 4-VI - Comparison of the retrospective results with the literature 103
Table 4-VII - Results of postoperative angle between the Heartmate II inflow cannula and the pump body 104
Table 4-VIII - Postoperative φ and θ deviations for sternotomy and thoracotomy procedure 105
Table 4-IX - Critical anatomical structures considered for each MCS device 107
Table 4-X - Preoperative planned position without collision compared to postoperative ones 118
Table 5-I - State of the art of CFD simulation assessing the blood flow of the left ventricle with an inflow cannula 127
Table 5-II - Boundary conditions in the context of LVAD inflow cannula 129

Table 5-III - Objectives of computational fluid dynamic simulations in the context of LVAD inflow cannula.....130

Résumé en français

L'insuffisance cardiaque (IC) se définit par l'incapacité du cœur à pomper suffisamment de sang pour répondre aux besoins de l'organisme, conduisant ainsi à la défaillance de certains organes. Près de 23 millions de personnes à travers le monde sont aujourd'hui touchées par cette pathologie qui représente la principale cause de décès en Europe et aux Etats-Unis. La transplantation cardiaque reste actuellement la thérapeutique de référence pour le traitement de l'IC terminale. Alors que la prévalence de l'IC ne cesse d'augmenter, le nombre limité de greffons constitue une problématique majeure.

Les pompes cardiaques, ou dispositifs d'Assistance Circulatoire Mécanique (ACM) de longue durée, ont acquis un rôle prépondérant dans ce contexte de pénurie de greffon. Ils représentent aujourd'hui l'unique alternative à la transplantation cardiaque. L'objectif de cette thèse est d'élaborer une méthodologie d'aide à la décision pour fournir aux chirurgiens des informations pour la planification et l'aide à l'implantation d'ACM dans le but de diminuer les complications ainsi que la morbidité per- et post-opératoires.

❖ Contexte clinique

Les ACMs ont pour objectifs de remplacer partiellement ou en totalité le fonctionnement du ou des ventricules cardiaques. Deux catégories sont à distinguer : le cœur artificiel total (TAH – Total Artificial Heart) et l'assistance ventriculaire (VAD – Ventricular Assist Device). Implanté par sternotomie, le TAH est composé de deux ventricules artificiels qui viennent remplacer ceux du cœur natif (Figure 1). Le VAD est au contraire implanté sur le cœur malade (qui reste en place) par sternotomie ou thoracotomie. Le dispositif monogauche ou LVAD (Left Ventricular Assist Device) est à ce jour le VAD le plus implanté. Composé d'une pompe intrathoracique, il supporte la fonction du ventricule gauche en propulsant la quantité de sang adéquate dans l'aorte. Il possède

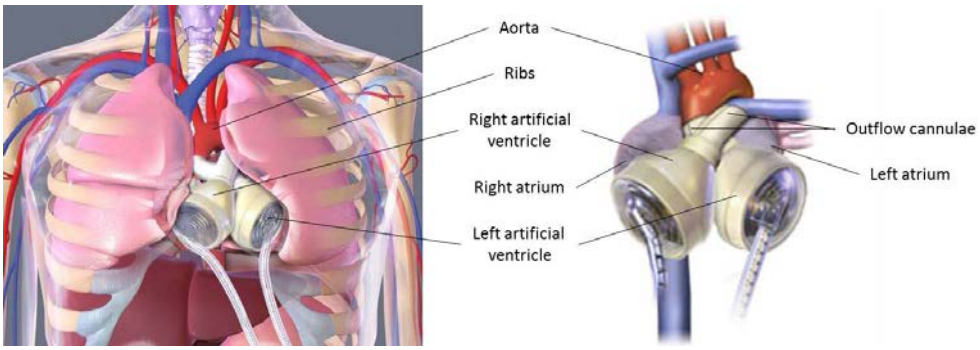

Figure 1 - Composition du cœur artificiel total (TAH - Total Artificial Heart)
Source: Syncardia.com

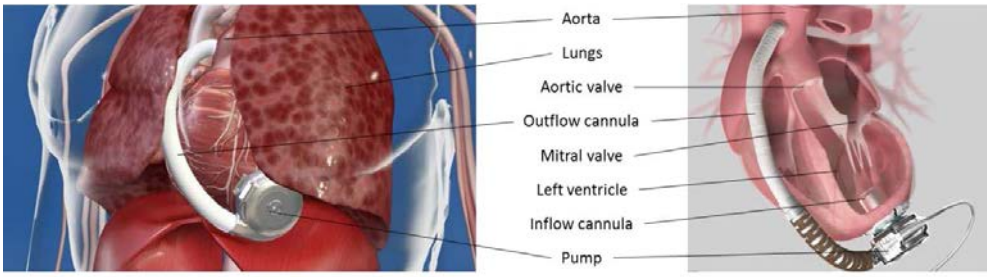

Figure 2 - Composition du dispositif monogauche (LVAD- Left Ventricular Assist Device)
Source: sjm.com

une canule apicale anastomosée à l'apex, une canule d'éjection suturée à l'aorte et un rotor situé entre les deux canules (Figure 2).

Les dispositifs d'ACM sont recommandés pour les patients présentant une IC terminale ne répondant pas aux traitements médicaux optimaux. Ils peuvent être utilisés en attente de greffe ou bien comme support permanent pour les patients ayant une contre-indication à la greffe. Bien que ces dispositifs assurent aux patients une meilleure mobilité et qualité de vie, devenant ainsi plus fréquemment utilisés, de nombreuses questions sont encore à élucider et diverses complications per- et post-opératoires peuvent survenir (thrombose de pompe, insuffisance cardiaque droite, dysfonctionnement du dispositif…).

- **Problématiques soulevées dans le cadre des ACMs**

Afin de limiter les évènements indésirables relatifs à l'implantation d'ACMs, plusieurs recommandations pré- et peropératoires existent. Cependant, il n'existe pas de technique standardisée et universelle, malgré la difficulté de l'intervention et l'état critique du patient. Une identification des facteurs associés au TAH et LVAD pouvant engendrer des complications per- et post-opératoires est une étape préalable à l'élaboration et au développement d'une solution de planification assistée par ordinateur opérationnelle.

Des modifications physiologiques apparaissent suite à l'implantation d'ACM ainsi que des variations mécaniques, fluidiques et morphologiques. Une multitude de facteurs peuvent influencer l'efficacité du dispositif et être responsables de complications. Si un certain nombre d'études ont été publiées dans ce domaine, il semble cependant difficile à ce stade des recherches de pouvoir anticiper le choix du dispositif idéal pour un patient donné ainsi que son positionnement en considérant tous les facteurs potentiellement responsables de complications. Deux catégories de contraintes sont donc étudiées au sein de ces travaux: (i) les conflits entre le dispositif et les organes environnants qui favorisent le dysfonctionnement de certains organes et (ii) la configuration d'implantation de la canule apicale du LVAD qui peut altérer l'hémodynamique du système cardiovasculaire. L'approche envisagée s'appuie sur deux axes complémentaires: une approche

géométrique pour une planification assistée par ordinateur et une approche biomécanique pour une analyse des interactions fonctionnelles et physiologiques associée à l'implantation de la canule apicale. La Figure 3 illustre l'approche générale que nous proposons.

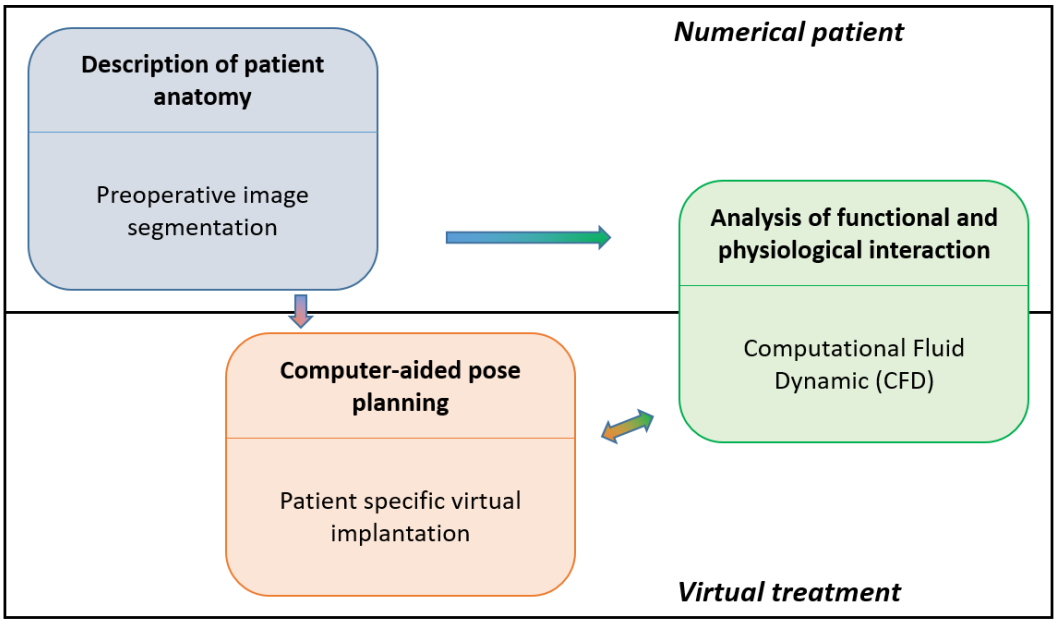

Figure 3 – Aide à la décision préopératoire pour la planification d'implantation d'ACM

❖ **Description des structures anatomiques**

En routine clinique, les chirurgiens utilisent des données cliniques ainsi que le CT (Computerized Tomography) scan afin de sélectionner les patients éligibles à l'implantation d'ACM. Alors que le CT pourrait être exploité pour anticiper le positionnement du dispositif par rapport à l'anatomie du patient en déterminant l'interaction dispositif-tissus, il est aujourd'hui principalement utilisé à titre qualitatif (détection de cancer, appréciation du parenchyme pulmonaire, calcifications des vaisseaux…).

Dans un premier temps, il s'agit d'identifier une stratégie appropriée de représentation virtuelle du patient dans l'objectif général d'une planification assistée par ordinateur. Trois modes d'utilisation de la segmentation peuvent être envisagées dans ce contexte: la visualisation, l'analyse quantitative pour la planification ou bien la simulation numérique. Après une analyse approfondie de l'état de l'art, plusieurs méthodes de segmentation ont été implémentées, adaptées et comparées pour chacune des structures d'intérêt suivantes : l'aorte, le cœur, les poumons et la cage thoracique (Figure 4).

La segmentation de l'aorte est aujourd'hui de plus en plus utilisée en clinique. L'évaluation d'une méthode de segmentation a montré que cette approche n'est pas une limite dans le contexte des ACMs. Une étude de l'état de l'art a révélé la nécessité d'une approche de segmentation fondée sur

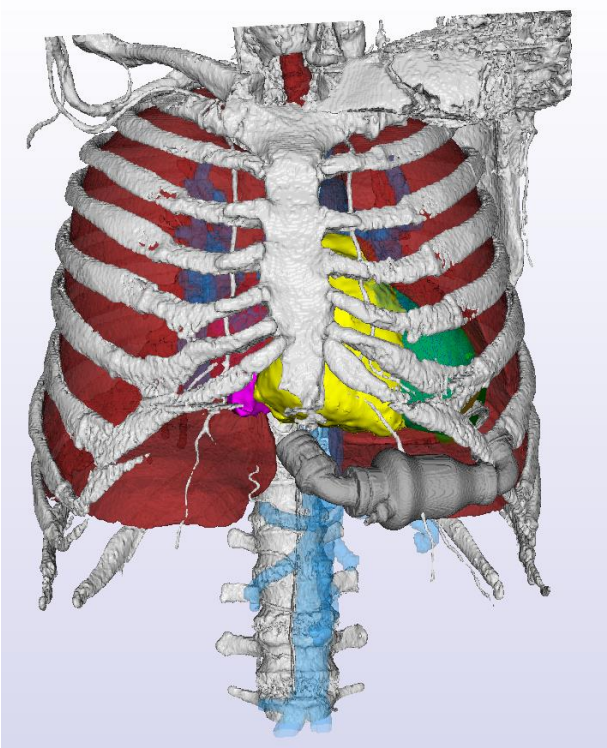

Figure 4 – Représentation du patient virtuel dans le cadre de la planification d'implantation d'ACM

des critères de forme (shape-based) pour l'extraction des cavités cardiaques. Une méthode de segmentation multi-atlas a été mise en œuvre. Les tests réalisés sur des données patients ont démontré son efficacité. Bien que celle-ci présente encore quelques limitations liées à l'inhomogénéité du contraste ou la présence de dispositif intracardiaque, les résultats restent satisfaisants pour être utilisés lors de la segmentation thoracique ou la planification. Nos études sur la segmentation des poumons et de la cage thoracique ont cependant révélé d'importantes limitations. Les difficultés sont principalement liées à la variabilité des pathologies pulmonaires dans le contexte des ACMs ainsi que la présence d'agent de contraste et d'artéfacts métalliques au sein des CTs.

- **Approche géométrique**

En se basant sur les résultats obtenus pour les segmentations des structures anatomiques d'intérêts, une nouvelle approche de planification assistée par ordinateur a été étudiée. Celle-ci consiste en un positionnement interactif d'une représentation 3D du dispositif au sein d'un patient virtuel (Figure 5). L'approche exploite une analyse de densité des structures afin de déterminer les conflits entre le dispositif et le thorax, ainsi que la segmentation multi-atlas du cœur pour spécifier les régions de superposition (collisions) entre le dispositif et le ventricule droit. Actuellement, les

recommandations cliniques préconisent d'implanter le LVAD de manière à avoir une canule apicale orientée vers la valve mitrale. En se basant sur ces recommandations ainsi que sur des études rétrospectives, des indices pertinents représentant le positionnement de la canule apicale ont été définis. Le potentiel de cette planification de pose assistée par ordinateur est prouvé lors d'une étude comparant une position virtuelle avec les poses postopératoires actuelles.

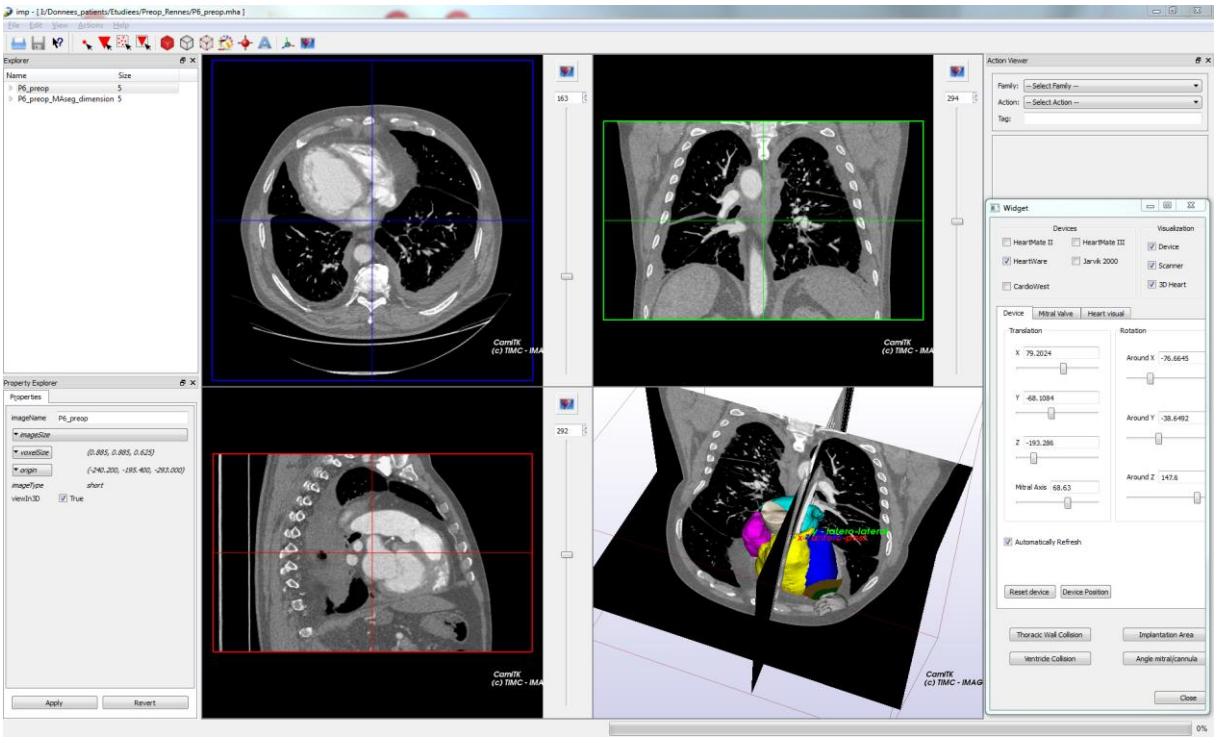

Figure 5 – Solution de planification

❖ **Approche biomécanique**

Une des problématiques importante liée à la planification d'implantation de LVAD réside dans le manque d'information concernant l'hémodynamique du ventricule gauche sous assistance. Non-invasive, la simulation fluide présente aujourd'hui un grand intérêt et se développe de plus en plus dans le domaine cardiovasculaire. L'objectif de l'approche biomécanique envisagée est d'étudier une méthodologie de modélisation en mécanique des fluides afin de pouvoir analyser l'influence du positionnement de la canule apicale sur l'hémodynamique du ventricule gauche.

La littérature actuelle ne relate que peu d'articles dans ce domaine et présente une variabilité importante dans la construction du modèle. Deux modes d'écoulement ont été étudiés : laminaire et turbulent (LES), ainsi que la pertinence de certaines approches de post-traitements. Ces modèles ont présenté des résultats similaires pour la répartition spatiale de la vélocité et du temps de résidence. La Figure 6 illustre la répartition du temps de résidence pour le modèle LES. L'hémodynamique ventriculaire induite par une canule apical orientée vers la valve mitrale et vers le septum (ventricule droit) a par la suite été étudiée. D'après les résultats obtenus, une

configuration vers le septum contribuerait à la création de vortex permettant ainsi un meilleur balayage de la cavité et favorisant le drainage du ventricule. Venant à l'encontre des recommandations cliniques actuelles, ces résultats mettent en avant la nécessité d'études plus approfondies sur le sujet. Notons cependant que lors de cette étude, seul l'aspect fluidique a été étudié. Les contraintes mécaniques telles que les contraintes de cisaillement du myocarde ou les phénomènes de sussions n'ont pas été considérés. A plus long terme, ces modèles de simulations pourraient être exploités afin d'augmenter l'information contenue dans l'imagerie cardiaque.

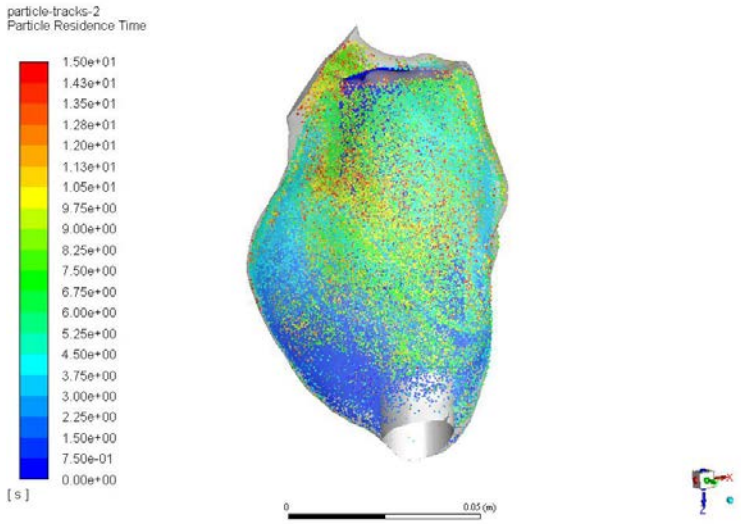

Figure 6 –Répartition du temps de résidence au sein de la cavité ventriculaire gauche sous assistance

Pour conclure, les principales contributions de cette thèse peuvent être résumées de la manière suivante: i) une évaluation approfondie de la littérature afin de fournir une vue d'ensemble des problématiques liées à l'implantation de dispositifs d'ACM ; ii) le développement d'une approche originale de planification assistée par ordinateur exploitant la segmentation pour une représentation virtuelle de l'anatomie du patient ; iii) l'analyse de deux modèles numériques en mécanique des fluides et de la pertinence d'approches de post-traitement d'un point de vue clinique.

Introduction

Heart Failure (HF) is a condition that appears when the heart is unable to pump blood with normal efficiency. This may lead to organs and tissues dysfunction and failure. Over 23 million people are currently living with HF worldwide, and this number is rising. Congestive HF is when HF progresses to an advanced stage. While the gold standard treatment is cardiac transplantation, there is a significant lack of heart donors worldwide.

Currently, the unique alternative to heart transplantation is a Mechanical Circulatory Support (MCS). MCS devices partially or completely replace the function of a failing heart. Two main categories are distinguished: Total Artificial Heart (TAH) and Ventricular Assist Device (VAD). Implanted through sternotomy (incision through the entire sternum), the TAH is composed of two artificial ventricles that replace the native ones. On the contrary, a VAD consists of an additional intrathoracic pump cannulated at the native heart. Its purpose is to support the ventricle function (right or left), resulting in adequate cardiac output into the corresponding artery. The most common VAD is the Left Ventricular Assist Devices (LVAD). Implanted through a sternotomy or a thoracotomy (lateral incision into the chest wall) the intrathoracic pump is composed of an inflow cannula anastomosed to the cardiac apex, an outflow cannula to the aorta, and a rotor located between these two. MCS devices are recommended only for patients with congestive HF unresponsive to optimal medical treatment, either as a bridge to transplantation or as a permanent implantation (destination therapy) for patient contraindicated to heart transplant. These devices ensure better patient mobility and quality of life, becoming thus more common.

To limit the risk of adverse events, several recommendations pertaining to pre- and intraoperative management for MCS implantation exist. However, despite the patient status and surgical procedures involved being very complex, there is no universal standard technique. In addition, significant intraoperative and postoperative complications are still reported so far (pump thrombosis, right-heart failure, device malfunction etc.) and a large number of unknown problems remain. Currently, surgeons exploit mainly patients' clinical data, echocardiography and Computerized Tomography (CT) scan to preoperatively select eligible patients by excluding those with limited expected survival. CT scan could also be used to explicitly assess device-tissue interactions.

This thesis investigates decision-support methodology in order to provide valuable information to surgeons for the planning and definition of a clinical strategy with the objective of decreasing postoperative complications and morbidity. This work has been jointly performed by ANSYS

France, LTSI (Laboratoire Traitement du Signal et de l'Image – Université de Rennes 1, INSERM) and the University Hospital of Rennes.

Many factors may influence MCS device efficiency and lead to complications. In order to devise a computer-aided planning in this context, the approach is to first analyse various issues raised by MCS implantation. Two categories of constraints leading to adverse events are distinguished: (i) conflicts between the device and intrathoracic organs which may promote organs dysfunction; (ii) the implantation configuration and setting adjustments that may alter blood flow and hemodynamics in the cardiovascular system. Two main approaches, geometric and biomechanical, are considered.

In current practice, CT is primarily used qualitatively rather than quantitatively. Our approach is aimed at investigating the feasibility and potential of a computer-aided implantation planning methodology for long term MCS device implantation. We first address the issue of anatomical structures description (heart, aorta, lungs and chest wall) with the aim of virtual patient representation. Then, we present a novel pose planning solution based on heart segmentation and grey-level analyses.

One significant challenge in computer-aided planning for LVAD implantation is the many unknowns around the influence of the implantation configuration on hemodynamics (into the pump, aorta, or left ventricle). Computational modelling of cardiac hemodynamic becomes more reliable and presents several advantages. Non-invasive, a large number of settings may be analysed through Computational Fluid Dynamic (CFD). The goal of the biomechanical approach is to investigate a methodology for CFD modelling in order to analyse the influence of the inflow cannula implantation configuration on the left ventricle hemodynamic. Different CFD models are assessed as well as the pertinence of several post-processing approaches.

The document is organized as follows:

- Chapter 1 introduces the clinical context by first describing the cardiovascular system as well as the heart function and physiology. The heart failure pathology, diagnostic and associated treatments are also featured. Focusing on MCS implantation, we present the different categories of devices with their specificities and detail the steps of the surgical procedure.
- Chapter 2 sketches an overview of factors related to MCS implantation that may lead to intraoperative and postoperative adverse events. Focusing on TAH and LVAD devices, the physiological changes involved by these devices are first presented. Then mechanical, fluidic and morphological issues are detailed. Finally, we develop the main objectives of the

thesis and the proposed approach based on: description of patient anatomy, computer-aided pose planning and analysis of functional and physiological interactions.

- Chapter 3 deals with the identification of a strategy for virtual patient representation. Numerous methods have been developed in the literature but segmentation may still present challenging issues, especially when dealing with several pathological cases. This chapter presents for the aorta, heart, lungs and thoracic wall an overview of segmentation methods from the literature. Then, several approaches are considered and compared to assess the feasibility of a 3D patient representation.
- Chapter 4 presents a novel computer-aided planning approach including an interactive positioning of a 3D geometrical representation of the implanted device within a virtual representation of the patient. Conflicts between the device and the RV or thoracic wall are detected using heart segmentation and a density analysis process. Based on clinical recommendations and retrospective analyses, relevant quantitative device positioning indicators are determined and included into the planning solution. Potential benefits and drawbacks of the methodology are also highlighted and discussed, through a comparison of planned and postoperative positioning.
- Chapter 5 deals with the elaboration of CFD model and aims at analysing left ventricle hemodynamic under LVAD support. Cardiovascular fluid simulation may be difficult because of the complexity of human blood flow behaviours. Very few works investigating factors related to the inflow cannula and affecting the left ventricle hemodynamic have been previously reported. Regarding the variability in CFD models presented in the literature, the goal of this chapter is to evaluate the influence of some parametrization settings on hemodynamic results in order to elaborate a representative model. The pertinence of several post-processing approaches with the goal of improving the clinical knowledge or define pose criteria for the decision support solution are also analysed. Finally, two inflow cannula configurations are analysed through CFD simulations.

Chapter 1 - Clinical Context

The cardiovascular system is a complex structure managing the blood circulation within the human body. When the heart does not function properly, all organs are affected, degrading thus the patient health. Heart failure is a serious pathology with a survival rate at 1 year of 63% (Bleumink et al. 2004). It is the second most costly condition for healthcare (Miller et al. 2013) by representing 1.5% to 4% of total US health care cost.

Congestive heart failure corresponds to an advanced stage of heart failure, which gold standard treatment remains the heart transplantation. However, some patients are contraindicated to heart transplant and there is a significant lack of donors. To overcome these limitations, Mechanical Circulatory Support (MCS) devices are currently presented as an alternative and become more common. This first chapter introduces the clinical context by presenting the cardiovascular system function and anatomy. Heart failure pathology and diagnosis are then detailed, followed by the description of MCS devices. The surgical procedure associated is finally featured in order to highlight the complexity of the implantation.

1. Cardiovascular system

The cardiovascular system is composed of the heart, vessels and the blood. Its function is to deliver proteins, nutrients and oxygen to the tissues, but also to transport carbon dioxide and waste products of the metabolism. An average person has about 5 litters of blood in the circulatory system. The flow is maintained through the entire circulatory system by the heart, a muscular organ playing the role of a pump.

1.1. Blood circulation

In the human body, there are two circulatory pathways: the pulmonary circulation considered as a low pressure circulation, and the systemic circulation with a high pressure circulation (Figure 1.1). The first one ensures the circulation between the heart and the lungs in order to remove the carbon dioxide and to re-oxygenate the blood and the second one links the heart with the rest of the body in order to carry oxygen and nutrients to all body tissues and organs.

The larger vessels called arteries carry blood out of the heart to organs, whereas veins bring back blood to the heart. The two main arteries begin at the heart level and are the pulmonary artery (right side) and the aorta (left side). The main veins, all ending at the heart are the cava veins

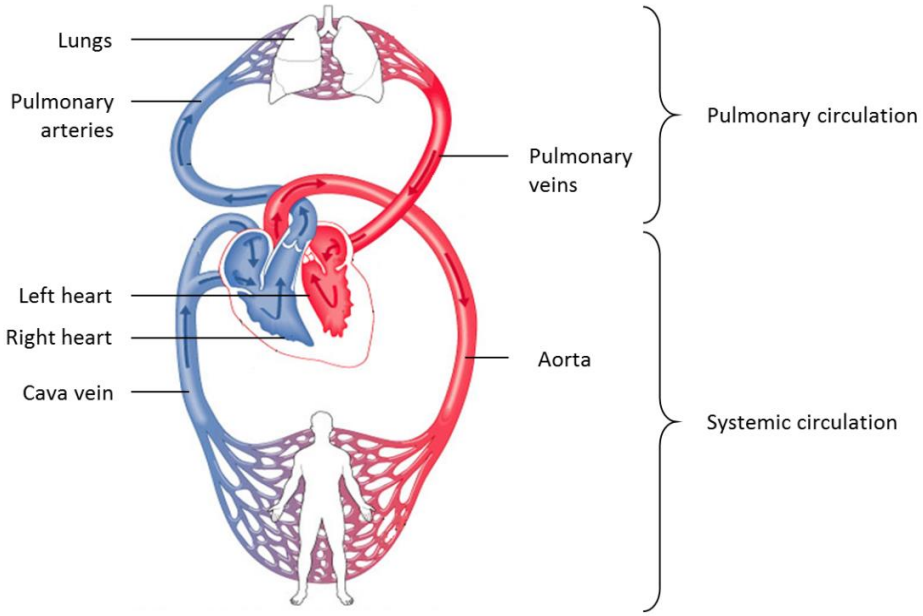

Figure 1.1 - Blood circulation
Source: 2011 Pearson Education, Inc.

(inferior and superior, right side) and the pulmonary veins (left side)(Figure 1.2). The external heart surface is surrounded by coronary arteries, aimed to vascularise the heart muscle.

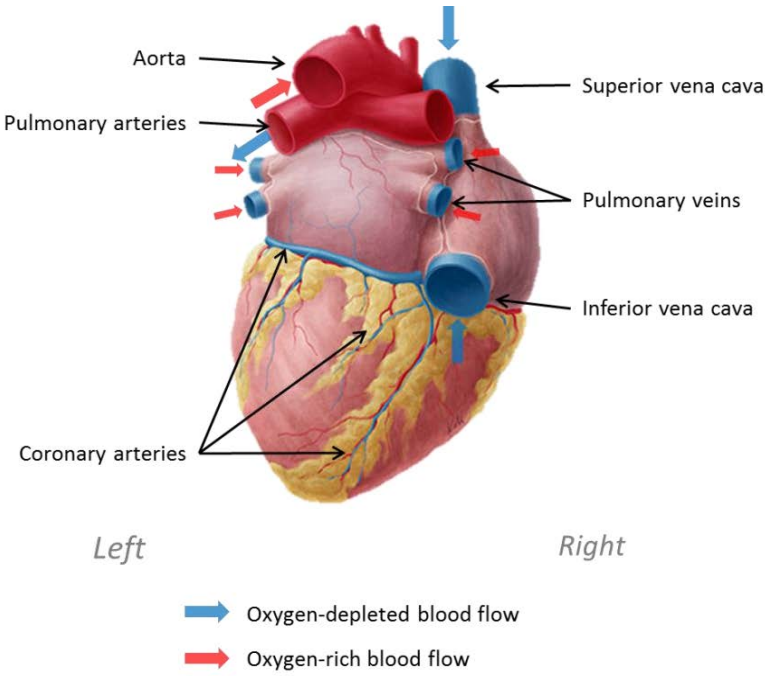

Figure 1.2 - Heart vessels[1]

[1] https://www.kenhub.com/en/start/diaphragmatic-surface-of-the-heart

1.2. The heart

The heart is located between the two lungs in the central compartment of the thoracic cavity (middle mediastinum). Its upper part lies to the vertebral column whereas the lower tip, the apex, lies to the sternum (Figure 1.3). The normal heart is composed of four distinct cavities: two atria corresponding to the upper chambers, and two ventricles that are the larger chambers located in the lower part. The ventricles are separated by the Inter-Ventricular Septum (IVS) and the atria by the inter-auricular septum.

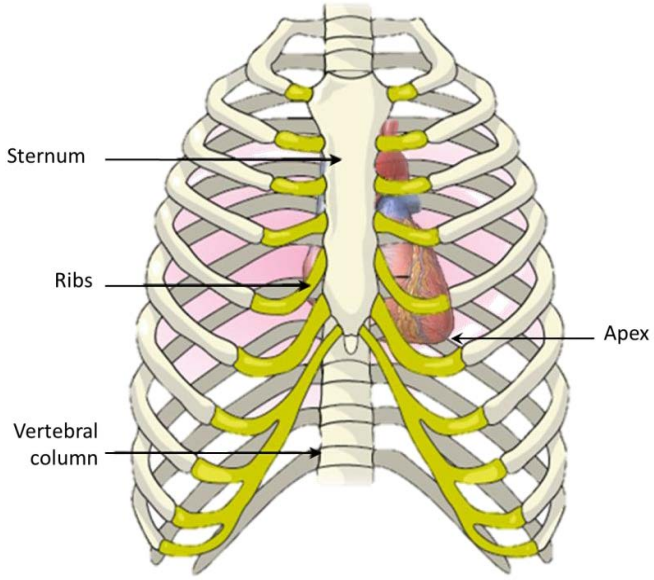

Figure 1.3 - Heart location in the thoracic cavity

Two sides can be distinguished in the heart, the right heart and left heart. Each side is composed of an atrium and a ventricle. The right heart gets back oxygen-depleted blood from the entire body and sends it to the lungs. Blood enters within the right atrium through the vena cava, goes into the Right Ventricle (RV) and is pushed into the pulmonary artery. In the left heart, oxygen-rich blood from the lungs enters into the left atrium through the pulmonary veins, goes into the Left Ventricle (LV), and is pushed into the aorta to be distributed to the rest of the body (Figure 1.4).

To allow the blood to circulate in only one direction, the heart contains four valves. The two atrioventricular valves are located between the atria and the ventricles, and attached to heart muscles in the ventricle by chordae tendineae. The Mitral Valve (MV) is in the left heart and the tricuspid valve in the right heart. The two semilunar valves are between the atria and the arteries leaving the heart: the Aortic Valve (AoV) in the left heart and the pulmonary valve in the right heart. Their opening and closing are regulated by the pressure gradient across them.

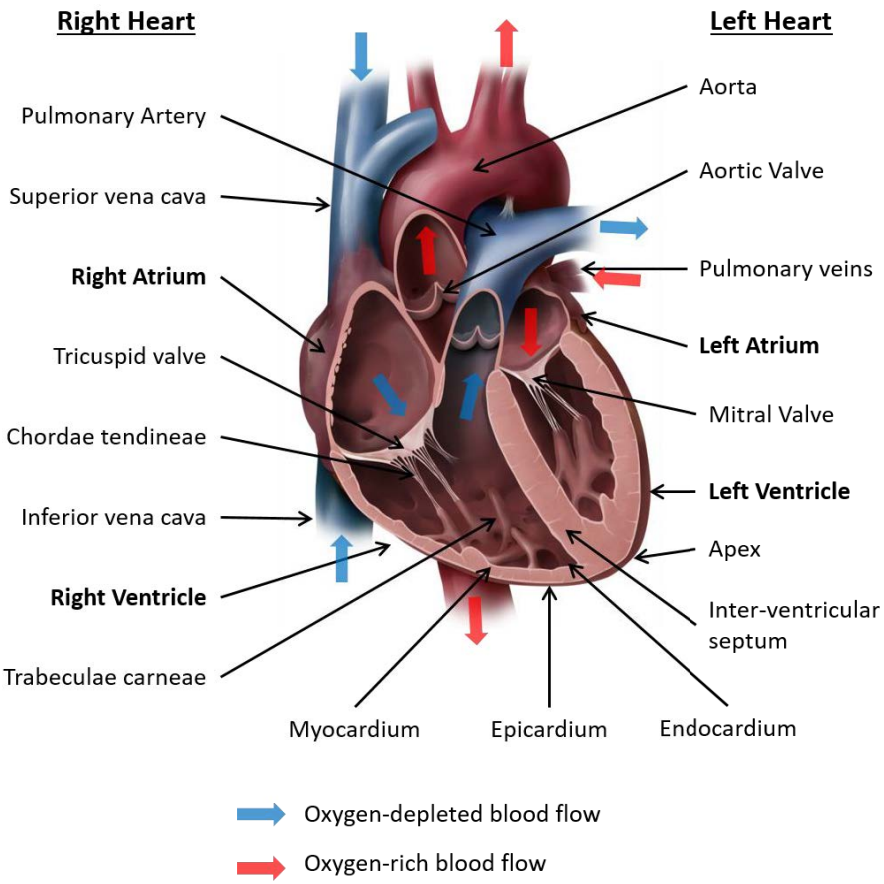

Figure 1.4 - Intracardiac anatomy and circulation
Source: University of Ottawa Heart Institute

The cardiac wall is composed of three layers:

- Endocardium is a thin membrane corresponding to the inner wall of the heart whose function is to regulate the myocardial contractility. This non adherent surface for blood collection is more irregular in ventricles because of the presence of trabeculae and chordae.
- Epicardium is the outer layer of the heart wall, composed of elastic fibrous tissue to protect the heart from trauma or friction. This thin membrane helps in the normal growth and maturation of the myocardium.
- Myocardium is the densest layer of the heart wall located between the epicardium and endocardium. This muscle tissue is responsible for the contraction of the heart. Ventricles have thicker walls than atrium, and more specifically the LV. Indeed, the thickness of myocardium is different between ventricles (much thicker for the LV that is working at high pressure whereas the RV is working with low pressure).

A fibrous sac called pericardium encloses the all heart and a fluid which acts as a lubricant to allow normal heart movement within the chest.

1.3. Mechanical and electrical physiology

The heart is composed of two pumps functioning in parallel that correspond to the right and left heart. The heart has an automatic nervous system, contractions are spontaneous and regular. The cardiac cycle represents a succession of electrical and mechanical actions that are repeated every heartbeat.

Two general mechanical events have been identified: the systole corresponding to the contraction of the myocardium, and the diastole which is the relaxation and filling of the heart. One heart beat is composed of three main actions (Figure 1.5):

- General diastole is the general relaxation of the 4 cavities. The two auriculo-ventricular valves are opened whereas the two semilunar valves are closed. This configuration allows the filling of the 4 cavities.
- Auricular systole is the contraction of the two atria in order to expel the blood into the ventricles.
- Ventricular systole is the contraction of the two ventricles, with the auriculo-ventricular valves closed and the semilunar ones open, thus ejecting the blood within the arteries.

Heart contractions are controlled by a repetitive electrical activity which is produced by cells located in the myocardium. This activity is represented by a curved named PQRSTU. The P wave corresponds to the atria depolarization which will allow the contraction of the atria (auricular

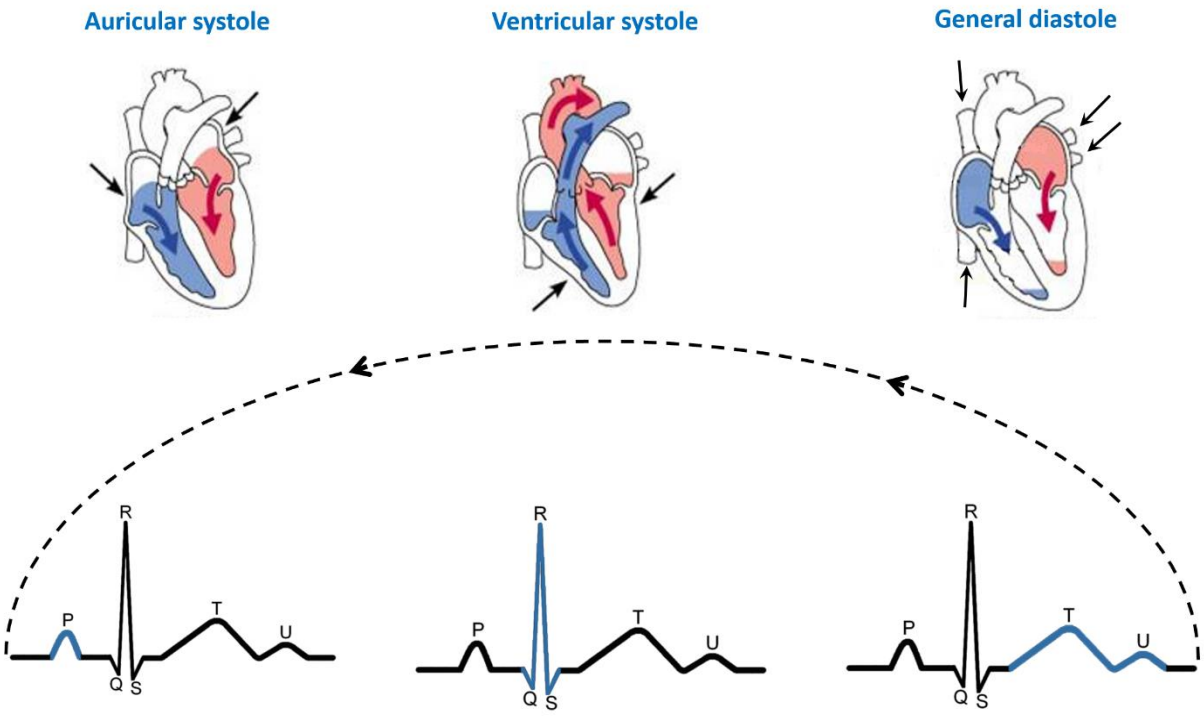

Figure 1.5 - Electrical and mechanical phases during a cardiac cycle

systole). The QRS complex is the rapid ventricles depolarization responsible of the ventricular contractions (ventricular systole), whereas the TU waves are the ventricles and papillary muscles repolarization, allowing the general diastole (Figure 1.5).

These depolarizations and repolarizations are conducted by 4 different elements composing the heart. The sinoatrial node initiates the cardiac cycle while the atrioventricular node controls the electrical impulse to the ventricles. Similarly, the bundle of His causes the ventricles' contraction while the Purkinje fibres create the synchronized contraction. Both are located into the ventricular wall (Figure 1.6).

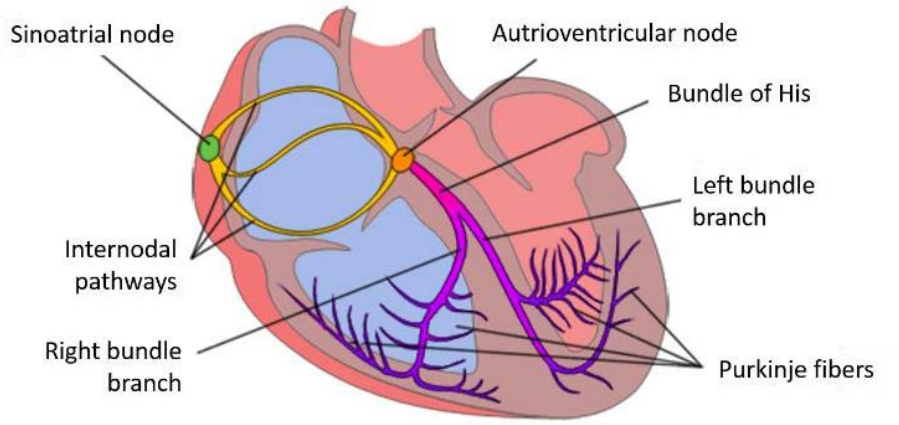

Figure 1.6 - Cardiac conduction system[2]

When the heart or blood vessels efficiency is affected, the term cardiovascular disease is employed. Leading cause of death in the United States, cardiovascular diseases represented in 2013 a death rate of 30.8% (Mozaffarian et al. 2016). Among cardiovascular diseases can be mentioned the Heart Failure (HF) which is a typical degeneration of the heart function marked with a still too high morbidity and mortality. Third cause of cardiovascular disease death, projections predict that the prevalence of HF will rise by 46% between 2012 and 2030.

2. Heart failure

HF is a chronic and progressive condition in which the heart is unable to pump blood with normal efficiency and to keep up with the demands of the body (McMurray et al. 2012). With insufficient blood being delivered, organs and tissues do not receive enough oxygen and nutrients to function properly. It can occur at any age but is most common in the elderly (Figure 1.7). Worldwide, 1-2% of people have HF (e.g.: France: 2.2%; UK: 1.3%; Canada: 1.5%, US: 1.9% in 2014) and it

[2] https://inhalotherapie.com/apprendre/electrocardiologie/systeme-de-conduction-electrique-du-coeur/

represents 1-4% of all hospital admissions in developed countries (Ponikowski et al. 2014).

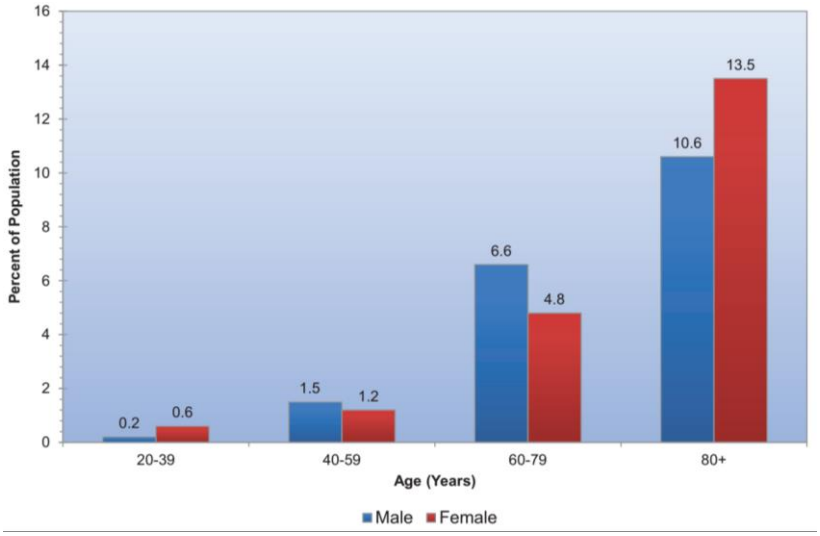

Figure 1.7 - Prevalence of heart failure by sex and age (2009–2012).
Source: National Center for Health Statistics and National Heart, Lung, and Blood Institut (Mozaffarian et al. 2016)

2.1. Pathology and symptoms

Right, left or both ventricles can be affected. Right HF is characterized by the difficulty of the RV to pump the blood into the lungs. It causes blood flow backs in the veins and fluid retention in the lower extremities. Left HF is defined by a left heart dysfunction and represents the vast majority of HF pathology. When the heart cannot fill enough the cavity because of a stiff muscle which is unable to relax, we talk about diastolic left HF. On the contrary, systolic left HF is when the LV fails to contract normally and does not push enough blood into the circulation system. Systolic left HF represents the majority of left HF.

Many conditions can lead to HF. The most common reason is the damage of the heart muscle due to a "heart attack" (coronary disease). However, it can also be caused by high blood pressure (e.g. pulmonary hypertension), cardiomyopathy (e.g. heart muscle disease), heart valve damage, arrhythmia (irregular heart rhythm), congenital heart condition, viral infection, etc. (Dickstein et al. 2008). Some risk factors may also promote this pathology such as obesity, high cholesterol, diabetes, alcohol, tobacco or toxins.

Before having symptoms, the heart tries to compensate the alteration of the blood flow by pumping faster, increasing the muscle mass in order to pump more strongly, or enlarging the heart chamber in order to pump more blood. However, these natural reactions temporarily operate. Shortness of breath and unusual fatigue often happen in the end (Clark 2006). These symptoms can develop

rapidly and tend to get worst over the time, leading to frequent hospitalization. Patients with a HF clearly have an impaired quality of life compared to healthy population, losing their physical capacities, autonomy, as well as emotional happiness (Heo et al. 2009).

2.2. Diagnosis and treatments

Currently, 48% of patients with HF die within one year of its diagnosis (Cowie et al. 2000). Thus, it is important to identify this disease at an early stage. Clinical history and results from physical examination provide the principal means in assessing the probability of HF. First examinations include evaluation of symptoms, blood pressure measurements, listening of the heartbeat and lungs for breathing alteration. To confirm HF presumption, further investigations are made by various clinical evaluations (Dickstein et al. 2008; McMurray et al. 2012), such as:

- Laboratory tests to search abnormal blood cells, infection or important level of specific substances such as sodium, potassium, and natriuretic peptides that are elevated in HF. Biological impact of HF on peripheral organs is also evaluated through renal and hepatic functions.
- Stress tests to show the heart performance under different levels of stress and detect exercise intolerance
- ElectroCardioGram (ECG) to record the heart rhythm and detects abnormalities or irregularities
- Echocardiogram to record the heart's structure and motion to determine poor blood flow, muscle damage or abnormal contraction
- Magnetic Resonance Imaging (MRI) of the entire heart to detect and characterize tissue damages
- Coronary angiography performed through catheterization to detect blockage of the coronary arteries

Patients' HF is classified according to the severity of the symptoms and functional limitations. The most common system is the New York Heart Association (NYHA) classification (The Criteria Committee of the New York Heart Association 1994) (Table 1-I). Grades are used to classify the shortness of breath severity across all pathologies, while stages focus on HF severity. For refractory or terminal HF represented by the class III-IV, end-stage or congestive HF terms are employed. The Interagency Registry for Mechanically Assisted Circulatory Support (INTERMACS) classification is increasingly used to stratify advanced HF (NYHA class III and IV). Figure 1.8 illustrates the stratification of the INTERMACS classification system. Profile 7 corresponds to less

Table 1-I - The New York Heart Association Classification
Source: (The Criteria Committee of the New York Heart Association 1994)

Class	Patient main symptoms
I (Mild)	No symptoms during typical physical activity
II (Mild)	Normal physical activity may cause fatigue, palpitations, or shortness of breath, but comfortable at rest
III (Moderate)	Even mild activity may cause fatigue, palpitation, or shortness of breath, but likely comfortable at rest
IV (Severe)	Unable to carry on any physical activity without symptoms which are present even at rest

Stage	Objective Assessment
A	Presence of HF risk but no heart disease and no symptoms
B	Presence of minimal heart disease but no structural changes in heart (mild symptoms)
C	Evidence of moderately severe heart disease and symptoms
D	Evidence of severe heart disease with continued symptoms and limitations

advanced congestive HF (included in NYHA class III), and profile 1 to patient in refractory cardiogenic shock (part of NYHA class IV).

The purposes of HF treatments are to treat the underlying conditions (coronary disease, diabetes, *etc.*) in order to reduce symptoms, avoid the worsening of the patient conditions and improve its quality of life. The treatment depends on the type and severity of the pathology. For most people, it involves lifestyle changes such as salt restriction, stress management, get enough sleep, and elimination of tobacco and alcohol, or medication treatment. There are several classes of medication depending on whether the heart needs to be relaxed or strengthened. This treatment improves the heart muscle function controlling the blood pressure and the pumping action of the heart.

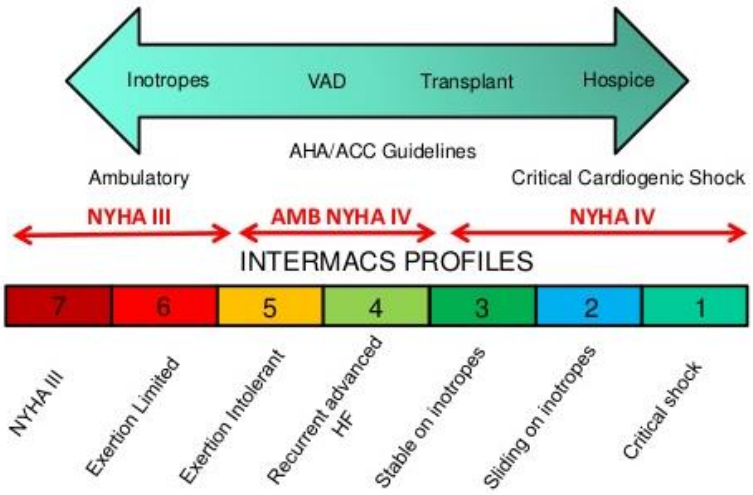

Figure 1.8 - INTERMACS classification system compared to NYHA classification
Source: Duke Clinical Research Institute

In selected cases of HF, medication may not be sufficient, making surgical procedure necessary in order to improve the failing heart. Several procedures may be performed depending on clinical conditions (Delmo Walter & Hetzer 2013):

- Bypass surgery. Aimed to restore the blood flow into the coronary arteries; this procedure consists in using a biological conduct (vein or artery harvested from another part of the body (leg, arm or chest)) in order to bring good blood flow beyond the coronary stenosis.
- Heart valve repair/replacement. The surgeon may remove calcification or extra tissue, as well as repair the cords or reattach them. When the valve cannot be repaired, it is mainly replaced by a prosthetic one which is mechanical or biological. This procedure can be made by an open heart surgery, a minimally invasive surgery or a cardiac catheterization.
- Ventricular reconstruction. The goal is to reshape the heart in order to improve its function. This is an option for patient with ventricular dilatation. This procedure is usually performed with bypass operation or valve repair.
- Intra-Cardiac Device (ICD) implantation. These devices monitor the heart rhythm by delivering electrical stimulation. It enables the heart to pump blood more efficiently. Among ICDs there are pacemakers that speed the heart rate, or defibrillators that paces or shocks the heart when it beats at a dangerous rhythm. Defibrillators can also be used as a pacemaker.
- Heart transplant. It consists in replacing the diseased heart by a healthy one from an organ donor. This surgery is for patient with end-stage HF, when all other alternative treatments have failed.
- Mechanical Circulatory Support (MCS) devices implantation. Implanted into the chest or abdomen, these devices help the heart to pump blood to the rest of the patient body. This solution is used when a patient needs Heart Transplant (HTx) that is impossible because of a lack of donor or contra-indication.

2.3. End-stage Heart Failure (HF) and heart transplant

If the first HTx was performed in 1967 in South Africa with an 18-days survival, nowadays, more than 4 000 HTx occur worldwide per year (Stehlik et al. 2012). With a survival rate of 50% at 10 years, HTx is considered as the gold standard treatment for congestive HF. According to the International Society of Heart and Lung Transplant (ISHLT) transplant registry, the number of HTx has increased over the last decades (Figure 1.9). However, it is still insufficient comparing to the dramatic increase of the number of candidates (Figure 1.10).

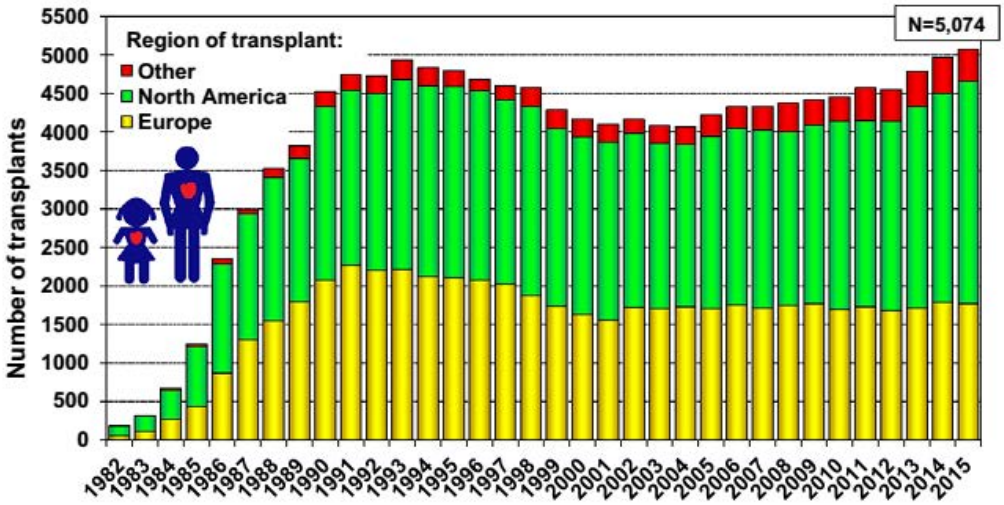

Figure 1.9 - Number of adult and pediatric heart transplants by year (transplants: 1982–2015) and geographic region

Source: The Registry of the International Society for Heart and Lung Transplantation: Thirty-fourth Adult Heart Transplantation Report-2017 (Lund et al. 2017)

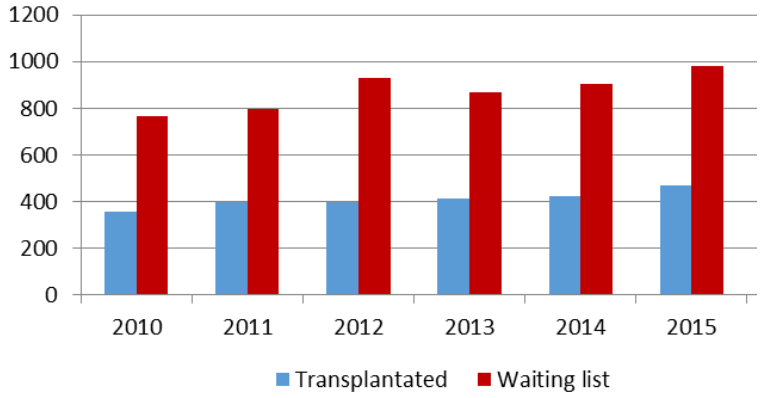

Figure 1.10 - Number of patients in the waiting list compared to transplanted ones, by year, in France.

Source: (Agence de la biomedecine 2015)

Currently, the only alternative to HTx is the implantation of MCS devices. With the steady advance of technologies, there has been an important improvement of these devices and a major increase of their use over the last years.

2.4. Mechanical Circulatory Support (MCS) devices

Cardiac mechanical pumps are devices that partially or totally replace the function of a failing heart. All have the same composition (Figure 1.11). They consist of a blood pump (pumping chamber) that replaces or assists the failing ventricle(s), and an external controller (pneumatic or electronic) that runs the device and manages operating parameters such as alarms and speed. The pump and

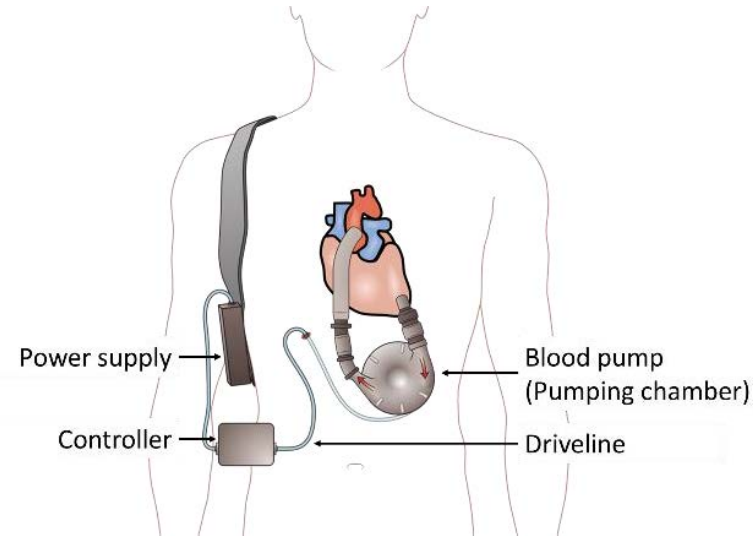

Figure 1.11 - Mechanical Circulatory Support composition – Example of left ventricular assist device (LVAD)

the control unit are connected via a driveline. The energy source of the rotor can be pneumatic, hydraulic, electric or electromagnetic.

MCS devices were first used to keep the patient alive waiting for HTx. Nowadays, they can be used in four different ways (Stewart & Givertz 2012):

- Bridge To Transplant (BTT): the device is implanted temporarily to support the heart functions while waiting for a compatible heart donor. By restoring the systemic blood circulation, the organs' functions are improved, thus maintaining the patient in a sufficient good health to undergo future HTx. This strategy may even improve health of a contra-indicated patient to become a potential organ transplant recipient. Use of MCS maximizes also post-HTx survival (Karamlou et al. 2013).
- Bridge To Recovery (BTR): the device is implanted as a bridge to recovery when the heart has the potential to recover and to be strong enough to pump blood efficiently. After this period during which the VAD assists the heart, the patient returns to medical management. If the design of the pump allows it, the device is explanted. In the other case, the device is deactivated. However, VAD deactivation is currently a controversial issue among clinicians and institutions, due to the important complications that it may promote.
- Destination Therapy (DT): the device is implanted for a permanent support (or definitively). Some patients are contra-indicated to HTx because of their age (patients older than 70 years are ineligible for HTx) or specific health conditions (Flécher 2014). Currently, the only existing alternative for these patients is a MCS device implantation.
- Bridge To Decision (BTD): the device is implanted for a short-term period during which clinicians develop a definitive treatment strategy.

MCS represents a solution to overcome the lack of donors, and for patients with contra-indications to HTx. If they were mostly used as a temporary solution to bridge the time to HTx, nowadays, they are largely considered as a destination therapy (Figure 1.12).

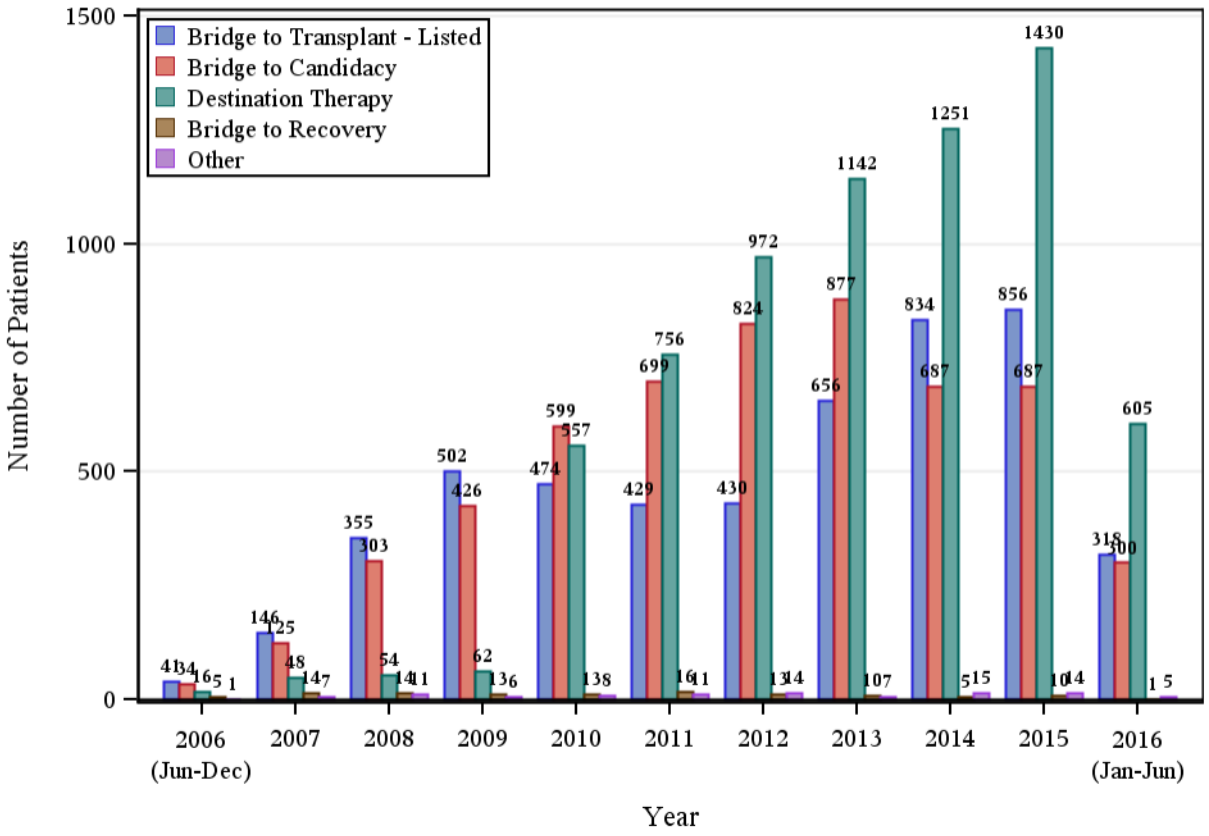

Figure 1.12 - INTERMACS – Implants per year by device strategy, 2006 to 2016.
Source: INTERMACS Federal Partner Report 2016 – Q2 (Kirklin et al. 2016)

Two categories of MCS devices exist: Total Artificial Heart (TAH) and Ventricular Assist Device (VAD). Similar to heart transplant, the TAH replaces the native heart functions, and requires the removal of the two failing ventricles. On the contrary, VADs are cannulated to the sick native heart and used to support the heart function and the blood flow. MCS devices are distinct from the cardiopulmonary bypass machines that are used in the operating theatre and allow open heart surgery. One should also differentiate long term mechanical support from short term mechanical support (days or few weeks) such as extracorporeal membrane oxygenation, intra-aortic balloon pump, Impella device, Tandem heart etc. that is beyond the scope of this thesis.

2.5. Total Artificial Heart (TAH) pump

A TAH pump is a prosthetic device which external wall is made out of metal (titanium for biocompatibility), plastic or ceramic. This pump is intrathoracic and composed of two artificial

ventricles that replace the native RV and LV. These artificial ventricles are independent or fixed to each other (Figure 1.13). Each one contains the two corresponding mechanical valves (or biological valves for TAH in development), and an Outflow Cannula (OC) that links the ventricle to its corresponding artery: pulmonary artery for the RV and aorta for the LV. The motor-driven pumping system can be hydraulic or pneumatic.

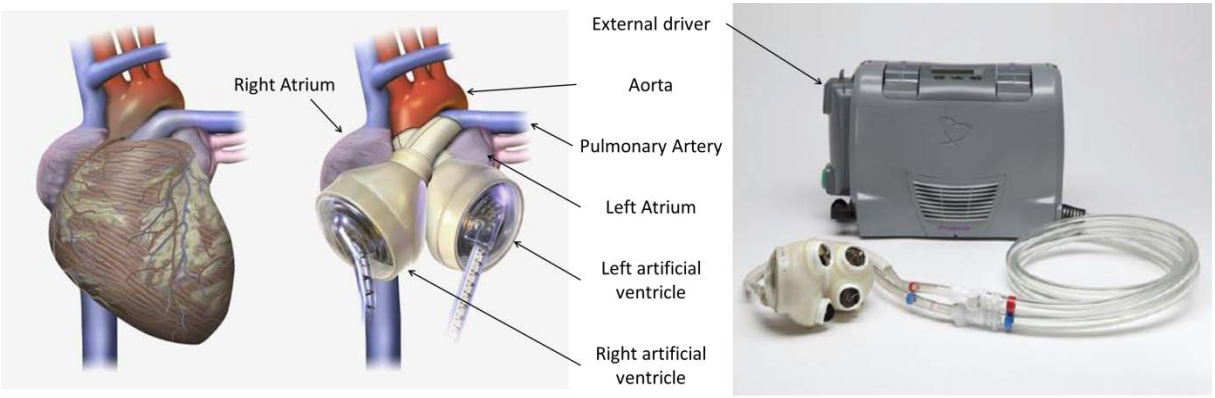

Figure 1.13 - Total Artificial Heart - TAH
Source: Syncardia.com

The first in-human TAH implantation was made in 1969 in Houston (US), with the Liotta heart (Dr. Denton A. Cooley & Dr. Domingo Liotta) (Cook et al. 2015). But this device did not receive the Food and Drug Administration (FDA) approval. Over the past 50 years, several TAH have been developed worldwide (Cohn et al. 2015; Sunagawa et al. 2016). The eight principal TAH are presented in Annex 1. One did not receive the FDA approval; two only underwent animal implantation and were not considered adequate for human implantation; two received a FDA approval over the last two decades; and three TAH prototypes are currently under development and underwent only animals testing.

2.6. Ventricular Assist Devices (VAD) pump

VADs are aimed to help the cardiac circulation of the ventricle(s). They can be implanted to support the RV (RVAD – Right Ventricular Assist Device), the LV (LVAD – Left Ventricular Assist Device) or both (BiVAD – Bi-Ventricular Assist Device). For LVAD and RVAD, the blood circulates through the blood pump via two cannulas: the Inflow Cannula (IC) where the blood enters into the pump and the OC that carries the blood out of the pump (Figure 1.14). The IC is anastomosed to the right atrium or the RV for the RVAD and to the apex or the left atrium for the LVAD. The OC is commonly anastomosed to the pulmonary artery for the RVAD, and to the aorta for the LVAD. The BiVAD is a combination of one RVAD and LVAD.

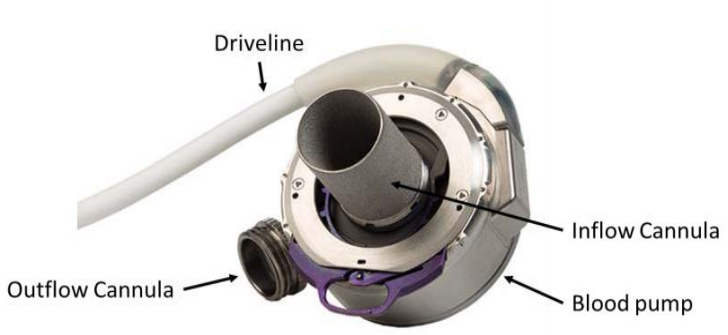

Figure 1.14 - Ventricular Assist Device pump – VAD - Example of a LVAD
(HeartMate III - Thoratec Inc., Pleasanton, CA)
Source: sjmglobal.com

This blood pump can be positioned in three different places represented in Figure 1.15 (Cuttone et al. 2011):

- Extra-corporeal position: the blood pump is external and anastomosed to the heart with long OC and IC tubes. These devices can also be connected to oxygenators (*e.g.*: Levitronix Centrimag pump from Thoratec Inc.).
- Para-corporeal position: the blood pump is external but anastomosed with short OC and IC tubes. The device is in contact with the patient (*e.g.*: pVAD from Thoratec Inc.).
- Intra-corporeal position also called intra-thoracic: the blood pump is located inside the thorax, near the heart (*e.g.*: HeartMate II LVAD from Thoratec Inc.).

The first VAD implant was in 1966 by Dr. Debakey (Liotta 2002). Since then, an important evolution of these devices can be noticed. They are classified into two categories:

- Pulsatile-Flow VAD (PFVAD) represents the first generation. This type of pneumatic device (air-powered) is composed of a volume displacement pump and two mechanical valves.

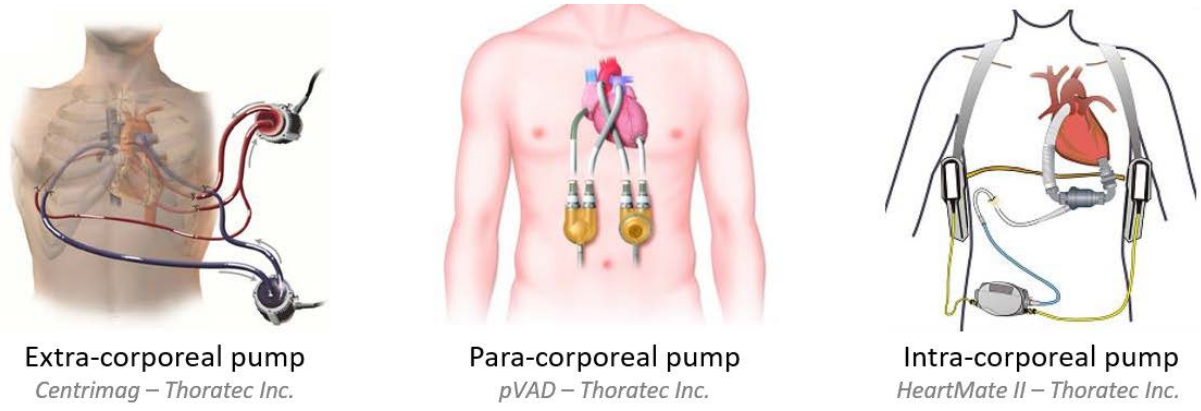

Figure 1.15 - Device positioning

- Continuous-flow VAD (CFVAD) represents the second and third generation of VAD. The second generation devices are designed with an axial or centrifugal flow pump and a "contact-" bearing design. The third generation devices use a centrifugal or mixed (axial and centrifugal) flow pump with "noncontact-" bearing design. Frictions of motion between the different parts of the devices are reduced thanks to a rotor that is in full magnetic/hydraulic levitation, thus improving the durability.

CFVADs are smaller compared to PFVADs, and present a better reliability and durability. Worldwide, many VADs have been developed, varying the technologies, geometries, lengths, sizes, *etc.* The Annex 2 presents several devices from each generation.

3. Surgical procedure

3.1. Patient selection and preoperative exams

A patient is a potential candidate to MCS device implantation according to multiple factors, such as symptoms, age, body size and medical conditions. The current recommendations for MCS are patients (Wilson et al. 2009):

- with refractory end-stage ventricular HF (NYHA Class IV),
- with life expectancy inferior to 2 years
- who are not a candidate for heart transplant or that are in the waiting list,
- whose all medical managements failed to respond,
- with an ejection fraction less than 25%,
- who have demonstrated functional limitation with a peak oxygen consumption of less than or equal to 14 ml/kg/min.

Patients with class III on the NYHA classification have shown higher survival rate at 2 years with medical therapy (70-80%) than CFVAD (58%) (Stewart & Stevenson 2011). Therefore, to date, only patients with a class IV are considered as potential candidates to MCS. For some who have blood clotting disorders, other severe organ disease, or infections that cannot be treated with antibiotics, the MCS is unappropriated. The success is also based on psychological outcomes. An important part of the selection considers thus psychology and patient management. Patients experience relatively high levels of psychological distress even after MCS device implantation. They must be perfectly capable of undergoing it.

After selection, medical professionals choose the appropriate device according to the instructions for use and how long the MCS device will support the patient health. These two determinant factors help to choose between the type of MCS (TAH, LVAD, RVAD or BiVAD). However, the choice

of the final device is less conventional and depends on some physiological parameters, clinical current practices and habits.

3.2. Surgical intervention

MCS device implantation is a surgical procedure that takes 3 to 6 hours. The surgical process varies from a patient to another and from surgeon to surgeon. In this sub-section, the main steps are briefly explained. The clinical guidelines for device pose as well as clinical recommendations during surgery and potential intraoperative complications will be more detailed in Chapter 2.

- Patient preparation

The MCS device implantation is performed under general anaesthesia. Anaesthesiologist starts placing monitoring intravenous lines that will deliver the patient medicines. Next, a breathing tube connected to a ventilator is placed down the throat to deliver air to lungs during surgery, and finally, the surgical site is prepared and sterilized. The surgeon can then operate.

- Thoracic incision

An incision is made to provide access to the heart and the aorta. For TAH, the surgical incision is performed through a median sternotomy (surgically sawing through the entire sternum) (Figure 1.16), whereas for VADs, median sternotomy or thoracotomy (incision into the chest wall, which is minimally invasive) can be performed. Different thoracotomies have been executed through the literature (Hanke et al. 2015). However, sternotomy is currently most commonly used (Feldman et al. 2013).

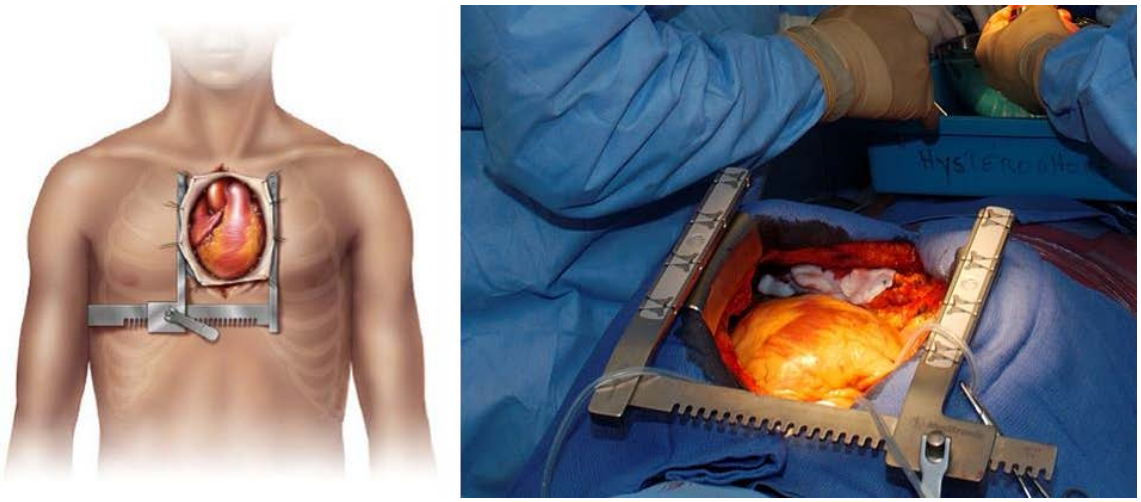

Figure 1.16 - Conventional incision - Sternotomy

- Heart-Lung machine

For TAH implant, an ExtraCorporeal Circulation (ECC) is performed right after the incision, with a heart-lung machine (also called cardiopulmonary bypass pump) (Figure 1.17). Extracorporeal

circulation takes the function of the heart and lungs for the length of the surgery. First, a tube is connected to the right atrium, vena cava, or femoral vein in order to reroute the blood entering the heart into the machine. Then, blood is filtered and oxygenated within the pump and a cannula is anastomosed to the ascending aorta, or the femoral artery to return oxygenated blood into the body. Subsequently, the heart is stopped in order to be replaced by the extracorporeal circulation machine.

For VAD implants, the surgical procedure may vary. In the case of a sternotomy opening, a cardiopulmonary bypass with a still beating heart is the most frequently used procedure. Though, the heart may be stopped in order to procced at the same time to some associated surgery (aortic valve replacement for example). On the contrary, with a thoracotomy opening, the most common type of procedure is a beating heart without cardiopulmonary bypass.

Figure 1.17 - Extracorporeal circulation

- Insertion of the MCS device

The surgical MCS device insertion process varies according to the type of device. For a TAH implantation, both ventricles are excised (Figure 1.18). Contrary to HTx, 1 cm of ventricular muscle around the atrioventricular valves is left. The mitral and tricuspid valve leaflets are excised, while preserving the annulus. The great vessels (pulmonary artery and aorta) are then transected just above the respective valves and separated from one another. The TAH atrial connects are sutured to the respective valve annulus, and the OCs are anastomosed to the respective vessels. Two incisions are made in the left upper abdomen for the drivelines.

For a VAD, the entire heart is conserved. In the case of LVAD, the insertion first starts with the ventricular whole localization via a transoesophageal echocardiogram. An IC ring is then sutured to the ventricular epicardium and the myocardium wall inside the ring removed. Depending on the LVAD, the myocardium may first be removed, followed then by the IC ring suture

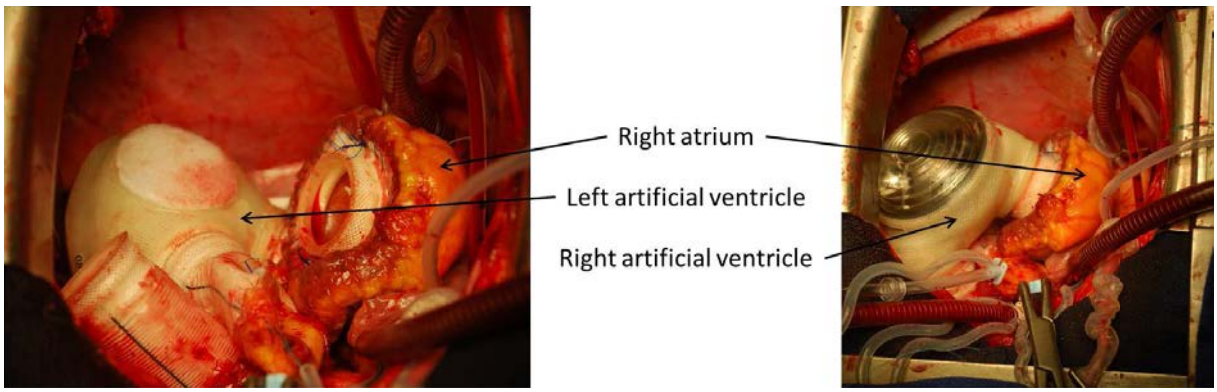

Figure 1.18 - TAH implantation (example of the Syncardia TAH)

(Figure 1.19). The IC is finally fixed to the ring and the OC anastomosed to the corresponding artery. According to the type of LVAD, the pump can be placed next to the heart in the chest, or in a pump pocket localized in the left upper abdomen right below the heart and diaphragm. Notice that RVAD implantation is similar to the LVAD one, but at the RV. In the same way, BiVADs implantation corresponds to the insertion of a LVAD with a RVAD. Most drivelines are tunnelled through an incision in the abdomen.

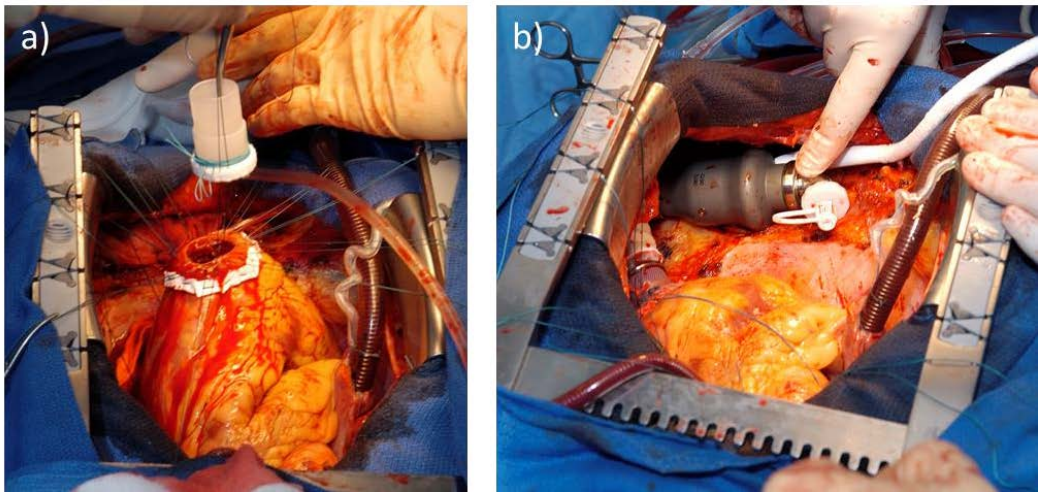

Figure 1.19 - LVAD implantation with a) the insertion of the inflow cannula ring; b) the insertion of the LVAD within the intrathoracic space.

- Device adjustment and patient closure

Once the MCS device is implanted and connected to the controller, cardiac cavities, the cannulae and pump are purged to remove all air inside. The device is then started and the pump capacity is increased as the extracorporeal circulation capacity is decreased. Finally, the MCS device speed is adjusted according to anatomical and physiological parameters. This procedure ends with the heart-lung machine removal and the chest closure.

3.3. Medical follow-up and complications – INTERMACS analysis

According to INTERMACS study, the use of MCS has several benefits for patients. This prospective analysis is based on data collected from June 23, 2006. In 2016, 166 hospitals were participating and 17,708 patients with MCS device implanted were enrolled (Kirklin et al. 2016). Results showed that such devices improve the patient's quality of life in terms of "Usual Activities" and "Self-care". Relieving some HF symptoms such as tiredness or breathlessness, many routine activities can be resumed. In the most recent studies, 80% of patients are alive at 1 year, and 70% are living at 2 years. Therapy with the permanent LVAD device doubled also the one-year survival rate of patients with congestive heart failure as compared with drug treatment alone. Nevertheless, significant postoperative adverse events have been reported so far (Copeland et al. 2012)

Bleeding represented the most important postoperative complication between 2012 and 2014, with a percentage of 26.7% (Kirklin et al. 2015). Patients may present chest bleeding right after surgery, or internal bleeding may occur later and be determinant. **Infections** take the second place with a rate of 24.9%. It most frequently occurs in the first few weeks or months after implant. But it may also happen at any time during support. This cannot be cured and needs empirical antibiotic treatment. Some patients such as immunosuppressed or diabetic ones are more likely to present infections, influencing preoperatively the choice of MCS device (Givertz 2011). **Cardiac arrhythmia** is a quite common complication after MCS device implantation (13.9%). HF promotes atrial arrhythmia and its prevalence increases with severity of the disease (NYHA class I and II: ~4%, whereas in class IV it is nearly 50%). After LVAD implantation ventricular arrhythmia may appear and more particularly in the first 30 days rather than after. With a cardiac arrhythmia, the mortality rate increases to 54% (otherwise 9%) (Kadado et al. 2017). **Thrombosis events**, representing 2.3% of the complications, can be caused by blood clots leaving the pump, high blood pressure, or bleeding into the brain. The rates of strokes appear to have declined with the CFVAD and use of anticoagulation. But the ongoing risk has not been eliminated. Finally, **Right heart failure** takes the sixth place with 1.7% of adverse events. Patients who underwent LVAD implantation presented initially only a severe weakness of the LV. Though, all were at risk for developing right HF after surgery. In most of the cases, this complication can be managed with short-term medication support, but severe cases may require a HT or a RVAD additionally to the LVAD as bridge to transplant. To limit the number of right HF complications, a "risk-score" based on clinical and hemodynamic predictors is preoperatively calculated by healthcare practitioners (Mangi 2011). If the score is too high, this patient directly benefits from a BiVAD or TAH.

Several others complications may appear, but the principal cause of death after MCS device implant is **neurologic events** (19.2%) and **multisystem organ failure** (14.8%). Device malfunction which

was a major cause of hospitalization and mortality in patients with PFVAD, represents nowadays with CFVAD only 3.5% of deaths. CFVAD have thus demonstrated improved durability. Malfunction still occurs, but alarms indicate these problems that are generally minor and easy to deal with. An entire VAD replacement remains possible when needed but is rarely performed in clinical practice.

4. Summary

Although HTx patients demonstrated better quality of life than those with a LVAD (Jakovljevic et al. 2014), MCS implants represent a great alternative to the shortage of donor. With MCS, 79% of destination therapy patients (NYHA class III or IV) at 24 months improved to class I or II (Rogers et al. 2010). Furthermore, since 2001, there has been a decrease of 50% in the hospitalization costs, related to LVAD implantation (Slaughter et al. 2011). This may be explained by better logistics, selection and management of patients thanks to the increase number of implantation (Mishra et al. 2012), as well as the development of technologies. However, several complications are still related to the MCS device implantation, and further investigations could help surgeons anticipate and limit intraoperative and postoperative adverse events. Next chapter presents issues raised by MCS device implantation and the positioning of our works in relation to the state of the art.

References

Agence de la biomedecine, 2015. Rapport de l'activité de greffe cardiaque - Année 2015. Available at: https://www.agence-biomedecine.fr/annexes/bilan2015/donnees/organes/03-coeur/synthese.htm.

Bleumink, G.S. et al., 2004. Quantifying the heart failure epidemic: Prevalence, incidence rate, lifetime risk and prognosis of heart failure - The Rotterdam Study. *European Heart Journal*, 25(18), pp.1614–1619.

Clark, A.L., 2006. Origin of symptoms in chronic heart failure. *Heart (British Cardiac Society)*, 92(1), pp.12–16.

Cohn, W.E., Timms, D.L. & Frazier, O.H., 2015. Total artificial hearts: past, present, and future. *Nature Reviews Cardiology*, 12(10), pp.609–617.

Cook, J.A. et al., 2015. The total artificial heart. *Journal of thoracic disease*, 7(12), pp.2172–80.

Copeland, J.G. et al., 2012. Experience with more than 100 total artificial heart implants. *Journal of Thoracic and Cardiovascular Surgery*, 143(3), pp.727–734.

Cowie, M.R. et al., 2000. Survival of patients with a new diagnosis of heart failure: a population based study. *Heart (British Cardiac Society)*, 83(5), pp.505–10.

Cuttone, F. et al., 2011. L'assistance ventriculaire mécanique. *Sang Thrombose Vaisseaux*, 23(10), pp.539–544.

Delmo Walter, E.M. & Hetzer, R., 2013. Surgical treatment concepts for heart failure. *HSR proceedings in intensive care & cardiovascular anesthesia*, 5(2), pp.69–75.

Dickstein, K. et al., 2008. ESC Guidelines for the diagnosis and treatment of acute and chronic heart failure 2008. *European Heart Journal*, 29(19), pp.2388–2442.

Feldman, D. et al., 2013. The 2013 International Society for Heart and Lung Transplantation Guidelines for mechanical circulatory support: Executive summary. *The Journal of heart and lung transplantation: the official publication of the International Society for Heart Transplantation*, 32(2), pp.157–87.

Flécher, E., 2014. Assistance circulatoire mécanique de longue durée en 2014: une alternative à la transplantation cardiaque? *La Presse Médicale*, 43(7–8), pp.809–812.

Givertz, M.M., 2011. Ventricular assist devices: Important information for patients and families. *Circulation*, 124(12), pp.305–312.

Hanke, J.S. et al., 2015. Minimally-invasive LVAD Implantation: State of the Art. *Current cardiology reviews*, 11(3), pp.246–51.

Heo, S. et al., 2009. Quality of life in patients with heart failure: ask the patients. *Heart & lung: the*

journal of critical care, 38(2), pp.100–8.

Jakovljevic, D.G. et al., 2014. Effect of Left Ventricular Assist Device Implantation and Heart Transplantation on Habitual Physical Activity and Quality of Life. *The American Journal of Cardiology*, 114(1), pp.88–93.

Kadado, A.J., Akar, J.G. & Hummel, J.P., 2017. Arrhythmias after left ventricular assist device implantation: Incidence and management. *Trends in Cardiovascular Medicine*.

Karamlou, T. et al., 2013. Mechanical circulatory support pathways that maximize post-heart transplant survival. *Annals of Thoracic Surgery*, 95(2), pp.480–485.

Kirklin, J.K. et al., 2016. Intermacs Interagency Registry for Mechanically Assisted Circulatory Support Quarterly Statistical Report 2016 Q2. *The Data and Clinical Coordinating Center University of Alabama at Birmingham*.

Kirklin, J.K. et al., 2015. Seventh INTERMACS annual report: 15,000 patients and counting. *Journal of Heart and Lung Transplantation*, 34(12), pp.1495–1504.

Liotta, D., 2002. Early clinical application of assisted circulation. *Texas Heart Institute journal / from the Texas Heart Institute of St. Luke's Episcopal Hospital, Texas Children's Hospital*, 29(3), pp.229–30.

Lund, L.H. et al., 2017. The Registry of the International Society for Heart and Lung Transplantation: Thirty-fourth Adult Heart Transplantation Report-2017; Focus Theme: Allograft ischemic time. *Journal of Heart and Lung Transplantation*, 36(10), pp.1037–1046.

Mangi, A.A., 2011. Right Ventricular Dysfunction in Patients Undergoing Left Ventricular Assist Device Implantation: Predictors, Management, and Device Utilization. *Cardiology Clinics*, 29(4), pp.629–637.

McMurray, J.J. V. et al., 2012. ESC Guidelines for the diagnosis and treatment of acute and chronic heart failure 2012: The Task Force for the Diagnosis and Treatment of Acute and Chronic Heart Failure 2012 of the European Society of Cardiology. Developed in collaboration with the Heart. *European Heart Journal*, 33(14), pp.1787–1847.

Miller, L.W., Guglin, M. & Rogers, J., 2013. Cost of ventricular assist devices can we afford the progress? *Circulation*, 127(6), pp.743–748.

Mishra, V. et al., 2012. Hospital costs fell as numbers of LVADs were increasing: experiences from Oslo University Hospital. *Journal of Cardiothoracic Surgery*, 7(1), p.76.

Mozaffarian, D. et al., 2016. *Heart disease and stroke statistics-2016 update a report from the American Heart Association*,

Ponikowski, P. et al., 2014. Heart failure: Preventing disease and death worldwide. *European Society of Cardiology*, 373(9667), pp.941–955.

Rogers, J.G. et al., 2010. Continuous Flow Left Ventricular Assist Device Improves Functional Capacity and Quality of Life of Advanced Heart Failure Patients. *Journal of the American College of Cardiology*, 55(17), pp.1826–1834.

Slaughter, M.S. et al., 2011. Temporal changes in hospital costs for left ventricular assist device implantation. *Journal of Cardiac Surgery*, 26(5), pp.535–541.

Stehlik, J. et al., 2012. The Registry of the International Society for Heart and Lung Transplantation: Thirty-first Official Adult Heart Transplant Report—2014; Focus Theme: Retransplantation Lars. *The Journal of Heart and Lung Transplantation*, 31(10), pp.1052–1064.

Stewart, G.C. & Givertz, M.M., 2012. Mechanical circulatory support for advanced heart failure: Patients and technology in evolution. *Circulation*, 125(10), pp.1304–1315.

Stewart, G.C. & Stevenson, L.W., 2011. Keeping left ventricular assist device acceleration on track. *Circulation*, 123(14), pp.1559–1568.

Sunagawa, G. et al., 2016. Future Prospects for the Total Artificial Heart. *Expert Review of Medical Devices*, 13(2), pp.191–201.

The Criteria Committee of the New York Heart Association, 1994. Nomenclature and criteria for diagnosis of diseases of the heart and great blood vessels. , Little, Br(9th), pp.253–256.

Wilson, S.R. et al., 2009. Evaluation for a ventricular assist device: Selecting the appropriate candidate. *Circulation*, 119(16), pp.2225–2232.

Chapter 2 - Issues related to device implantation

Recently, the number of MCS implantations has significantly increased. RVAD and BiVAD implantations have slowly incremented, but LVAD implantations dramatically expended over the last decade. Nevertheless, several complications still arise and a considerable number of unknowns and questions remain. This chapter attempts to sketch an overview of the different issues raised by MCS implantation. Many factors may contribute to adverse events. We especially present and discuss factors the surgeons may control, such as parameters related to device implantation, configuration, tuning and monitoring. If our analysis focuses on LVADs and TAHs, the questions raised by RVADs and BiVADs are the same as for LVADs.

Our analysis of the problematics is organised as follows. Interactions between the MCS implants and anatomical structures are summarized in Section 1. The second section develops factors modifying the mechanical and fluidic alterations. Then, morphological interactions potentially responsible for postoperative complications are addressed in Section 3. Finally, Section 4 highlights the positioning and objectives of our work.

1. Interactions between the MCS implants and anatomical structures

MCS implantable devices have significant impacts on patient anatomy and physiology. Blood flow is clearly affected as well as geometry, behavior and properties of many anatomical structures. In the following specific anatomical structures interacting with MCS implants are highlighted. These interactions have the potential of leading to adverse events or deterioration of the MCS efficiency.

- Physiological changes related to TAH

Figure 2.1 illustrates the different types of interactions due to TAH implantation. Anastomosed to the native heart, the TAH device necessarily modifies and constrains the heart structures geometry. For instance, sutured to the device, the two atria are also anastomosed together, modifying thus their intrathoracic position in space and relative to each other. This interaction potentially alters their function. However, the two cavities are not considered as critical by surgeons because of their softness, mobility, and relatively poor contractility. In the same way, the aortic and pulmonary arteries hemodynamics and geometry are modified by their respective Outflow Cannula (OC). One should appreciate that their initial portion replaced using a Dacron conduct will not expand or react as the rest of the biological vessel. Moreover their position in the mediastinum may be distorted

depending on each anatomical situation required by the placement of the TAH. Nevertheless, modifications of these two arteries will not be evocated in the following.

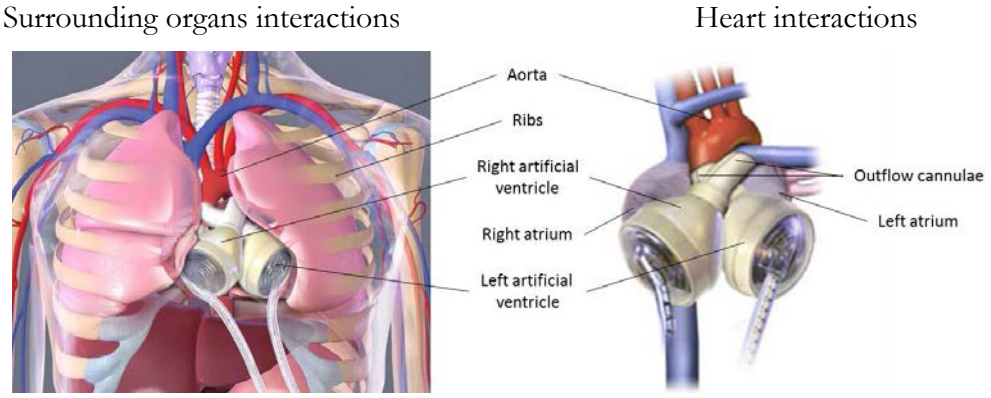

Figure 2.1 - Interactions with the Total Artificial Heart (TAH)
Source: Syncardia.com

TAH may sometimes be in contact with the chest wall which can lead to patient chest pains. It may also promote calcifications between the ribs and the TAH, complicating subsequently open heart surgeries. But the main and life-threatening risk in such anatomical conflict will be the impossibility to close intraoperatively the chest. With the potential of being anticipated by surgeons preoperatively, this constraint will be more investigated.

- Physiological changes related to LVAD

Figure 2.2 illustrates the different types of interactions due to LVAD implants. As for the TAH, the LVAD may be in conflict with the thoracic wall and potentially provoke the same complications. In addition, Right Ventricle (RV) volume and shapes also change with the device implantation. Sometimes this right heart cavity may be compressed by the pump itself, promoting

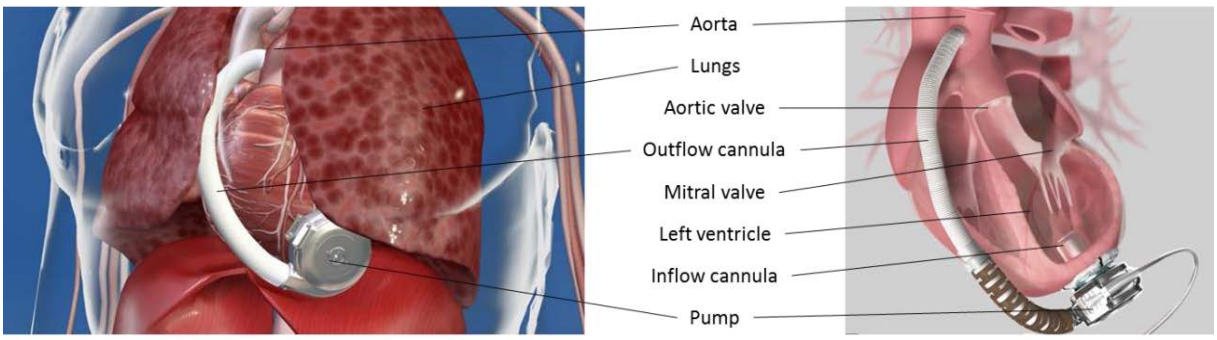

Figure 2.2 - Interactions related to the Left Ventricular Assist Device (LVAD) implantation
Source: heartware.com

RV geometrical modification and functions' alteration. The outflow tract when anastomosed to the ascending aorta may also be placed in front of the RV and interact with its normal function. Patients presenting those cases are more likely to develop postoperative right HF.

The LVAD IC may be sutured to different heart structures such as Left Ventricle (LV) or left atrium. Nowadays, instructions recommend suturing it to the LV. A hole is made at the apex to insert the IC which is then sutured (some devices are first sutured and the hole is subsequently performed). The apical region presents therefore important stress. Furthermore, the intrathoracic pump may have such a critical aspiration that suction events between the LV wall and the IC distal end may appear promoting right HF and device dysfunction. When these events are detected, it is recommended to decrease the pump speed (and to appreciate giving fluid to the patient). In addition, starting-up the device results in a depletion of the LV. This reduction in LV volume reduces LV work by lowering pressure and volume overload, which decreases LV wall stress and may thus contribute to reverse modelling (Jhun et al. 2014). However, it also brings the LV wall closer to the IC distal end point potentially promoting suction events.

Finally, blood flow distribution within the LV cavity is impacted. Vortices, recirculation and stagnation are likewise present in the LV. Vortices contribute to suction events (Kheradvar et al. 2007) but also minimize cardiac work and facilitate the blood mass coming into the LV. The apical region has also been identified to prone thromboembolic complications (May-Newman et al. 2016). Elsewhere, obstructing the IC, suction events temporarily alter blood circulation as well as LVAD pump.

Aortic blood flow disorders and turbulences have also clearly been identified in patients under LVAD support (Yoshida et al. 2017). Figure 2.3 illustrates the OC anastomosis to aorta. The major alteration is the presence of reverse flow which compromises cardiac hemodynamics. Reverse flow can cause harmful effects to the Aortic Valve (AoV) (Alonazi et al. 2015). AoV dysfunction associated to LVAD implantation is a major postoperative complication related to patient death.

Areas of stagnation and recirculation have been diagnosed. These phenomena contribute to thrombi formation (Quaini et al. 2011) which may affect the rotor efficiency and even stop it. A blood clot may also provoke embolic event migrating to the brain. INTERMACS data showed that 7% of patients had a stroke within the 6 first months, 11% within 1 year and 19% within 3 years (Kirklin et al. 2013). Previously, it was preconized to close the AoV in order to concentrate blood down to the Inflow Cannula (IC). However, thromboses are formed next to the AoV, especially

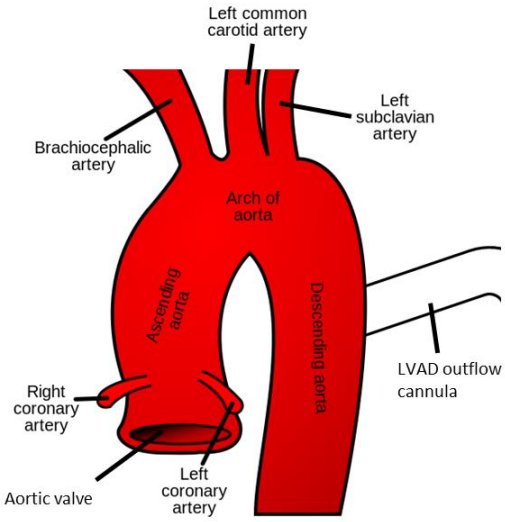

Figure 2.3 - Outflow cannula anastomosis to aorta

when this latter remains closed (John et al. 2010). To close the aortic valve may also expose the patient to a dramatic and fatal issue in case of LVAD interruption (no possibility for the native left ventricle to eject blood in the aorta). On the contrary, a permanent opening causes damages due to the important stress on the leaflets (Alonazi et al. 2015). Recently, it has therefore been recommended to let the AoV function, but no recommendations about the opening frequency have been clearly mentioned to date.

LVAD outflow promotes important aortic pressures and Wall Shear Stress WSS (Karmonik, Partovi, Loebe, et al. 2014) resulting in a dilation of the aorta (Fine et al. 2016). WSS is potentially responsible of flow instability and turbulence, as well as wall tissue damages. Thus, blood distribution through LVAD and its outflow conduct significantly impacts the aortic structure and function. But it also has a consequence on the three arteries perfusion located in the aortic arch. In charge of routing blood towards the brain and the upper limbs, it is essential to well supply them. However, the probability that thrombi enter into these three upper branches and provokes stroke events is also affected (Zhang et al. 2016).

To conclude, MCS implants involve a multitude of physiological modifications that may be sources of postoperative complications. Two types of MCS device interactions may be distinguished, geometrical constraints and fluidic modifications with sometimes mechanical repercussions. Next section presents the different factors potentially impacting the mechanical and fluidic properties of the aorta and left ventricle.

2. Mechanical and fluidic issues

Many settings can be adjusted by the surgeons for the TAH (cardiac frequency, length of the diastole and systole, ejection pressure, etc. for each artificial ventricle) where only the pump speed is controlled for the LVAD. However, TAH implantation does not present so much degree of freedom to position the device as the LVAD does. In this section we focus on LVADs. In medical sciences, several methods exist to evaluate hemodynamics or to relate postoperative outcomes to surgical process and patient conditions. First, the different approaches used for experiment analyses are featured. Then, a general overview of factors influencing the aorta properties and hemodynamics is provided, followed in the next part by those related to the LV. Finally, an insight of works and results from the literature, assessing through computational modelling the issues related to the inflow and outflow LVAD cannulae implantation are presented.

2.1. Related approaches

Clinical methods measuring physiological data on patients has been considered. Cardiac output before and after efforts may provide significant information about pump efficiency and patient health (Aymami et al. 2016). In the same way, medical imaging is often used for retrospective studies. MRI and Doppler echocardiography are the two modalities presenting cardiac blood flow information. MRI provides spatially and temporally flow patterns and evaluate mechanical parameters such as flow rate, recirculation and stasis, WSS, and pressure variations (Taylor & Draney 2004). However, MCS devices are composed of metal and magnets which are not compatible with magnetic field. On the contrary, Doppler echocardiography is really helpful in the context of LVAD therapy (Estep et al. 2010). It is applied in daily life to optimize the pump speed; assess mitral regurgitation or myocardium recovery. More generally, it is used to measure LV and RV hemodynamics in patients with cardiovascular disease (Porter et al. 2015). Echocardiography has the ability to evaluate chambers dimensions, mitral inflow velocities during systole and diastole, stroke volume, cardiac output and pressures. Although this technic is non-invasive and provides real measurements, it is heavily operator dependent and parameters variation is limited in number. Moreover, performing an echocardiography in a LVAD patient remains challenging.

Animal model experiments have significantly contributed in cardiovascular disease understanding over the years (Chorro et al. 2009). They provide information on aetiology, pathophysiology or efficacy and mechanism of action of medications (Leong et al. 2015). Valuable for their similarity in anatomy and physiology with humans, in-vivo studies are easier to manage compared to human ones and less subject to environmental variations. However, results may be unsuitable or too diverse to compare with humans. Furthermore, these studies require major investment of time and

resources, and also involve ethical concerns. Non-animal models are more flexible and can be used to develop new technologies that may not be safe for human and animals. It allows greater control of variables and reduces experimental time and cost compared with in-vivo models (Ryan et al. 2016). Although it has been significantly developed with the use of biomaterials, the complexity of the cardiovascular system is often simplified with in-vitro models, and they do not enable the natural progression of multiple pathologies.

Distinct from experimental technics, computational methods have more and more been investigated over the last years. Rapid, economical and allowing low-risk prototyping (Morris et al. 2016), approaches involving virtual models have already been investigated in cardiovascular domain (HF, congenital heart diseases, valve prosthesis, VADs, etc.). These methods may be beneficial for device design, clinical trials and treatment strategies improvement (Taylor & Draney 2004). Currently, prediction of intervention outcomes is one of the main challenging issues. Two main technics are distinguished: lumped parameter models and Computational Fluid Dynamic (CFD) modelling. The first one consists in simplifying complex physical system into discrete entities (differential equations) that describe the behaviour of system components. Also known as zero-dimensional computational model, it does not afford 3D information such as flow field visualization. On the contrary, CFD provides temporal and spatial resolutions which are difficult to obtain with other types of experiments.

All these types of method have been considered in the context of MCS.

2.2. Parameters influencing the aorta properties and hemodynamics

Many criterions may impact the aortic blood flow distribution and promote turbulences, WSS, thrombogenesis, stroke or aorta alteration. Herein we give a brief overview of the factors modifying the aorta physiology giving as examples experiments from the literature.

- Pump specificities

The pump speed is a major factor impacting blood flow within the aorta. (Bonnemain et al. 2013) demonstrated it through numerical simulations comparing flow rates and pressure patterns according to the percentage of VAD support. In the same way, (Litwak et al. 2005) evaluated with an adult mock circulation the waveform pulsatility, and (Bazilevs et al. 2009) studied stagnation and WSS with computational study. Results revealed that stagnation and WSS increase with the pump speed, but also increment the amount of outflow.

LVAD outflow grafts design also influences the aortic blood flow distribution. (Bhat et al. 2017) demonstrated through CFD studies that flow into the aortic arteries depends on the width from the graft. They also found that 10 mm graft is more hemodynamically sensitive to angle of insertion

than 14 mm graft. (Stühle et al. 2011) evaluated 3 commercially available cannulas for cardiopulmonary bypass and demonstrated through numerical simulations the significant influence of the cannula design on the blood distribution. Currently, OCs are flexible tubes that differ only by the diameter. If LVAD OC does not present different tips design as cardiopulmonary bypasses ones, it may be envisaged in the future to optimise the outflow distribution.

Investigations have also highlighted pros and cons of each LVAD category. For instance, (Litwak et al. 2004) demonstrated identical amounts of aortic blood flow between PFVAD and CFVAD through in-vivo experiments. In the same way, (Filipovic & Schima 2011) concluded through CFD simulations that both PFVAD and CFVAD presented complex intra-aortic flow patterns but no preference were found. However, PFVADs seemed to present more backflow while CFVADs presented occasional episodes of partial ventricular suction. (Yang et al. 2010) evaluated with CFD simulations the WSS impact, turbulence and blood flow distribution in great vessels. They showed that PFVAD provided better pulsatility, while continuous support caused less blood damage. Although CFVADs present nowadays a better reliability and durability; some effects on aortic blood distribution and flow behaviours remain unclear.

- OC anastomosis configuration

The OC anastomosis is the process presenting the larger number of possible configurations during LVAD implantation. During the surgery, surgeons cut the outflow graft to the length to reach the aorta. This length may be a determinant parameter influencing the WSS and blood flow velocity entering into the aorta. But currently, its impact has not been investigated and there is no recommendation for it. Two principle sites of OC anastomosis are currently used into surgery: the descending and ascending aorta. Generally, surgeons choose the location according to the surgical way of implantation. For instance, descending aorta anastomosis is preconized with a thoracotomy, due to the difficulty to access the ascending aorta with this surgical process, while the OC is anastomosed to the ascending aorta during a sternotomy. (Litwak et al. 2005) have shown that less flow was present within the aorta arch with a descending aorta anastomosis. In the same way, (Mazzitelli et al. 2013) evaluated a better contribution in upper arteries with ascending aorta anastomosis, although (Bonnemain et al. 2013) calculated similar mean flow rate. Currently, many issues are still open and we do not know which site should be preconized. Notice that if the current

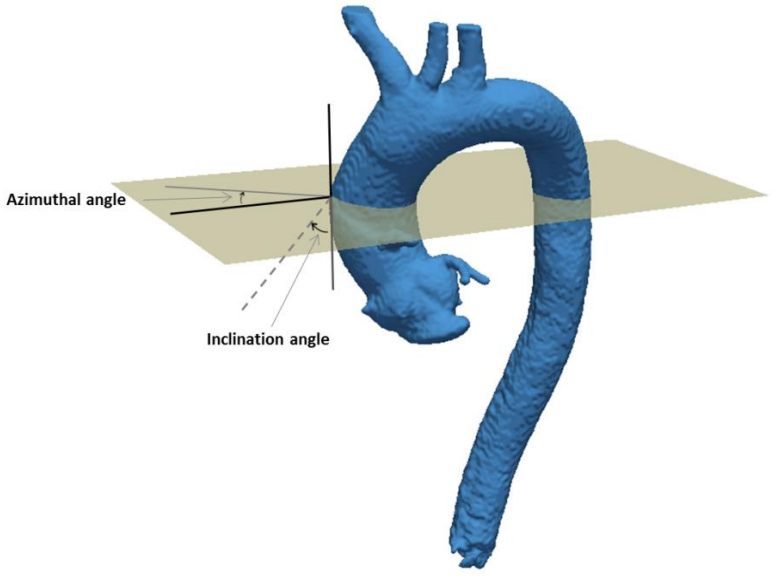

Figure 2.4 - Azimuthal and inclination angles defining aortic anastomosis direction.

practice recommends an aortic anastomosis, some have considered other site in the literature such as subclavian artery (Neidlin et al. 2016). Different optimal sites should be considered, depending on the patient's specific vascular anatomy.

In the same way, questions are also raised for the anastomosis location within a specific aortic segment (ascending, descending aorta). Several articles evaluated the impact of the location on the outflow efficiency. (May-Newman et al. 2006) compared a "distal" and "in-plane" position in the descending aorta, studying WSS through CFD simulations, whereas (Karmonik et al. 2012) evaluated a lateral and anterior anastomoses in the ascending aorta. More generally, (Lafortune & Aris 2015) studied this issue considering the distance between the OC suture and the AoV. All the investigated locations present their pros and cons.

Angulation of the OC for ascending aorta anastomosis is one of the most studied issues. Two angles may be differentiated: the azimuthal and the inclination one (Figure 2.4). According to the inclination angle, the anastomosis is more or less large. (Benk et al. 2013) compared stagnation and backward flows through an in vitro study, between a small and a large anastomosis. They also investigated, as well as (Callington et al. 2015), the effects of the anastomosis geometry on the aortic pressure, flow, and WSS distributions. All interpretations seemed to converge on the same results: WSS and vortices increased with both inclination and azimuthal angle whereas stagnation near the AoV decreased. (Osorio et al. 2013) also demonstrated through CFD simulation that angulation has a significant role in thrombogenesis. In order to reduce the incidence of cerebral embolization, they presented an alternative approach consisting of adding an aortic bypass to the

OC as well as (Argueta-Morales et al. 2010) did. OC angulation may also have an impact on aortic arch arteries contribution and stoke probability. (Zhang et al. 2016) demonstrated that cannula location and thrombogenesis sources affect the thrombi distribution in the aorta.

- Anatomic morphology

The aorta morphology varies from a patient to another and many features could be dissociated: diameter, ascending aorta length, aorta arch curvature, supra-aortic arteries positioning, wall thinness and stiffness, etc. (Tse et al. 2013) demonstrated with intricate geometrical features that hemodynamics in the aorta is highly dependent on geometrical variations. Despite it has been identified with specific pathologies, no study has yet evaluated features impact in the context of LVAD. It could be supposed that according the aorta geometry, an OC configuration insertion is more or less favourable.

Several works from the literature have demonstrated that the cannula length, pump speed, type of support (PFVAD or CFVAD), anastomosis configuration as well as the anatomic morphology impact the aorta properties and blood flow repartition. However, a precise implantation configuration optimizing the aorta function and structure is still unclear.

2.3. Parameters influencing the pump inflow

As for the aorta, the presence of LVAD support clearly modifies the LV hemodynamics (McCormick et al. 2013), properties as well as the pump inflow. Contrary to the LVAD outflow, fewer investigations have been made to investigate the potential sources of modifications. It may be explained by the fact that it is too difficult to analyse LV blood flow through medical images. MRI acquisition is not possible with LVADs; too many metallic artefacts are present on Computerized Tomography (CT) images and echocardiographies present areas of shadows related to the IC.

- Pump specificities

Not many studies have investigated the impact of continuous vs pulsatile support on LV hemodynamics. (Gohean et al. 2013) used a computational model, to show that PFVAD provided higher LV unloading as compared to CFVAD. But flow patterns were not investigated.
The pump speed also affects the LV hemodynamics and pump efficiency, as well as the anatomical configuration. (Addetia et al. 2017) clearly demonstrated through the evaluation of 31 echocardiographies that both LV and RV geometry changed with pump speed. They noticed a decrease of the LV volume becoming less spherical and more conical with the increase amount of circulatory support, whereas on the contrary, RV volume increased. Impacting at the same time

the interventricular septum, this volume reduction increased the number of potential suction events. (Li et al. 2002) also demonstrated with a numerical simulation that when the support is too important, the pump is not efficient anymore. However, a pump speed increment, decreases the volume of blood stagnation (Fraser et al. 2011). More investigations are thus necessary to find the appropriate balance between these effects.

The efficiency of different IC tips has also been evaluated. For instance, (Liu et al. 2012) used a CFD to investigate the blood flow fields in four different IC designs, as well as (Fraser et al. 2011) for three clinically available cannulas. Both examined turbulent effects, flow velocity or potential thromboembolic region. In the same way, using an in-vitro study (Laumen et al. 2010) evaluated how the tip geometry influences the dynamics flow, whereas (Bachman et al. 2011) dealt with the degree of ventricular decompression and collapse for two forms of IC. Nonetheless, considering all current commercialized LVADs, IC geometry is most of the time a cylinder.

The impact of IC length have also been assessed in the literature. Firstly, a too long IC may have damaging effects on Mitral Valve (MV) and AoV function, due to an important pressure induced by the MCS aspiration on valves' leaflets and chordae. Additionally, a long IC is more likely to come into contact with the LV wall, promoting thus suction events. According to (Ong et al. 2013) who used CFD simulations, vortex intensities also increased with the IC length, as well as stagnation at the apex leading to thrombogenesis. In the same way, (May-Newman et al. 2016) demonstrated using a mock circulatory loop that flow alterations arise as the IC is inserted further into the LV. On the contrary, (Schmid et al. 2008) made a retrospective analysis on 216 patients and showed that 3.8% of patients with long length cannula had thromboembolic events versus 23.2% of patients with a short length cannula.

In summary, several issues are still present and more investigations are necessary. Contrary to the OC, the IC is rigid and not adjustable during the surgery process. However, the IC diameter and length vary from a LVAD to another. It can be envisaged that specific IC length or radius may be preconized according to the LV anatomy and shape. If such studies would further help device designer, it may also have an impact when surgeons choose the device preoperatively.

- IC anastomosis configuration and anatomic morphology

The IC anastomosis configuration impacts the blood flow fields as well as the OC does. According to the recommendations, IC must be located at the LV apex. Only few studies evaluated the efficiency of anastomosing it in another site. (Korakianitis & Shi 2007) and (Hsu et al. 2015) used numerical methods to investigate the hemodynamic response using two distinct inlet cannulations: the atrium and the apex. Results were consistent with recommendations, concluding that a cannulation at the apex was beneficial by decreasing LV wall tension and dilation promoting thus

LV recovering. In the same way, (Prisco et al. 2017) have shown through CFD simulations that a diaphragmatic cannulation increased stagnations due to a slower clearance half-time.

IC orientation may also affect the pump efficiency and suction events. Figure 2.5 illustrates through postoperative radiographies two IC configurations. An IC pointing toward the MV is supposed to favour the blood entering into the pump and to limit LV wall collapses with the IC distal end. Therefore, it is recommended to orient it coaxially to the MV main axis. However, currently no study has investigated the impact of the orientation on LV stagnation, WSS or flow rate. Notice that for some devices, two other angulation types may be controlled: the elbow and circumferential one (Figure 2.6). (Chiu et al. 2016) evaluated through CFD the stress accumulation of the platelets to represent thrombogenic potential, and demonstrated their influence on it.

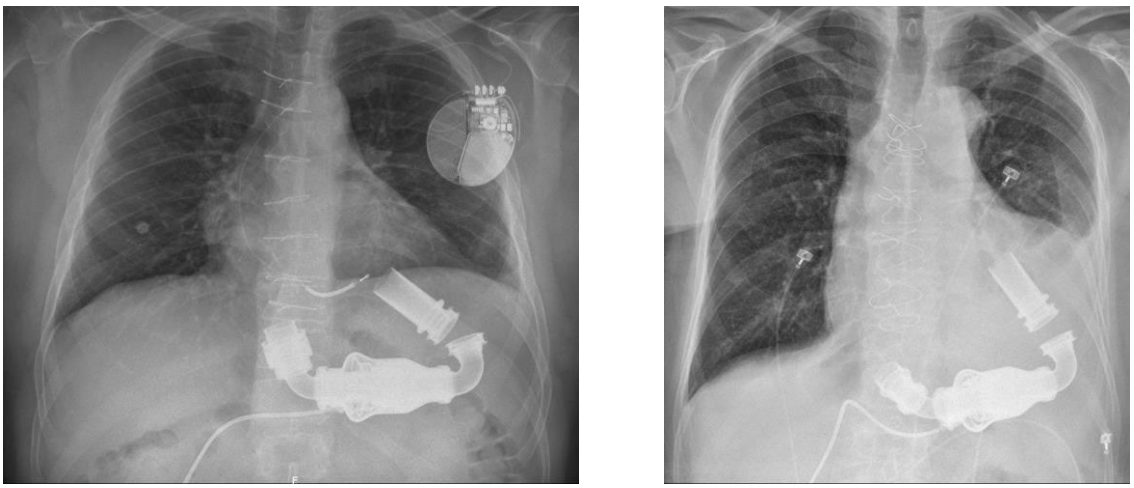

Figure 2.5 - Illustration of two configurations of the HM II inflow cannula through postoperative radiographies

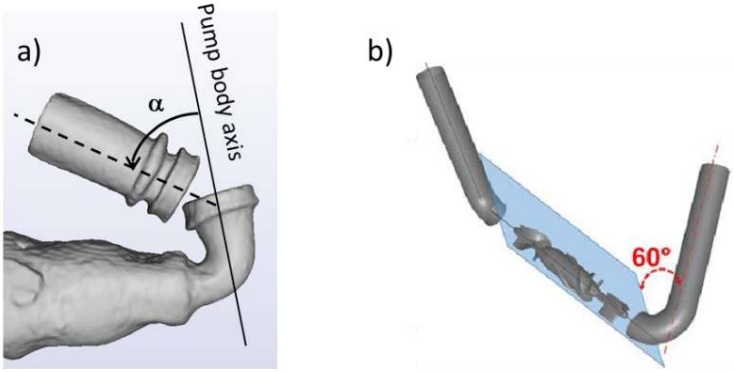

Figure 2.6 - Two manageable angles for the inflow cannula implantation configuration of the HM II. a) Elbow angle b) Circumferential angle
Source of b): (Chiu et al. 2016)

(Litwak et al. 2008) suggested through an in-vivo study that a bovine LV is more conical than in a human LV, favouring thus stagnation and development of thrombus. The LV geometry may therefore impact blood flow repartition, myocardium WSS, stagnation, etc. However, no studies have examined this issue yet.

Pump efficiency and blood flows are clearly influenced by IC and OC anastomoses configurations, anatomiscal shapes and pump settings. Physiological modifications due to LVAD support are summarized Figure 2.7, as well as potential factors of influence related to the two anastomoses. All parameters evocated are interdependent.

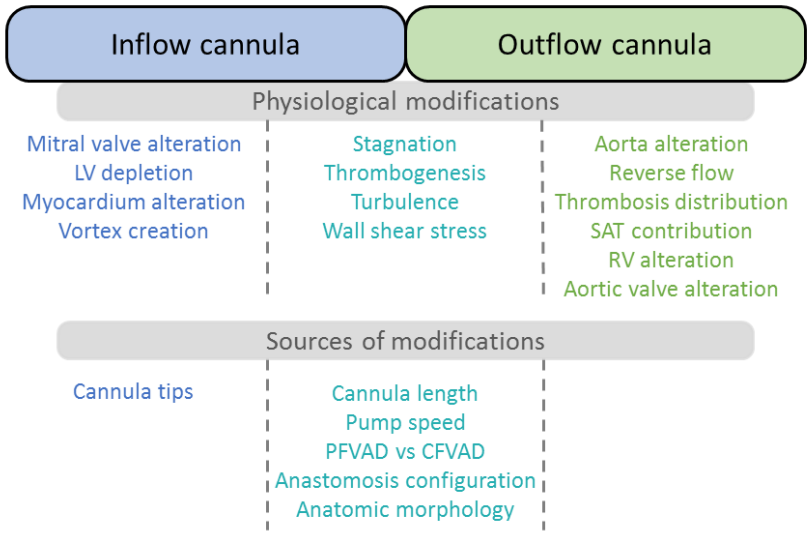

SAT = Supra-Aortic Trunks; PFVAD = Pulsatile Flow Ventricular Assist Device; CFVAD = Continuous Flow Ventricular Assist Device; RV = Right Ventricle; LV = Left Ventricle

Figure 2.7 - Resume of physiological modifications and potential sources related to LVAD implantation

2.4. Computational modelling contributions

CFD simulation enables to estimate complex physiological parameters and to visualize flow field that cannot be measured by any clinical methodology. Non-invasive, this type of experimental allows a large number of settings analysis. It tends nowadays to be used for diagnostic assessment. Although validation of CFD simulation is complex and selection of appropriate boundary conditions presents several difficulties due to sparsity of data, it seemed interesting to give an overview of CFD results from the literature. Our objective was to highlight how computational modelling has been used in the context of VADs.

Three main categories have been identified: i) works investigating factors impacting the LV hemodynamics (Table 2-I); ii) articles assessing the aorta blood flow with an ascending aortic anastomosis (Table 2-II); iii) works considering descending aortic or subclavian arteria anastomosis (Table 2-III). The three tables were elaborated as follows, the first column organizes all works depending on their subject of analysis (ascending anastomose, configuration, use of bypass, etc.). The second column enunciates the studied elements with their associated articles, while the third column presents the results.

Table 2-I - Factors influencing physiological modifications of the left ventricular hemodynamics

P° = Pressure; MV = Mitral Valve; RT = Residence Time; WSS = Wall Shear Stress; WSS_{ED} = WSS at End-Diastol; WSS_{ES} = WSS at End-Systol; LV = Left Ventricle; V = Volume

With vs Without LVAD *(Prisco et al. 2017)* *(Jhun et al. 2014)* *(McCormick et al. 2013)*	With	Vortex more important ↘ P° and ↗ MV inflow Basal region: Low velocity & important RT Apical region: Low velocity & important RT High WSS at the apex
Amount of support *(Fraser et al. 2011)* *(Jhun et al. 2014)*	WSS_{ED} > WSS_{ES} ↗ Pump speed	Proportional ↘ WSS Proportional ↘ LV_{Volume} ↘ $V_{Stagnation}$
Position *(Prisco et al. 2017)*	Apical vs Diaphragmatic	Modest difference in stagnation Apical: faster clearance half-time Diaphragmatic: more stagnation in apex & lateral wall
Cannula length *(Ong et al. 2013)* *(Fraser et al. 2011)*	↗ Length	Proportional ↗ vortex intensity ↗ Stagnation near the apex ↗ WSS at the basal region ↘ WSS at the apex
Cannula tips *(Liu et al. 2012)* *(Tsukiya et al. 2011)* *(Fraser et al. 2011)*	Trumpet / Caged / Blunt / Beveled	Worst: Caged (turbulent effect) Best compatibility: Trumpet (no low velocity, no backflow) More obstruction: Blunt & Beveled
	Lantern-like	Potential region of thrombus formation: between the inlet holes & the struts
	12F / 16F / 24F (Medtronic)	Worst: 24F (↗ risk of blood clotting within IC)
Suction events *(Ong et al. 2012)*	Suction events promote the alteration of vortex patterns	

Table 2-II - Factors influencing physiological modifications of the aortic hemodynamics related to ascending anastomosis

P° = Pressure; WSS = Wall Shear Stress; Anc = Anterior configuration; Asc = Ascending configuration; Arc = Arch of aorta configuration; UDsc = Upper Descending configuration; IPc = In-Plane configuration; AoV = Aortic Valve; BP = ByPass

Ascending a**orta** *(Argueta-Morales et al. 2010)* *(Inci & Sorgüven 2012)* *(Karmonik et al. 2012)* *(Karmonik, Partovi, Schmack, et al. 2014)* *(Karmonik, Partovi, Loebe, et al. 2014)* *(Chiu et al. 2016)* *(Menon et al. 2013)* *(Filipovic & Schima 2011)* *(Bhat et al. 2017)* *(Quaini et al. 2011)* *(Brown et al. 2012)* *(Yang et al. 2009)* *(Zhang et al. 2016)* *(May-Newman et al. 2004)*	Near anastomosis (Karmonik et al. 2012) *(Bazilevs et al. 2009)* *(Karmonik, Partovi, Schmack, et al. 2014)* *(Karmonik, Partovi, Loebe, et al. 2014)* *(Yang et al. 2009)*	Higher disorder, turbulence and reverse flow Important P° and WSS
	Contralateral wall *(Karmonik, Partovi, Loebe, et al. 2014)*	Important P°
	CFVAD (vs PFVAD) *(Karmonik, Partovi, Schmack, et al. 2014)* *(Filipovic & Schima 2011)*	↗ WSS & P° Similar washout near the AoV
	Configurations *(May-Newman et al. 2006)* *(Yang et al. 2009)* *(Karmonik et al. 2012)* *(Zhang et al. 2016)*	An_C more ordered flow than L_C An_C less probability of thrombi in BCA As_C preferred than Ar_C and UDs_C IP_C less important WSS D_C more turbulence than P_C
	Lower Position *(Callington et al. 2015)* *(Lafortune & Aris 2015)* *(Quaini et al. 2011)* *(Brown et al. 2012)*	↗ Root WSS ↗ Recirculation near AoV ↘ Stagnation and chaotic flow near AoV
• Configuration Proximal (P_C) / Distal (D_C) / In-Plane (IP_C) *(May-Newman et al. 2006)* *(Yang et al. 2009)* Lateral (L_C) / Anterior (An_C) *(Karmonik et al. 2012)* *(Zhang et al. 2016)* Ascending (As_C) / Arch (Ar_C) / Upper descending (UDs_C) (Brown et al. 2012)	↗ Angle inclination *(Inci & Sorgüven 2012)* *(Karmonik, Partovi, Loebe, et al. 2014)* *(Osorio et al. 2013)* *(Callington et al. 2015)* *(Gramigna 2014)* *(Poullis 2012)* *(Chiu et al. 2016)* *(Menon et al. 2013)* *(Quaini et al. 2011)* *(May-Newman et al. 2004)*	↗ WSS ↗ Vortices and bulk fluid velocity ↘ Stagnation near AoV ↗ Risk of thrombogenesis ↗ Backward flow ↗ Recirculation Impact on head-neck vessels perfusion
	Azimuthal angle (≠ 90°) *(Callington et al. 2015)*	Swilling effect of particles ↗ WSS
	↗ Assistance (speed) *(Inci & Sorgüven 2012)* *(Bazilevs et al. 2009)* *(Yang et al. 2010)*	↗ WSS ↗ Stagnation
• Orientation azimuthal, inclination *(Argueta-Morales et al. 2010)* *(Inci & Sorgüven 2012)* *(Karmonik, Partovi, Loebe, et al. 2014)* *(Guimond 2012)* *(Osorio et al. 2013)* *(Callington et al. 2015)* *(Chiu et al. 2016)* *(Menon et al. 2013)*	Clamped AoV *(Karmonik, Partovi, Schmack, et al. 2014)* *(Mazzitelli et al. 2013)* *(May-Newman et al. 2004)* *(Lafortune & Aris 2015)* *(Poullis 2012)*	↗ Stagnation near AoV ↗ Vortex motion ↗ WSS
	Tips and width *(Menon et al. 2013)* *(Bhat et al. 2017)*	Influence on BCA perfusion Small graft more sensitive to inclination
• Bypass (BP) *(Argueta-Morales et al. 2010)*	Bypass *(Argueta-Morales et al. 2010)* *(Osorio et al. 2013)*	↘ Risk of stroke Innominate artery BP worst Left carotid artery BP better
	Peak systole *(Prather 2015)*	↗ Stagnation

Table 2-III - Factors influencing physiological modifications of the aortic hemodynamics related to descending and subclavian arteria anastomoses

AoV = Aortic Valve

Ascending ***vs*** **Descending** *(Kar et al. 2005) (May-Newman et al. 2006) (Mazzitelli et al. 2013)*	Ascending *(Kar et al. 2005) (Mazzitelli et al. 2013)*	Less stagnation in the aorta Still presence of turbulences Better contribution in upper arteries
	Descending *(Kar et al. 2005) (May-Newman et al. 2006)*	Reverse flow More stagnation near AoV
Descending *(May-Newman et al. 2006) (Bazilevs et al. 2009) (Mazzitelli et al. 2013)*	Clamped AoV *(Bazilevs et al. 2009)*	Unsteady flow, laminar
	Open AoV *(Bazilevs et al. 2009)*	Turbulent flow
Subclavian arteria *(Karmonik et al. 2015)*	Peak systole *(Karmonik et al. 2015)*	Ineffectiveness of the device

Despite several works have investigated the mechanical and fluidic issues imposed by MCS implants, many contradictions still appear and several phenomena are still unclear. To give an example, two different LVADs were considered in (Chiu et al. 2016): the Heartmate II (HM II) and the HeartAssist 5. According to the results, more important the elbow angle was (50° compared to 25°), less the thrombogenic potential was. On the contrary, clinical guidelines currently recommend not twisting or excessively angling this IC. Additionally, for the HeartAssist 5 results presented a lower thrombogenic potential with a 60° circumferential angle, whereas the HM II had lowest thrombogenic potential for 0°. More investigations are therefore necessary to evaluate all parameters impacting blood circulation, in order to optimize the pump implantation.

3. Morphological issues

Some postoperative complications such as right HF, chest pain or blood flow alterations are led by geometrical and anatomical constraints. Despite surgeons have preoperative and per-operative recommendations; they still face difficulties related to morphological issues. In this section we develop these difficulties and present questions surgeons currently raise, for both LVAD and TAH. Finally, a state of the art of work assessing the anatomical compatibility of MCS devices is provided.

3.1. Aortic calcifications and heart motion

Patients with HF may present aortic calcifications due to atherosclerosis. In the case of TAH, calcified areas are excised. The surgeon has to adjust adequate length for both outflow tracts and may also have to deal with different diameters between native vessels and Dacron conducts. For LVAD OCs anastomoses, area without calcification is selected or alternative sites may be considered (El-Sayed Ahmed et al. 2014). In both cases, anticipating calcification locations may help to preoperatively find potential areas of anastomoses and decrease identification time during the surgical procedure. Furthermore, the heart still beats after implantation which could for instance cause LVAD IC position and orientation modifications and promote suction events.

3.2. Intrathoracic space

Intrathoracic space raises several major issues in the context of MCS implantation. For instance, at the end of the surgical process, the chest wall may be difficult to close. Very large compared to available chest cavity space, these devices may compress or dislodge critical intrathoracic organs and/or the chest wall. If the TAH is stopped by the vertebral column before being in contact with the aorta, it may compress the pulmonary artery, left and right atrium resulting in physiology alteration. In the same way LVAD dislodgement increases the potential of RV compression and promotes deviation of the IC from its initial orientation and position. As mentioned in the previous section, an incorrect orientation promotes a multitude of adverse events. Intrathoracic space is therefore an important issue that must be anticipated and avoided.

In the case of the Syncardia TAH device, a minimum body surface area of 1.7 m^2 and a distance from the anterior border of T10 vertebra to the posterior part of the sternum of at least 10cm (Cook et al. 2015) are required. These features are roughly determined from the patient preoperative CT scan. On the one hand, these quantitative criteria exclude paediatric and small patients who may undergo TAH placement (Moore et al. 2014). (Leprince et al. 2005) demonstrated that the Syncardia TAH device can be used in patients with a BSA between 1.5m^2 and 1.7m^2. On the other hand, surgeons are sometimes peroperatively still confronted to the lack of space even respecting this BSA of 1.7m^2. These eligibility criteria related to the intrathoracic space are therefore not always applicable. In addition, intrathoracic space dimensions present variations over time due to heart and breathing motions. A study revealed that depending on the patient size, the distance between the sternum and the atrial septum can varies of over 10 mm between inspiration and expiration (Zhang et al. 2000). Quantitative criteria for TAH compatibility are measured on CT scan which protocol suggests a deep-inspiration breath-hold. Therefore, surgeons do not take into consideration preoperatively the smallest thoracic volume. If criteria exist for TAH, it is not the

case for LVAD implantation. These elements highlight the necessity of a patient specific planning for MCS implantation.

When the LVAD is fully running, the LV is discharged and its size decreased consequently. Depending on the pump speed, the LV dimensions under LVAD support is modified. More generally, these motions (depletion, heart beating and breathing motion) raise issues about the impact of intrathoracic volume variations on MCS position and interactions with surrounding organs. For TAH as for LVAD, these variations may be determinant to assess the anatomical compatibility.

More generally, surgeons have not enough experiments and feedback with new devices, and only a limited experience with RVAD devices. Indeed isolated right HF is rare and is most often combined with left HF, requiring a BiVAD support or TAH implantation in that case. Isolated RVAD implantations are highly limited in number and associated with a very poor outcome. However, RVAD implantation may be required when RV refractory dysfunction appears after LVAD implantation (Russell et al. 2006). To overcome the lack of dedicated and specific device to support the right side of the heart, surgeons consider using LVAD as RVAD. But the RV wall is so thin that in general it is difficult to insert the LVAD IC within this cavity. Furthermore, the right side of the heart works at low pressure and this may generate suction events with collapse of the RV wall around the inflow cannula. The flow pressure that is then ejected into the pulmonary artery may also be too high and inadequate for such low pressure system. As for LVAD, the question of intrathoracic space is raised for RVAD, especially when a LVAD has previously been implanted in the chest. Anticipating intrathoracic geometrical positioning should facilitate their implantation and limit surgeons' apprehensions and related complications.

3.3. Solutions from the literature

Several methods have been developed in the past few decades to explore the anatomical compatibility of MCS (Claussen 1983). Iterative implantation on animals, cadavers implantation, measurements on chest radiographs or evaluation based on 3D medical images were used with the main objective of optimizing the MCS design or finding anatomical fit criteria. In thoracic and cardiovascular field, medical imaging is largely used to represent structural or functional information. Valuable for providing a satisfactory representation of patients' anatomy, it allows studying the dedicated pathologies in real conditions and with real organ motions. Often used in the clinical routine and easy to set up, a large cohort survey may be envisaged. Medical imaging seems the best way to investigate anatomical compatibility of MCS. Herein are the different modalities used in the context of HF:

- CT scans provides a representation of lungs, heart, aorta or thorax. Giving structural information, it allows surgeons to identify additional disease or abnormal organ deformations. It can be used to assess patients with implanted cardiac devices.
- MRI is a non-irradiating modality used to evaluate the heart anatomy and function in patients with various heart diseases. Cavities and valves function may be studied as well as myocardium viability and blood flow through the major vessels. Pericardium (the membrane that surrounds the heart) may also be investigated.

Echocardiography is usually used in investigating abnormalities of the heart and blood vessels. It also provides audible sounds such as blood flow, in order to assess patients' health. The limited region of interest focuses on the heart cavities and structures.

In the context of MCS, few studies have dealt with thoracic compatibility considering anatomical representation from pre-operative imaging. Figure 2.8 summarizes these computerized approaches. Three main objectives may be distinguished: finding anatomical criteria for MCS implantation eligibility, optimization of MCS design and anticipating the device anatomical fit. Most of them have considered a multiple thoracic structures representation using CT volumes and segmentation. The two exceptions were (Fujimoto et al. 1985) with a general model and (Dickstein et al. 2008) with MRI. While the method of segmentation was not specifically addressed in (Moore et al. 2014; Moore et al. 2015; Ryan et al. 2017), manual delineations were performed in (Chatel et al. 1993; Zhang et al. 1999; Zhang et al. 2000; Warriner et al. 2004), semi-automatic methods were implemented in (Drummond & Antaki 2008; Noecker et al. 2007), threshold followed by automated standard image processing tools (region growing, morphology operations) were used in (Fritschi et al. 2013) and (Park et al. 2014) used Mimics (Materialise, Leuven, Belgium), a medical imaging software that propagates a 2D selected region of interest into a 3D model.

Few articles dealt with the assessment and the determination of MCS anatomical fit criteria. For most of them, the underlying issue was related to patient eligibility in the context of TAH. Indeed, (Chatel et al. 1993) introduced a computerized three-dimensional modelling of cardiovascular structures to measure volumetric and geometric parameters defining the shape and intrathoracic space. (Moore et al. 2014) evaluated whether current fit criteria from (Copeland et al. 1999) fulfilled based on virtual implantation performed for three case reports. In the same way, two TAH designs were compared in (Moore et al. 2015) with paediatric and small patients. Only the work reported in (Ryan et al. 2017) dealt with virtual fit in the context of LVAD devices. A virtual implantation was performed in small patients in order to determine the lowest appropriate paediatric patients' size for a specific device.

Most of the articles' objective is to optimize the MCS design. For instance, (Komoda et al. 1992) used six healthy subjects to measure criterion that restrict size and shape of TAH, as (Fujimoto et al. 1985) did with a general morphological model. (Noecker et al. 2007) tested their new pump on 11 CTs, while (Fritschi et al. 2013) analysed interactions between the TAH and mediastinum on CTs. Finally, (Drummond et al. 2006; Drummond & Antaki 2008) designed their device on 3D structures segmented from a CT. Due to the difficulty of finding one MCS size and shape that should fit all cases, (Claussen 1983) have put forward the related idea of fitting an artificial heart before the operation. Only (Noecker et al. 2007) mentioned the potential of their system for preoperative discussion among medical staff.

Over the last years, only four articles presented a virtual implantation of MCS with the aim of preoperatively anticipate anatomic compatibility. (Zhang et al. 1999; Zhang et al. 2000) introduced a prototype TAH implantation simulation environment with both objectives of optimizing the device design and assessing the anatomic compatibility of a patient. In the same way, (Warriner et al. 2004) demonstrated the feasibility of implementing a rapid preoperative screening method in order to design LVAD or TAH implantation, as well as enabling selection or rejection of candidates

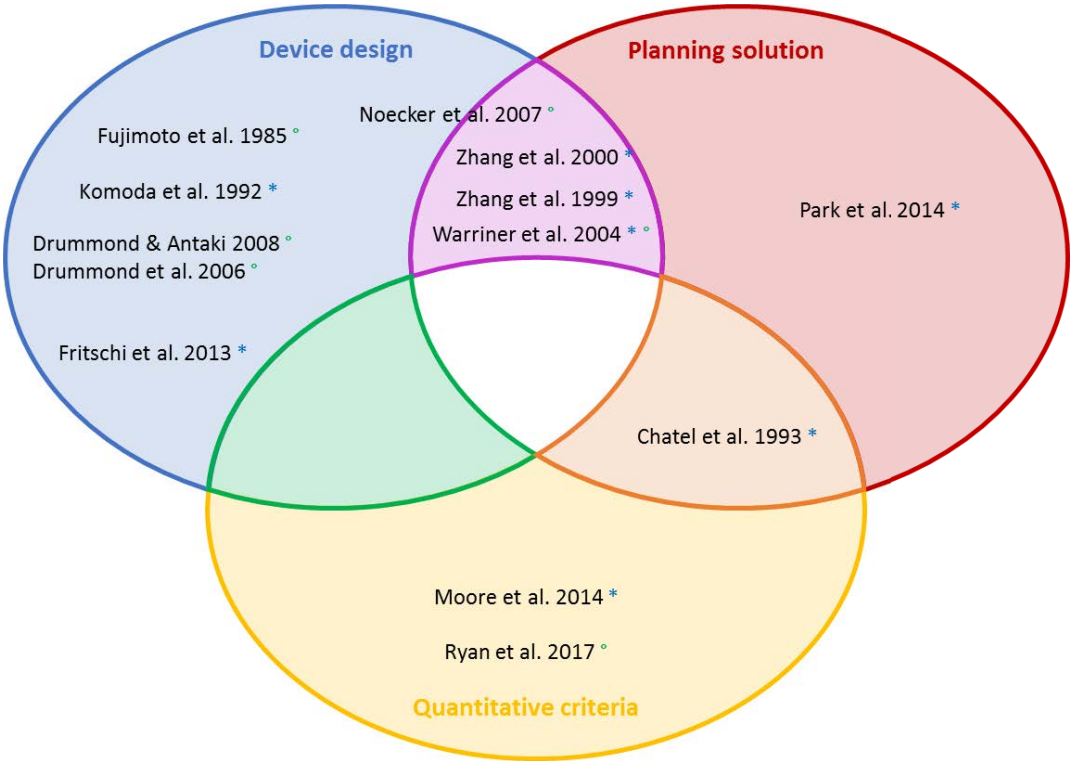

Figure 2.8 - Computerized approaches in the context of MCS.
*° represents articles addressing LVAD issues whereas * are those addressing TAH issues*

and determining the optimal anatomical device fit. To our knowledge, (Park et al. 2014) is the only article that explicitly addressed the planning issue. Through case reports, they proposed a 3D modelling to determine if Syncardia TAH fit for patient with quantitative criteria below the recommendation.

To conclude, all works dealt with morphological issues without taking into consideration heart and breathing motions. Most articles with the objective of planning were positioned on TAH implantation and only enabled visual inspection. Requirements substantially differ from those for LVAD implantation. The few works that consider VAD do not examine the IC anatomical compatibility. (Sacks et al. 2015) evoked the used of CT scans to predict future adverse outcomes related to the IC orientation, but for patients already implanted. More recently, (Farooqi et al. 2016) presented the use of 3D printing for visualization of 3D cardiac anatomy of patients with specific congenital defects (congenital cardiac malformation in which there is ventriculo-arterial and/or atrioventricular discordance). Planning LVAD implantation based on preoperative CT scan has not yet been specifically addressed, and to our knowledge no tool exists in clinical practice to help surgeons anticipating preoperatively anatomic compatibility with TAH or LVAD.

4. Work positioning and proposed approach

Surgeons are preoperatively and per-operatively faced to many questions that still remain unanswered. Nowadays, they take their decision using their professional experiences and habits. The aim of this thesis is to provide information that could support surgeon decisions in future MCS implantation process. The proposed approach aims at preoperatively planning and simulating artificial heart implantation surgery (Figure 2.9).

The device is currently selected based on clinical data. Pre-operative images could be used quantitatively to plan and optimize the treatment strategy before surgery, especially for LVAD implantation. This question is open and has still to be investigated in MCS context. More precisely, the issue we address in our work can be expressed as follows: *Does the MCS device fit the intrathoracic space and with a suitable position in a specific patient?* The proposed approach is to evaluate MCS compatibility according to the patient anatomy through a computer-aided pose planning. Based on virtual preoperative positioning, the solution necessitates an appropriate description of patient anatomy. Such a clinical decision support system could be used to determine preoperatively the optimal anatomical device fit and which MCS seems the most appropriate. Notice that the final decision will always be taken by the health professional.

Hemodynamics is an important part of cardiovascular physiology and has a significant impact to ensure the proper functioning of MCS. As mentioned previously, incorrect blood flow may promote deterioration of the LVAD efficiency or lead to significant adverse health consequences. Considering the large number of issues raised by LVAD, we focus on fluid dynamics related to the IC. Surgeons have less information about it and reported works are limited compared to OC. In this thesis we therefore focus on the analysis of functional and physiological interactions related to the IC configuration, through computational modelling. The aim is to provide general information that could be integrated within a virtual treatment solution as optimisation pose criterion.

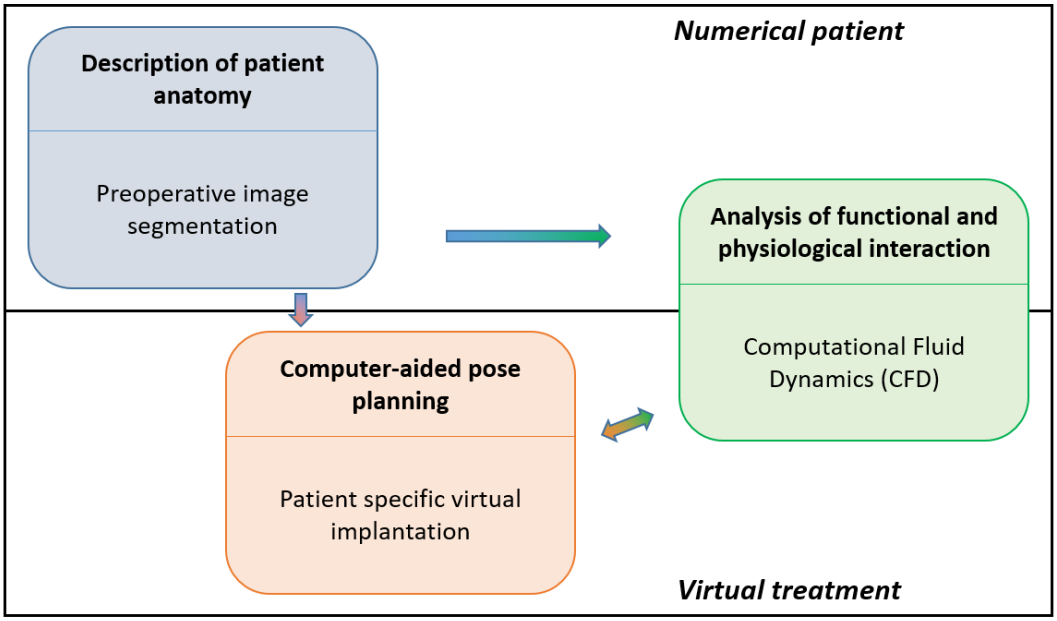

Figure 2.9 - Preoperative decision support for MCS computer-aided planning

References

Addetia, K. et al., 2017. 3D Morphological Changes in LV and RV During LVAD Ramp Studies. *JACC: Cardiovascular Imaging*.

Alonazi, K.A., Lovell, N.H. & Dokos, S., 2015. Simulation of aortic valve dynamics during ventricular support. *Proceedings of the Annual International Conference of the IEEE Engineering in Medicine and Biology Society, EMBS*, 2015–Novem, pp.1881–1885.

Argueta-Morales, I.R. et al., 2010. Use of computational fluid dynamics (CFD) to tailor the surgical implantation of a ventricular assist device (VAD): A patient-specific approach to reduce risk of stroke. *Journal of the American College of Surgeons*, 211(3), pp.S26–S27.

Aymami, M. et al., 2016. Rest and Exercise Adaptation of the Right Ventricular Function in Long-Term Left Ventricular Assist Device Patients: A Prospective, Pilot Study. *Journal of Cardiac Failure*, 22(3), pp.240–241.

Bachman, T.N. et al., 2011. In Vitro Evaluation of Ventricular Cannulation for Rotodynamic Cardiac Assist Devices. *Cardiovascular Engineering and Technology*, 2(3), pp.203–211.

Bazilevs, Y. et al., 2009. Patient-specific isogeometric fluid – structure interaction analysis of thoracic aortic blood flow due to implantation of the Jarvik 2000 left ventricular assist device. *Computer Methods in Applied Mechanics and Engineering*, 198(45–46), pp.3534–3550.

Benk, C. et al., 2013. Effect of cannula position in the thoracic aorta with continuous left ventricular support: Four-dimensional flow-sensitive magnetic resonance imaging in an in vitro model. *European Journal of Cardio-thoracic Surgery*, 44(3), pp.551–558.

Bhat, S. et al., 2017. Effect of Outflow Graft Size on Flow in the Aortic Arch and Cerebral Blood Flow in Continuous Flow Pumps. *ASAIO Journal*, 63(2), pp.144–149.

Bonnemain, J. et al., 2013. Numerical simulation of left ventricular assist device implantations: Comparing the ascending and the descending aorta cannulations. *Medical Engineering and Physics*, 35(10), pp.1465–1475.

Brown, A.G. et al., 2012. Importance of realistic LVAD profiles for assisted aortic simulations: evaluation of optimal outflow anastomosis locations. *Computer Methods in Biomechanics and Biomedical Engineering*, 15(April 2015), pp.669–680.

Callington, A. et al., 2015. Computational fluid dynamic study of hemodynamic effects on aortic root blood flow of systematically varied left ventricular assist device graft anastomosis design. *The Journal of Thoracic and Cardiovascular Surgery*, 150(3), pp.696–704.

Chatel, D. et al., 1993. Criteria for anatomical compatibility of the total artificial heart: computerized three-dimensional modeling of the cardiovascular anatomy. *Artificial Organs*,

17(12), pp.1022–1035.

Chiu, W.-C. et al., 2016. Ventricular Assist Device Implantation Configurations Impact Overall Mechanical Circulatory Support System Thrombogenic Potential. *ASAIO journal (American Society for Artificial Internal Organs: 1992)*, pp.285–292.

Chorro, F.J., Such-Belenguer, L. & López-Merino, V., 2009. Animal Models of Cardiovascular Disease. *Revista Española de Cardiología (English Edition)*, 62(1), pp.69–84.

Claussen, K.A.H.S.C., 1983. The use of computer graphics to find an optimal fit for a human total artificial heart. *ASAIO Trans.*, 9, pp.29–103.

Cook, J.A. et al., 2015. The total artificial heart. *Journal of thoracic disease*, 7(12), pp.2172–80.

Copeland, J.G. et al., 1999. Arizona experience with CardioWest Total Artificial Heart bridge to transplantation. In *Annals of Thoracic Surgery*. pp. 756–760.

Dickstein, K. et al., 2008. ESC Guidelines for the diagnosis and treatment of acute and chronic heart failure 2008. *European Heart Journal*, 29(19), pp.2388–2442.

Drummond, A. & Antaki, J., 2008. Virtual Fit Study of Pediatric Heart Assist System. *Digital Human Modeling: Trends in Human Algorithms*, pp.71–89.

Drummond, A., Bachman, T. & Antaki, J., 2006. Three-dimensional virtual anatomic fit study for an implantable pediatric ventricular assist device. *Lecture Notes in Computer Science (including subseries Lecture Notes in Artificial Intelligence and Lecture Notes in Bioinformatics)*, 3994 LNCS, pp.855–861.

El-Sayed Ahmed, M.M. et al., 2014. Left ventricular assist device outflow graft: alternative sites. *Annals of cardiothoracic surgery*, 3(5), pp.541–5.

Estep, J.D. et al., 2010. The role of echocardiography and other imaging modalities in patients with left ventricular assist devices. *JACC. Cardiovascular imaging*, 3(10), pp.1049–1064.

Farooqi, K.M. et al., 2016. 3D Printing to Guide Ventricular Assist Device Placement in Adults With Congenital Heart Disease and Heart Failure. *JACC: Heart Failure*, 4(4), pp.301–311.

Filipovic, N. & Schima, H., 2011. Numerical Simulation of the Flow Field Within the Aortic Arch During Cardiac Assist. *Artificial Organs*, 35(4), pp.73–83.

Fine, N.M. et al., 2016. Proximal thoracic aorta dimensions after continuous-flow left ventricular assist device implantation: Longitudinal changes and relation to aortic valve insufficiency. *Journal of Heart and Lung Transplantation*, 35(4), pp.423–432.

Fraser, K.H. et al., 2011. Computational fluid dynamics analysis of thrombosis potential in left ventricular assist device drainage cannulae. *ASAIO journal (American Society for Artificial Internal Organs: 1992)*, 56(3), pp.157–163.

Fritschi, A.J. et al., 2013. Image based evaluation of mediastinal constraints for the development

of a pulsatile total artificial heart. *Biomedical engineering online*, 12(1), p.81.

Fujimoto, L.K. et al., 1985. Anatomical considerations in the design of a long-term implantable human left ventricle assist system. *Artificial organs*, 9(4), pp.361–374.

Gohean, J.R. et al., 2013. Verification of a Computational Cardiovascular System Model Comparing the Hemodynamics of a Continuous Flow to a Synchronous Valveless Pulsatile Flow Left Ventricular Assist Device. *Asaio Journal*, 59(2), pp.107–116.

Gramigna, V., 2014. *Influence of Aortic Outflow Cannula Orientation On Epiaortic Flow Pattern During Pulsed Cardio Pulmanory Bypass*.

Guimond, S.A., 2012. *Computational fluid dynamics investigation of the orientation of a pediatric left ventricular assist device cannula to reduce stroke events*.

Hsu, P.-L. et al., 2015. In-Series Versus In-Parallel Mechanical Circulatory Support for the Right Heart: A Simulation Study. *Artificial Organs*.

Inci, G. & Sorgüven, E., 2012. Effect of LVAD Outlet Graft Anastomosis Angle on the Aortic Valve, Wall, and Flow. *ASAIO Journal*, 58(4), pp.373–381.

Jhun, C.-S., Sun, K. & Cysyk, J.P., 2014. Continuous flow left ventricular pump support and its effect on regional left ventricular wall stress: finite element analysis study. *Medical & Biological Engineering & Computing*, 52(12), pp.1031–1040.

John, R. et al., 2010. Aortic valve pathophysiology during left ventricular assist device support. *The Journal of heart and lung transplantation: the official publication of the International Society for Heart Transplantation*, 29(12), pp.1321–1329.

Kar, B. et al., 2005. The effect of LVAD aortic outflow-graft placement on hemodynamics and flow: Implantation technique and computer flow modeling. *Texas Heart Institute journal / from the Texas Heart Institute of St. Luke's Episcopal Hospital, Texas Children's Hospital*, 32(3), pp.294–298.

Karmonik, C., Partovi, S., Schmack, B., et al., 2014. Comparison of hemodynamics in the ascending aorta between pulsatile and continuous flow left ventricular assist devices using computational fluid dynamics based on computed tomography images. *Artificial Organs*, 38(2), pp.142–148.

Karmonik, C., Partovi, S., Loebe, M., et al., 2014. Computational fluid dynamics in patients with continuous-flow left ventricular assist device support show hemodynamic alterations in the ascending aorta. *Journal of Thoracic and Cardiovascular Surgery*, 147(4), p.1326–1333.e1.

Karmonik, C. et al., 2015. Hemodynamic assessment of partial mechanical circulatory support: data derived from computed tomography angiographic images and computational fluid dynamics. *Cardiovascular Diagnosis and Therapy*, 5(2), pp.160–165.

Karmonik, C. et al., 2012. Influence of LVAD Cannula Outflow Tract Location on Hemodynamics

in the Ascending Aorta: A Patient-Specific Computational Fluid Dynamics Approach. *ASAIO Journal*, 58(6), pp.562–567.

Kheradvar, A., Milano, M. & Gharib, M., 2007. Correlation between vortex ring formation and mitral annulus dynamics during ventricular rapid filling. *ASAIO journal (American Society for Artificial Internal Organs: 1992)*, 53(1), pp.8–16.

Kirklin, J.K. et al., 2013. Fifth INTERMACS annual report: risk factor analysis from more than 6,000 mechanical circulatory support patients. *The Journal of heart and lung transplantation: the official publication of the International Society for Heart Transplantation*, 32(2), pp.141–56.

Komoda, T. et al., 1992. Study of Anatomic Constraints Using Three Dimensionally Reconstructed Images for Total Artificial Heart Implantation. *ASAIO*.

Korakianitis, T. & Shi, Y., 2007. Numerical comparison of hemodynamics with atrium to aorta and ventricular apex to aorta VAD support. *ASAIO journal (American Society for Artificial Internal Organs: 1992)*, 53(5), pp.537–548.

Lafortune, P. & Aris, R., 2015. Coupled electromechanical model of the heart: parallel finite element formulation. *International Journal for Numerical Methods in Biomedical Engineering*, 28(1), pp.72–86.

Laumen, M. et al., 2010. Flow analysis of ventricular assist device inflow and outflow cannula positioning using a naturally shaped ventricle and aortic branch. *Artificial Organs*, 34(10), pp.798–806.

Leong, X.F., Ng, C.Y. & Jaarin, K., 2015. Animal Models in Cardiovascular Research: Hypertension and Atherosclerosis. *BioMed Research International*, 2015(ii).

Leprince, P. et al., 2005. Patients with a body surface area less than 1.7 m2have a good outcome with the CardioWest Total Artificial Heart. *Journal of Heart and Lung Transplantation*, 24(10), pp.1501–1505.

Li, X., Bai, J. & He, P., 2002. Simulation study of the Hemopump as a cardiac assist device. *Med. Biol. Eng. Comput.*, 40(March), pp.344–353.

Litwak, K.N. et al., 2005. Ascending aorta outflow graft location and pulsatile ventricular assist provide optimal hemodynamic support in an adult mock circulation. *Artificial Organs*, 29(8), pp.629–635.

Litwak, K.N. et al., 2004. Effects of Left Ventricular Assist Device Support and Outflow Graft Location Upon Aortic Blood Flow. *ASAIO Journal*, 50(5), pp.432–437.

Litwak, K.N. et al., 2008. Retrospective analysis of adverse events in preclinical ventricular assist device experiments. *ASAIO journal (American Society for Artificial Internal Organs: 1992)*, 54(4), pp.347–350.

Liu, G.M. et al., 2012. Numerical simulation of LVAD inflow cannulas with different tip. *International Journal of Chemical Engineering*, 2012.

May-Newman, K. et al., 2016. *The Effect of Inflow Cannula Length on the Intraventricular Flow Field of the EvaHeart LVAD-Assisted Heart*,

May-Newman, K., Hillen, B. & Dembitsky, W., 2006. Effect of Left Ventricular Assist Device Outflow Conduit Anastomosis Location on Flow Patterns in the Native Aorta: *ASAIO Journal*, 52(2), pp.132–139.

May-Newman, K.D. et al., 2004. Effect of LVAD outflow conduit insertion angle on flow through the native aorta. *Journal of Medical Engineering & Technology*, 28(3), pp.105–109.

Mazzitelli, R. et al., 2013. Three-Dimensional Numerical Simulations of the Aortic Flow in Presence of a Left Ventricle Assist Device with Two Outflow Graft Placements. *International Journal of Privacy and Health Information Management*, 1(2), pp.76–95.

McCormick, M. et al., 2013. Simulating left ventricular fluid-solid mechanics through the cardiac cycle under LVAD support. *Journal of Computational Physics*, 244, pp.80–96.

Menon, P.G. et al., 2013. Aortic outflow cannula tip design and orientation impacts cerebral perfusion during pediatric cardiopulmonary bypass procedures. *Annals of Biomedical Engineering*, 41(12), pp.2588–2602.

Moore, R.A. et al., 2014. Virtual implantation evaluation of the total artificial heart and compatibility: Beyond standard fit criteria. *The Journal of Heart and Lung Transplantation*, 33(11), pp.1180–3.

Moore, R.A. et al., 2015. Virtual Implantation of the 50cc Total Artificial Heart. *ISHLT: 35th Annual Meeting and Scientific Sessions*, 34(4), p.abstract #223.

Morris, P.D. et al., 2016. Computational fluid dynamics modelling in cardiovascular medicine. *Heart*, 102(1), pp.18–28.

Neidlin, M. et al., 2016. Hemodynamic analysis of outflow grafting positions of a ventricular assist device using closed-loop multiscale CFD simulations: Preliminary results. *Journal of Biomechanics*, 49(13), pp.2718–2725.

Noecker, A.M. et al., 2007. The Cleveland Clinic PediPump: anatomic modeling and virtual fitting studies in a lamb model. *Asaio J*, 53(6), pp.716–719.

Ong, C. et al., 2012. Fluid Structure Interaction Simulation of Left Ventricular Flow Dynamics under Left Ventricular Assist Device Support. *IEEE EMBS*, pp.1–4.

Ong, C. et al., 2013. Numerical investigation of the effect of cannula placement on thrombosis. *Theoretical biology & medical modelling*, 10(1), p.35.

Osorio, A.F. et al., 2013. Computational fluid dynamics analysis of surgical adjustment of left

ventricular assist device implantation to minimise stroke risk. *Computer methods in biomechanics and biomedical engineering*, 16(6), pp.622–38.

Park, S.S. et al., 2014. Total artificial heart in the pediatric patient with biventricular heart failure. *Perfusion*, 29(1), pp.82–8.

Porter, T.R. et al., 2015. Guidelines for the use of echocardiography as a monitor for therapeutic intervention in adults: A report from the american society of echocardiography. *Journal of the American Society of Echocardiography*, 28(1), pp.40–56.

Poullis, M., 2012. Computational fluid dynamic analysis to prevent aortic root and valve clots during left ventricular assist device support. *J Extra Corpor Technol*, 44(4), pp.210–215.

Prather, R.A.Y., 2015. *a Multi-Scale Cfd Analysis of Patient- Specific Geometries To Tailor Lvad Cannula Implantation Under Pulsatile Flow Conditions: an Investigation Aimed At Reducing Stroke Incidence in LVADs*.

Prisco, A.R. et al., 2017. Impact of LVAD Implantation Site on Ventricular Blood Stagnation. *ASAIO Journal*, 63(4), pp.392–400.

Quaini, A., Canić, S. & Paniagua, D., 2011. Numerical characterization of hemodynamics conditions near aortic valve after implantation of Left Ventricular Assist Device. *Mathematical biosciences and engineering: MBE*, 8(3), pp.785–806.

Russell, S. et al., 2006. Patient Management Guidelines. , pp.1–75.

Ryan, A.J. et al., 2016. Towards 3D in vitro models for the study of cardiovascular tissues and disease. *Drug Discovery Today*, 21(9), pp.1437–1445.

Ryan, J.R. et al., 2017. Virtual Implantation of the Infant Jarvik 2015 for Eligibility Criteria Establishment. *The Journal of Heart and Lung Transplantation*, 36(4), pp.S13–S14.

Sacks, J. et al., 2015. Utility of cardiac computed tomography for inflow cannula patency assessment and prediction of clinical outcome in patients with the HeartMate II left ventricular assist device. *Interactive CardioVascular and Thoracic Surgery*, 21(5), pp.590–593.

Schmid, C. et al., 2008. Influence of Inflow Cannula Length in Axial-flow Pumps on Neurologic Adverse Event Rate: Results From a Multi-center Analysis. *Journal of Heart and Lung Transplantation*, 27(3), pp.253–260.

Stühle, S. et al., 2011. Numerical simulation of hemodynamics in the ascending aorta induced by different aortic cannulas. *Minimally Invasive Therapy & Allied Technologies*, 20(2), pp.125–131.

Taylor, C.A. & Draney, M.T., 2004. Experimental and Computational Methods in Cardiovascular Fluid Mechanics. *Annual Review of Fluid Mechanics*, 36(1), pp.197–231.

Tse, K.M. et al., 2013. A computational fluid dynamics study on geometrical influence of the aorta on haemodynamics. *European Journal of Cardio-thoracic Surgery*, 43(4), pp.829–838.

Tsukiya, T. et al., 2011. Computational fluid dynamic analysis of the flow field in the newly developed inflow cannula for a bridge-to-decision mechanical circulatory support. *Journal of artificial organs: the official journal of the Japanese Society for Artificial Organs*, (June), pp.25–33.

Warriner, R.K. et al., 2004. Virtual anatomical three-dimensional fit trial for intra-thoracically implanted medical devices. *ASAIO Journal*, 50(4), pp.354–359.

Yang, N. et al., 2010. Comparative Study of Continuous and Pulsatile Left Ventricular Assist Devices on Hemodynamics of a Pediatric End-to-Side Anastomotic Graft. *Cardiovascular Engineering and Technology*, 1(1), pp.88–103.

Yang, N. et al., 2009. Numerical study of blood flow at the end-to-side anastomosis of a left ventricular assist device for adult patients. *Journal of biomechanical engineering*, 131(11).

Yoshida, S. et al., 2017. Visualization of vortex flow and shear stress in the aortic root during left ventricular assist device support. *The Journal of Thoracic and Cardiovascular Surgery*, 154(3), p.877–878.e1.

Zhang, B. et al., 2000. Noninvasive assessment method to determine the anatomic compatibility of an implantable artificial heart system. *ASAIO Journal*, 46(5), pp.590–595.

Zhang, B. et al., 1999. Three-dimensional thoracic modeling for an anatomical compatibility study of the implantable total artificial heart. *Artificial Organs*, 23(3), pp.229–234.

Zhang, Y., Gao, B. & Yu, C., 2016. The hemodynamic effects of the LVAD outflow cannula location on the thrombi distribution in the aorta: A primary numerical study. *Computer Methods and Programs in Biomedicine*, 133, pp.217–227.

Chapter 3 - Anatomical structures description

Medical imaging is currently one of the main ways to observe anatomy and physiology. Segmentation of medical images is largely used in computer aided diagnosis. More generally, it represents a key step towards clinical decision support requiring accurate and patient-specific description, visualization or characterization of anatomical structures. Manual delineation may become time-consuming, that is why semi-automatic and automatic methods have been developed over the last decades. A multitude of approaches have been proposed in the literature. However, segmentation presents still challenges and several open issues, especially in pathological cases or when multiple structures have to be distinguished in low-contrasted, noisy or motion-artefact images.

The primary goal of this work is to define a strategy for virtual patient representation in the aim to elaborate a computer aided planning for long term MCS device implantation. This chapter provides a general insight of existing methods and select or adapt the most suitable approaches in order to investigate their performance in this context. First section details imaging modalities used and a general classification of segmentation methods. Then, in order to highlight potentials and issues raised by segmentation, an overview of the literature for each critical organ is presented, and several methods are evaluated and compared dealing essentially with pathological cases.

1. Medical imaging and segmentation methods

Several anatomical structures are in the neighbourhood of MCS device. In the context of virtual planning for MCS implantation, we choose four organs that come into consideration: the heart, aorta, lungs, and thoracic bones. Next section introduces images used in clinical routine that represents these structures. A general classification of segmentation methods with an overview of each class techniques is provided in the second section.

1.1. Medical imaging in MCS context

Surgeons routinely use the Doppler-echocardiography for diagnosis and follow up of patients who are candidates for MCS device implantation. This modality provides preoperatively and postoperatively many information such as shape of the heart, size of cavities, associated valvulopathy, tissue damages and pumping capacity. However, it is yet not compatible with patient specific virtual representation for MCS device implantation. The field of view is too restricted and only the heart is mainly visible within the image. MRI and CT scan are two modalities which create

an image including all thoracic structures. Some patient underwent preoperative MRI acquisition, but it is not an exploitable imaging modality in an effectively operational planning system. Indeed, a large number of patients already have an Intra-Cardiac Device (ICD) (*e.g.* pacemaker) making preoperative MRI acquisition impossible for them. Preoperative CT scan is always used in the patients' selection process (as mentioned in chapter 1). We intend thus to use this modality as reference for the planning solution.

As for modalities, CT acquisition protocol also varies. For instance, low-dose CT scans are used for lung cancer detection while CT angiographies are for the evaluation of blood vessels disease. Criteria were defined in order to allow clear identification of required structures. These criteria were based on structures visibility, slice thickness and field of view. CTs must be contrast-enhanced with a thin slice (≤1.25mm) and the region of interest is defined from the first ribs to a minimum of 7cm below the apex (maximal length devoted to the device).

The dataset used in this chapter, is composed of a set of CTs from the University Hospital of Rennes. A total of 32 preoperative CTs from 28 patients implanted between 2010 and 2016 were retained. All patients suffered preoperatively of a congestive heart failure (grade III or IV from NYHA) and CTs slice thickness varied between 0.625mm to 1.25mm while the number of slices lies between 281 and 1321.

1.2. Classification of segmentation methods

A large number of algorithms were developed for CT segmentation, making classification a real difficulty. Taxonomy varies from an article to another. For instance, (Niessen 2008) classified all methods into three categories: low-level, model-based and hybrid methods, while (Kang et al. 2012) preferred to consider five categories: boundary driven, region-based, graph-cut, model-fitting and hybrid methods. Herein, we ensured the classification from (Mansoor et al. 2015) which defined five categories:

- **Thresholding-based** methods consist in partitioning the image, based on attenuation values called Hounsfield Unit (HU). Regularly followed by morphological operations, these methods are simple and effective for well-contrasted objects. However, they do not take into consideration spatial characteristics and variability.
- **Region-based** methods evaluate neighbouring pixels/voxels based on the fact that all voxels from the same region have similar HU values. Region growing, watershed transform, graph-based and fuzzy connectedness are part of this class. Including spatial information, these methods are more accurate and efficient than thresholding-based ones.

- **Shape-based** methods use prior information considering global and local variation of the shape and texture. Approaches are based on shape registration and transformation. Atlas-Based and Deformable Model (DM) fall into this class as well as boundary-based approaches such as active contours, level sets and Active Shape Model (ASM).
- **Machine learning-based** methods can adjust parameters learning from the data. This class is also called pixel/voxel-based classification. Mostly used for parameters identification, these approaches are useful for detecting and quantifying pathological conditions.
- **Neighbouring anatomy-based** methods segment an organ exploiting surrounding anatomical structures segmentation. They are thus greatly dependent of other segmentations.

Each mentioned classes has its pros and cons. (Mansoor et al. 2015) provided an overview of these advantages and disadvantages in Table 3-I. In addition, the anatomical structures and pathologies of interest influence segmentation techniques employed. For instance, machine learning-based methods are most of the time exploited for specific pathology. In chest application it is in majority used for nodules detection, characterization or classification. In cardiovascular it is generally used for coronary centreline extraction or calcium detection. Necessitating a huge number of data for

Table 3-I - Major classes of segmentation methods with their advantages and disadvantages
Source: (Mansoor et al. 2015)

Segmentation class	Application	Advantages	Disadvantages
Thresholding-based methods	Identification and segmentation of well-defined normal structures and isolated lesions	Basic, intuitive, fast, least expensive computationally	Fails to deal with attenuation variations Fails to categorize pathologic classifications
Region-based methods	Normal structures, regions with minimal noise, minimal abnormality	Fast, works well with more-subtle attenuation variations	Fails to segment regions with moderate to high levels of abnormality or when pathologic condition abuts adjacent structures
Shape-based methods	Abnormal pathologic conditions that defy segmentation of normal anatomy	For a well-conceived representative template segmentation accuracy can be high	Representative training features difficult to create, computationally expensive, performance highly dependent on the feature set and training data
Neighbouring anatomy-guided methods	Identification and classification of pathologic conditions	Works well for cases in which attenuation-based matrices fail	Computationally expensive, severe pathologic condition could throw it off
Machine learning-based methods	Delineation of pathologic conditions with signature textured patterns	Works well to identify ill- defined diffuse pathologic conditions, categorizes pathologic classifications	Computationally expensive, no good separation among classes of pathologic conditions

the learning step, the lack of large training datasets is often mentioned as an obstacle in the literature (Litjens et al. 2017). Machine learning-based approaches are thus not suitable in MCS context. In next section, the quality of the dataset was evaluated in order to highlight the potential challenges for segmentations.

2. Evaluation of preoperative CT scans

In the context of MCS device implantation, CT scans quality may be altered by two principal factors. In a first hand, metallic artefacts due to ICD may be present. About 56% of patients from the dataset presented in section 1.1 had an ICD. On the other hand, perfect contrast agent homogeneity is impossible in practice. To evaluate the influence of contrast media on CT quality, four categories were distinguished: Good contrast, medium one, no or low contrast and finally

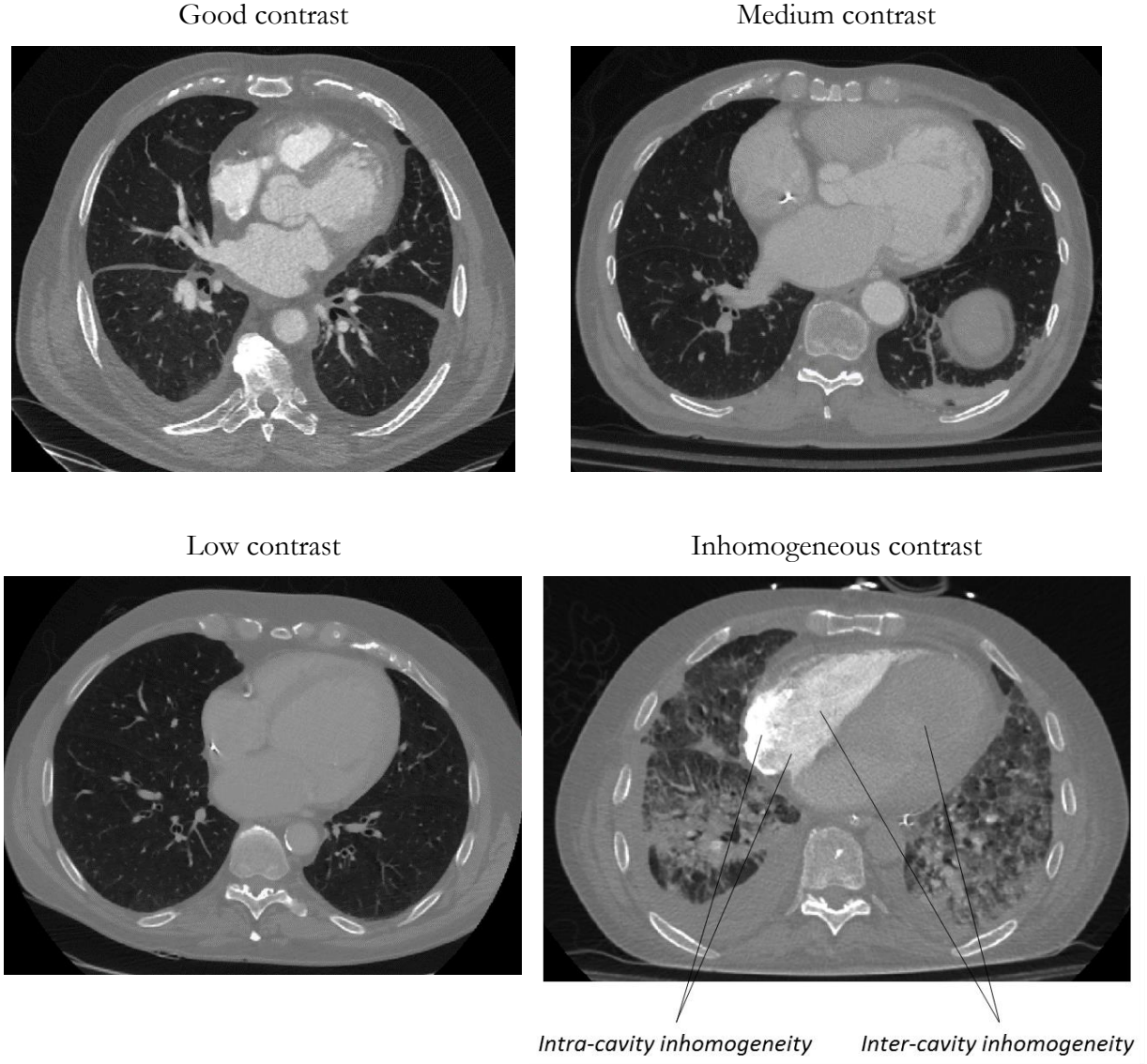

Figure 3.1 - Illustration of the contrast quality in CT scan

inhomogeneous one. The inter-cavity and intra-cavity inhomogeneity were also differentiated. Inter-cavity inhomogeneity consisted in a difference in concentration of contrast media between the left cavity and the right cavity. An intra-cavity inhomogeneity was characterized by an inhomogeneous repartition within the right cavity. Figure 3.1 illustrates each of these categories.

Our analysis was based on 3 regions manually delineated with Itk-Snap[3] (Figure 3.2). The left and right hearts were segmented on an axial slice to evaluate the concentration and inter-cavity homogeneity. The right cavities were delineated on a sagittal slice to analyse the presence of intra-cavity inhomogeneity.

Left heart delineation on an axial slice

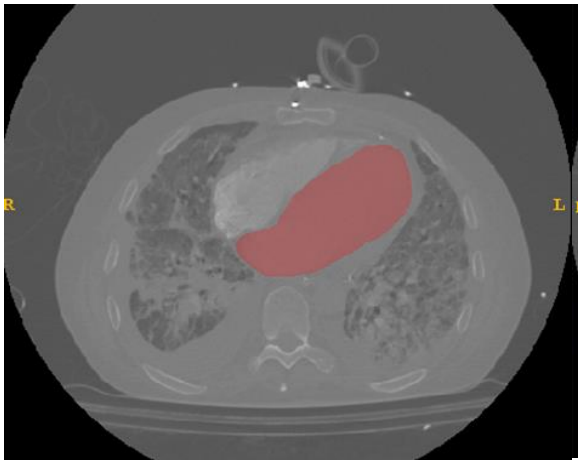

Right heart delineation on an axial slice

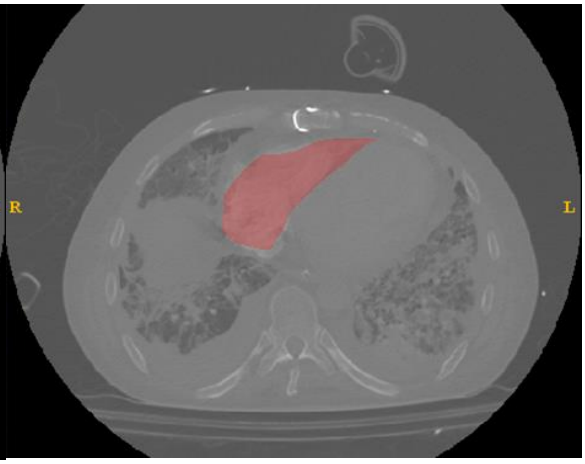

Right heart delineation on a sagittal slice

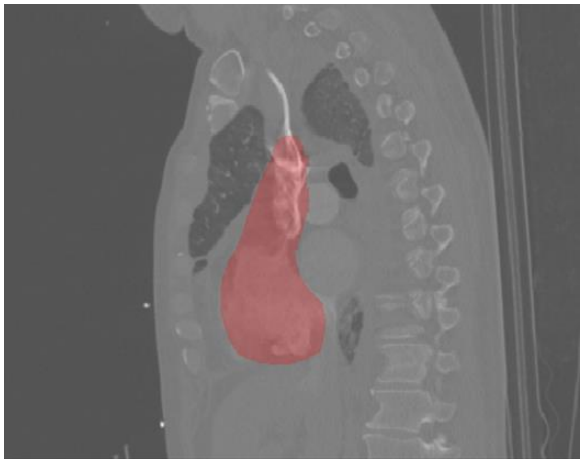

Figure 3.2 - 2D segmentations for the evaluation of the CT contrast quality

[3] Yushkevich, P. a. et al., 2006. User-guided 3D active contour segmentation of anatomical structures: Significantly improved efficiency and reliability. NeuroImage, 31(3), pp.1116–1128.

The mean and standard deviation from the histogram of each segmentation were used to classify CTs. In the following, $\bar{M}_{RH}$ characterizes the mean value of the histogram from the axial right heart segmentation, $\bar{M}_{LH}$ the mean value of the histogram from the axial left heart segmentation, SD_{RHsag} the standard deviation from the sagittal right heart segmentation, and finally the difference $D_{LH/RH}$ is defined by:

$$D_{LH/RH} = |\bar{M}_{LH} - \bar{M}_{RH}| \quad (1)$$

$\bar{M}_{RH}$ and $\bar{M}_{LH}$ were used to evaluate the sufficient presence of contrast, $D_{LH/RH}$ to analyse the inter-cavity homogeneity and SD_{RHsag} intra-cavity homogeneity. Figure 3.3 represents the approach used to categorise CTs while Table 3-II summarizes results obtained. In the dataset, about 53% of the CTs were considered as correctly contrasted (good and medium) which means that about half presented low or inhomogeneous contrast. Notice that CTs with ICD presented more inhomogeneity than those without ICD. The presence of metal artefacts may potentially alter these results. However, inhomogeneity within a cavity because of contrast media or metallic artefacts will have the same impact on the final CT quality interpretation. To conclude, there is a high variability of CT quality that may impact segmentation processes in the context of MCS.

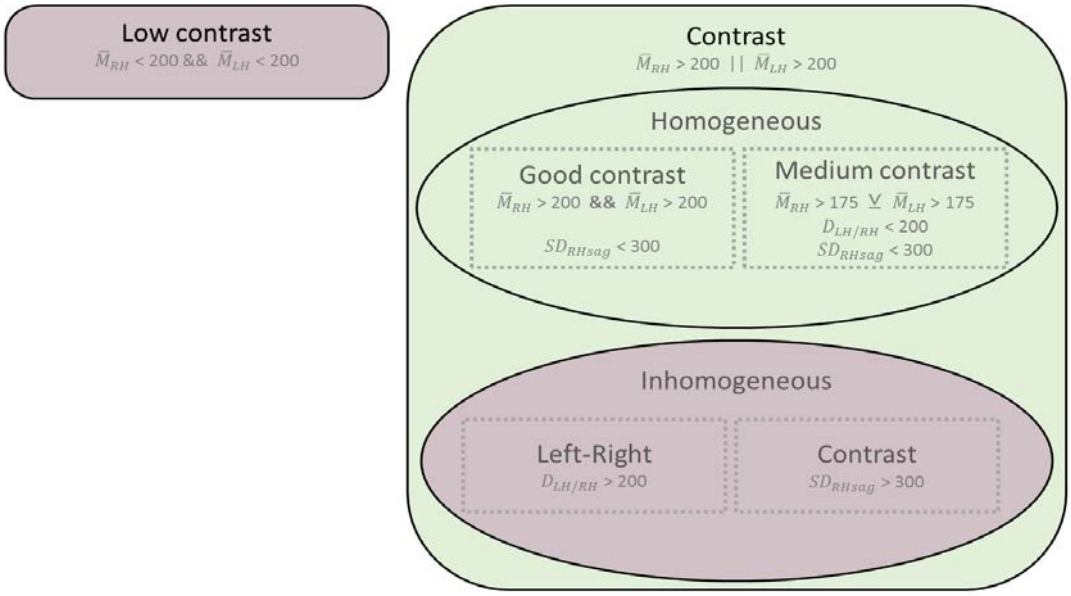

Figure 3.3 - Definition of contrast inhomogeneity in a CT scan

Table 3-II - Contrast quality in our database (32 CTs)

	With ICD	**Without ICD**
Low or inhomogeneous contrast	32 %	15%
Correct contrast	21 %	32%

3. Cardiovascular structures

MCS devices are directly connected to the heart, making this structure the most critical one for virtual patient representation. In addition, both LVADs and TAH present an outflow cannula anastomosed to the aorta. This section focuses thus on the aorta and heart segmentation.

3.1. Aorta

Various segmentation techniques have been proposed to extract vascular structures from medical images, such as pattern recognition techniques, model-based approaches, mathematical morphology, multiscale filtering approaches, vessel tracking, and matched filtering (Lesage et al. 2009; Jin et al. 2013). In the field of vascular interventions, there are currently several tools for clinical use in order to facilitate interpretation and exploitation of pre-operative CT images. They provide the practitioner with visualization functions as well as segmentation tools. Initially, the existing generic solutions relied mainly on radiology interpretation stations offered by the major medical imaging companies. More recently, solutions dedicated to the planning of endovascular interventions have emerged to complement the existing offer.

Therenva was one of the first companies to propose a dedicated solution for the planning of endovascular surgery. The planning software Endosize integrates modules for planning TEVAR (Thoracic EndoVascular Aortic Repair), TAVI (Transcatheter Aortic Valve Implantation) and

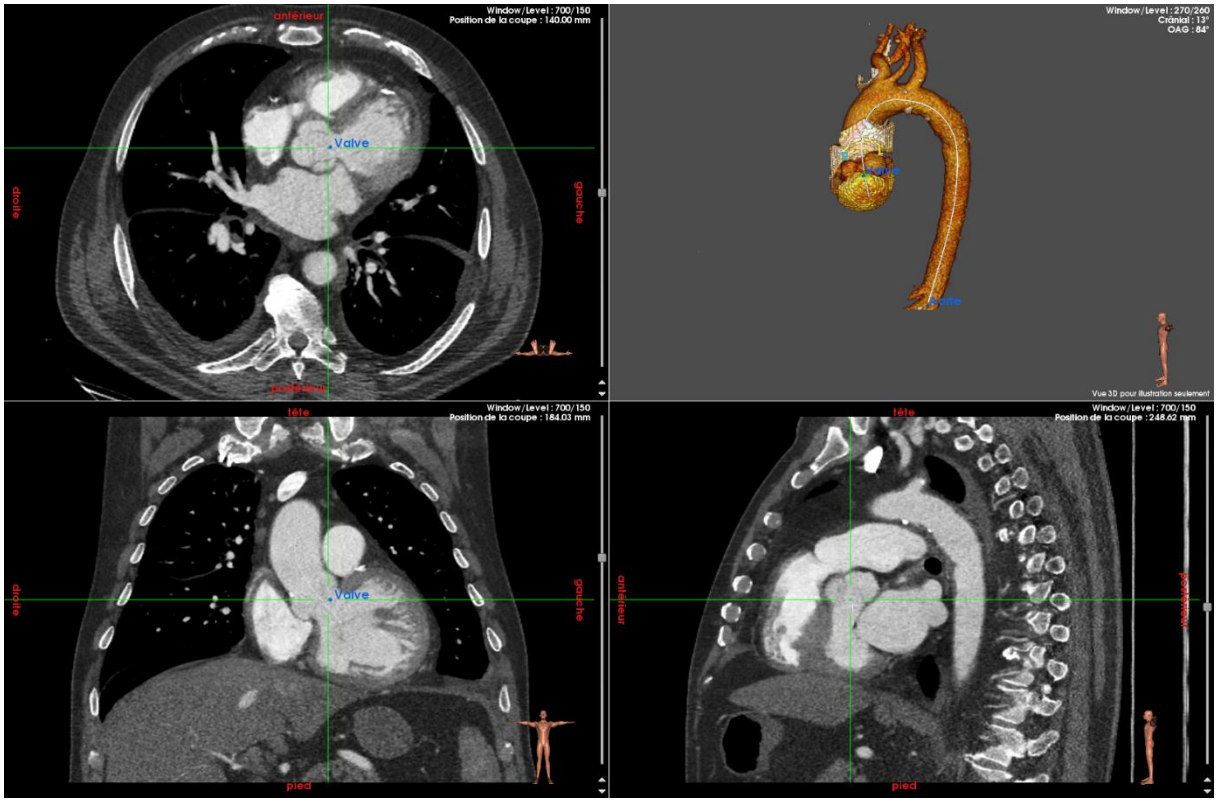

Figure 3.4 - Endosize software *(Therenva, Rennes, France)*

EVAR (EndoVascular Aneurysm Repair) surgical process. After importation of a patient's preoperative CT scan by the user, a workflow analyses the image including vascular segmentation, measurements, definition of the surgical strategy and generation of the planning report. The computation time for processing took approximately 1 second, which was compatible with interactive software (Kaladji et al. 2010). A volume-rendering process allows visualizing 3D vascular geometry and CT slices, as illustrated in Figure 3.4.

This software can also be used in Research with the possibility of exporting anatomical data such as surface description of the vascular lumen, vessel centrelines and contours. Based on three specific points selected by the user within the lumen, the automatic segmentation uses boundary and region-based algorithms with morphological operations to remove bones connected to vasculature structures. But vascular segmentation presents challenging issues due to the variability of contrast, acquisition noise, artefacts, anatomical size and curvature (Lesage et al. 2009). We thus evaluated this aortic segmentation process in the context of MCS implantation.

Herein, we opted for the TAVI module which provides a segmentation of the aorta from the aortic valve to the aorto-iliac bifurcation. Figure 3.5 illustrates the difference between a contrast-enhanced and no injected aorta. Without injection, the extraction seems difficult if not impossible. Endosize software being developed for contrast-enhanced CTs, we decided to select among the 32 CTs from the dataset presented section 2, those with injected contrast within the aorta. A total of 28 CTs were retained. We defined the maximum distance $\delta_{TAVI\text{-}Manual}$ between the contour provided by Endosize and a manual one provided by an expert. This distance was visually evaluated on axial slices, and three grades were distinguished:

- Grade 1 represented a satisfactory segmentation with $\delta_{TAVI\text{-}Manual} < 1mm$.
- Grade 2 was for $1mm < \delta_{TAVI\text{-}Manual} < 3mm$.
- Grade 3 represented an important over estimation with a $\delta_{TAVI\text{-}Manual} > 3mm$.

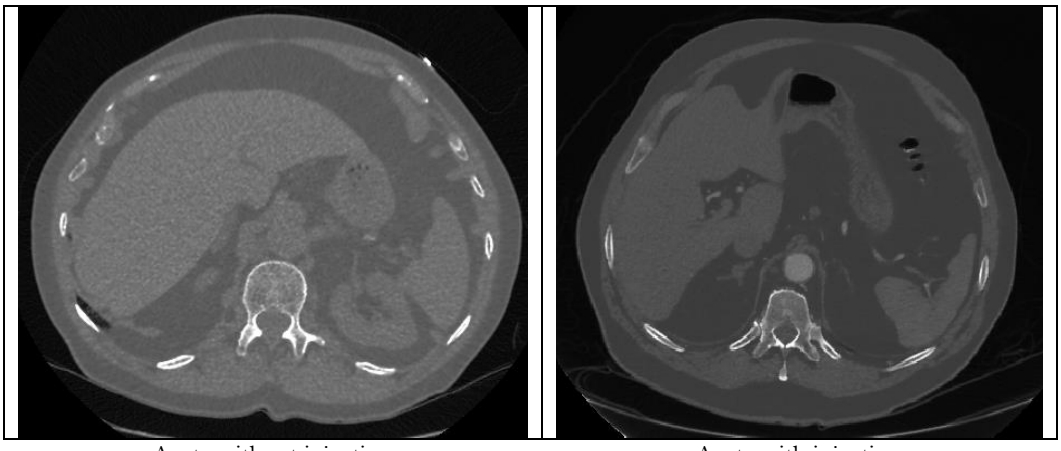

Aorta without injection Aorta with injection

Figure 3.5 - Illustration of contrast-enhanced CT at the aorta level

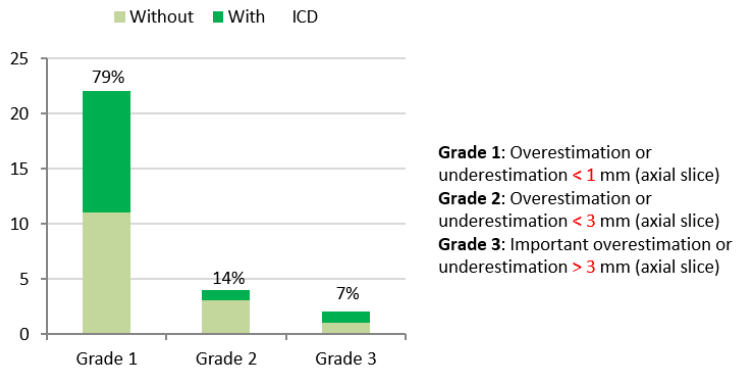

Figure 3.6 - Results for aortic segmentation with the TAVI module from Endosize software *(Therenva, Rennes, France)*

Results illustrated in Figure 3.6 showed that 79% of the segmentations were considered as satisfactory. In addition ICD devices did not seem to be responsible for over- or under-estimation. However, a low or inhomogeneous contrast, as well as acquisition artefacts may promote segmentation failure. Two examples of Grade 2 and Grade 3 aorta segmentation are represented in Figure 3.7.

Notice that evaluation criteria used in this experiment was stringent compared to mean distance or overlap score. Nevertheless, although results highlight that challenges still remain for the aorta, the segmentation seems quite satisfactory in the context of MCS device implantation.

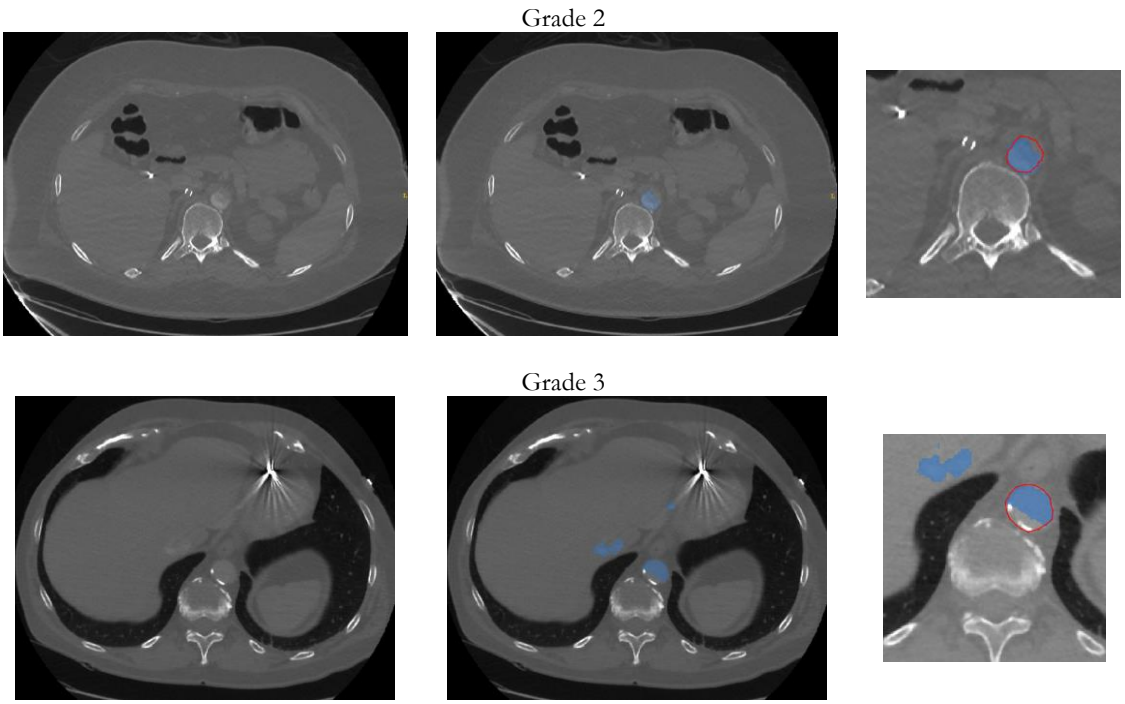

Figure 3.7 - Grade 2 and grade 3 illustration of the aorta segmentation

3.2. Heart segmentation, related works

In the context of cardiac image segmentation, structures of interest varied between the whole heart (Larrey-Ruiz et al. 2014), (Zhong et al. 2013), the myocardium (Zhu et al. 2014), or specific cavities such as the LV (Gao et al. 2011), left atrium (John & Rahn 2005) or RV (Antunes et al. 2013). Some authors also investigated the extraction of several structures at the same time. For instance, (Zhu et al. 2013) focused on the LV, RV and myocardium; (Jochen Peters et al. 2010) proposed a method for the LV endocardium and epicardium delineation, and (Kang et al. 2016) investigated the four cavities segmentation without the Left Myocardium (LMy). In the context of MCS, the LMy with all four heart chambers must be extracted. The right myocardium is one of the most difficult structures to segment due to its thinness and lack of well-defined boundaries. Hence why, the RV and its myocardium may be considered as one unique structure.

Two articles proposed a review of automatic techniques for the whole heart and heart chambers segmentation (Kang et al. 2012), (Zhuang 2013). But other methods have recently been developed. We have reported in Annex 3 the list of the different approaches segmenting the all five structures (left atrium, LV, right atrium, RV and LMy) on contrast-enhanced CTs. Recent approaches have attempted to use Convolutional Neural Networks (CNN) (Litjens et al. 2017) to segment heart but it has only been applied for specific cavities such as the LV (Zreik et al. 2016). To the best of our knowledge, only shape-based methods have been proposed over the last decade. More specifically ASM, DM and Multi-Atlas (MA) have been proposed. Incorporation of pixel intensity knowledge with a priori knowledge (object structure information, such as shape, object orientation, etc.) is necessary because of the proximity between the cavities and their similar intensities.

Since 2007, among the main breakthrough works reported in the literature, one can mention ASM, DM and MA segmentation methods. (Zheng et al. 2008) introduced in their ASM approach a novel Marginal Space Learning algorithm for localizing the heart chambers that reduces the number of testing hypotheses. (Ecabert et al. 2008) presented a DM method that was improved in (Ecabert et al. 2011) with a deformable and parametric adaptation using a similarity transformation as well as a multi-linear transformation. (J. Peters et al. 2010) proposed a new DM method called Simulated Search that evaluated a set of boundary detection functions and estimated geometric boundary detection error in order to optimize this step. (Kirisli et al. 2010) presented an MA approach using a non-rigid registration. (Zhuang et al. 2015) and (Zhuang et al. 2013) proposed a hierarchical locally affine registration, while (Zuluaga et al. 2013) used a cross correlation metric to select the

best atlases for propagation. All these articles evaluated their algorithm with quantitative criteria such as the Dice Score (DSC) $DSC = 2 * \frac{|V \cap U|}{|V|+|U|}$ where V and U indicate two segmented regions to be compared; and/or the mean absolute surface distance that quantifies the distance between automatically segmented surface and a gold standard. Authors used manual delineations made by experts as gold standard segmentation, except (J. Peters et al. 2010) who used a semi-automatic segmentation with manual corrections, and (Ecabert et al. 2011) who used a multi-step approach finally composed of corrections made by a clinical expert. Regarding reported results, the ASM approach was less effective for all heart structures than DM and MA approaches. Three methods are competitive, the MA method from (Zhuang et al. 2015) denoted in the following by MA_{Zhuang}, the MA from (Kirisli et al. 2010) denoted as $MA_{Kirisli}$, and the DM from (Ecabert et al. 2011) denoted as $DM_{Ecabert}$. Table 3-III regroups results from these 3 approaches. Comparing the MA approaches, $MA_{Kirisli}$ provided better absolute surface distance values than MA_{Zhuang}, for all structures except for the RV. But considering DSC values, MA_{Zhuang} was better for the atrium and myocardium and similar to $MA_{Kirisli}$ for both ventricles. These two MA segmentation methods are therefore very competitive. (Ecabert et al. 2011) evaluated only absolute surface distance criteria.

Table 3-III - Results from the literature of three competitive heart segmentation methods

Note – AD = mean Absolute surface Distance; DSC = Dice Score; wh = whole heart; LV = Left Ventricle; LMy = Left Myocardium; RV = Right Ventricle; LA = Left Atrium; RA = Right Atrium; Ao = Aorta; PA = Pulmonary Arteries

	Database	Gold Standard	Performance
MA_{Zhuang}	15 CTs	Manual delineation	AD_{wh} = 1,17 ± 1,39 mm DSC_{wh} = 0,89 ± 0,02 AD_{LV} = 0,90 ± 0,78 mm DSC_{LV} = 0,94 ± 0,03 AD_{LMy} = 1,09 ± 1,01 mm DSC_{LMy} = 0,83 ± 0,05 AD_{RV} = 1,12 ± 1,16 mm DSC_{RV} = 0,91 ± 0,03 AD_{LA} = 1,67 ± 1,96 mm DSC_{LA} = 0,87 ± 0,04 AD_{RA} = 1,70 ± 1,77 mm DSC_{RA} = 0,85 ± 0,05 AD_{Ao} = 0,73 ± 0,81 mm DSC_{Ao} = 0,91 ± 0,03 AD_{PA} = 1,14 ± 1,55 mm DSC_{PA} = 0,80 ± 0,11
$DM_{Ecabert}$	37 CTs	Multi-step approach (heart model extended to the image and correction by a clinical expert)	AD_{wh} = 0,70 ± 1,03 mm AD_{LV} = 0,77 ± 1,14 mm AD_{LMy} = 0,68 ± 0,96 mm AD_{RV} = 0,63 ± 0,66 mm AD_{LA} = 0,70 ± 0,87 mm AD_{RA} = 0,82 ± 1,00 mm AD_{Ao} = 0,60 ± 1,14 mm AD_{PA} = 0,50 ± 0,49 mm
$MA_{Kirisli}$	1380 CTs	Manual delineation	AD_{wh} = 0,99 ± 1,25 mm DSC_{wh} = 0,89 ~ 0,95 AD_{LV} = 0,62 ± 0,63 mm DSC_{LV} = 0,95 AD_{LMy} = 1,04 ± 1,15 mm DSC_{LMy} = 0,95 AD_{RV} = 1,40 ± 1,47 mm DSC_{RV} = 0,90 AD_{LA} = 0,66 ± 0,84 mm DSC_{LA} = 0,94 AD_{RA} = 1,44 ± 1,88 mm DSC_{RA} = 0,89 AD_{Ao} = 0,44 ± 0,60 mm DSC_{Ao} = 0,94

Comparing the three methods, $DM_{Ecabert}$ presented better results for the LMy and right cavities, while $MA_{Kirisli}$ was better for left cavities.

These three approaches are very competitive and highlighted favourable performances of actual heart segmentation methods. However, issues still remain due to the high variability in anatomic structure and intensity distributions which are influenced by the disease state, imaging protocols, artefacts, or noise (Kang et al. 2012).

3.3. Heart segmentation, methods and experiments

Generally, DM based techniques are very sensitive to initialization and free to take arbitrary shape, if they do not incorporate prior knowledge of anatomical structures. Atlas-based methods solve this problem by integrating a priori data. In addition, (Zhuang et al. 2013) evaluated their algorithm on 15 CTs while (Kirisli et al. 2010) used the largest dataset with 1,380 CTs. Similar to what we can find in the context of LVAD the dataset was composed of CT scans from patients who were suspected to have cardiac problems and exhibiting different types of pathology or including stents and pacemakers. We evaluated a MA approach, and more specifically the $MA_{Kirisli}$ available in open-source.

Next section details the segmentation technique and analyses results from (Kirisli et al. 2010). Then, the method is tested in the context of MCS device implantation and results are compared to those reported in the literature from general dataset. Finally, we modified some atlases in order to investigate the impact on the segmentation process.

3.3.1. MA based segmentation method

Based on eight atlas images that were manually labelled, the $MA_{Kirisli}$ approach is fully automatic. The height images are registered with a two-stage approach composed of first an affine transformation as initialization and secondly non-rigid registration using a β-spline transform model. Then, propagation and combination of labelled images with a per-voxel majority voting procedure are performed. Available in open source, this segmentation takes about 25 minutes on a PC with an Inter Core i7 processor, 3.20 GHz, 16Go RAM, and GPU (NVIDIA Quadro 5000). Figure 3.8 illustrates the segmentation result obtained with one CT from our dataset.

(Kirisli et al. 2010) evaluated their method with four different analyses. First, a leave-one-out test was performed on the eight atlas images comparing all labelled slices with manual delineation. To evaluate the similarity between the two samples, they calculated the DSC. With a value of 0.96 for the whole heart segmentation, this method seems very promising. However, the atlases did not include CT images with ICDs. A non-negligible number of patients eligible for MCS implantation already have an ICD like a pacemaker (almost 50%). Such devices create significant artefacts that

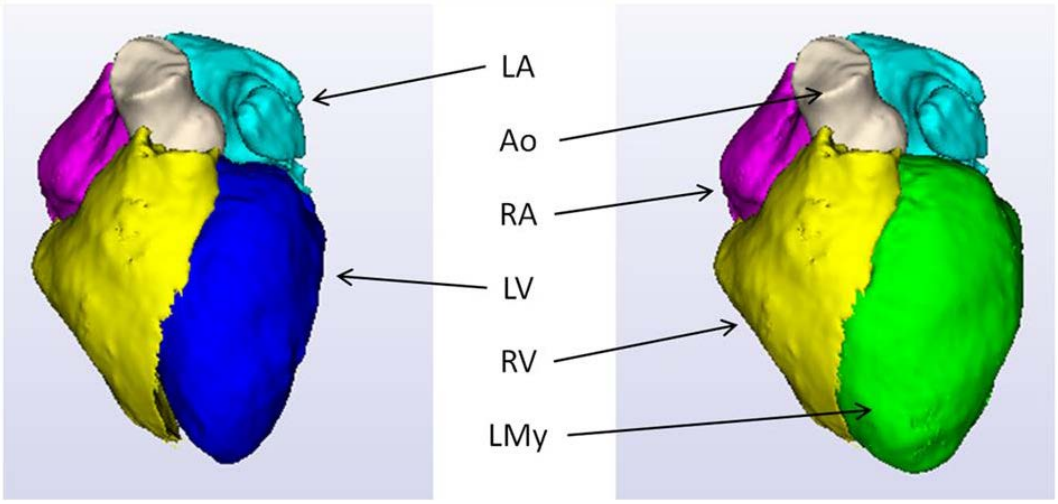

LA - Left Atrium; Ao – Aorta; RA - Right Atrium; LV - Left Ventricle; RV – Right Ventricle; LMy – Left Myocardium

Figure 3.8 - Multi-atlas based heart segmentation from preoperative CT scan

may result in heart segmentation alterations. This performance should therefore be altered by ICDs. They made a multicentre quantitative 2D experiment on 20 randomly-selected CTs. For each CT, nine randomly selected slices from the three orthogonal directions (axial, sagittal or coronal) were compared with manual delineation. Even if the dataset included CTs with ICDs and stents, authors did not mentioned how many were considered. Thirdly, a 2D qualitative evaluation based on grade classification was performed on 100 CTs, to finally be extended to all 1,380 CTs. No quantitative information about ICD, pathology or contrast quality was provided. In addition, classification took into account all segmented regions. In the context of TAH and LVADs, only the RV, LV and the whole heart are important. When it comes to exploit this method in the context of MCS, it is necessary to re-evaluate its performance and specifically heart segmentation focusing on the RV, LV and whole heart.

3.3.2. Comparison to the results from the literature

In this experiment, the 32 preoperative CTs detailed in section 1 were segmented with the $MA_{Kirisli}$ method. A manual delineation of the whole heart, the RV and LV endocardium was made every 15 slides by a medical operator for being used as gold standard segmentation. On average, 8.5 segmented slices per CT were obtained. The minimum was 4 slices and the maximum 16. This gap is related to the variability in heart size and slice thickness. To make the comparison with literature data, a mean DSC was calculated between the automatic and manual segmentation. The two first lines from Table 3-IV provides the leave-one-out and multicentre analysis results from (Kirisli et al. 2010), while the rest of the table corresponds to results from our dataset. Results from the literature provide indications on what is expected. Notice that our experiment does not evaluate

Table 3-IV - Results obtained with $MA_{Kirisli}$ heart segmentation approach

Study	Number of CT	DSC_{wh}	DSC_{LV}	DSC_{RV}
Leave-one-out	8	0.96	0.95	0.90
Multicentre	20	0.91	0.93	0.85
MCS - all	32	0.80	0.81	0.68
MCS – ICD (G_{ICD})	14	0.75	0.73	0.64
MCS - no ICD ($G_{no\text{-}ICD}$)	18	0.83	0.86	0.72
MCS – no well contrasted ($G_{no\text{-}WC}$)	15	0.74	0.73	0.61
MCS – well contrasted (G_{WC})	17	0.85	0.87	0.75

the all heart slices as in the leave-one-out experiment. However, the multicentre analysis was made on 9 slices, which is quite similar with the average number of segmented slices evaluated herein. Four groups have been distinguished in our dataset. G_{ICD} represents CTs with ICD, while $G_{no\text{-}ICD}$ represents those without ICD. Similarly, G_{WC} corresponds to well-contrasted CTs while $G_{no\text{-}WC}$ contained CTs that present a low or inhomogeneous contrast media. In the following results from Table 3-IV and corresponding to the mean DSC obtained for the whole heart, the LV and the RV are denoted respectively as DSC_{wh}, DSC_{LV} and DSC_{RV}.

According to the results, CTs from G_{ICD} presented a lower mean DSC_{wh}, DSC_{LV} and DSC_{RV}, than those from $G_{no\text{-}ICD}$. The presence of ICD seems therefore to alter the performance of the segmentation method. In the same way, CTs with a good contrast media provided better results compared to no-well contrasted CTs. Nevertheless, regarding more specifically the results for each CT, this difference is explained by two segmentations in G_{ICD} and $G_{no\text{-}WC}$ that failed (DSC<0.3). Figure 3.9 illustrates the DSC obtained for the whole heart segmentation of each CT. Recalculating the mean DSC_{Wh}, DCS_{LV} and DSC_{RV} without these two failed segmentations (PC#7_1 and PC#7_2), results are similar as for $G_{no\text{-}ICD}$ and G_{WC}.

This experiment highlighted that ICD and/or low or inhomogeneous contrast potentially promotes MA segmentation failures. Taking into consideration these results, we modified some atlases in order to improve results.

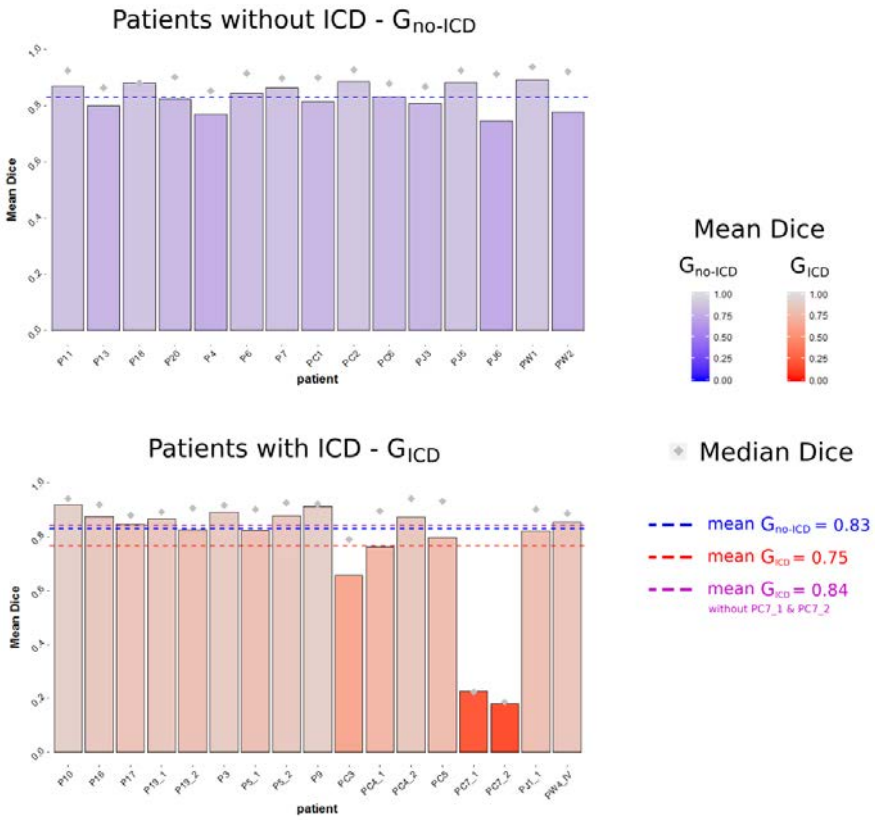

Figure 3.9 - Dice results for the whole heart segmentation with the multi-atlas approach $MA_{kirisli}$

3.3.3. Modification of the atlas

The $MA_{Kirisli}$ atlases were composed of 8 well-contrasted CTs from patient without ICD. The selection of appropriate atlases can affect the segmentation method accuracy, reliability and process speed (Fritscher et al. 2015). We investigated a configuration including more representative cases. In the following, the group of atlases from $MA_{Kirisli}$ and the new group presented in this section are denoted respectively as atlas-K and atlas-ICD. MA_{ICD} represents the MA segmentation method using the atlas-ICD.

Atlas-ICD was composed in order to take into account the presence of ICD and contrast media inhomogeneity. Six labelled images were retained from atlas-K and two labelled images from our dataset were added. Both were from patients with an ICD. The first CT (P#9) was a well-contrasted CT whereas the second (P#10) presented contrast inhomogeneity. $MA_{Kirisli}$ segmentations previously obtained for these two CTs were manually corrected by an expert and added to this new group of atlases.

The $MA_{Kirisli}$ method was evaluated on the 32 CTs presented in section 1.1. P#9 and P#10 were removed from the dataset for the evaluation of the MA_{ICD} approach. Only 30 CTs segmented with MA_{ICD} are thus evaluated. DSC_{Wh}, DCS_{LV} and DSC_{RV} obtained with the $MA_{Kirisli}$ and MA_{ICD} method

are listed in Table 3-V. The datasets were distinguished according to CTs with or without ICD, and regarding the contrast homogeneity. Results obtained with the MA_{ICD} were similar to those from $MA_{Kirisli}$. The segmentation method efficiency was therefore not improved by adding in the atlases, CTs with media inhomogeneity and ICD.

Table 3-V - Results obtained with MA_{ICD} heart segmentation approach

Study	Dataset		DSC_{wh}		DSC_{LV}		DSC_{RV}	
	$MA_{kirisli}$	MA_{ICD}	$MA_{kirisli}$	MA_{ICD}	$MA_{kirisli}$	MA_{ICD}	$MA_{kirisli}$	MA_{ICD}
MCS - all	32	30	0.80	0.79	0.81	0.80	0.68	0.68
MCS - ICD	14	12	0.75	0.74	0.73	0.71	0.64	0.60
MCS - no ICD	18	18	0.83	0.83	0.86	0.87	0.72	0.74
MCS – no well contrasted	15	14	0.74	0.73	0.73	0.72	0.61	0.60
MCS – well contrasted	17	16	0.85	0.84	0.87	0.87	0.75	0.76

To conclude, the proposed group of atlases did not affect the MA segmentation results. The selection of appropriate atlases is a difficult task. Considering only CTs of patient without ICD or well contrasted yielded results comparable to those obtained with the original set of atlases (atlases-K). The presence of ICD or inhomogeneous contrast may therefore not be the only source of alteration. Nevertheless, MA approach provided promising results for the whole heart and the LV with a dice score about 0.80. Significant challenges still remain for the RV delineation (DSC_{RV}=0.68). If LV segmentation issue is relatively overcome now, extraction of the RV is still difficult due to the high variation among subjects, its complex and irregular shape (Antunes et al. 2013).

4. Surrounding structures

Anastomosed to the heart, intrathoracic MCS devices are directly in contact with the lungs, and may also be in conflict with thoracic bones (chest wall). This section investigates thus segmentation of these two anatomical structures.

4.1. Lungs segmentation, related works

Since 2000, a large number of lungs segmentation methods have been developed. If some approaches only focused on lungs extraction, others also aimed at detecting pathological conditions or specific areas. Table 3-VI gathers articles from the literature based on four reviews (Sluimer et al. 2006), (Rikxoort & Ginneken 2013), (El-Baz et al. 2013), (Mansoor et al. 2015) and additional

works recently published. Notice that only fully automatic segmentation approaches were retained, and neighbouring anatomy-based approaches were generally not envisaged for lungs segmentation. This table highlights the wide variety of approaches. To give some examples, (Leader et al. 2003) combined 2D pixel-value threshold with two sets of classification rules, whereas (Korfiatis et al. 2008) elaborated an adaptive 3D thresholding-based method using a texture classification. (Sluimer et al. 2005) segmented pathological lungs with a probabilistic atlas-based segmentation. (Abdollahi et al. 2012) used a Markov-Gibbs random field segmentation, and (Zhou et al. 2014) elaborated an iterative weighted averaging and adaptive curvature threshold with a fuzzy-c-means clustering. More recently, (Mesanovic et al. 2017) used a region growing method followed by morphological operators for the extraction of lung parenchyma (thin-walled alveoli).

Table 3-VI - Lung segmentation articles

Threshold	**Region**	
(Silva et al. 2001) (Leader et al. 2003) (Zheng et al. 2003) (Li et al. 2007) (Gao et al. 2007) (Li et al. 2008) (Pu et al. 2008) (Wang, Li & Li 2009) (Wang, Li, Doi, et al. 2009)	(Brown et al. 2000) (Lo et al. 2011) (Armato & MacMahon 2003) (Armato III & Sensakovic 2004) (Shojaii et al. 2005) (Yim et al. 2005) (Sun et al. 2006)	(De Nunzio et al. 2011) (Hua et al. 2011) (Lassen et al. 2011) (Mansoor, Bagci, Xu, et al. 2014) (Özsavag et al. 2014) (Wang & Guo 2016) (Wu et al. 2016) (Mesanovic et al. 2017)

Shape		**Machine learning**
(Kitasaka et al. 2003) (Sluimer et al. 2004) (Sluimer et al. 2005) (Itai et al. 2007) (Silveira et al. 2007) (El-Baz et al. 2008)	(van Rikxoort et al. 2009) (Sofka et al. 2011) (Sun et al. 2012) (Sun 2013) (Rebouças Filho et al. 2017) (Soliman et al. 2017)	(Hu et al. 2001) (Korfiatis et al. 2007) (Korfiatis et al. 2008) (Prasad et al. 2008) (Abdollahi et al. 2012) (Zhou et al. 2014) (Hosseini-Asl et al. 2016)

The results revealed that some methods were more or less adapted according to the investigated lungs pathology or abnormality (Mansoor et al. 2015). Table 3-VII illustrates the effectiveness of the class of methods according to pulmonary abnormalities (Mansoor et al. 2015). In the context of MCS device implantation, the presence on preoperative CTs of specific abnormality such as lungs nodules is excluded because of the eligibility criteria. In Table 3-VII, we highlighted in green the abnormalities potentially present in patients eligible for MCS implantation. According to this table, thresholding-based and region-based approaches do not seem to be well-adapted in this context. Shape-based and machine learning-based approaches present a better potential of success.

Table 3-VII - Effectiveness of class of methods for segmentation of the lung fields and evaluation of the presence of abnormality in the context of MCS implantation
Source: adapted from (Mansoor et al. 2015)

Area or Abnormality	Evaluation of the possibility of abnormality	Class of methods				
		Threshold	Region	Shape	Machine Learning	Neighbouring anatomy
Lung field	--	+	+	+	+	+
Beaded septum	--	N/A	-	N/A	+	N/A
Varicose bronchiectasis	+	N/A	N/A	N/A	N/A	N/A
Micro nodules	--	N/A	N/A	N/A	N/A	N/A
Tree-in-bud pattern	--	N/A	N/A	N/A	+	N/A
Perilymphatic distribution	+	N/A	N/A	N/A	N/A	N/A
Interstitial emphysema	+	N/A	N/A	N/A	N/A	N/A
Bleb	+	+	+	+	+	-
Bulla	--	+	+	+	+	-
Cavity	--	+	+	+	+	-
Cyst	-	+	+	+	+	+
Interstitial pneumonia	-	+	+	+	+	+
Air-filled bronchiectasis	--	+	+	+	+	+
Pulmonary fibrosis	+	-	-	+	+	-
Consolidation	-	-	-	+	+	-
Centrilobular emphysema	--	-	-	+	+	-
Crazy-paving pattern	-	-	-	+	+	+
Ground-glass opacity	--	-	-	+	+	-
Honeycombing	--	-	-	+	+	-
Halo sign	--	-	-	+	+	-
Mycetoma	-	-	-	+	+	-
Infarction	++	-	-	+	+	+
Pleural effusion	-	-	-	+	+	+
Pleural plaque	--	-	-	+	+	+

Note – Evaluation: -- = Never; - = Rare; + = Possible; ++ = Frequent
Effectiveness: N/A = not available or not implemented for that pattern, + = method can be used successfully;- = method may fail

However, these methods were not available or not implemented for 50% of potential pathologies present in the context of MCS.

4.2. Lungs segmentation, methods and experiments

Over the years, segmentation methods have been developed focusing on specific lung pathologies. Consequently, using segmentation in a general context where there is a high variability of pathologies makes it more challenging. In this section, we present and compare several approaches: thresholding-based, region-based and shape-based methods.

4.2.1. Thresholding-based methods

Two thresholding-based methods have been investigated. The first one called morphological segmentation (Morpho_seg) has specifically been developed while the second one has been implemented from an open-source library. The morphological approach is based on morphological operator, thresholding and connected component labelling. Figure 3.10 provides the workflow of the proposed method. First, a threshold between -900HU to -400HU is applied on the original CT scan, followed by a median filter. Then the 3 major resulting components are extracted. Considering a region of interest expanding from the angle of Louis to 7cm below the apex, these components correspond to the background and both lungs. The background is afterward removed analysing components position within the CT. Finally a closing filter is applied.

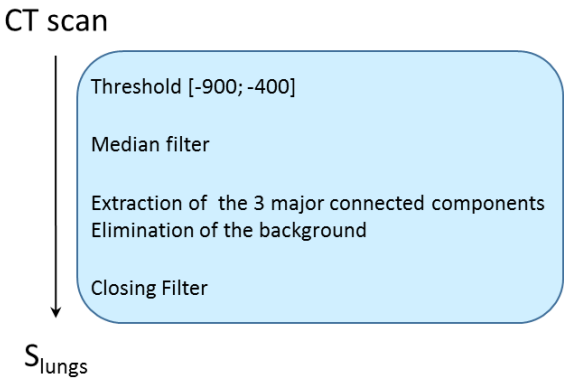

Figure 3.10 - Lungs segmentation method based on thresholding

An open-source library called Chest Imaging Platform (www.chestimagingplatform.org) has also been tested. Developed for lung phenotyping, this open-source module can be integrated in 3D slicer and offers a collection of tools for lung images processing. For instance, it can be used to perform disease-specific quantification but also to extract and convert into 3D models the lobes, airway anatomy and lungs (Cheng et al. 2016). This method is composed of 3 steps. Firstly, the background is removed with a thresholding filter. Based on the image histogram, thresholding values are afterward determined to extract lungs. Then, airway trees still being present, an additional step is performed in order to isolate airway trees with a region growing approach. Finally, the two lungs are separated by removing the airway. We considered this method as a thresholding-based one because region growing is only used for the airway segmentation and not for lungs.

4.2.2. Region growing method

To evaluate region growing-like method in the context of lungs segmentation, a free software using region growing-based fuzzy-connectedness segmentation algorithm has been tested (Mansoor, Bagci, Foster, et al. 2014). This open-source multi-platform software, called CIDI-Lung-Seg, provides the lung-field annotation in CT images through an automated or a single-click solution. The method is composed of an initial phase consisting on seed points' selection, automatically or manually performed by the user. The algorithm localizes candidate seeds determining the lung region via the extraction of the skin boundary and rib cage made through a strict thresholding. Then, final seed selection is done using a threshold operator over CT attenuation values -700 HU through -400 HU. Once points have been selected, the fuzzy-connectedness segmentation is performed. During the evaluation of this method, we noticed that automatic segmentation failed for 78% of the dataset. For these cases we performed a single-click initialisation.

4.2.3. Multi-atlas segmentation

To evaluate a MA approach, we first created atlases. Among the 32 preoperative CTs presented in section 1.1, six were selected. Five presented lungs without pathology and one patient had some opacifications. Slices were then manually segmented by an expert with Itk-Snap software. Figure 3.11 illustrates manual segmentation of two CTs presenting healthy and opacified lungs. The MA method evaluated herein is the $MA_{Kirisli}$ (Kirisli et al. 2010) were the cardiac atlases were replaced by our lung atlases. As mentioned in section 3.3.1, an affine transformation and β-spline

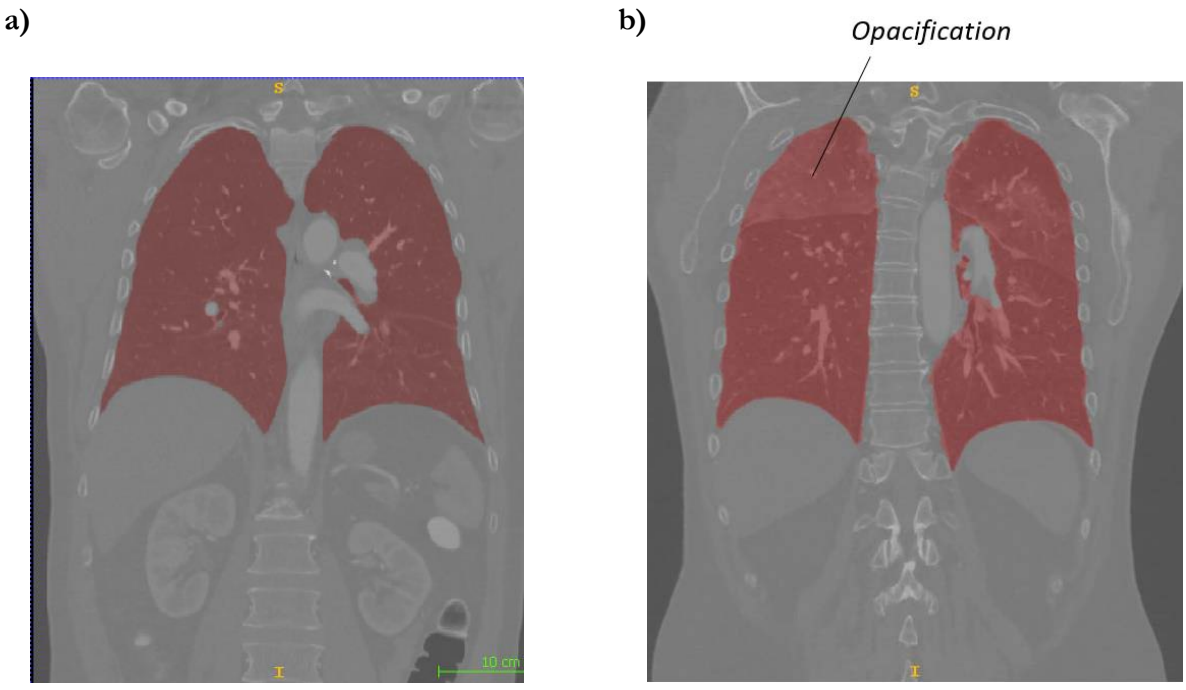

Figure 3.11 - Illustration of segmented lungs atlases; a) without opacifications; b) with opacifications

transform model are used to register the six images, followed by propagation and combination of labelled images with a per-voxel majority voting procedure. This approach has been tested on the remaining 26 preoperative CTs from section 1.1.

4.2.4. Lungs segmentation results

To compare the semi-automatic or automatic segmentation with a manual one, a grade classification was elaborated. Four different grades were distinguished. Grade 1 describes segmentations with an under/over estimation inferior to 1 mm, whereas Grade 2 represents a small under/over estimation between 1mm and 5 mm. Grade 3 defines under/over estimation with a difference superior to 5 mm; and finally, Grade 4 corresponds to failed segmentation. Figure 3.12 illustrates the difference between a grade 3 and grade 4, while Figure 3.13 illustrates results obtained for each of the four methods.

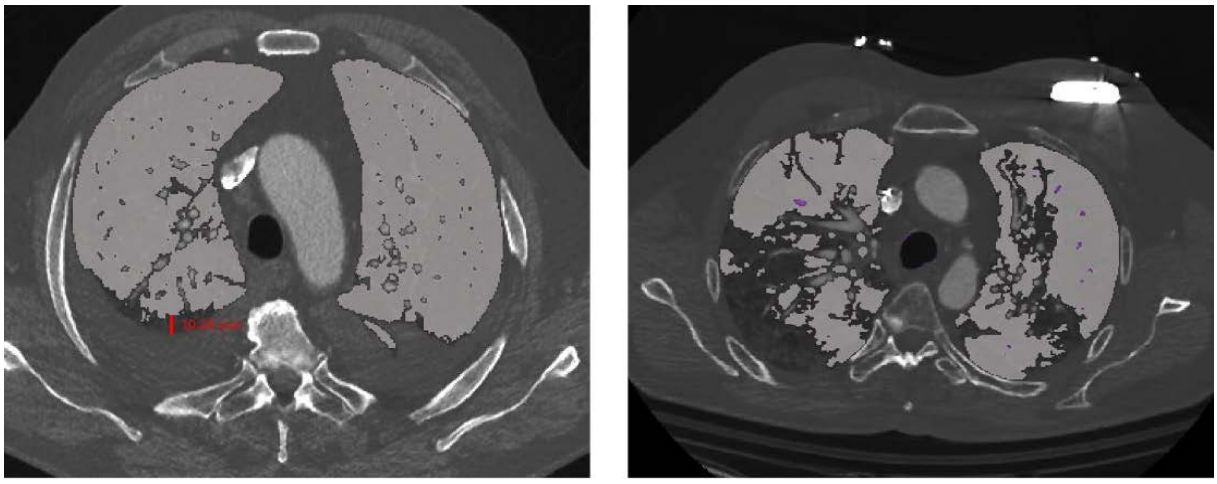

Figure 3.12 - Lungs segmentation classification, illustration of grade 3 and failed segmentation

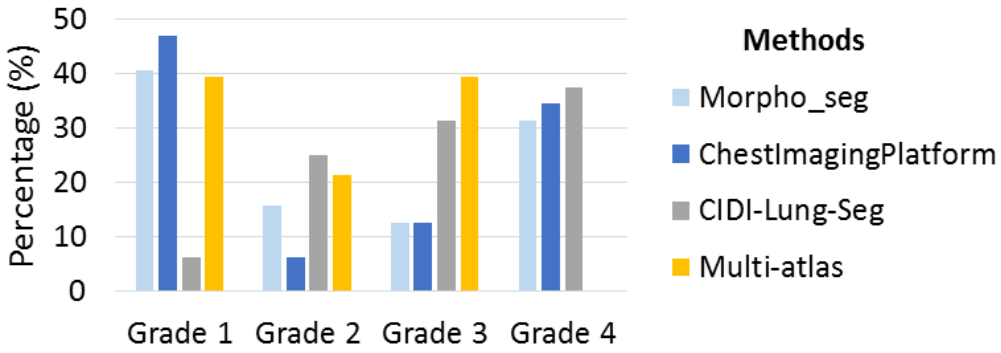

Figure 3.13 - Lungs segmentation results for thresholding-based, region-based and shape-based methods

The region growing method (CIDI_Lung_seg) presented the worst score with the lowest rate of grade 1 and the highest number of failed segmentation. Results for the two thresholding-based segmentation approaches were quite similar. Even if these two methods obtained better grade 1 classification than the MA segmentation, they also displayed more failure. The MA approach presented no failed segmentation at all. In this context, it is difficult to define the most appropriate method. Is it preferable to have no failure and more Grade 3? Or is it better to optimise Grade 1, allowing lungs segmentation failure? In any case, neither method achieved 50% of grade 1. These results highlighted the significant difficulty to segment lungs not focusing on specific pathology. It was envisaged to increase figures by performing both MA and thresholding-based segmentation, and manually select the best one, but only 50% of grade 1; 14% of grade 2 and 36% of grade 3 were obtained.

In the context of MCS, lungs segmentation presents therefore a significant limitation for both 3D visualisation in a computer-aided solution or thoracic segmentation through a neighbouring anatomy-based method.

4.3. Chest wall segmentation, related works

Rib cage and thoracic cavity are two anatomical terms that must be distinguished. The rib cage is composed of thoracic bones whereas the thoracic cavity corresponds to the chamber of the body enclosing intrathoracic organs (mainly the heart and lungs) and protected by the thoracic wall. Rib cage segmentation consists thus in segmenting the skeleton while the thoracic cavity segmentation consists in a volume defined by the chest wall surface. The main difference remains thus in considering intercostal muscles (thoracic cavity) or not (rib cage). Figure 3.14 illustrates the thoracic wall definition, the rib cage segmentation as well as the thoracic cavity segmentation. Both segmentations are investigated in next sections. Annex 4 and Annex 5 summarize characteristics and results for the methods mentioned in next sections.

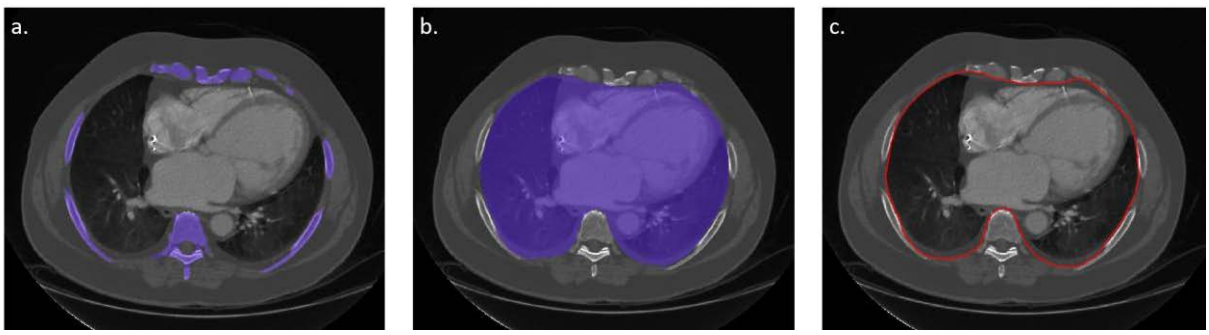

Figure 3.14 - Illustration of the rib cage segmentation (a.); Thoracic cavity segmentation (b.); and Thoracic wall delineation (c.)

4.3.1. Rib cage segmentation

The rib cage is composed of the spine, the sternum, 12 ribs (7 true ribs in the upper side, 5 false ribs below), and the costal cartilages located between the ribs and the sternum. Its segmentation consists in extracting all these elements. Only two approaches have been developed for that purpose. In the one hand, (Zhou et al. 2004) proposed a 3D region growing approach for fat, skin and rib cage segmentation. Computing time was about 10 minutes, and the analysis on 139 CTs highlighted that all regions were recognized correctly for 93% patient cases. On the other hand, (Narkbuakaew et al. 2014) used a 3D K-means clustering controlled by a hierarchical concept for segmentation on 3D CT of the liver. Even if the process took less time (103 seconds), results showed that this method was unable to extract costal cartilages. These two approaches have been developed for non-contrast enhanced CTs. The presence of contrast injection may significantly increase the segmentation difficulty. Additionally, only visual inspection by an expert was performed and costal cartilages extraction presented limitations. Approaches that extract bones structures and costal and cartilages ones separately might therefore be more efficient.

Over the literature, the rib cage bones segmentation, without cartilages, has been more investigated than extraction of the all rib cage. (Fu et al. 2017) developed a single atlas-based method for the segmentation of the skeleton from whole-body CT scan. Segmenting a total of sixty-two bones, the process was time consuming (20 minutes). (Xu et al. 2014) used a multi-scale Hessian analysis and an iterative relative fuzzy-connectedness to segment in 5 minutes the structures of interest. Qualitative evaluation made by two experts revealed 95% of accuracy. However, for both articles, it was not mentioned if CTs were contrast-enhanced or not. Based on CT scans with contrast media, (Brahim et al. 2017) presented a multiple pixel thresholding followed by morphological operators method. Evaluating 30 patients CTs, they found that for 30% of the extracted rib cages, the sternum was not segmented. In the same way, (Udupa et al. 2014) used an iterative relative fuzzy connectedness delineation algorithm, that was compared with a delineation created from a combination of methods (iterative live wire, thresholding, manual tracing and correction). The analysis on 50 thoracic CTs provided an Hausdorff distance of 10,6 ± 2,4 mm. Finally, (Yip et al. 2014) developed an atlas-based segmentation. Compared with manual delineation from 2 experts, results highlighted that the deformable registration algorithms was the best approach. With a dice similarity index of 77 ± 3%, and a Hausdorff distance of 0.34 ± 0.08 cm, this approach took only 241 ± 21 sec and seems promising.

Costal cartilages are low density structures whose associated HU values on CT scans are similar to HU values of tissues. Extraction of this region is therefore a significant challenge. Only two recent articles proposed an automatic approach for this type of segmentation. (Pazokifard et al. 2015)

presented a graph cuts method whereas (Zhao et al. 2014) developed a statistical shape model-based segmentation. However, both articles considered non-contrast enhanced CTs.

To conclude, segmentation of the rib cage presents important challenges particularly due to the presence of contrast and the high difficulty of extracting costal cartilages. To our knowledge, no breakthrough have been reported until now for the rib cage segmentation in the context of contrast-enhanced CT.

4.3.2. Thoracic cavity segmentation

Several articles have investigated the thoracic cavity segmentation. First, three methods have been developed for non-contrast enhanced CTs. (Chittajallu et al. 2009) used a graph-based method minimizing the global energy for inner thoracic region segmentation, whereas (Vandemeulebroucke et al. 2012) presented an automatic segmentation for motion masks using feature extractions and level sets. (Bae et al. 2014) investigated a semi-automatic multi-organ segmentation for fat quantification of patients, where the thoracic cavity was segmented with a 3D surface-fitting approach. Secondly, (Choi & Kim 2010) developed a new active contours method called gradient vector flow that presented good performances. (Huang et al. 2014) used an ASM and obtained an area overlap of 93.91% comparing their automatic segmentation with manual delineation. However, these two articles did not mention information about computation time and CT contrast. Finally, (Zhou et al. 2005) presented a 3D region growing method to separate automatically region from CT images into 7 parts: skin, subcutaneous fat, muscle, bone, diaphragm, thoracic cavity and abdominal cavity. Evaluating their algorithm on CT with and without contrast media, they highlighted that the accuracy of bone frame segmentation is not high enough, especially in the case of contrast media enhanced CT. Few years later, (Cheirsilp et al. 2015) used a multi-organ method to extract the thoracic inner wall. Evaluating their solution on 37 CTs (21% with contrast) they obtained a mean DSC of 99,32% $\pm$ 1,28, and more specifically of 99,58 % $\pm$ 0,63 for contrasted CTs. Taking only 17,6 sec, this promising process necessitates the body, airway tree, aorta and lungs segmentation.

In the context of MCS, the rib cage as well as the thoracic cavity segmentation may be envisaged. On the one hand, the only method for thoracic cavity segmentation performed on contrast-enhanced CTs was highly dependent on several anatomical structures segmentation. The body and airway tree are not considered as critical structures herein and results from the previous section highlighted the huge difficulty in segmenting lungs. This multi-organ method based on these three structure segmentations must therefore not be envisaged herein. On the other hand, the state of the art on rib cage segmentation highlights that thoracic bones extraction is very tough and presents

still significant challenges mainly related to costal cartilages delineation, especially for contrast-enhanced CTs. Next section proposes therefore two methods for rib cage segmentation.

4.4. Rib cage segmentation, methods and experiments

Regions representing injected structures present HU values similar as high density bones region. To overcome this limitation, a neighbouring anatomy-guided approach has been developed using the heart and aorta segmentations which provided both satisfactory results. Next section details the two proposed algorithms and results obtained.

4.4.1. Morphological approach

An overview of the two developed methods is provided in Figure 3.15. The first algorithm is composed of three major steps. First, a pre-processing is performed with a median and a curvature anisotropic diffusion filter, in order to reduce acquisition noise and metallic artefacts in the CT. In parallel, the aorta segmentation S_{aorta_Endo} (see section 3.1) is cleaned removing remaining heart structures. For that, the heart segmentation S_{heart_MA} obtained with the $MA_{kirisli}$ method is used as a mask. The obtained segmentation is denoted as S_{aorta}. The aorta and heart structures are removed from the original CT, using respectively S_{aorta} and S_{heart_MA}. Next step performs a thresholding operation to extract all voxels with an HU value superior to V_{th}. Each distinct object (connected component) is then labelled according to its size. The major connected component is selected and a closing filter applied to fill holes. Segmentation obtained at this stage of the algorithm is denoted as S_{v1} in the following. To finalize this first approach, an additional closing filter with a larger spherical structuring element is performed.

The second algorithm has been developed in order to remove potential remaining tissue regions. Based on S_{v1}, the method combines three further steps consisting in firstly extracting the spine in order to avoid its alteration, secondly selecting tissue regions, and thirdly removing these regions and applying post-processing. The spine is automatically located using its position according to the aorta. A region S_{spine} containing the spine with the beginning of the ribs is isolated from $S_{v1,}$ and a bounding box B_{spine} containing this region defined. Limits of B_{spine} along the x and y axes are calculated as follows:

$$X_{min}^{spine} = X_C^{aorta} - \frac{l_x}{2} \quad (2)$$

$$X_{max}^{spine} = X_C^{aorta} + \frac{l_x}{2} \quad (3)$$

$$Y_{\min}^{spine} = 0 \quad (4)$$

$$Y_{max}^{spine} = Y_{max}^{aorta} \quad (5)$$

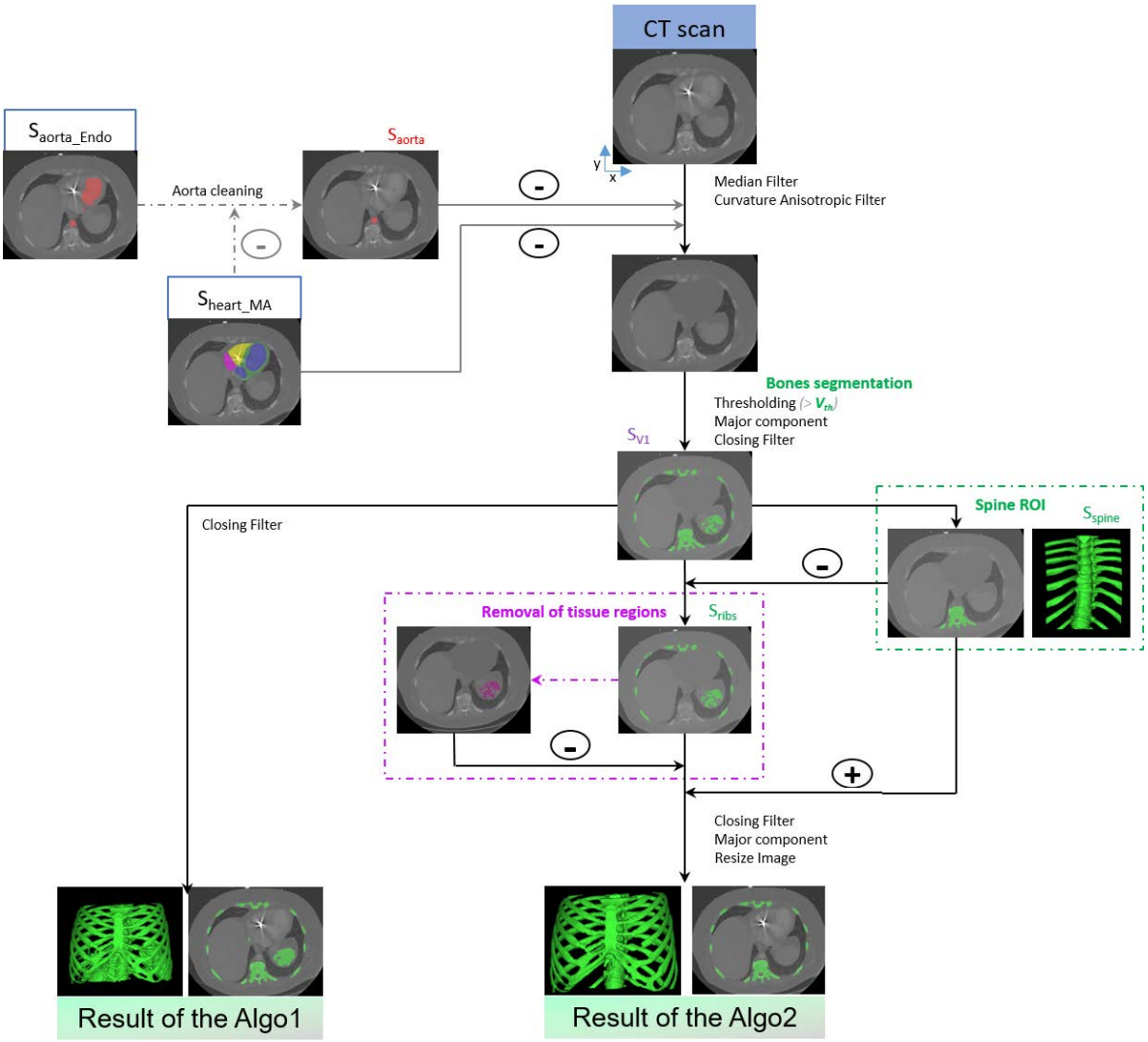

Figure 3.15 - Rib cage segmentation method based on thresholding

where X_{min}^{spine}; X_{max}^{spine}; Y_{min}^{spine} and Y_{max}^{spine} represent the minimal and maximal x and y coordinates of B_{spine}; Y_{max}^{aorta} is the maximal coordinate of the 3D aorta along the y axis; and X_C^{aorta} is the x coordinate associated to the 3D aorta centroid. B_{spine} is defined to include all the CT slices along z axis and with an x length l_x equal to 95mm. l_x was determined empirically on three different CTs from the dataset. Two segmented regions denoted S_{spine} and S_{ribs} corresponding to the spine and the ribs respectively are obtained using B_{spine} as a mask on S_{v1}.

The second step removing remaining tissue regions from S_{ribs} is illustrated in Figure 3.16. For each slice S_{V1}^i, a labelling process is performed and a 2D intrathoracic ellipse ε^i is created. Each labelled slice is denoted as L^i, and ε^i is characterized by its centre of coordinates $\{C_x^i, C_y^i\}$, its latero-lateral (R_x^i) and antero-posterior (R_y^i) radius. These four parameters are defined as follows:

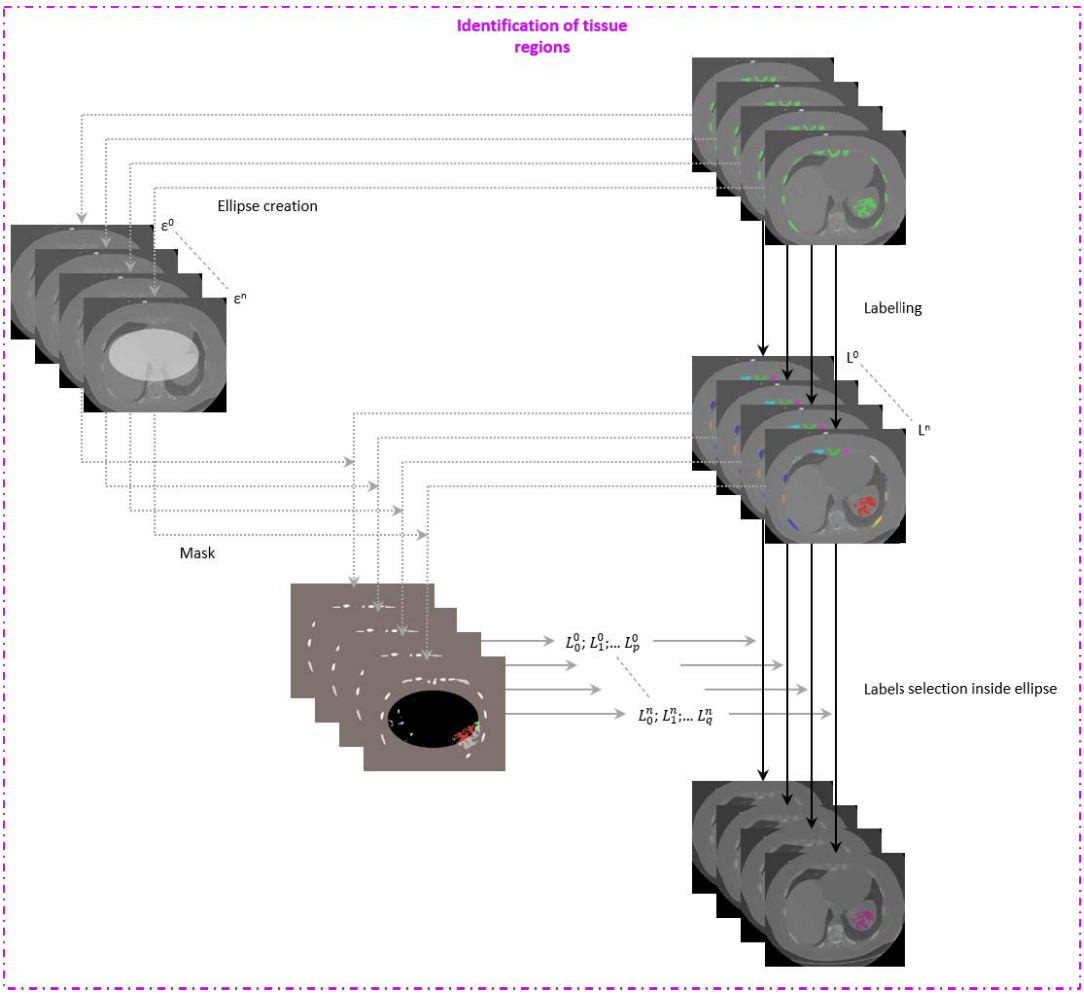

Figure 3.16 - Identification of tissue regions in the rib cage segmentation method

$$C_x^i = X_{min}^i + \frac{X_{max}^i - X_{min}^i}{2} \tag{6}$$

$$C_y^i = Y_{min}^i + \frac{Y_{max}^i - Y_{min}^i}{2} \tag{7}$$

$$R_x^i = \frac{X_{max}^i - X_{min}^i}{2} * 0.85 \tag{8}$$

$$R_y^i = \frac{Y_{max}^i - Y_{min}^i}{2} * 0.7 \tag{9}$$

where $X_{min}^i, X_{max}^i, Y_{min}^i$ and Y_{max}^i characterize the minimal and maximal x and y coordinates from the ribs segmentation in the slice S_{input}^i. The major axis is defined as 85% of the maximum distance between the ribs on the left and the right side, while the minor axis is defined as 70% of the maximum distance between the anterior and posterior side of the ribs. The ellipse ε^i is then used as a mask on the labelled slice L^i to determine each bounded region denoted as L_k^i. These regions

corresponding to tissue are removed from S_{V1}^{i}. S_{spine} is then added to the 3D ribs segmentation and a closing filter with an extraction of the major connected component finalizes this method.

4.4.2. Results

In the proposed algorithms, only one parameter is to be adjusted: V_{th}. Different values were analysed in order to determine the most appropriate one according to the CT. V_{th} varied within the following range of HU values {80; 90; 100; 110; 120}. With a V_{th} below 80 HU it is not possible to separate segmented tissue regions from the rib cage, while above 120 HU costal cartilages are not extracted. For both algorithms, we evaluated the results through a grade classification. Three grades were distinguished. The first one called "Success" represents rib cage segmentation where all structures were extracted with no over- or under-estimation. The second grade "Partial success" characterizes segmentations whose over- or under-estimations are not located in the region of interaction with the device (for instance right upper ribs). Finally, the third one defined as "Failed" corresponds to segmentations where some rib cage structures are missing, or additional organs are present. Figure 3.17 illustrates the three types of classification, while Figure 3.18 presents the results.

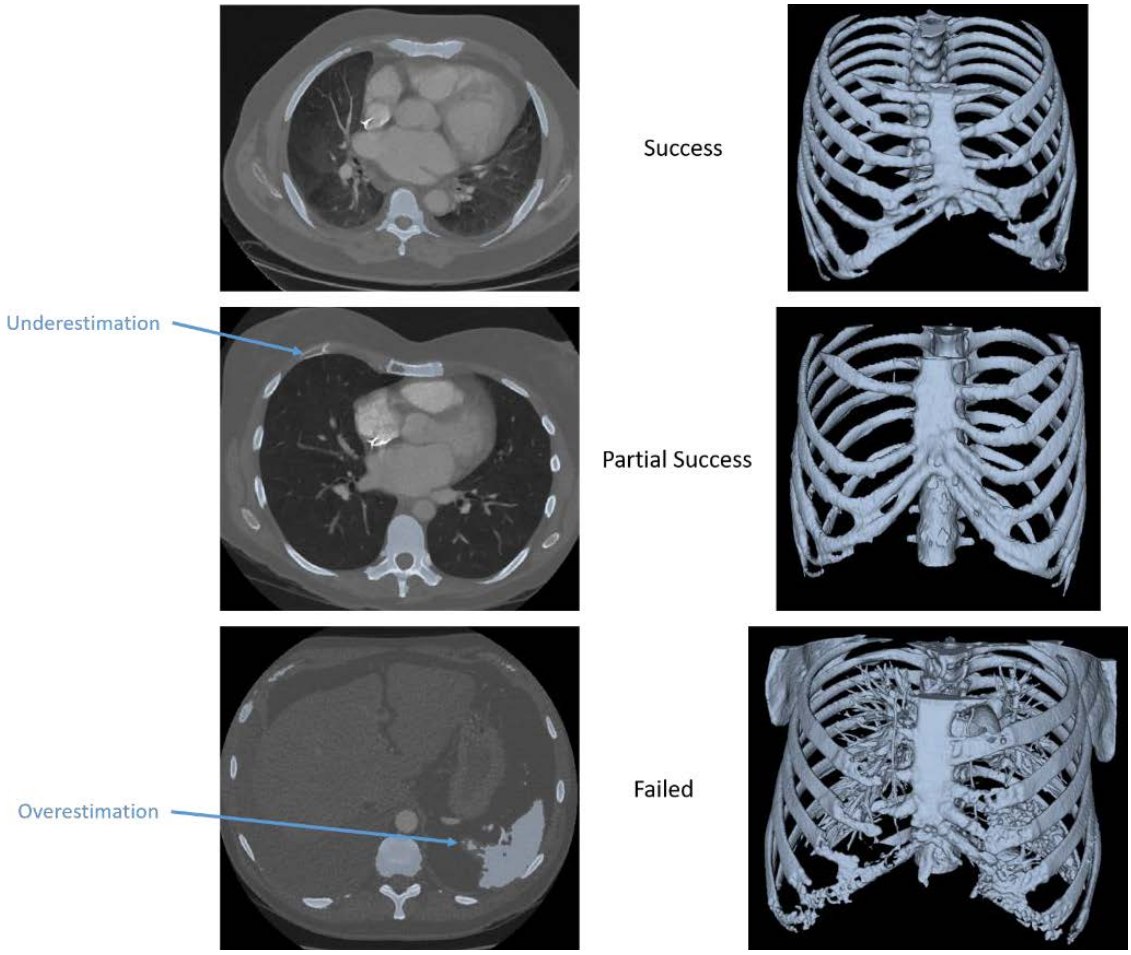

Figure 3.17 - Example of rib cage segmentation results

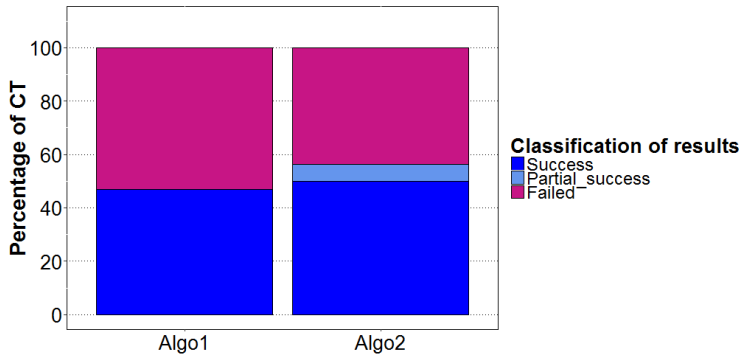

Figure 3.18 - Rib cage segmentation results (32 CTs)

According to the graph, only 47% of the segmentations succeeded with the first algorithm, and 50% were obtained with the second algorithm. Accepting "Partial success" grade, 56% of satisfactory segmentation can be reached with Algo 2. Four different sources were identified to explain the failure of the process. Table 3-VIII enumerates the different sources of rib cage segmentation failure according to each patient. First, with incorrect heart segmentation the process cannot remove all injected structures. Second, metallic artefacts alter the CT scan with white and black regions. Sometimes these artefacts cover part of ribs structures that cannot be extracted. The third reason is due to the presence of opacified areas in lungs regions located near the ribs in the back. These areas are generally segmented with the rib cage. Finally, the process may fail to find a V_{th} that extracts costal cartilages without other organs tissues. The rib cage is a combination of high (external part of the bone) and low density structures (internal part of the bones and costal cartilages). This variation of density makes the entire rib cage segmentation challenging. With a thresholding-based method, it seems difficult to find a V_{th} low enough to consider costal cartilages

Table 3-VIII - Sources of rib cage segmentation failures (12/32 CTs)

Patients With ICD	Incorrect heart segmentation	Metallic artefacts	Lungs with opacification	Costal cartilages
PC3	✓	×	×	✓
PC4	×	×	×	✓
PC5	×	×	×	✓
PC7_1	✓	✓	×	✓
PC7_2	✓	✓	×	✓

Patients Without ICD	Incorrect heart segmentation	Metallic artefacts	Lungs with opacification	Costal cartilages
P7	×	×	×	✓
P13	×	×	✓	✓
P20	×	×	×	✓
PC2	×	×	✓	×
PC6	×	×	✓	×
PJ3	×	×	×	✓
PJ6	×	×	×	✓

and not too low to avoid any confusion with organ tissues. This analysis confirms that the major source of rib cage segmentation failure is due to the difficulty in segmenting the costal cartilages.

5. Conclusion

The main objective of this chapter was to evaluate the feasibility of constructing a numerical model of the patient to elaborate a computer-aided planning for MCS device implantation. Based on an extensive analysis of the literature, several segmentation methods have been developed and/or evaluated for the description of the aorta, heart structures, lungs and rib cage. In a computer-aided planning process, segmentation of anatomical structures can be used for three different purposes (Table 3-IX). 3D visual representation is a first way to improve perception (Figure 3.19). Segmentation could also be used for quantitative analysis to provide to the practitioner relevant information for decision support. Then, many questions still remain particularly about blood flow repartition of patients under MCS. 3D geometry could be exploited for numerical simulations.

Table 3-IX - Way of use of anatomical segmentations in the context of MCS

	3D visualisation	Quantitative analyses	Numerical simulations
Lungs	✓	×	×
Heart structures	✓	✓	✓
Aorta	✓	✓	✓
Rib cage	✓	✓	×

Segmentation of the aorta was not a limitation in the context of MCS. It can be used for rib cage segmentation and 3D visualisation. For the heart cavities and myocardium segmentation, the state of the art raised the necessity of using a shape-based method. The evaluation of a multi-atlas approach demonstrated the effectiveness of this method, but also the presence of some limitations related to ICD and contrast media inhomogeneity. Results for the whole heart segmentation were however satisfactory enough for being used in the rib cage segmentation. Investigation on the rib cage extraction highlighted significant challenges due to the costal cartilages segmentation, specifically in contrast-enhanced CTs. Results are not sufficient at this early stage of the work and further investigation is necessary. In the same way, extraction of lungs structures has proved to be a difficult issue due to the variability of lungs pathology for patients eligible for MCS device implantation.

If 3D visualization may tolerate errors, quantitative analysis and numerical simulation necessitate precise 3D description of anatomical structures. Taking into account segmentation results and considering the clinical interest of each structure in the context of MCS device implantation

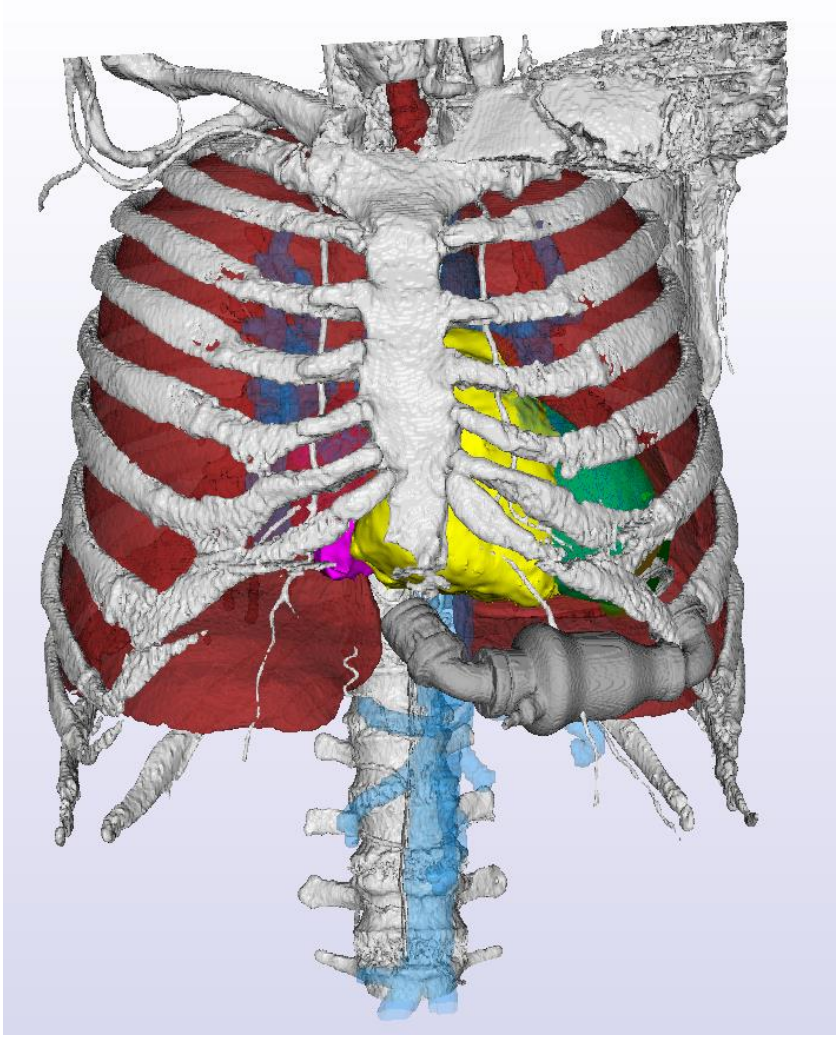

Figure 3.19 - Virtual patient for computer-aided planning for MCS device implantation

planning, we decided to use the four organs for 3D visualization. The rib cage and the heart are used for quantitative analyses for the pose planning approach, and the left ventricle segmentation for computational modelling.

References

Abdollahi, B. et al., 2012. A novel Gaussian Scale Space-based joint MGRF framework for precise lung segmentation. In *Proceedings - International Conference on Image Processing, ICIP*. IEEE, pp. 2029–2032.

Antunes, S. et al., 2013. Automatic right ventricle segmentation in CT images using a novel multi-scale edge detector approach. *Computing in Cardiology Conference (CinC), 2013*, pp.815–818.

Armato, S.G. & MacMahon, H., 2003. Automated lung segmentation and computer-aided diagnosis for thoracic CT scans. *International Congress Series*, 1256, pp.977–982.

Armato III, S.G. & Sensakovic, W.F., 2004. Radiology and Surgery Original Investigations Automated Lung Segmentation for Thoracic CT: *Acad Radiol*, pp.1011–1021.

Bae, J. et al., 2014. Thoracic cavity segmentation algorithm using multiorgan extraction and surface fitting in volumetric CT. *Medical Physics*, 41(33), pp.41908–2323.

Brahim, W. et al., 2017. Semi-Automated rib cage segmentation in CT images for mesothelioma detection. *IPAS 2016 - 2nd International Image Processing, Applications and Systems Conference*, pp.1–6.

Brown, M.S. et al., 2000. Knowledge-based segmentation of thoracic computed tomography images for assessment of split lung function. *Medical physics*, 27(3), pp.592–598.

Cheirsilp, R. et al., 2015. Thoracic cavity definition for 3D PET/CT analysis and visualization. *Computers in Biology and Medicine*, 62, pp.222–238.

Cheng, G.Z. et al., 2016. Three-dimensional printing and 3D slicer powerful tools in understanding and treating structural lung disease. *Chest*, 149(5), pp.1136–1142.

Chittajallu, D.R., Balanca, P. & Kakadiaris, I.A., 2009. Automatic delineation of the inner thoracic region in non-contrast CT data. In *Proceedings of the 31st Annual International Conference of the IEEE Engineering in Medicine and Biology Society: Engineering the Future of Biomedicine, EMBC 2009*. pp. 3569–3572.

Choi, S. & Kim, C., 2010. Automatic initialization active contour model for the segmentation of the chest wall on chest CT. *Healthcare Informatics Research*, 16(1), pp.36–45.

Ecabert, O. et al., 2008. Automatic model-based segmentation of the heart in CT images. *IEEE Transactions on Medical Imaging*, 27(9), pp.1189–1202.

Ecabert, O. et al., 2011. Segmentation of the heart and great vessels in CT images using a model-based adaptation framework. *Medical Image Analysis*, 15(6), pp.863–876.

El-Baz, A. et al., 2008. A New Stochastic Framework for Accurate Lung Segmentation. *Medical image computing and computer-assisted intervention: MICCAI ... International Conference on Medical Image Computing and Computer-Assisted Intervention*, 11, pp.322–330.

El-Baz, A. et al., 2013. Computer-aided diagnosis systems for lung cancer: Challenges and methodologies. *International Journal of Biomedical Imaging*, 2013.

Fritscher, K., Magna, S. & Magna, S., 2015. A novel atlas-selection approach for multiple atlas segmentation based on Manifold Learning and Random Forests using Multi-Scale Image Patches. , (April 2016), pp.10–17.

Fu, Y. et al., 2017. Automatic and hierarchical segmentation of the human skeleton in CT images. *Physics in Medicine and Biology*, 62(7), pp.2812–2833.

Gao, M. et al., 2011. 4D cardiac reconstruction using high resolution CT images. *Functional Imaging and Modeling of the Heart*, 6666(9), pp.153–160.

Gao, Q. et al., 2007. Accurate lung segmentation for X-ray CT images. *Proceedings - Third International Conference on Natural Computation, ICNC 2007*, 2(Icnc), pp.275–279.

Hosseini-Asl, E. et al., 2016. 3-D Lung Segmentation by Incremental Constrained Nonnegative Matrix Factorization. *IEEE Transactions on Biomedical Engineering*, 63(5), pp.952–963.

Hu, S., Hoffman, E.A. & Reinhardt, J.M., 2001. Automatic lung segmentation for accurate quantitation of volumetric X-ray CT images. *IEEE Transactions on Medical Imaging*, 20(6), pp.490–498.

Hua, P. et al., 2011. Segmentation of Pathological and Diseased Lung Tissue in CT Images Using Graph-Search Algorithm. *Iee*, pp.2072–2075.

Huang, W. et al., 2014. Abdominal wall extraction using constrained deformable model and abdominal context. In *Annual International Conference of the IEEE Engineering in Medicine and Biology Society*. pp. 4699–4702.

Itai, Y., Kim, H. & Ishikawa, S., 2007. A Segmentation Method Of Lung Areas By Using Snakes And Automatic Detection Of Abnormal Shadow On The Areas. *International Journal of Innovative Computing, Information and Control*, 3(2), pp.277–284.

Jin, J. et al., 2013. Vascular tree segmentation in medical images using Hessian-based multiscale filtering and level set method. *Computational and Mathematical Methods in Medicine*, 2013.

John, M. & Rahn, N., 2005. Automatic left atrium segmentation by cutting the blood pool at narrowings. In *Lecture Notes in Computer Science (including subseries Lecture Notes in Artificial Intelligence and Lecture Notes in Bioinformatics)*. Springer, pp. 798–805.

Kaladji, A. et al., 2010. Sizing for endovascular aneurysm repair: Clinical evaluation of a new automated three-dimensional software. *Annals of Vascular Surgery*, 24(7), pp.912–920.

Kang, D. et al., 2012. Heart chambers and whole heart segmentation techniques: review. *Journal of Electronic Imaging*, 21(1), p.10901.

Kang, H.C., Lee, J. & Shin, J., 2016. Automatic four-chamber segmentation using level-set method

and split energy function. *Healthcare Informatics Research*, 22(4), pp.285–292.

Kirisli, H.A. et al., 2010. Evaluation of a multi-atlas based method for segmentation of cardiac CTA data: a large-scale, multicenter, and multivendor study. *Medical physics*, 37(12), pp.6279–6291.

Kitasaka, T. et al., 2003. Lung area extraction from 3D chest X-ray CT images using a shape model generated by a variable Bézier surface. *Systems and Computers in Japan*, 34(4), pp.60–71.

Korfiatis, P. et al., 2007. Combining 2D wavelet edge highlighting and 3D thresholding for lung segmentation in thin-slice CT. *British Journal of Radiology*, 80(960), pp.996–1005.

Korfiatis, P. et al., 2008. Texture classification-based segmentation of lung affected by interstitial pneumonia in high-resolution CT. *Medical physics*, 35(12), pp.5290–5302.

Larrey-Ruiz, J. et al., 2014. Automatic image-based segmentation of the heart from CT scans. *EURASIP Journal on Image and Video Processing*, 2014(1), p.52.

Lassen, B. et al., 2011. Lung and Lung Lobe Segmentation Methods at Fraunhofer MEVIS. *Proceedings of the Fourth International Workshop on Pulmonary Image Analysis*, pp.185–99.

Leader, J.K. et al., 2003. Automated Lung Segmentation in X-Ray Computed Tomography: Development and Evaluation of a Heuristic Threshold-Based Scheme. *Academic Radiology*, 10(11), pp.1224–1236.

Lesage, D. et al., 2009. A review of 3D vessel lumen segmentation techniques: Models, features and extraction schemes. *Medical Image Analysis*, 13(6), pp.819–845.

Li, Q., Li, F. & Doi, K., 2008. Computerized detection of lung nodules in thin-section CT images by use of selective enhancement filters and an automated rule-based classifier. *Acad Radiol*, pp.165–175.

Li, W., Nie, S. & Cheng, J., 2007. A fast automatic method of lung segmentation in CT images using mathematical morphology. *World Congress on Medical Physics and …*, 14, pp.2419–2422.

Litjens, G. et al., 2017. A Survey on Deep Learning in Medical Image Analysis. *Computer Vision and Pattern Recognition*, 42(December 2012), pp.60–88.

Lo, P. et al., 2011. Historic Automated Lung Segmentation Method: Performance on LOLA11 Data Set. *Fourth International Workshop on Pulmonary Image Analysis (LOLA11)*, 27(3), pp.592–598.

Mansoor, A., Bagci, U., Xu, Z., et al., 2014. A Generic Approach to Pathological Lung Segmentation. *IEEE Trans. Med. Imag.*, 33(12), pp.2293–2310.

Mansoor, A., Bagci, U., Foster, B., et al., 2014. CIDI-lung-seg: A single-click annotation tool for automatic delineation of lungs from CT scans. *2014 36th Annual International Conference of the IEEE Engineering in Medicine and Biology Society, EMBC 2014*, pp.1087–1090.

Mansoor, A. et al., 2015. Segmentation and Image Analysis of Abnormal Lungs at CT: Current

Approaches, Challenges, and Future Trends. *Radiographics : a review publication of the Radiological Society of North America, Inc*, 35(4), pp.1056–76.

Mesanovic, N. et al., 2017. *Automatic CT Image Segmentation of the Lungs with Region Growing Algorithm*,

Narkbuakaew, W. et al., 2014. Bone segmentation in CT-liver images using K-means clustering for 3D rib cage surface-modeling. *WSEAS Transactions on Biology and Biomedicine*, 11(1), pp.183–193.

Niessen, W., 2008. Model-Based Image Segmentation for Image-Guided Interventions. *Image-Guided Interventions: Technology and Applications*, pp.219–239.

De Nunzio, G. et al., 2011. Automatic lung segmentation in CT images with accurate handling of the hilar region. *Journal of Digital Imaging*, 24(1), pp.11–27.

Özsavag, E.E. et al., 2014. Automatic Segmentation of Anatomical Structures from CT Scans of Thorax for RTP. *Computational and Mathematical Methods in Medicine*, 2014, pp.1–15.

Pazokifard, B., Sowmya, A. & Moses, D., 2015. Automatic patient-customised 3D reconstruction of human costal cartilage from lung MDCT dataset. *International Journal of Computer Assisted Radiology and Surgery*, 10(4), pp.465–472.

Peters, J. et al., 2010. Accurate segmentation of the left ventricle in computed tomography images for local wall thickness assessment. In *Lecture Notes in Computer Science (including subseries Lecture Notes in Artificial Intelligence and Lecture Notes in Bioinformatics)*. Springer, pp. 400–408.

Peters, J. et al., 2010. Optimizing boundary detection via Simulated Search with applications to multi-modal heart segmentation. *Medical Image Analysis*, 14(1), pp.70–84.

Prasad, M.N. et al., 2008. Automatic Segmentation of Lung Parenchyma in the Presence of Diseases Based on Curvature of Ribs. *Academic Radiology*, 15(9), pp.1173–1180.

Pu, J. et al., 2008. Adaptive Border Marching Algorithm: Automatic Lung Segmentation on Chest CT Images. *NIH Public Access*, 32(6), pp.452–462.

Rebouças Filho, P.P. et al., 2017. Novel and powerful 3D adaptive crisp active contour method applied in the segmentation of CT lung images. *Medical Image Analysis*, 35, pp.503–516.

van Rikxoort, E.M. et al., 2009. Automatic lung segmentation from thoracic computed tomography scans using a hybrid approach with error detection. *Medical Physics*, 36(7), pp.2934–2947.

Rikxoort, E.M. Van & Ginneken, B. Van, 2013. Automated segmentation of pulmonary structures in thoracic computed tomography scans: a review. *Physics in Medicine and Biology*, 58(17), pp.R187-220.

Shojaii, R., Alirezaie, J. & Babyn, P., 2005. Automatic lung segmentation in CT images using watershed transform. *Proceedings - International Conference on Image Processing, ICIP*, 2, pp.1270–1273.

Silva, A. et al., 2001. Fast Pulmonary Contour Extraction in X-ray CT Images: A Methodology and Quality Assessment. *Spie*, 4321, pp.216–224.

Silveira, M., Nascimento, J. & Marques, J., 2007. Automatic segmentation of the lungs using robust level sets. In *Annual International Conference of the IEEE Engineering in Medicine and Biology - Proceedings*. IEEE, pp. 4414–4417.

Sluimer, I. et al., 2006. Computer analysis of computed tomography scans of the lung: A survey. *IEEE Transactions on Medical Imaging*, 25(4), pp.385–405.

Sluimer, I., Niemeijer, M. & van Ginneken, B., 2004. Lung field segmentation from thin-slice CT scans in presence of severe pathology. *Proc. SPIE Med. Imag*, 5370, pp.1447–1455.

Sluimer, I., Prokop, M. & Van Ginneken, B., 2005. Toward automated segmentation of the pathological lung in CT. *IEEE Transactions on Medical Imaging*, 24(8), pp.1025–1038.

Sofka, M. et al., 2011. Multi-stage learning for robust lung segmentation in challenging CT volumes. In *MICCAI*. pp. 667–674.

Soliman, A. et al., 2017. Accurate lungs segmentation on CT chest images by adaptive appearance-guided shape modeling. *IEEE Transactions on Medical Imaging*, 36(1), pp.263–276.

Sun, S., 2013. Automated 3-D Segmentation of Lungs With Lung Cancer in CT Data Using a Novel Robust Active Shape Model Approach. *IEEE transactions on medical imaging*, 31(2), pp.1–33.

Sun, S., Bauer, C. & Beichel, R., 2012. Automated 3-D segmentation of lungs with lung cancer in CT data using a novel robust active shape model approach. *IEEE Transactions on Medical Imaging*, 31(2), pp.449–460.

Sun, X., Zhang, H. & Duan, H., 2006. 3D Computerized Segmentation of Lung Volume With Computed Tomography. *Academic Radiology*, 13(6), pp.670–677.

Udupa, J.K. et al., 2014. Body-Wide Hierarchical Fuzzy Modeling, Recognition, and Delineation of Anatomy in Medical Images. *Med Image Anal*, 18(5), pp.752–771.

Vandemeulebroucke, J. et al., 2012. Automated segmentation of a motion mask to preserve sliding motion in deformable registration of thoracic CT. *Medical Physics*, 39(2), pp.1006–1015.

Wang, J., Li, F., Doi, K., et al., 2009. A novel Scheme for detection of Diffuse Lung Disease in MDCT by Use of Statistical Texture Features. *Phys. Med. Biol*, 54(April), pp.6881–6899.

Wang, J. & Guo, H., 2016. Automatic Approach for Lung Segmentation with Juxta-Pleural Nodules from Thoracic CT Based on Contour Tracing and Correction. *Computational and Mathematical Methods in Medicine*, 2016, pp.1–13.

Wang, J., Li, F. & Li, Q., 2009. Automated segmentation of lungs with severe interstitial lung disease in CT. *Medical physics*, 36(10), pp.4592–4599.

Wu, W. et al., 2016. Automatic Liver Segmentation on Volumetric CT Images Using Supervoxel-

Based Graph Cuts. *Computational and Mathematical Methods in Medicine*, 2016.

Xu, Z. et al., 2014. Efficient Ribcage Segmentation from CT Scans Using Shape Features. In *IEEE Eng Med Biol Soc*. pp. 2899–2902.

Yim, Y., Hong, H. & Shin, Y.G., 2005. Hybrid lung segmentation in chest CT images for computer-aided diagnosis. In *Proceedings of the 7th International Workshop on Enterprise Networking and Computing in Healthcare Industry, HEALTHCOM 2005*. IEEE, pp. 378–383.

Yip, S., Perk, T. & Jeraj, R., 2014. Development and evaluation of an articulated registration algorithm for human skeleton registration. *Physics in Medicine and Biology*, 59(6), p.1485.

Zhao, Q. et al., 2014. Estimation of cartilaginous region in noncontrast CT of the chest. *Proc. SPIE 9035, Medical Imaging 2014: Computer-Aided Diagnosis*, 9035, p.90350N–7.

Zheng, B. et al., 2003. A simple method for automated lung segmentation in X-ray CT images. *Proc SPIE*, 5032, pp.1455–1463.

Zheng, Y. et al., 2008. Four-Chamber Heart Modeling and Automatic Segmentation for 3D Cardiac CT Volumes Using Marginal Space Learning and Steerable Features. In *IEEE Transactions on Medical Imaging*. pp. 1668–1681.

Zhong, H. et al., 2013. Automatic heart isolation in 3D CT images. In *Lecture Notes in Computer Science (including subseries Lecture Notes in Artificial Intelligence and Lecture Notes in Bioinformatics)*. Springer, pp. 165–180.

Zhou, S., Cheng, Y. & Tamura, S., 2014. Automated lung segmentation and smoothing techniques for inclusion of juxtapleural nodules and pulmonary vessels on chest CT images. *Biomedical Signal Processing and Control*, 13(1), pp.62–70.

Zhou, X. et al., 2004. Automated segmentations of skin , soft-tissue , and skeleton from torso CT images. *Medical Imaging (SPIE)*, 5370, pp.1634–1639.

Zhou, X. et al., 2005. Preliminary Study for Automated Recognition of Anatomical Structure from Torso CT images. In *Annual International Conference of the IEEE Engineering in Medicine and Biology Society*. pp. 650–653.

Zhu, L. et al., 2014. A complete system for automatic extraction of left ventricular myocardium from ct images using shape segmentation and contour evolution. *IEEE Transactions on Image Processing*, 23(3), pp.1340–1351.

Zhu, L. et al., 2013. Automatic delineation of the myocardial wall from CT images via shape segmentation and variational region growing. *IEEE Transactions on Biomedical Engineering*, 60(10), pp.2887–2895.

Zhuang, X. et al., 2013. A registration and atlas propagation based framework for automatic whole heart segmentation of CT volumes. *Medical Imaging: Image Processing*, 8669, p.86693W.

Zhuang, X., 2013. Challenges and methodologies of fully automatic whole heart segmentation: a review. *Journal of healthcare engineering*, 4(3), pp.371–408.

Zhuang, X. et al., 2015. Multiatlas whole heart segmentation of CT data using conditional entropy for atlas ranking and selection. *Medical Physics*, 42(7), pp.3822–3833.

Zreik, M. et al., 2016. Automatic Segmentation of the Left Ventricle in Cardiac CT Angiography Using Convolutional Neural Network. *2016 IEEE 13th International Symposium on Biomedical Imaging (ISBI)*, pp.40–43.

Zuluaga, M.A. et al., 2013. Multi-atlas propagation whole heart segmentation from MRI and CTA using a local normalised correlation coefficient criterion. *Lecture Notes in Computer Science (including subseries Lecture Notes in Artificial Intelligence and Lecture Notes in Bioinformatics)*, 7945 LNCS, pp.174–181.

Chapter 4 - Geometrical approach

This chapter presents a computer-aided solution that could allow surgeons to anticipate intrathoracic device implantation in order to limit intraoperative and postoperative complications. This solution focuses on two specific sources of complications: collisions of MCS device with surrounding organs, and incorrect orientation of LVAD inflow cannula.

We first describe the different MCS devices considered in this works. Then, indices characterizing the inflow cannula pose are defined and LVADs implanted without computer-aided planning are analysed. Assumptions made on geometrical constraints and their relevance are introduced. The proposed pose planning approach is then presented detailing the methods used for inflow cannula pose analysis and evaluation of surrounding anatomical constraints, as well as the implementation of the solution. Finally, the potential benefits and limitations of computer-aided planning method are highlighted.

1. Devices and their specificities

Considering the number of MCS devices clinically available, we focus on those that are currently implanted in the Thoracic and Cardiovascular Surgery Department of the University Hospital of Rennes (France). One TAH and four LVADs are taken into consideration.

The Syncardia (also called CardioWest and previously named Jarvik 7) is the most implanted TAH over the world. It is composed of two independent rigid spherical pulsatile pumps (Figure 4.1) and each pump includes two chambers (air and blood) separated by a polyurethane membrane. Generally used on adults, its weight is of 160 g for a volume of 70cc for each artificial ventricle. A smaller one has also been developed for adolescents and women statures (artificial ventricles of 50cc). This TAH is only used for bridge to transplant.

LVADs considered are continuous-flow devices. These devices (Figure 4.2) present a variability of

Figure 4.1 - Syncardia TAH

Figure 4.2 - LVADs considered in the thesis

size, weight, geometry and Inflow Cannula (IC) length (Table 4-I). Their geometry and characteristics can be briefly described as follows:

- The HeartMate II (HM II) (Thoratec Inc. Pleasanton, CA) is an axial pump in titanium with U-shaped geometry. In order to adapt its position within the intrathoracic cavity, the inflow conduit contains a portion of flexible silicone segment. More than 23,000 HM II have currently been implanted worldwide, and according to (John et al. 2011) this device presents a remarkable efficiency on survival and functional health improvement of patients.
- The HeartWare HVAS (HVAS) (HeartWare Inc., Framingham, MA) is a centrifugal pump presenting a circular geometry and with a smaller volume and IC length than the HM II. Its efficiency and durability have also been brought forward by clinical studies (Popov et al. 2012).
- The HeartMate III (Thoratec Inc. Pleasanton, CA) represents novel centrifugal-flow LVADs that utilize a fully magnetically levitated technology foundation. This device has recently obtained the European certification mark (CE marking) and is entering the clinical practice. As the HVAS its geometry is circular.

Both HM II and HVAS can reach a flow rate of 10 L/min while the HeartMate III can reach 13 L/min. These three LVADs are composed of an IC which is inserted within the LV, a pump

Table 4-I - LVADs characteristics

Device	Weight [g]	Volume [cc]	Rpm	Debit [L/min]
Second generation				
- HeartMate II	281	63	6.000-15.000	Up to 10
- Jarvik 2000	90	25	7.000-13.000	Up to 12
Third generation				
- HeartWare HVAS	145	45	2.000-5.000	Up to 10
- HeartMate III	200	50	2.000-5.500	Up to 13

located in the pericardial cavity, and a power cable going through the abdomen in order to rely the pump to two external batteries.

- The Jarvik 2000 Flowmaker (Jarvik Heart Inc., New York, NY) is an axial pump whose specificity is its small size. The turbine and the pump motor are inside the titanium cylinder IC, avoiding thus intra-pericardial conflicts. Contrary to the other ones, the power cable is located on the scalp to reduce driveline infections. The maximum flow provided by this LVAD is 12 L/min.

Among the 4 investigated LVADs, the most implanted worldwide are the HM II, HVAS and Jarvik 2000. Although these devices are more commonly implanted, intraoperative and postoperative complications are still reported. In this work, we focus on two specific sources of complications: those related to the IC pose and those related to geometrical constraints. The first source of complications only concern LVADs whereas the second one is for all MCS devices. Next section presents postoperative assessment of IC pose.

2. Metrics for LVAD inflow cannula pose

According to clinical recommendations the LVAD IC must be pointed toward the Mitral Valve (MV) in order to optimize blood flow and limit suction events with the Inter-Ventricular Septum (IVS). Issues raised in the context of LVAD IC position and results from the literature are first presented. Secondly, a novel approach evaluating the IC position and orientation according to anatomical structures is described. Finally, results from retrospective analyses are detailed with the main objective of defining an approach for computer-aided planning.

2.1. Literature and related issues

Only few studies have examined the IC orientation significance in terms of LVAD efficiency. Three retrospectives analyses investigated the relationship of the IC orientation with postoperative outcomes (Table 4-II).

Table 4-II - Results of retrospective studies evaluating the influence of the IC orientation on postoperative outcomes.

	Number of patients	Devices	IC orientation promoting complications
(Imamura et al. 2017)	27	HVAS	IVS
(Kazui et al. 2015)	311	HM II	IVS
(Truong et al. 2013)	24	HM II / XVE	IVS + anterior

The LV unloading is a key to prevent heart failure recurrence. (Imamura et al. 2017) demonstrated that a low coronal angle deviation (low angle toward IVS) promoted this LV unloading and was associated to better prognosis. For this experiment 27 patients with a HVAS implanted were considered. (Truong et al. 2013) showed that deviation toward IVS and anterior wall was associated with mortalities. Lateral and posterior wall orientation did not seem to be related to complications. 24 patients with HM II or Heartmate XVE LVAS devices were selected in this study. Finally, (Kazui et al. 2015) demonstrated that among 311 patients with a HM II, those presenting pump dysfunction or thrombus had also more important septal deviations compared to patients without complications. Results converged on same conclusions and confirmed recommendations: the LVAD IC must be oriented toward the MV and away from the IVS.

Nonetheless, in these three studies the IC orientations were defined according to standard x, y, z CT axes (Figure 4.3.a). Regarding the 3D general representation of the heart within the thoracic cavity (Figure 4.3.b), the LV is positioned in a posterior configuration compared to the RV. The coronal angle defined in the literature represents an orientation toward the right lateral side rather than an IVS deviation. The 3D pose of the IC has therefore not been explicitly defined with respect to anatomical structures of interest.

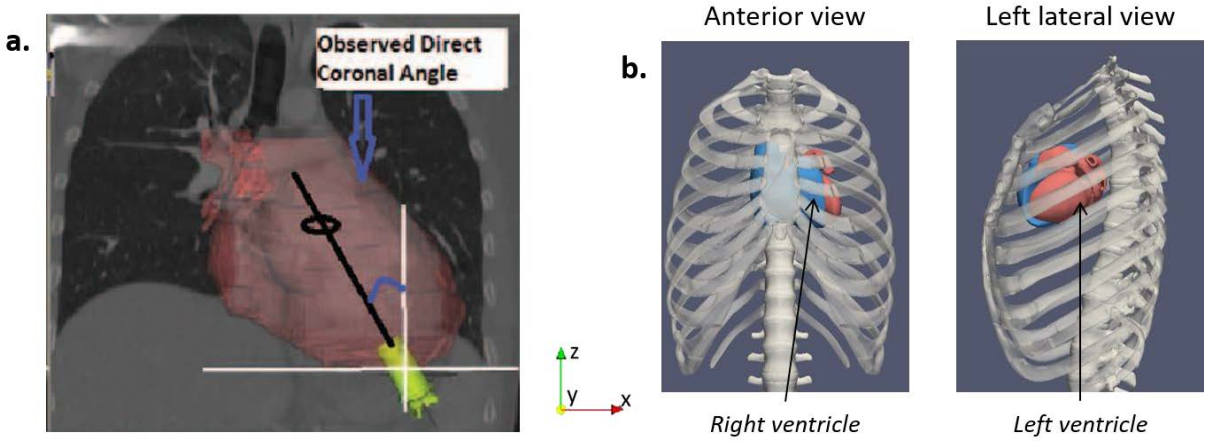

Figure 4.3 - a. Inflow cannula to mitral valve alignment. Definition of the coronal angle (deviation toward IVS) b. 3D representation of the heart within the thoracic cavity
Source image a.: (Truong et al. 2013)

In the following we evaluate the IC orientation through quantitative indices taking into account the 3D characteristics of the heart and device. Figure 4.4 illustrates the workflow for retrospective analyses.

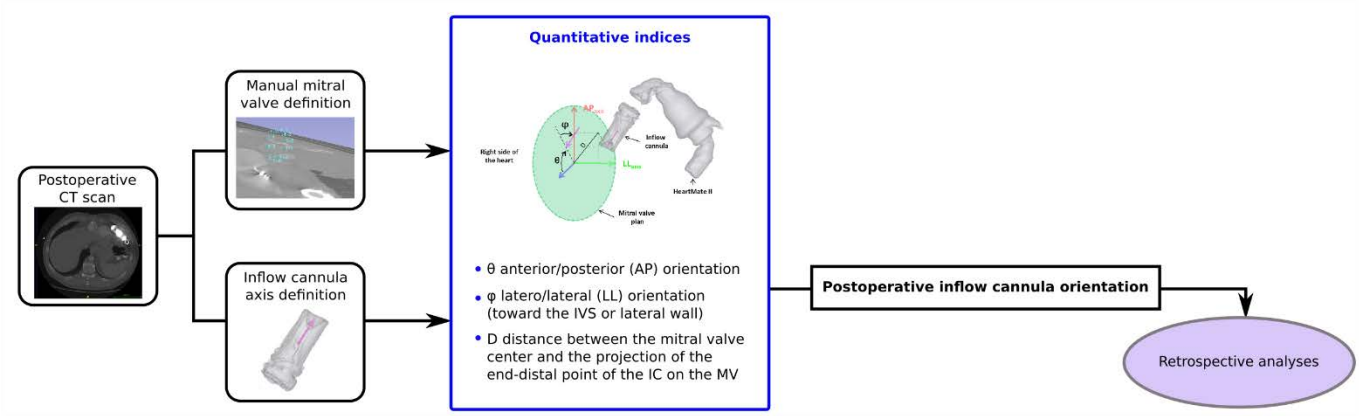

Figure 4.4 - Workflow for retrospective analyses

2.2. Definition of indices characterizing the inflow cannula pose

The MV presents specific features that may be used to recognize anterior, posterior, lateral and IVS directions. To evaluate the IC orientation we considered thus the MV characteristics.

This valve is composed of a fibrous ring known as MV annulus and its 3D anatomical configuration is similar to a saddle shape that we approximated as an ellipse $\boldsymbol{\Omega_{MV}}$. $\boldsymbol{\Omega_{MV}}$ was defined in the mean plane of the mitral annulus points selected by an expert (heart failure surgeon). The MV is also composed of two leaflets that manage the blood flow and act as a one way inlet. Where these leaflets come together, two characteristics points named anterior and posterior commissure point are defined. The anterior commissure point is denoted $\mathbf{P_{com}}$ in the following. To characterize the

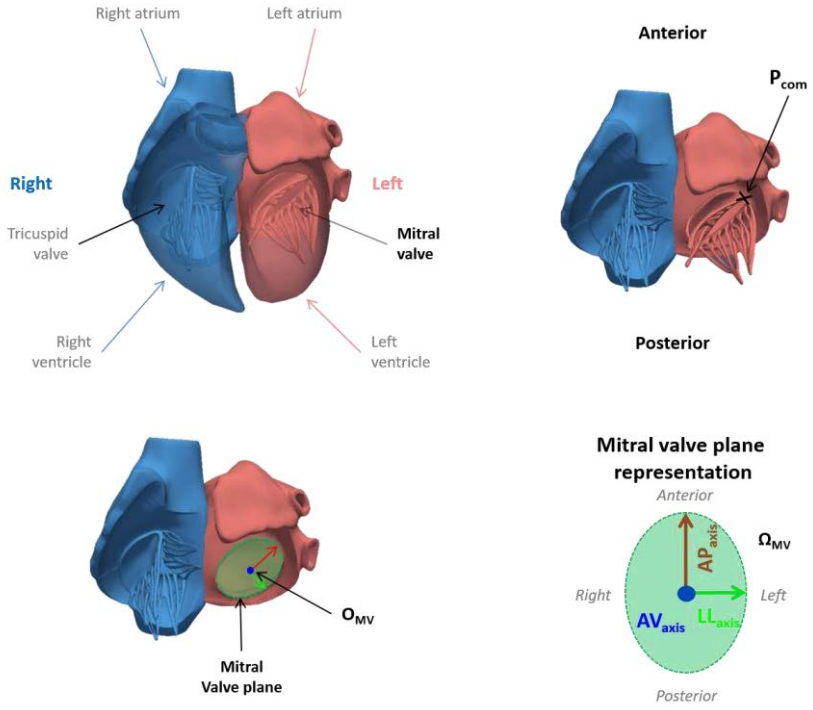

Figure 4.5 - Mitral valve representation and its associated coordinate system

IC pose, a local orthonormal coordinate system was associated to this ellipse. $\boldsymbol{\Omega_{MV}}$ combined with $\mathbf{P_{com}}$ allows defining the anteroposterior axis and the latero-lateral axis. Figure 4.5 describes this coordinate system defined as follows:

- $\mathbf{O_{MV}}$ the centroid of the annulus points,
- $\mathbf{AP_{axis}}$ the anteroposterior axis oriented toward $\mathbf{P_{com}}$ and defined by the vector $\overrightarrow{O_{MV}P_{com}}$,
- $\mathbf{LL_{axis}}$ the latero-lateral axis on Ω_{MV} and perpendicular to AP_{axis} (oriented toward the left part of the body),
- $\mathbf{AV_{axis}}$ axis defined by the vector normal to the Ω_{MV} plane and pointing toward the apex.

All cannula from LVADs are metallic with a cylindrical geometry. We described the IC axis by a vector $\overrightarrow{\boldsymbol{v_{IC}}}$ and the point $\mathbf{C_{IC}}$ representing the centre of the IC distal end. Figure 4.6 represents these elements, as well as the 3 major indices characterizing the orientation and position of the IC, defined by:

- $\boldsymbol{\theta}$ for the anteroposterior orientation
- $\boldsymbol{\varphi}$ for the latero-lateral orientation (toward the IVS or lateral wall),
- $\mathbf{D_{(P,O)}}$ the Euclidian distance between O_{MV} and point P, which is the projection along AV_{axis} of C_{IC} on Ω_{MV}. Notice that for a same orientation, the IC can be positioned differently in space. This distance characterizes thus its position.

For both φ and θ, a percentage of deviation was also evaluated with respect to the maximal possible deviation (90°).

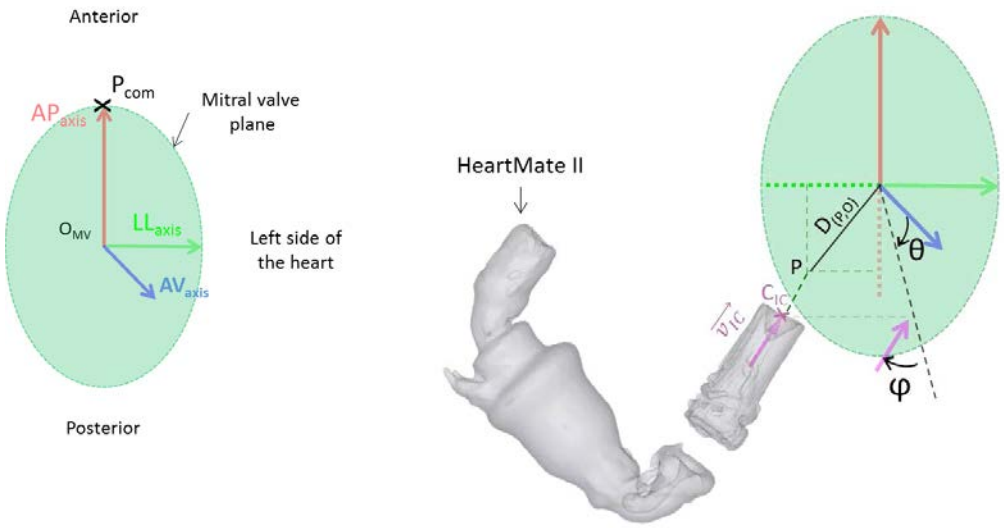

Figure 4.6 - φ, θ orientation and D(p,o) distance representation

Compared to others LVADs, the HM II shows another degree of freedom due to the presence of the flexible silicone segment. An angle α between $\overrightarrow{v_{IC}}$ and the pump body axis is therefore defined as in Figure 4.7. Three different configurations are considered. When α <15° the angulation is considered as normal, for α ∈ [15°; 30°] the angulation is qualified as medium, while α >30° represents an excessive angulation.

According to the intraoperative clinical guidelines, the IC must be coaxial to the MV normal and without twist for the HM II. The optimal positioning can thus be associated to φ = 0, θ = 0, $D_{(P,O)}$ = 0, and α = 0. The lower the absolute value of each parameter is, the better the cannula orientation is. These different parameters were analysed retrospectively in order to evaluate how surgeons implanted LVADs until now. Results are presented in next section through several experiments.

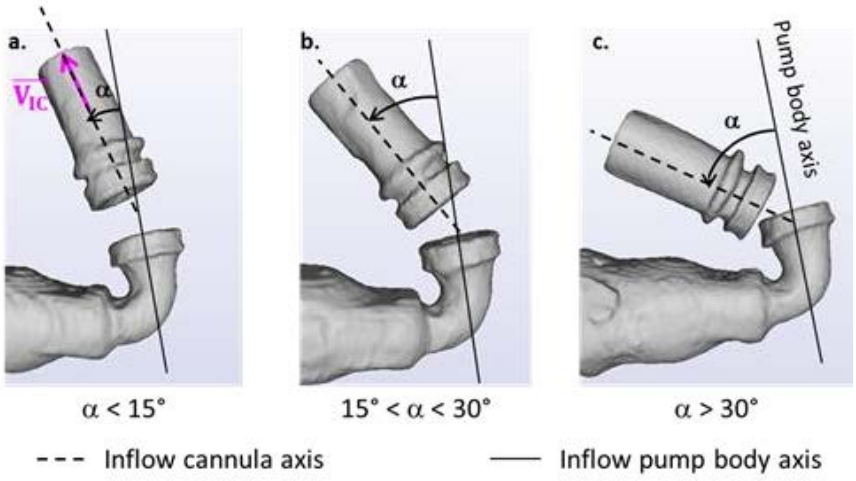

Figure 4.7 - The angle between the inflow cannula and the pump body: **a.** α <15° - a normal angulation, **b.** α ∈ [15°; 30°] – medium angulation; **c.** α > 30° - excessive angulation

2.3. Retrospective analyses

To highlight the pertinence of the indices defined previously, we retrospectively analysed 3D patient postoperative CT scans. 34 postoperative CTs of patients from the University hospital of Rennes and Nantes were evaluated (cf Chapter 3). All were implanted between 2010 and 2016 without computer-aided planning. Among them, 21 were fitted with a HVAS (8 by thoracotomy and 13 by sternotomy), 10 with HM II devices (sternotomy) and only 3 with the Jarvik 2000 (sternotomy). Next section investigates for all LVADs the relationship between the IC pose and postoperative complications, taking into account φ, **θ** orientations and the distance $D_{(P,O)}$ with respect to the MV, as well as α angulation for the HM II.

2.3.1. Relation between the device pose and postoperative complications

In order to evaluate the potential impact of IC pose on postoperative complications, we divided the cohort of patients into two groups. Group 1 corresponded to patients who presented thromboembolic events, pump dysfunction or pump thrombosis (15 patients), whereas Group 2 represented those without complications (19 patients). Two sources of complications were investigated: the influence of the IC pose with respect to the MV and the HM II IC-pump body angulation. For both analyses, results were compared to those from the literature.

- IC positioning

Table 4-III presents the mean and standard deviation of φ, θ and $D_{(P,O)}$ indices obtained for the 34 patients. According to the figures, the anteroposterior percentage of deviation (compared to the optimal pose) is similar for both Group 1 and Group 2, contrary to φ that is significantly higher for patients presenting complications. Furthermore, the position of the IC distal-end with respect to the MV centre does not seem to influence adverse events.

We also compared the difference between a deviation toward the IVS ($\varphi < 0$) and the lateral wall ($\varphi > 0$) (Table 4-IV). Among all patients with a deviation toward the IVS, those from Group 1

Table 4-III - Results for complicated (Group 1) and uncomplicated (Group 2) patients

	Approach	Mean	Median	Standard deviation
φ deviation (%)	**Group 1**	33,6	29,2	25,8
	Group 2	14,2	5,1	18,8
θ deviation (%)	**Group 1**	36,8	31,9	27,4
	Group 2	32,2	26,0	22,3
$D_{(P,O)}$ [mm]	**Group 1**	62,6	58,4	10,2
	Group 2	66,8	66,9	14,9

Table 4-IV - Lateral and IVS deviation for complicated and uncomplicated patients

	Approach	Number of patients	Mean	Median	Standard deviation
φ deviation – IVS (%)	**Group 1**	12	40,8	43,2	24,0
	Group 2	14	17,5	7,4	21,0
φ deviation - lateral (%)	**Group 1**	3	5,2	5,3	1,6
	Group 2	5	4,9	4,1	3,3

presented higher φ deviation than those without complications (Group 2). But deviation toward the lateral wall was similar for both groups.

In order to analyse the influence of the device geometry on the IC pose, each LVAD was also compared (Table 4-V). Among the three devices, the Jarvik 2000 presented less significant φ and θ deviations. This may be explained by its small size and its characteristic of being full inside the cavity. It might be easier to position it with no external constraints related to surrounding anatomical structures. In the same way, smaller than the HM II, the HVAS presented lower φ and θ deviations. But, the difference was not that big for φ. Table 4-VI compares results obtained with those from the literatures, as well as the number of patients and devices considered. These results could be used in the planning solution, adding information about the IC orientation in regard to the MV and IVS, in order to optimise the planning pose and evaluate the optimal device according to the patient anatomy.

Table 4-V - Comparison of φ and θ deviations according to the LVAD

	HVAS (21)	**HM II (10)**	**Jarvik 2000 (3)**
Mean deviation φ (%)	22.4	29.3	3.4
Mean deviation θ (%)	22.7	63.8	16.6
Median deviation φ (%)	8.1	19.3	2.9
Median deviation θ (%)	24.3	61.3	16.4

Table 4-VI - Comparison of the retrospective results with the literature

	Number of patients	**Devices**	**IC orientation promoting complications**
(Imamura et al. 2017)	27	HVAS	IVS
(Kazui et al. 2015)	311	HM II	IVS
(Truong et al. 2013)	24	HM II; XVE	IVS + anterior
Our method	34	HVAS; HM II; Jarvik 2000	IVS + device size

- IC-pump body angulation for the HM II

Three articles from the literature evaluated the influence of the HM II IC angulation with the pump body. (Han et al. 2015) and (Taghavi et al. 2013) both concluded that this factor did not seem to impact or predict the pump thrombosis creation, analysing respectively 90 and 49 patients' outcomes. Our results based on 10 patients agreed these two articles (Table 4-VII). Nevertheless,

(Kazui et al. 2016) established that positional change may contribute to LVAD dysfunction or failure but does not entirely account. Considering 326 patients, it can be supposed that this retrospective analysis provided more convincing results. Because of contradictions between the several analyses, it cannot be firmly concluded that this angle promotes postoperative complications. This remaining open question requires more investigations.

Table 4-VII - Results of postoperative angle between the Heartmate II inflow cannula and the pump body

**Patients with complications: thromboembolic events, pump dysfunction or thrombosis*

Patients	α [degree]	Patients	α [degree]
P3	$\alpha < 15$	P13	$\alpha > 30$
P4*	$\alpha > 30$	P14*	$15 < \alpha < 30$
P5	$\alpha < 15$	P15	$\alpha < 15$
P9	$\alpha < 15$	P16*	$\alpha < 15$
P10*	$\alpha < 15$	P17*	$\alpha < 15$

2.3.2. Influence of the surgical process on inflow cannula orientation

Although it does not represent the primary objective of our work, we also investigated the influence of the surgical way of implantation (sternotomy vs thoracotomy) on the device pose. The median sternotomy is the most common, traditional and major approach performed in cardiac surgery. This process involves significant surgical trauma, displacement of muscle, possibly ribs, and other tissues. Giving access to the entire heart, it makes possible several interventions (associated procedures if needed) during the same surgery. Besides, it allows rapid manipulation and less damage to the heart and cardiac muscles because of good accessibility. However, this procedure is invasive and increases risks of trauma, infections, inflammation, breathing problems and pains. It has also been accused to favour right ventricular failure in LVAD implantation (life-threatening complication). This approach is also risky in patients who benefited previously from cardiac surgery (redo patients). Indeed, to reopen the chest may be dangerous and may motivate the surgeon to try an alternative approach such as the thoracotomy.

Thoracotomy remains an interesting alternative approach to sternotomy. Its biggest advantage is to avoid to reopen the chest in redo patients and to protect the right ventricle. This procedure may be more painful for patients, and it requires most often a local anaesthetic injection in the nerves between the ribs. Mini-thoracotomy and minimal invasive surgery may also be promoted so patients can recover much faster and do not present routinely restrictions contrary to those who undergone sternotomies. With sternotomy, no mechanical stress must be applied on the broken sternum before it is fully healed which necessitates about six weeks. If thoracotomy seems better

as regards with patient's health, it also presents a low visibility condition, making it more challenging.

Currently, we do not know which procedure is better in the context of LVAD implantation and if it has an influence on the device final position and orientation. It could be supposed that the sternotomy presents more dislodgement probability during chest closure due to thoracic compression, but also more facilities to intraoperatively control the device pose. It also allows to perform associated procedures when needed. On the contrary, thoracotomy should present less dislodgement probability but also less flexibility to position the device. Herein, the influence of the surgical procedure on IC deviation is put into question. In order to disregard device geometry we selected only patients with HVAS. 13 patients underwent a sternotomy and 8 patients underwent a thoracotomy.

According to the results illustrated in Table 4-VIII , the surgical approach (sternotomy vs thoracotomy) did not seem to impact IC anteroposterior orientation. However, it significantly influenced the IC latero-lateral deviation. Sternotomy presents a lower average deviation toward IVS and seems therefore more adapted than thoracotomy. This result can also be related to percentage of complication: 30.5% of patients had complications with a sternotomy against 62.5% of thoracotomy procedures. But not only parameters related to IC pose are taken into account in the choice of the surgical process. Thoracotomy feasibility varies according to the anatomy of the patient, and medically speaking, both procedures have their pros and cons.

Table 4-VIII - Postoperative φ and θ deviations for sternotomy and thoracotomy procedure

	Approach	Number of patients	Mean deviation (%)	Standard deviation (%)
φ	**Sternotomy**	13	9,9	10,6
	Thoracotomy	8	42,8	25,7
θ	**Sternotomy**	13	20,5	11,4
	Thoracotomy	8	26,4	16,1

To summarize, we introduced new quantitative indices to define the LVAD IC pose considering the 3D characteristics of the MV. Through retrospective analyses, we confirmed that an IC oriented toward the IVS may promote postoperative complications such as device malfunction or thrombus creation. In addition, we found when comparing results for each LVAD that smaller the device was, easier to implant it toward the MV it was. Finally, the surgical way of implantation may also present an impact on the device pose. Nonetheless, it is important to notice that the IC position is

not the only parameter considered for the device choice and clinical strategy. Clinical data, surgeons' habits or others potential sources of complication are also taken into consideration. For instance, geometrical constraints due to surrounding organs must be considered.

3. Geometrical constraints

During MCS device implantation, surgeons are confronted to the difficulty in positioning the device according to surrounding organs. If some organs may be constrained without provoking vital postoperative complications, others are considered as critical. Firstly, anatomical structures involved as well as the different parts of the devices that will be taken into consideration, are detailed. Then a retrospective analysis evaluating constraints over the cohort is presented.

3.1. Study assumptions

MCS devices are constituted of both rigid and soft elements. Outflow cannulae are disregarded because of their softness and adjustable length. On the contrary, TAH artificial chambers as well as LVADs pump body and IC are composed of rigid wall, making them unneglectable. For anatomical compatibility, these structures are considered as critical.

The primary constraint surgeons are faced to, is between the device itself and the chest wall. As mentioned Chapter 2, a thoracic compression may be painful for the patient and promotes device dislodgement. For TAH the entire chest wall may be conflictual (sternum in the front and even the thoracic vertebrae in the back). In the case of LVADs, only thoracic structures located in the ventral cavity side may be in contact with the device pump. However, for the computer-aided planning thoracic congestion study is not separated into two parts according to the type of MCS. Consequently, both front and back side are considered for all MCS devices. Due to their very low density and their softness, the intercostal muscles are neglected. Furthermore, as mentioned in chapter 3, we considered a region of interest for the rib cage, starting from the sternal angle of Louis to 7 cm below the apex (maximum length of a device).

Around the MCS device, many intrathoracic organs are present: lungs, diaphragm, aorta, atria and RV for LVADs. Compression of the MCS device on some of these organs may be a determinant of dysfunction of the device itself or of the compressed organs. First of all, lungs and diaphragm are disregarded due to their softness, as well as right and left atria because of their mobility and poor contractility. Notice that located at the apex, LVADs may not be in contact with the two upper chambers. In addition, the aorta is too distant from LVADs, and a TAH will be blocked by the rachis before being in conflict with the descending aorta. The RV is on the contrary a significant critical surrounding structure for LVADs. As mentioned previously, conflicts with it may lead to

right heart failure and necessitate subsequent surgical intervention. The LVAD IC may also collide with the IVS provoking thus suction events. Table 4-IX enunciates anatomical structures considered for each MCS type of device in anatomical compatibility investigation. In order to evaluate their relevance, we analysed the presence of these constraints through a retrospective analysis.

Table 4-IX - Critical anatomical structures considered for each MCS device

Device	Critical anatomical structures
TAH	Thoracic wall
LVAD	Thoracic wall Right ventricle Interventricular septum

3.2. Retrospective analysis

Regarding recommendations related to TAH, risks of thoracic compression on the device has clearly been identified. Therefore, LVADs alone were investigated and only thoracic and RV collision with the pump body were analysed. IC suction events were not considered. 34 patients from the same database as in section 2.3.1 were exploited. Collisions between LVADs and the chest wall or RV were visually determined based on CT scans. Figure 4.8 illustrates both collisions on two different postoperative scans while Figure 4.9 summarizes results through a graph. About 56% of the patients presented a thoracic constraint while 13% had a RV compression. Figures highlighted that these conflictual events regularly happen, making them unneglectable.

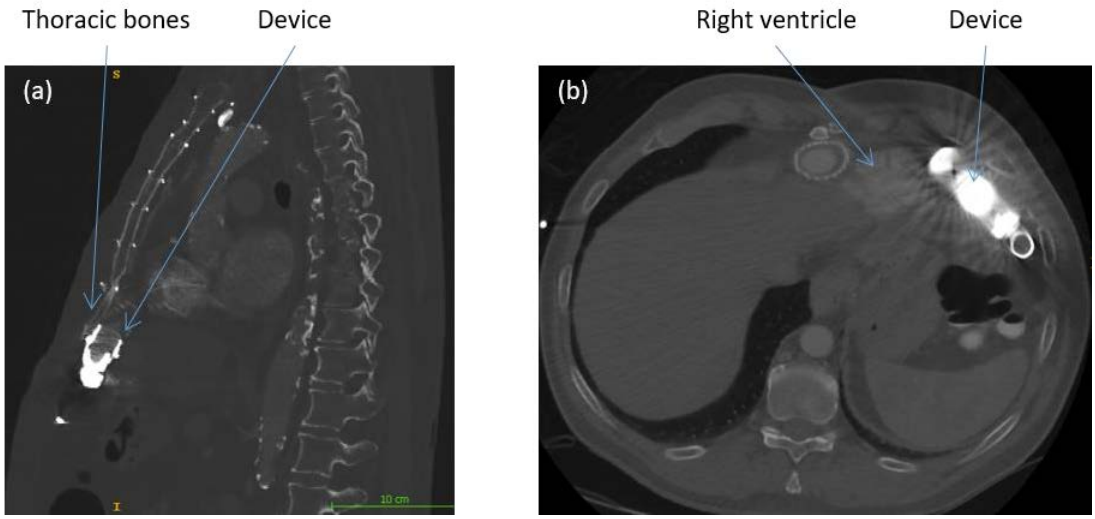

Figure 4.8 - Illustration from postoperative CT scans of collision between the device and the thoracic wall (a) or right ventricle (b)

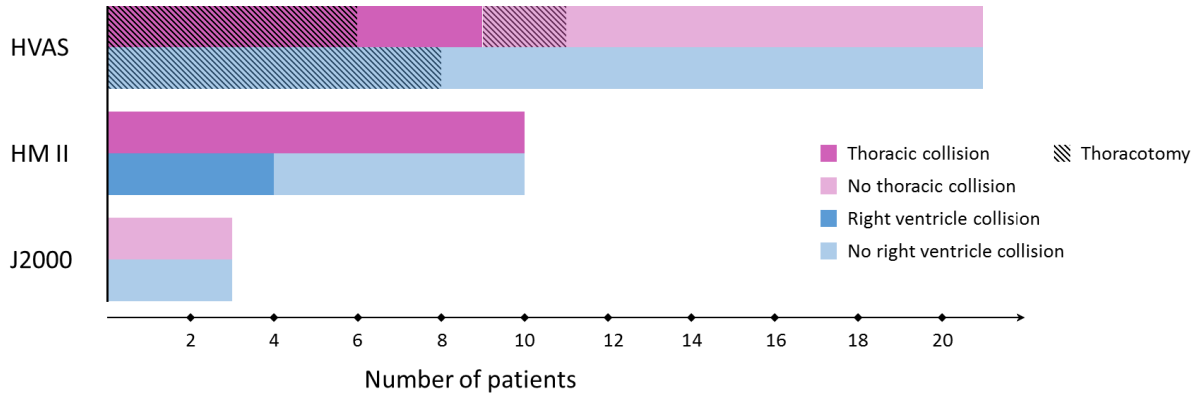

Figure 4.9 - Retrospective evaluation of collision between implanted LVAD and the thoracic wall or right ventricle

Comparing LVADs, the Jarvik 2000 presented no geometrical constraints with both anatomical structures. In the same way, there was no collision between the RV and HVAS device. This is probably related to device geometry. However 40% of patient with a HVAS had thoracic collision. In the case of HM II, 40% of the devices compressed the RV and all patients had thoracic collision. These figures can be related to the previous retrospective analyses. Results from section 2.3.2 demonstrated that though the IC was implanted intraoperatively with an orientation toward the MV, it was no longer coaxial to the MV normal after surgery, and more particularly for the HM II. External compression of the thorax on the device during chest closure may explain IC deviation. The HM II seems therefore to present more important geometrical constraints, confirming thus surgeons' feelings. Regarding the way of implantation for the 21 patients with HVAS, only 23% who underwent a sternotomy presented thoracic collision, against 75% of thoracotomies. Contrary to surgeons' thoughts, thoracotomy seems to promote thoracic collision more than sternotomy.
To conclude, this retrospective analysis confirms that the risks of MCS device compression on critical organs are high and may promote device dislodgment. In addition, IC pose has an impact on postoperative outcomes and IVS deviation promotes severe complications. In the following we present the computer-aided planning method for MCS device implantation.

4. Presentation of the planning solution

The main objective is to provide information to surgeons in order to help them to anticipate the device fit for a patient. In the current clinical workflow, patients are beforehand selected by surgeons, examining their clinical data and evaluating their morbidity bias. Then, the device and surgical strategy is defined. For the planning solution, two main issues are examined: the

intrathoracic space and the IC orientation in case of LVAD. With this solution, surgeons may preoperatively evaluate the IC pose according to the congestion. It consists in interactively positioning a 3D geometrical representation of the device within a virtual space composed from patient CT data. An analysis of collisions between the device and anatomical structures of interest are performed based on heart segmentation and dense structure analysis, while the LVAD IC pose with respect to the MV is characterized by quantitative criteria. Figure 4.10 provides an overview of the pose planning approach.

Firstly, the way that anatomical and device structures are represented is detailed. Then collision detection methods are described as well as the methods developed for IC orientation estimation. Finally, the environment used to develop the planning solution is presented.

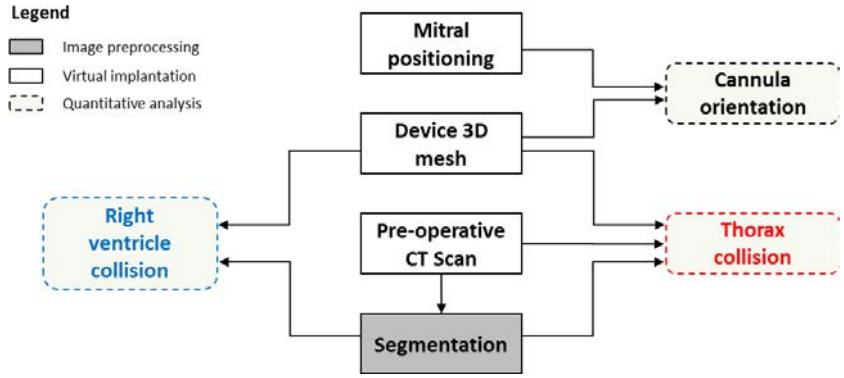

Figure 4.10 - Overview of the planning approach

4.1. Device and patients anatomy representation

A Cone Beam Computed Tomography (CBCT) acquisition is similar to CT but differs by its divergent X-rays forming a projection cone. It increases movement artefacts but also allows low X-ray dose that limits the metallic artefacts on medical images. This latter makes it interesting for device acquisition. In order to represent the MCS device by a 3D surface mesh, we used a 3D CBCT image and a semi-automatic segmentation (active contour method) with Itk-Snap[4]. MCS implants were finally composed of a multitude of points regularly distributed in space. Taking the example of the Jarvik 2000, Figure 4.11 represents the different steps for mesh creation. These 3D surface meshes are used in the pose planning for visualisation and quantitative criteria assessment.

[4] Yushkevich, P. a. et al., 2006. User-guided 3D active contour segmentation of anatomical structures: Significantly improved efficiency and reliability. NeuroImage, 31(3), pp.1116–1128.

Figure 4.11 - 3D mesh of the Jarvik 2000 created from a CBCT scan with an active contour method.

In the context of TAH, some simplifications have been made. Though independent, the two chambers of the Syncardia are finally combined during the surgical process with a Velcro system. Therefore, both artificial ventricles are considered as welded in this solution, as well as both native heart ventricles are. Notice that this separation was principally made to facilitate intraoperative sews and placement within the cavity. For LVADs, the HM II IC flexible part must not be twisted or excessively angled according to recommendations. Thus, this angulation is not authorised in the pose planning solution ($\alpha=0$). In addition, during collision detection process, LVAD IC and pump body are analysed separately in order to dissociate the type of collision (IVS, RV or chest wall). P_C and P_P define in the following all the points associated to the IC and the pump body respectively.
One critical issue concerning clinical computer-aided system concerns description of relevant anatomical structures. While numerous methods have been developed in the literature, there are still challenging issues. Besides, segmentation takes time and deletes information provided by image data. According to the number of anatomical structures and reasons mentioned previously, the planning solution was designed in order to limit the number of segmented structures. For representation of the patient anatomy, 3D slice views (coronal, transversal and sagittal planes) of the CT scans was provided, as well as a 3D representation of the heart cavities. In addition, the MV and tricuspid valve were represented by ellipses.

4.2. Collision detection methods and IC positioning

Three anatomical structures are considered as critical in the context of intrathoracic space. For all MCS devices, the thoracic wall is conflictual, but the RV and IVS only concern LVAD devices. In the following, collision detection methods based on heart segmentation and grey-level analyses are explained, as well as methods used to evaluate LVAD IC pose.

4.2.1. Right ventricle and inter-ventricular septum constraint for LVAD

For RV and IVS conflicts, the method is based on heart structures segmentation. We used the multi-atlas method from (Kirisli et al. 2010) that provides each heart cavities: RV, LV, left atrium, right atrium, as well as the left myocardium region. Regions representing the RV and the left myocardium are respectively denoted as R_{RV} and R_{LMy}. To analyse RV collisions with the LVAD, the detection process evaluates for each mesh node (P_p^i) of the pump body, whether it superimposes the RV. Points in collision with this cavity (P_{RV}) are defined by (1). In the same way, points of the IC in contact with the IVS (P_{IVS}) are obtained by (2), where (P_c^i) represents the i^{th} node of the IC mesh.

$$P_{RV} = \{P_p^i \in R_{RV}\} \quad (1)$$

$$P_{IVS} = \{P_c^i \in R_{LMy}\} \quad (2)$$

4.2.2. Thoracic constraint for MCS device

Numerous methods exist for thoracic skeleton segmentation, but as demonstrated in Chapter 3 there are still too many challenging issues. The approach developed for thoracic conflicts with MCS implants (LVAD and TAH) is therefore based on grey-level analysis and similar to RV and IVS conflicts detection. A threshold value was defined considering not only high- but also low-bone density (costal cartilages). Represented on the CT by voxel values > +200 HU, these elements present the same values as injected cavities. Therefore, points of the LVAD superimposed over bones (P_{bones}) are defined by (3), where (P_p^i) represents the i^{th} node of the pump body mesh, V_{Bth} represents voxels with a CT value >+200 HU, and R_{wh} the region of the whole heart, composed of the RV, LV, right atrium, left atrium, and left myocardium:

$$P_{bones} = \{P_p^i \in V_{Bth} \cap P_p^i \notin R_{wh}\} \quad (3)$$

4.2.3. Information about IC positioning for LVAD

A method evaluating the IC positioning has already been presented for retrospective analyses in section 2.2. The approach consists in simplifying the MV geometry as an ellipse Ω_{MV} with an associated coordinate system defined by the anterior commissure point (P_{com}). A vector is associated to the IC cylinder, and finally, φ and θ angles as well as the distance $D_{(P,O)}$ are calculated. In the planning solution, same methods are used but the MV plane definition varies. Not based on points selected by an expert, the approach uses heart segmentation to characterize Ω_{MV}. Ω_{MV} is defined in the mean plane approximating 3D points from the contact surface between the LV and left atrium regions. In the same way, the tricuspid valve is evaluated with the RV and right atrium regions.

To summarise, Figure 4.12 illustrates data and methods used for the proposed computer-aided pose planning solution. Heart segmentation and grey-level analysis for detection of surrounding anatomical constraints, as well as definition of quantitative criteria to characterize the device pose are the principal elements of this approach.

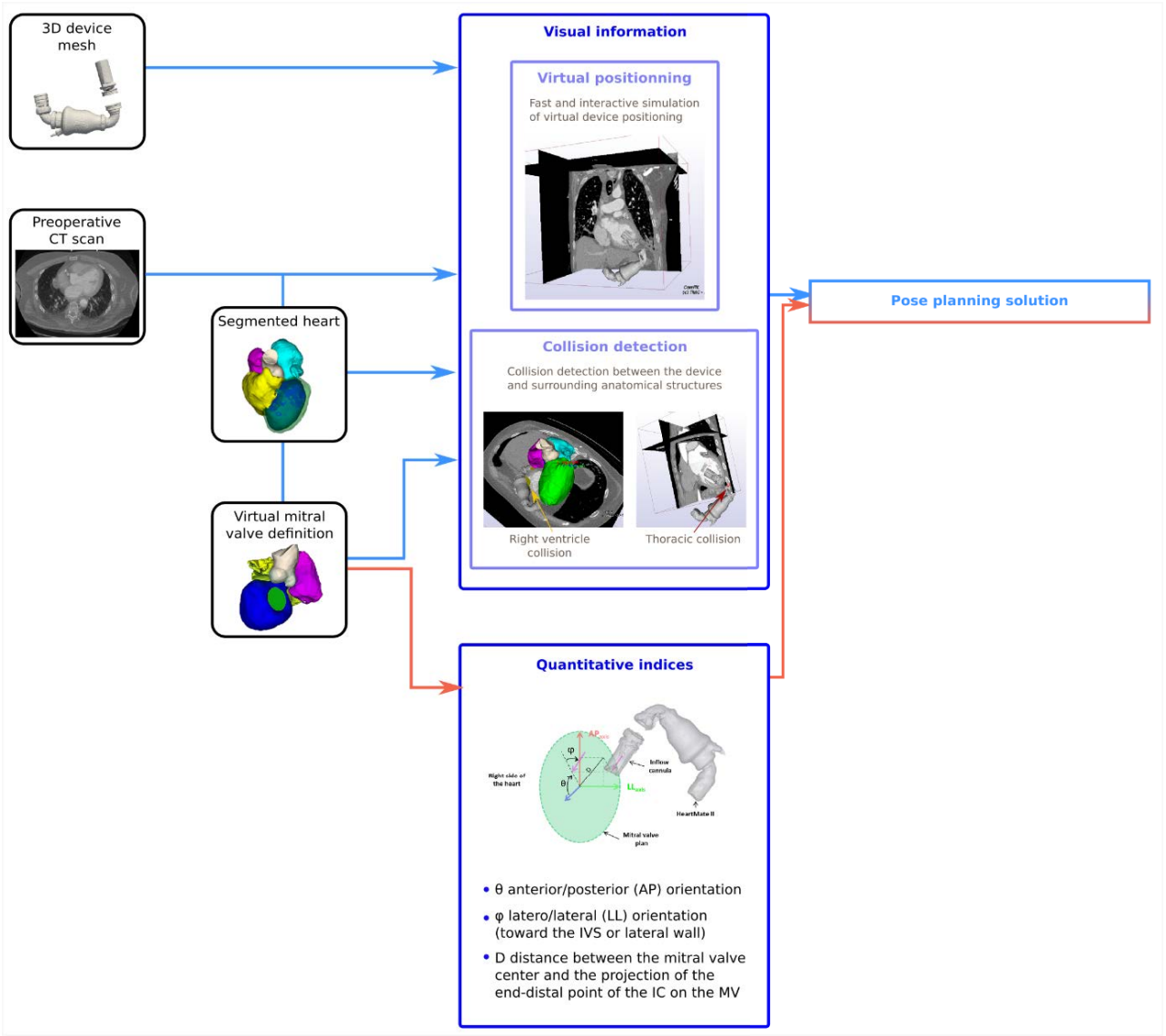

Figure 4.12 - Overview of the pose planning method

4.3. Implementation

CamiTK software (Computer Assisted Medical Intervention Toolkit, Grenoble, France) is an open-source modular cross-platform framework (Windows and Linux are supported) that was developed at TIMC-IMAG laboratory (http://www-timc.imag.fr/) (Fouard et al. 2012). Written in C++, it can handle medical images, surgical navigations and biomechanical simulations. This toolkit allows displaying and manipulating imaging data (MRI, CT scan, etc…) as well as meshes for reconstruction and simulation model.

Specially designed for researchers and clinicians use, CamiTK offers an interactive user interface based on VTK (Schroeder et al. 2006) and Qt (Qt n.d.). It provides support for easily managing different data formats, encapsulating existing libraries or new image processing algorithms (Figure 4.13). In this context we developed a collaborating module that were integrated into CamiTK.

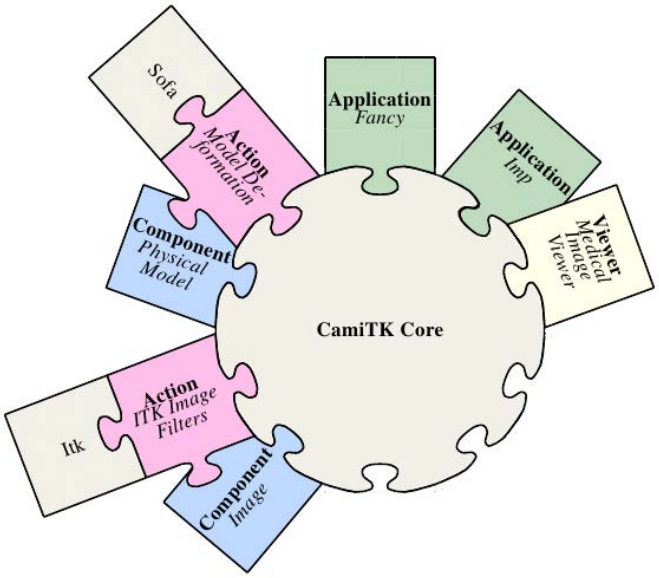

Figure 4.13 - CamiTK architecture with several collaborating modules
Source: http://camitk.imag.fr

This developed module integrates within the 3D slice view the 3D heart structures and allows the practitioner to navigate through the patient's preoperative CT scan (Figure 4.14). In addition, the MV and tricuspid valve are automatically positioned based on heart segmentation. This technique presenting issues related to the performance of segmentation, virtual valves description can interactively be readapted with an additional user interface created with Qt. 3D rigid linear transformations were implemented with VTK library. Orientation of the coordinate systems associated to the valves can also be controlled by the user. In order to facilitate the LVAD

positioning, a target area for IC implantation has also been created by projecting the MV on the left myocardium (Figure 4.15).

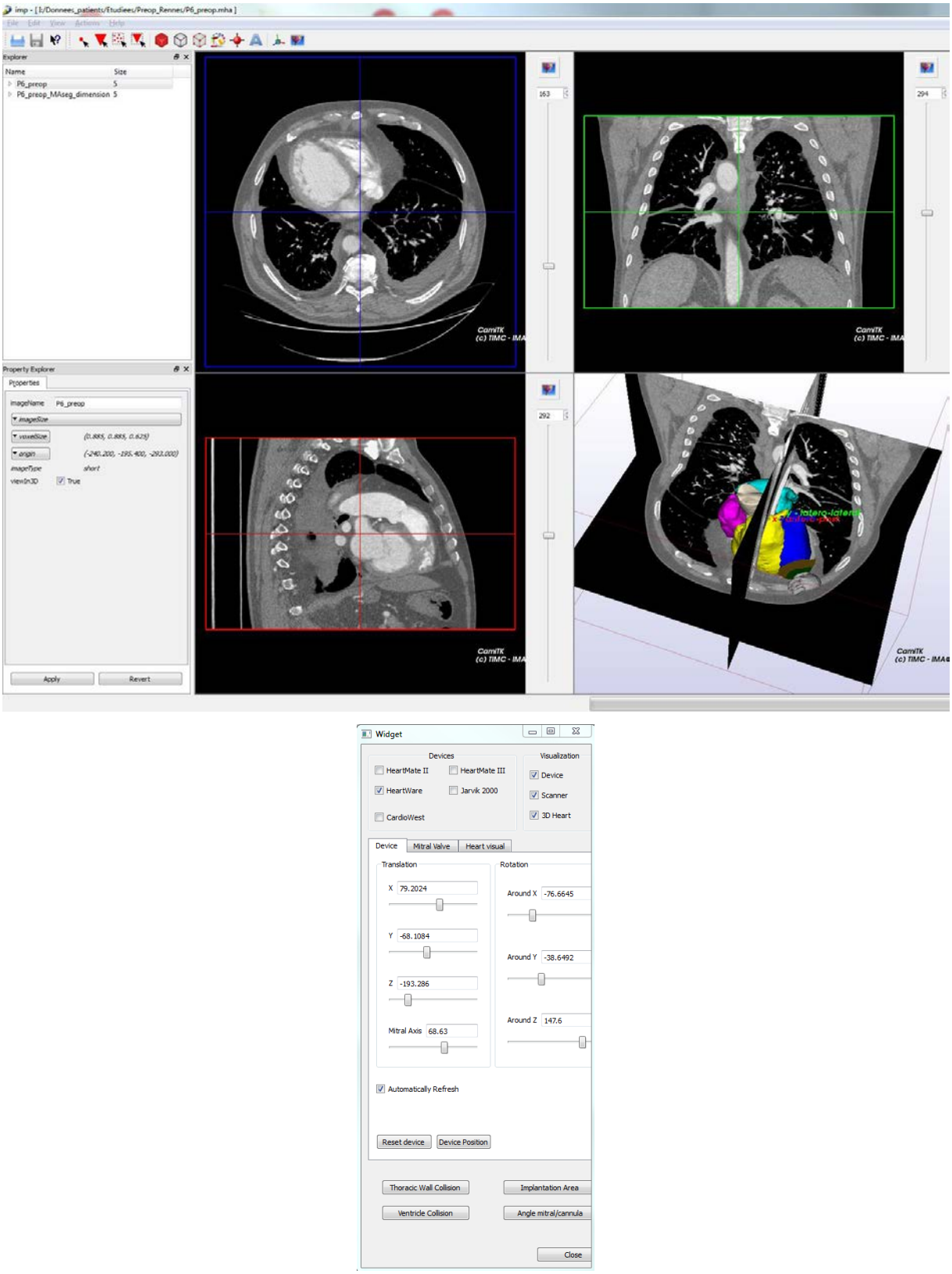

Figure 4.14 - Screenshot of the user interface

Figure 4.15 - Representation of the area of LVAD implantation

This developed interface also allows the health professional to choose a MCS implant that is represented in 3D and integrated within the 3D view. An automatic MCS device intrathoracic configuration is also calculated using valves information and heart segmentation. The LVAD is positioned at the apex, coaxial to the normal MV, and with the projection of $\mathbf{C_{IC}}$ (centre of the IC distal end) on the MV equal to O_{MV} (centre of the MV). In the same way, TAH is positioned so that artificial mitral and tricuspid valves are centred with virtual ones. In this automatic approach, no surrounding organs constraints are taken into consideration. Parts of the device superimposed with the RV, IVS or thorax are highlighted in different colours (Figure 4.16), allowing thus the practitioner to readapt the MCS device position avoiding collisions. In addition, information about IC pose are provided by the system (Figure 4.17).

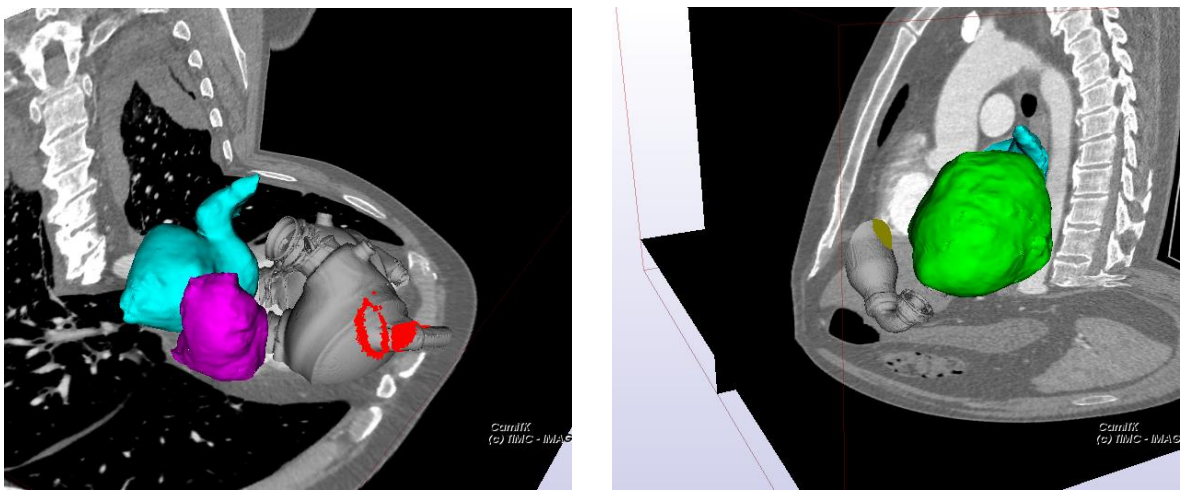

Figure 4.16 - Illustration of thoracic and right ventricular collision with respectively the Syncardia and Heartmate II device

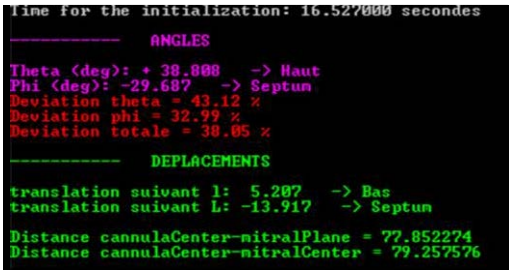

Figure 4.17 - LVAD IC orientation and position information

Computer-aided planning of device implantation based on heart segmentation and collision detection could impact surgeon's clinical strategy by anticipating the device pose according to patient anatomy. This solution could prove useful for patients with congenital heart disease where the heart exhibits structural abnormalities.

5. Potential and discussion

To analyse the potential of the proposed solution, we first investigated the feasibility of finding a better preoperative pose by comparing LVAD virtual position to postoperative orientations. Next section presents the approach used and results obtained. Then, the method based on heart segmentation to define the MV plane is evaluated comparing it with points selected by an expert. Finally, several limitations related to this solution are discussed.

5.1. Postoperative and planning comparison

The main objective of this experiment is to evaluate the potential of a general MCS device pose planning. For that, a comparison between a virtual pose and postoperative LVADs orientation that were positioned without the solution was made. Figure 4.18 illustrates the workflow of this experiment.

Among the datasets, only patients who underwent a preoperative and a postoperative contrast-enhanced CT scan with sufficient visibility were retained. 8 patients with a HM II were thus selected. A surgeon determined, by means of the computer-aided system, a virtual device implantation corresponding to clinical recommendations. Both geometrical constraints and IC positioning were considered. The MV geometry was configured with the same approach as retrospective studies (selection of points by experts) and six parameters were considered to compare the two poses: the angulation α, the chest wall and RV collision, as well as the indices representing the IC orientation and position (φ, θ, $D_{(P,O)}$). No RV and thoracic collisions are present for virtual poses and α obtained with the planning solution must be equal to zero, due to the system

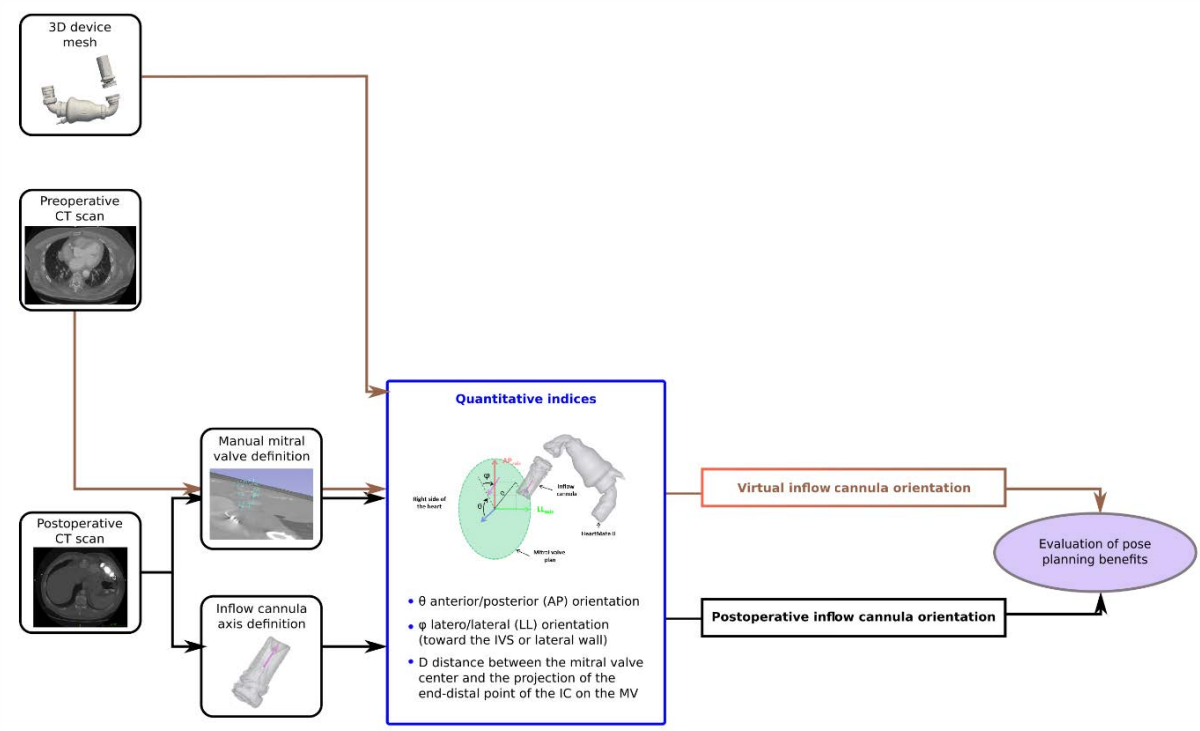

Figure 4.18 - Workflow for the evaluation of pose planning benefits

restrictions. For each patient, deviations Δ between virtual and postoperative indices were calculated as follows:

$$\Delta_{\varphi} = |\varphi_{planned}| - |\varphi_{postop}| \quad (4)$$

$$\Delta_{\vartheta} = |\vartheta_{planned}| - |\vartheta_{postop}| \quad (5)$$

$$\Delta_{D} = D_{(P,O)planned} - D_{(P,O)postop} \quad (6)$$

with $\varphi_{planned}$, $\theta_{planned}$, and $D_{(P,O)planned}$, the preoperative angles φ, θ, and the distance $D_{(P,O)}$ obtained with the virtual solution. φ_{postop}, θ_{postop}, and $D_{(P,O)postop}$ are the angles and distance obtained in the retrospective analysis (section 2.3 and 3.2). According to these expressions, if Δ <0, the planned index is better than the postoperative one. On the contrary, if Δ >0, the postoperative one is better than the planned index. Table 4-X presents results obtained for each patient.

The angle $\alpha_{planned}$ was necessarily better than or equal to the postoperative one for all patients. Similarly, all chest-wall collisions were removed in the virtual pose, and for the two patients presenting a RV compression (P#4 and P#17), it was averted. These results firstly demonstrated that it was possible to find a virtual positioning without curvature of the inflow graft tube or conflict with critical structures for all patients. In addition, in 62.5% of cases, there was improvement in the three quantitative parameters. For the other 37.5%, several parameters were improved to the detriment of other ones. Indeed, the angle θ was deteriorated for patients P#4 and P#17, in favour

of the two other indices. In the same way, the IC orientation was improved for P#5, to the detriment of the position. But for all, the improvements were greater than the deteriorations.

To summarise, in 100% of cases, planned latero-lateral orientations were better than postoperative ones (Δ_φ <0), as well as 75% of the anteroposterior orientations (Δ_θ <0). Similarly, 87.5% of patients presented lower $D_{(P,O)planned}$ values than $D_{(P,O)postop}$. This experiment highlighted the feasibility of preoperatively finding a better device position and IC orientation using preoperative virtual planning.

Table 4-X - Preoperative planned position without collision compared to postoperative ones

Patients	|Planned| - |postoperative| position	
	Δ_φ , Δ_θ [degree]	Δ_D [mm]
P3	Δ_θ = -16 Δ_φ = -4	Δ_D = -10.0
P4	Δ_θ = +1 Δ_φ = -77	Δ_D = -4.3
P5	Δ_θ = -18 Δ_φ = -9	Δ_D = +2.8
P9	Δ_θ = -13 Δ_φ = 0	Δ_D = -29.4

Patients	|Planned| - |postoperative| position	
	Δ_φ , Δ_θ [degree]	Δ_D [mm]
P10	Δ_θ = -25 Δ_φ = -28	Δ_D = -0.3
P13	Δ_θ = -59 Δ_φ = -16	Δ_D = -6.2
P16	Δ_θ = -25 Δ_φ = 0	Δ_D = -18.8
P17	Δ_θ = +18 Δ_φ = -24	Δ_D = -25.9

5.2. Evaluation of the semi-automatic MV definition

In the previous section, the MV was defined manually by points selected on the MV annulus ring. But in the planning solution, it is considered to automatically define the MV plane based on the heart segmentation. We evaluated thus the efficiency of this automatic method, comparing the automatic MV plane with the one defined manually. Figure 4.19 presents data and methods used for this evaluation.

Among the dataset composed of preoperative CTs, two patients with a Jarvik 2000 and two others with a HVAS were randomly selected. In addition, seven patients from the previous study were retained for this experiment. P3 was removed due to an overestimation of the left atrium region impacting the LV segmentation.

To compare the two MV planes obtained for each of the 11 patients, we evaluated the angle between their normal axes. Results are presented in Figure 4.20. A mean angle of 5.9° and a median of 5.6° were obtained, representing a difference from the maximal deviation (90°) of 6.5% and 6.2% respectively. Regarding each patient independently, only one obtained a variation superior to 10%. Considering the important IC deviations observed for patients presenting complications in

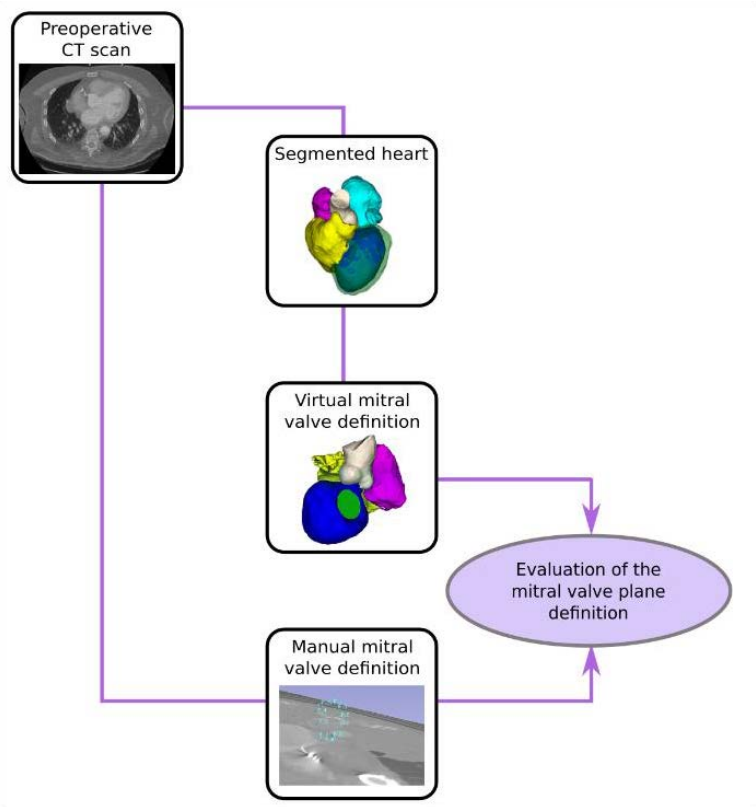

Figure 4.19 - Workflow for the evaluation of the automatic mitral valve plane definition within the pose planning solution

previous retrospective analyses, this variation seems negligible. It can therefore be concluded that the method used to define automatically the MV plane is quite valuable, although dependent on segmentation results. In the event of error, the user can readapt interactively the valve position in the planning solution.

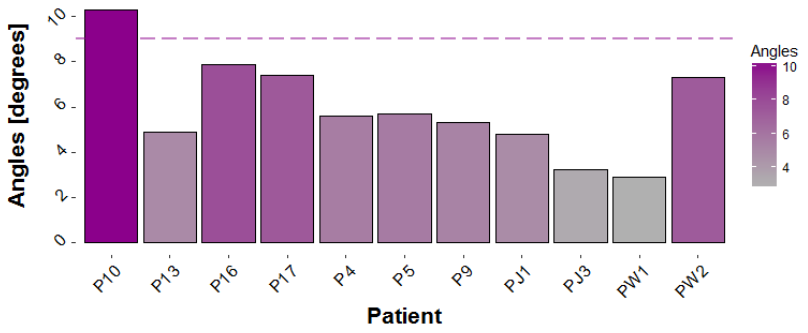

Figure 4.20 - Angles between the mitral valve plane defined by the heart segmentation and selected points

5.3. Discussion

Nowadays, there is no computer-aided solutions developed with the aim at preoperatively analysing MCS device pose. The proposed solution gives visual and quantitative indices related to the pose. An overview of studies and methods presented in this chapter are illustrated in Figure 4.21. The primary interest of this solution is the additional morphological criteria provided to surgeons for the selection of the device. However, in this stage of the research, several issues still remain.

Our planning method is based on a multi-atlas cardiac segmentation (Kirisli et al. 2010). We evaluated the segmentation approach in the chapter 3 and demonstrated that metal artefacts due to intra-cardiac devices render heart segmentation more difficult on CT imaging. To solve this issue, improvements could be made by introducing image pre-processing. Additionally, some patients eligible for LVAD implantation are contraindicated for contrast substance. An alternative method should be investigated for these patients (Shahzad et al. 2017).

An automatic device pose is provided in the planning solution, taking into account valves information but not surrounding organs conflicts. The best device pose is then determined interactively by the user. An automatic positioning method considering all mentioned parameters could be investigated.

Quantitative and visual criteria are based on clinical recommendations and results from retrospective analyses. But one patient from our dataset exhibited device dislodgement without thorax compression. This suggests that other factors may impact device position and orientation. More detailed investigations are thus necessary to further analyse factors of dislodgment, define additional objective criteria and help specify them. The importance of the different indices impact on postoperative complications must also be determined.

We also evaluated the potential benefits of a pose planning in the context of MCS device implantation, comparing a virtual preoperative pose to postoperative results. However, the significance of improvement needs to be investigated. In addition, a fundamental question still remains about how to implement the planned pose into the operating room. The use of anatomical landmarks such as coronary arteries could be envisaged. But it remains a challenging issue.

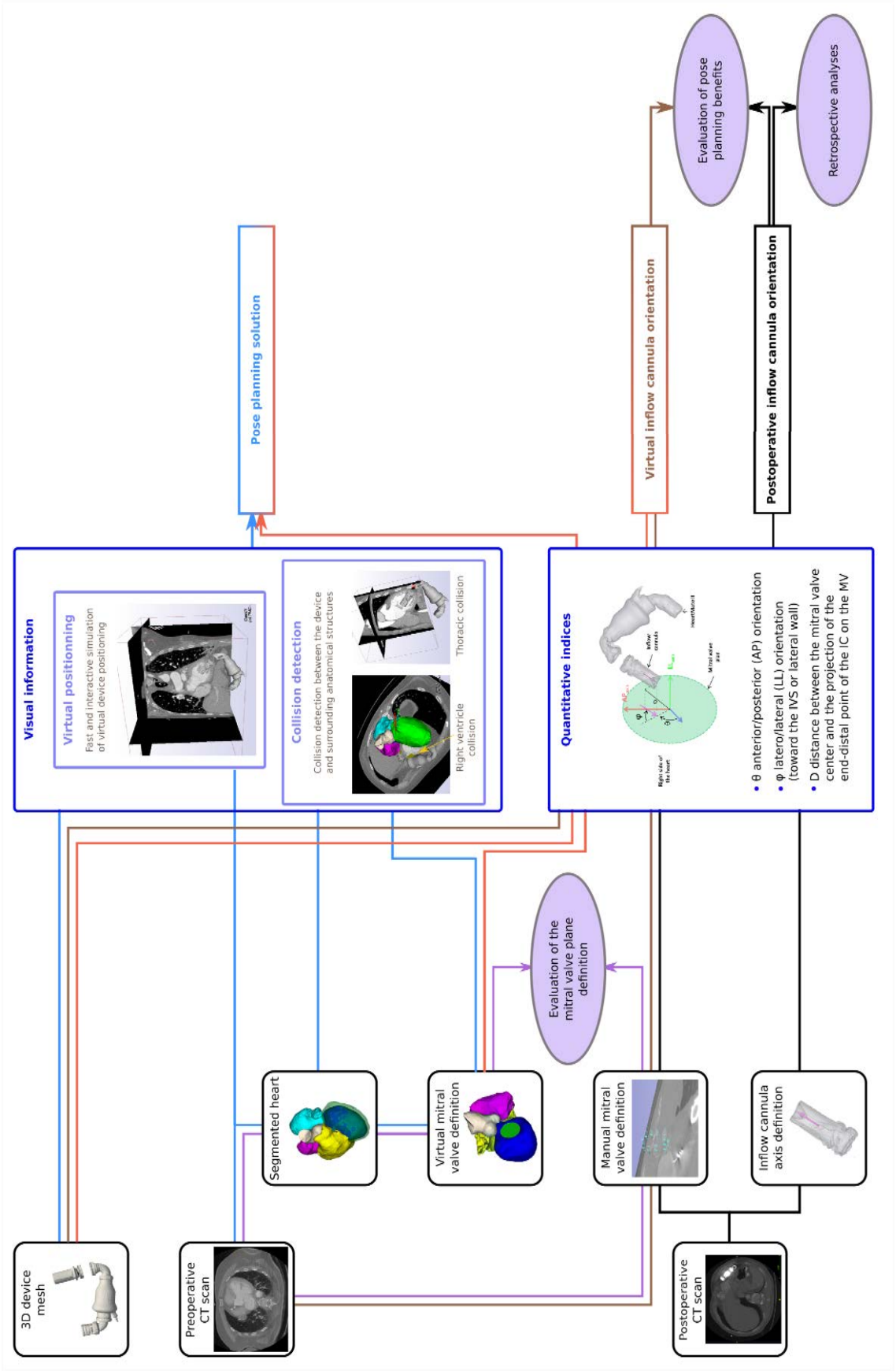

Figure 4.21 - Workflow of methods and studies presented in this chapter

In the proposed solution, quite a few approximations were made about anatomical structures configuration. Using preoperative CT scan, the solution analyses the device positioning considering a static geometry of the patient anatomy. Only the maximal thoracic volume is considered with the deep-inspiration breath-hold recommendation for CT scan protocol. In the same way, depletion of heart cavities after starting the MCS is not considered. This decrease of volume may generate more intrathoracic space for MCS device implantation but it can be supposed that this increase of space is compensated by the reduction of the thoracic volume related to breathing expiration. However, the left ventricular volume reduction seems more critical for the IC implantation configuration analysis, involving less intra-cavity space. In addition, valves modifications such as size and orientation are not taken into account. Anatomical valves variations should be investigated to determine if they can be neglected. Finally, cardiac motion itself may affect the device position. This limitation could be solved by using a preoperative multi-phase CT or combining CT with echocardiography in order to consider heart motion over time.

To summarize, health professionals currently select the appropriate device only based on maximal flow rate delivered by the device, clinical data, and mainly surgical experiences. Preoperative anatomical constraints are not investigated in the case of LVADs and analyses are limited for TAH. As things currently stand, the proposed computer-aided approach could be used to give additional preoperative information to surgeons for MCS device selection. Determining the most appropriate MCS according to the patient anatomical configuration could limit intraoperative and postoperative complications. However, many issues and unknowns still remain. In the next chapter we further investigate IC pose issues exploiting computational fluid dynamics simulations.

References

Collin, S. et al., 2015. Virtual positioning of ventricular assist device for implantation planning. *Irbm*, 1(6), pp.5–11.

Fouard, C. et al., 2012. CamiTK: A Modular Framework Integrating Visualization, Image Processing and Biomechanical Modeling. In *Soft Tissue Biomechanical Modeling for Computer Assisted Surgery*. pp. 323–354.

Han, J.J. et al., 2015. HeartMate II Left Ventricular Assist Device Geometry on Chest Radiograph Does Not Correlate with Risk of Pump Thrombosis. *ASAIO Journal*, p.1.

Imamura, T. et al., 2017. *Cannula and Pump Positions are Associated with Left Ventricular Unloading and Clinical Outcome in Patients with HeartWare Left Ventricular Assist Device*, Elsevier Inc.

John, R. et al., 2011. Lessons Learned From Experience With Over 100 Consecutive HeartMate II Left Ventricular Assist Devices. *The Annals of Thoracic Surgery*, 92(5), pp.1593–1600.

Kazui, T. et al., 2016. Left Ventricular Assist Device Inflow Angle and Pump Positional Change Over Time Adverse Impact on Left Ventricular Assist Device Function. *Annals of Thoracic Surgery*, 102(6), pp.1933–1940.

Kazui, T. et al., 2015. Left Ventricular Assist Device Inflow Cannula Mitral Alignment and Pump Migration Impact LVAD Dysfunction Over Long Term Support. *Circulation*, Core 5: My(Session Title: LVAD Thrombosis), pp.2014–2015.

Kirisli, H.A. et al., 2010. Evaluation of a multi-atlas based method for segmentation of cardiac CTA data: a large-scale, multicenter, and multivendor study. *Medical physics*, 37(12), pp.6279–6291.

Popov, A.F. et al., 2012. Clinical experience with heartware left ventricular assist device in patients with end-stage heart failure. *Annals of Thoracic Surgery*, 93(3), pp.810–815.

Qt, Qt: Cross-platform software development. Available at: https://www.qt.io/.

Schroeder, W., Martin, K. & Lorensen, B., 2006. *The VTK: an object-oriented approach to 3D graphics*,

Shahzad, R. et al., 2017. Automatic segmentation and quantification of the cardiac structures from non-contrast- enhanced cardiac CT scans. *Physics in Medicine and Biology*, 62(9), pp.0–15.

Taghavi, S. et al., 2013. Surgical technique influences HeartMate II left ventricular assist device thrombosis. *The Annals of thoracic surgery*, 96(4), pp.1259–65.

Truong, T. V. et al., 2013. Postimplant Left Ventricular Assist Device Fit Analysis Using Three-Dimensional Reconstruction. *ASAIO Journal*, pp.586–592.

Chapter 5 - Biomechanical approach

In LVAD therapy, a large number of questions related to optimisation of hemodynamic still subsist. Retrospective analyses from chapter 3 demonstrated that an Inflow Cannula (IC) deviation toward the Inter-Ventricular Septum (IVS) may promote postoperative complications such as thromboses production or suction events. In addition, clinical guidelines recommend orienting the LVAD IC toward the Mitral Valve (MV). However, no more precise metrics are provided. Understanding of velocity fields in time, wall-shear stress distribution, stagnation zones location and blood damage occurrence such as haemolysis, are fundamental to reduce the clinical complications (Zuin et al. 2016).

Computational modelling presents a powerful non-invasive modality to describe hemodynamic. With Computational Fluid Dynamic (CFD) simulations, unmeasurable clinical haemodynamic parameters can be computed with the potential of enhancing diagnostic assessment, device design and clinical trials. In the literature, major applications focused on the aortic blood flow distribution induced by LVAD outflow (J. F. Fraser, Gregory, and Stevens 2017). If CFD is a relatively mature field for larger vascular vessels such as the aorta (Mittal et al. 2015), modelling heart cavities hemodynamic presents numerous challenges due to the complexity of human body fluid behaviour. Only few works have investigated blood flow in a LV under LVAD support. This chapter aims at elaborating CFD simulations in order to investigate the influence of the IC orientation on thrombus creation to finally determine more precise recommendations that could in the long-term be integrated in a computer-aided planning.

First section analyses models and post-processing approaches used in the literature. Then, the approach for our CFD models creation is presented. In the third section, the influence of the simulation time and CFD model as well as the relevance of some post-processing approaches are evaluated analysing the LV hemodynamic involved by an IC oriented toward the MV. Hemodynamics involved by an IC toward the septum is investigated in the fourth section, and finally results are discussed.

1. CFD simulations assessing hemodynamic issues related to LVAD IC: a state of the art

CFD aims at solving the Navier-Stokes equations which describe the motion of viscous fluid. In medical context, elaboration and analyses of a CFD model can be described by 5 main stages: geometry creation, parametrization, calculation process, post-processing and validations. The

geometry can be created from a general model or based on clinical images using segmentation methods and reconstruction. **Parametrization** corresponds to both problem (model, materials and boundary conditions) and solver setting definition. These two first stages characterise the elaboration of the simulation. Then, the differential equations describing the flow are solved over all elements and at all time-steps during the **calculation process**. Analyses are finally performed through post-processing and validation of the model. **Post-processing** allows visualizing and extracting relevant data, while **validations** corroborate the model definition and results obtained.
Computational modelling is an emerging field in cardiovascular medicine. Despite it has made great progress in recent years, it is currently impossible to discretise the entire cardiovascular system (Morris et al. 2016). The heart is a complex model that must be simplified for CFD simulation and many assumptions have to be made. Indeed, a complete modelling of the problem will require very high computational time. Besides, complex pathologies are involved and modelling necessitates detailed knowledge of physiological metrics that may be inaccessible, difficult to obtain or risky for the patient. Defining the boundary conditions remains one of the most significant challenges. This section presents a state of the art of CFD simulations assessing the left ventricular hemodynamic through LVAD assistance. Models are investigated by first detailing the CFD modelling approaches and then presenting the post-processing and validation process used.

1.1. CFD simulations elaborations (geometry and parametrization)

To the best of our knowledge, nine works assessing the hemodynamic issues related to LVAD IC have been reported over the last years. Table 5-I presents these articles providing their subject of study and the geometric models considered. These articles present a considerable variability in CFD modelling. A brief overview of geometries and parametrization is provided herein.

1.1.1. Geometry

The first step for the elaboration of CFD simulation corresponds to an adequate representation of the anatomical structure. If (Tsukiya et al. 2011) did not consider ventricular wall in their simulations, (Jhun, Sun, and Cysyk 2014), (Liu et al. 2012) and (C Ong et al. 2012; ChiWei Ong et al. 2013) decided to simplify the LV by an ellipsoid. However, because of the high individual variability in both the anatomy and the response to LVAD treatment, it is crucial to consider a patient-specific approach (de Vecchi et al. 2016). Only three articles presented a 3D LV geometry created from medical images. (K. H. Fraser et al. 2011) and (M. McCormick et al. 2013; Matthew McCormick et al. 2009) segmented the LV cavity on an MRI from a healthy patient, while (Prisco et al. 2017) used a preoperative CT from a patient with a LVAD implanted.

Table 5-I - State of the art of CFD simulation assessing the blood flow of the left ventricle with an inflow cannula

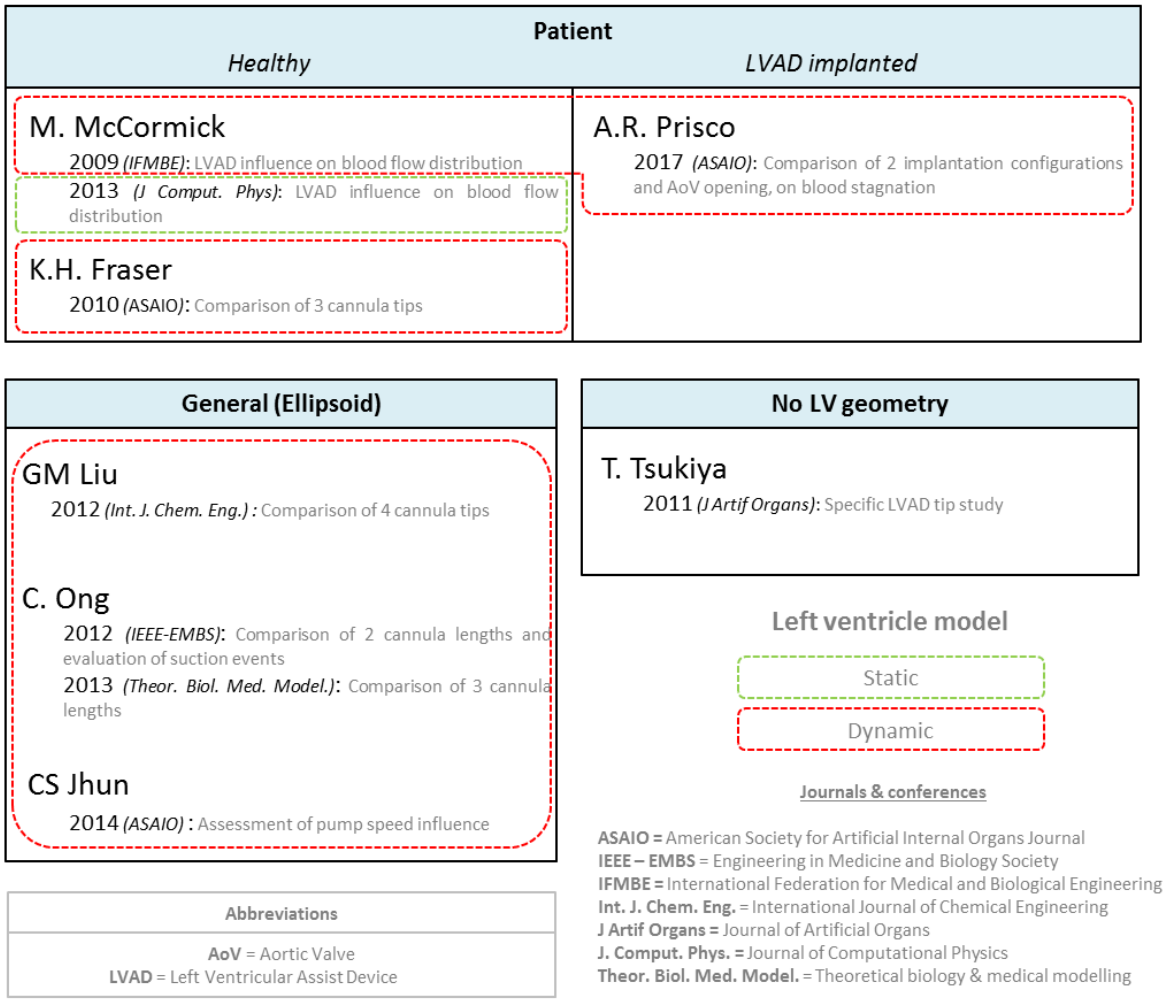

In cardiovascular, CFD modelling of dynamic heart cavities may present a real challenge because of the complex deformations during a cardiac cycle. But patients with a congestive heart failure present a small LV volume variation. Thus, major articles simplified the model considering a static geometry. However, (M. McCormick et al. 2013) simulated heart beats by defining the LV volume variation with a pressure volume relationship.

1.1.2. Models

In CFD, two main categories of flow can be distinguished: laminar and turbulent (Figure 5.1). A laminar flow is characterized by parallel paths which never interfere with one another, and the velocity at each point in the fluid is constant. Streamlines are smooth and motion of the particles is highly ordered. On the contrary, turbulent flows are highly stochastic with changes of pressure and velocity unpredictable in detail. In the literature presented above, four articles have neglected turbulences considering a laminar flow, while two used turbulent models. Blood flows

Laminar flow Turbulent flow

Figure 5.1 - Representation of a laminar and turbulent flow

encountered in human body are laminar, transitional or weakly turbulent regimes and by essence unsteady. Considering the size of the heart, the laminar hypothesis can be used as first assumption but might give very inaccurate results if one wants to assess transports and shear stress at the walls (Townsed 1976).

Turbulence models were developed for industrial usages. Most of them are made for steady fully developed turbulent flows. Three models are commonly used: standard k-epsilon (k-ε), k-omega (k-ω) and SST k-ω (Shear Stress Transport). They all are based on two partial differential transport equations for two variables: the turbulence kinetic energy and the turbulent dissipation. Standard k-ε model has been used by (Liu et al. 2012) while (Tsukiya et al. 2011) exploited the SST k-ω model. Standard k-ε gives a general description of turbulence in highly turbulent free shear flow while standard k-ω is applicable to wall-bounded flow. SST k-ω combines k-ω model near boundaries with k-ε for inner flow regions (Menter 1994). These approaches were developed for highly turbulent flows and an ad-hoc equilibrium between kinetic energy and its dissipation is incorporated which makes those approaches not compatible with a precise description of transitional flows and unsteady flows (Menter and Egorov 2010). To correctly describe the unsteady flow in the heart, a Scale Resolving Approaches should be considered like dynamic LES (Large Eddy Simulation) (Lilly 1992). This approach is not based on Averaged Navier-Stokes equation but on Filtered Navier-Stokes equations. The Filter is basically the size of the mesh and only the turbulent transport at a scale smaller than the mesh size is modelled. This approach enables a more precise description of the turbulent mixing process as all the large structures bringing energy to the turbulent process are resolved. The large turbulent structures are linked with the geometry structure and size and are responsible of the lack of generality of models like k-ε or k-ω where turbulent transport due to those structures is modelled. k-ε or k-ω model are fitted to aerospace experiments like free jets or wings boundary layers. That is the reason why their performance is lower on human body geometries and hemodynamics. As opposed to those model, LES are particularly suited to those complex geometries especially dynamic LES (Lilly 1992) which contains by essence no fitted constant. Moreover dynamic LES enables the description of laminar to transient flows which often occur in blood circulation. This description is much more precise than

the by-pass transition included in k-ω model which represents only turbulent to laminar transition from a completely turbulent flow.

1.1.3. Materials and boundary conditions

In cardiovascular CFD simulations, blood rheology has been defined as Newtonian or non-Newtonian fluid. Newtonian fluids consider the viscosity as constant while for a non-Newtonian fluid, viscosity varies according to shear rate. Blood is in majority composed of plasma which is a Newtonian liquid. But the presence of red blood cells and platelets make blood from a rheological point of view a shear-thinning fluid (non-Newtonian). Most of the time, blood is approximated as Newtonian based on the assumption that in large arteries the shear rate is large enough for the viscosity to be treated as effectively constant. Among the nine articles, only two studies characterized blood as non-Newtonian (C Ong et al. 2012; ChiWei Ong et al. 2013).

To define the physical conditions, patient-specific data, population data, physical models or assumptions may be exploited (Morris et al. 2016). Table 5-II enunciates characterizations of boundaries conditions used in the literature. The LV geometry was mostly defined without aortic valve, except (Jhun, Sun, and Cysyk 2014) who considered this valve as opened and (Prisco et al. 2017) closed or intermittently opened. In the same way, the IC outlet was in majority characterized by a constant outflow, except (C Ong et al. 2012) that used a linear increasing function. The MV was on the contrary represented by various models: a constant inflow (Liu et al. 2012), a sinusoid function (Matthew McCormick et al. 2009), inflow waveform from in-vivo measurements (Prisco et al. 2017) or even 0D model (M. McCormick et al. 2013). About half of these works considered

Table 5-II - Boundary conditions in the context of LVAD inflow cannula

	Aortic valve	Mitral valve inlet / Cannula outlet	Myocardium	Blood rheology
(Matthew McCormick et al. 2009)	None	Sinusoid inflow with Constant outflow	Incompressible Elastic	Newtonian
(K. H. Fraser et al. 2011)	None	0 pressure with Constant outflow	Wall	Newtonian
(Tsukiya et al. 2011)	None	0 pressure with Constant inflow	None	Newtonian
(C Ong et al. 2012)	None	Sinusoid inflow with Linear increasing outflow	Hyper elastic	Non-Newtonian
(Liu et al. 2012)	None	0 pressure with Constant inflow	Wall	Newtonian
(ChiWei Ong et al. 2013)	None	0 pressure with Transmitral velocity profile inflow	Hyper elastic	Non-Newtonian
(M. McCormick et al. 2013)	None	0D Windkessel inflow with Constant outflow	Traction-free	Newtonian
(Jhun, Sun, and Cysyk 2014)	Open	Constant outflow (inflow NM)	Incompressible Transversally isotropic	Not mentioned
(Prisco et al. 2017)	Closed Intermittently opened	0 pressure with Inflow waveform From in-vivo measurements	Rigid	Newtonian

a zero pressure boundary condition with a MV inflow or IC outflow defined. For the myocardium definition, properties may vary between rigid wall (no-motions allowed) and hyper elastic tissues (motion-free). Works considering the myocardium with elastic properties investigated the interaction between the blood flows with the myocardial walls by Fluid Structure Interaction (FSI) modelling.

1.2. Post-processing and validation

- Objectives and post-processing

CFD simulations works in the field of LVAD apical cannulation present a huge variability of purposes. Table 5-III summarizes the main objectives assessed in the literature. For instance, (M. McCormick et al. 2013; Matthew McCormick et al. 2009) investigated the interaction between fluid flow, myocardial mechanics and LVAD IC. (Jhun, Sun, and Cysyk 2014) explored the influence of the pump speed on the myocardial wall shear stress. But the majority of the articles investigated the cannula tip geometry and length. (K. H. Fraser et al. 2011) compared three clinically available cannulae, whereas (Liu et al. 2012) and (Tsukiya et al. 2011) analysed newly developed designed tips. (C Ong et al. 2012) and (ChiWei Ong et al. 2013) evaluated different cannula insertion. More recently, (Prisco et al. 2017) analysed the impact of LVAD implantation site on ventricular blood stagnation. All results have already been summarized in the chapter 2.

Different sort of post-processing approaches were used. Indeed, blood distribution and recirculation were evaluated through the flow streamlines, whereas areas of vortex were estimated with flow velocity vectors. Stagnation was determined with the evaluation of fluid velocity magnitude or the residence time of blood particles. LV 3D fibre stress distribution was also evaluated in articles assessing the LVAD influence on myocardial stress.

Table 5-III - Objectives of computational fluid dynamic simulations in the context of LVAD inflow cannula

Cannula geometry and length	Pump speed	Implantation position	Blood flow repartition
(K. H. Fraser et al. 2011) (Liu et al. 2012) (C Ong et al. 2012) (ChiWei Ong et al. 2013) (Tsukiya et al. 2011)	(Jhun, Sun, and Cysyk 2014)	(Prisco et al. 2017)	(Matthew McCormick et al. 2009) (M. McCormick et al. 2013)

- Validations

CFD simulation enables to study complex physiological flow. However, elaboration of the model requires simplifications at several steps, making it very complex. Results depend on various factors

like grid quality, boundary conditions and the computational model of the fluid. For this reason, it is important to validate a CFD computation model. Validation is a process where the accuracy of the computational model is assessed against real world data, using in-vitro or in-vivo experiments. But in the medical context, validation is very complex. It especially remains an issue in this cardiovascular context due to the difficulties involved with in-vitro and in-vivo imaging of LVAD (Matthew McCormick et al. 2009).

Among the presented articles, a large majority did not mention the validation stage. (Prisco et al. 2017) indicated that their results justify in-silico and ex-vivo studies without details. If (C Ong et al. 2012; ChiWei Ong et al. 2013) announced it as future works, only (K. H. Fraser et al. 2011) validated their model based on in-vivo experiments. They experimentally determined the pressure drops induced by their cannula and compared it with their simulation results.

Our work aims at elaborating a representative CFD modelling with the objective of comparing two IC configurations. Considering all works from the literature, a huge variability in geometry, parametrization and post-processing approaches may be noticed. Implementation of CFD simulation for the assessment of IC pose has therefore been investigated in the following. The main objective is to investigate the influence of some CFD modelling settings on results, as well as the pertinence of several post-processing approaches in a clinical point of view. Next section presents our approach for CFD modelling.

2. CFD modelling approach

In this section, we first present the approach used for the elaboration of the CFD geometry and definition of parametrization settings. Simulations were conducted in the CFD software Fluent 18.2 (ANSYS) (Fluent 2015).

2.1. Geometry

The 3D model of the LV was created from a preoperative contrast-enhanced CT scan of a patient that was eligible for LVAD implantation. Figure 5.2 presents the different steps involved in elaborating the geometry. The CT was segmented with the multi-atlas segmentation method presented in chapter 3 (Kirisli et al. 2010), and 3D mesh volumes of the LV endocardium, left atrium and aorta were constructed with Itk-Snap software (Yushkevich et al. 2006). The MV was defined by the mean plane of the surface contact between the LV and left atrium meshes, while the aortic valve was created with the LV and aorta meshes (cf chapter 4).

A step of smoothing was then performed on Fluent to create a mesh compatible with CFD simulations. This final mesh is characterized by a minimal and maximal cell size of 0.5 to 2 mm.

The 3D geometry of a HM II IC was defined by a cylinder of 53mm high, an inner diameter of 18mm and a thickness of 0.5mm. Two IC configurations were performed: toward the MV and toward the septum. For both configurations, the IC was inserted at the LV apex. As most of the articles from the literature, the LV was considered as static. Figure 5.3 illustrates the final geometry compatible with CFD simulations, and with an IC oriented toward the MV.

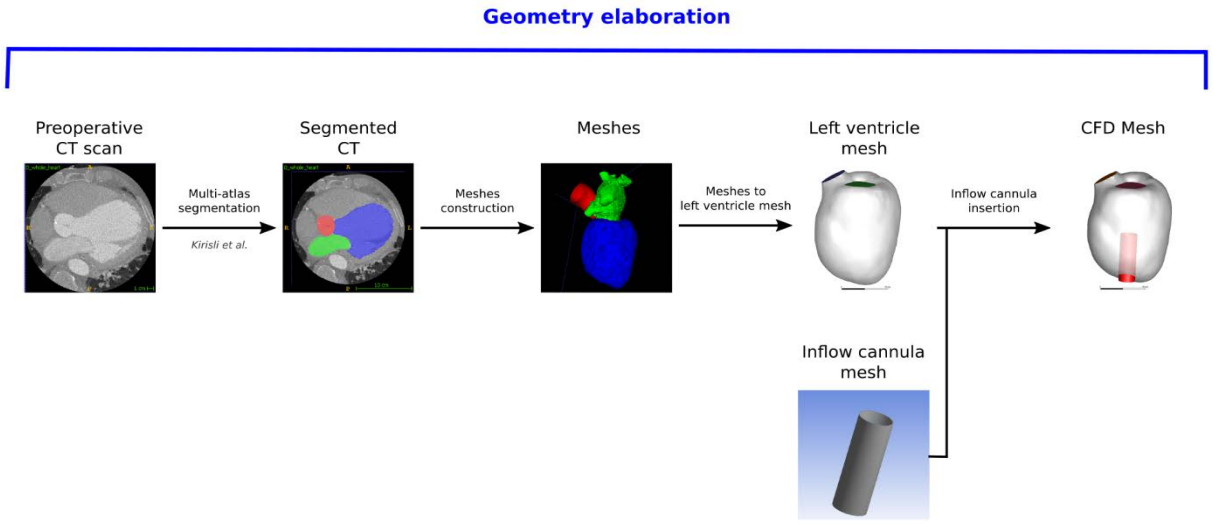

Figure 5.2 - Workflow of the left ventricle geometry elaboration for the static CFD model of this thesis

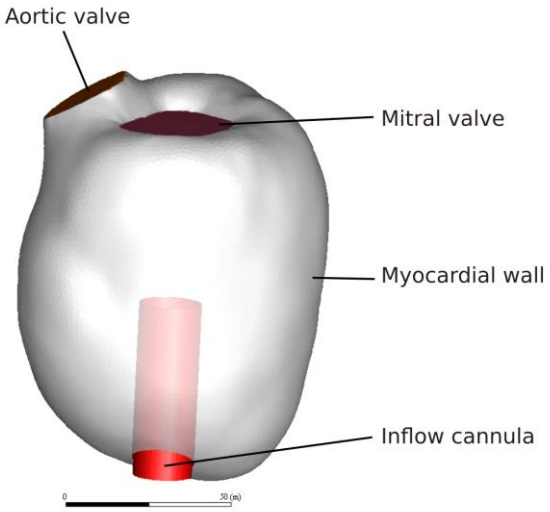

Figure 5.3 - Left ventricular CFD geometry with a LVAD inflow cannula

2.2. Parametrization of the model

During the problem definition, boundary conditions and physiological parameters have to be characterized. Boundary conditions correspond to the inlet and outlets of the model, while

physiological parameters include the rheology, simulation model and particles definition. All parameters considered are defined in Figure 5.4.

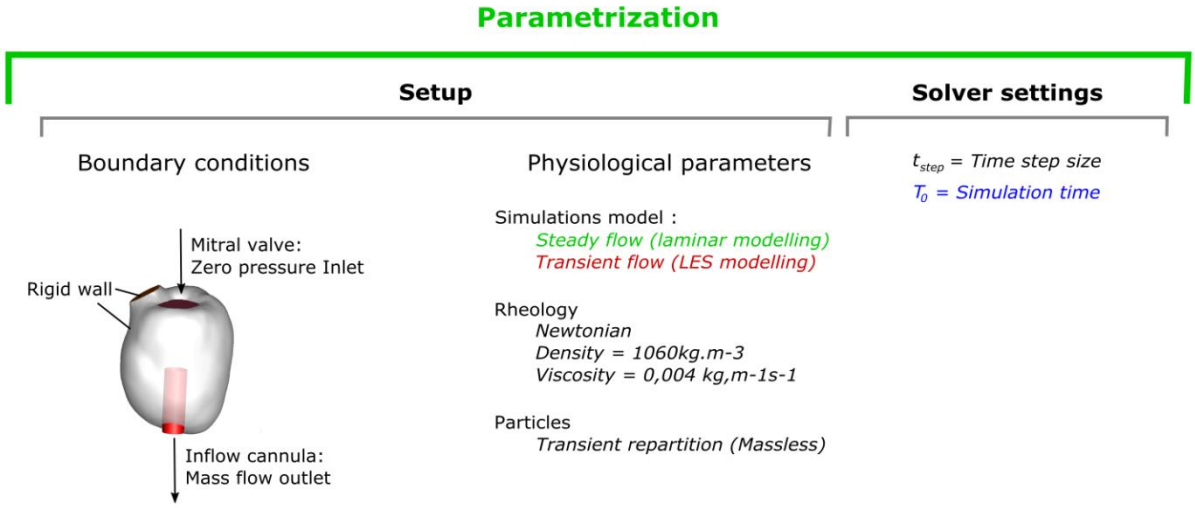

Figure 5.4 - CFD simulation settings parametrization

The myocardial wall was modelled as a rigid material and the aortic valve considered as close. A constant static pressure (0 Pa) was set on the MV inlet surface, while a constant mass flow rate of 5 L/min was given at the IC outlet part. Blood was modelled as a Newtonian fluid with a density of 1060 $kg.m^{-3}$ and a viscosity of 0.004 $kg.m^{-1}s^{-1}$ (Herman 2007). We first approximated the blood flow as laminar as most of the articles from the literature. However, we also investigated the LES model in order to compare the two models and highlight the impact of turbulences on results.
The aim of the simulations is to evaluate the impact of the IC pose on thrombus creation which is associated to stasis ereas. Hemostagnation is characterized by particles with a low velocity and/or a long residence time within the cavity. In order to analyse these two variables, we defined blood red cells as massless particles. Contrary to the scalar concentration method (Prisco et al. 2017), the Discrete Phase Model (DPM) approach does not comprise diffusion that involves errors at low velocity, particularly in a steady model. The residence time of massless particles is therefore determined in the following with the DPM method.

2.3. Numerical settings

CFD solution being calculated iteratively, one limitation with fluid simulation is the high computational time. Two parameters influencing the computational time are defined by the user: the time-step size t_{step} and the simulation time T_0 also called stop time.

t_{step} specifies the time between each iteration where the Navier-Stocks equations are being solved. For convergence while solving equations for CFD simulations, t_{step} must be defined according to the Courant–Friedrichs–Lewy (CFL) condition expressed as:

$$C = \frac{v\Delta t}{\Delta x} \leq 1, \tag{7}$$

C is called the "courant number", v defines the magnitude of the velocity, Δt is the time step and Δx represents the cells size. To capture all the flow fluctuations and ensure the simulation convergence, the "courant number" must be equal or smaller than 1. To ensure the CFL condition and limit the computation time, we defined $t_{step} = 10^{-4}$ sec.

The simulation time T_0 is defined by $T_0 = t_{step} * n_0$ where n_0 corresponds to the number of iterations defined by the user. It represents thus the period on which the evolution of the system is analysed. This number needs to be large enough to allow the solution to essentially stop changing between iterations (converge) and ensure that all phenomena are computed. However, a too large number involves a long computation time. A compromise must be determined. Finally, a segregated SIMPLEC solver with pressure-velocity coupling through PISO finite volume numerical discretization for pressure and velocity was used to solve the blood flow models.

3. Parametrisation and analyses of the coaxial configuration

This section aims at analysing the stagnation within supported LV through several post-processing approaches. To estimate areas of stagnation within the cavity, two approaches may be considered. On the one hand, space distribution of the residence time and velocity magnitude through flow fields' visualisation, velocity vectors or 3D particles distribution may be employed. On the other hand, the residence time can quantitatively be analysed through probability density function in order to statistically represent the distribution of the particles leaving the LV. Both approaches are investigated in the following. However, the blood flow model (laminar and LES) as well as the

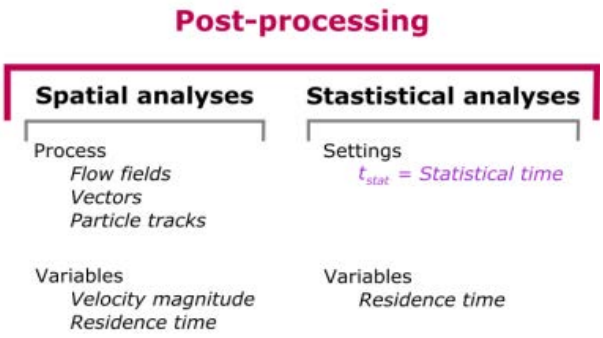

Figure 5.5 – Post-processing variables and settings

simulation time T_0 may influence the results. The first step is therefore to identify the optimal T_0 both ensuring the convergence of the results and limiting the computational time. In addition, the laminar and LES models are analysed and compared. Figure 5.5 summarizes the different post-processing variables and settings investigated in this section.

3.1. Stagnation distribution in space

3.1.1. Parametrization analyses

To analyse the fluid residence time and velocity magnitude, particles are tracked for remaining of T_0 of simulation time. According to T_0, the final variables' distribution in space may vary. We analyse thus the influence of this numerical setting on distribution. Figure 5.6 illustrates for the laminar model the repartition of the particles coloured by their residence time. In the graph, left images represent all particles tracked during T_0 ranging from 5 seconds (top) to 30 seconds (bottom), while the images in the diagonal line represent particles with a residence time between

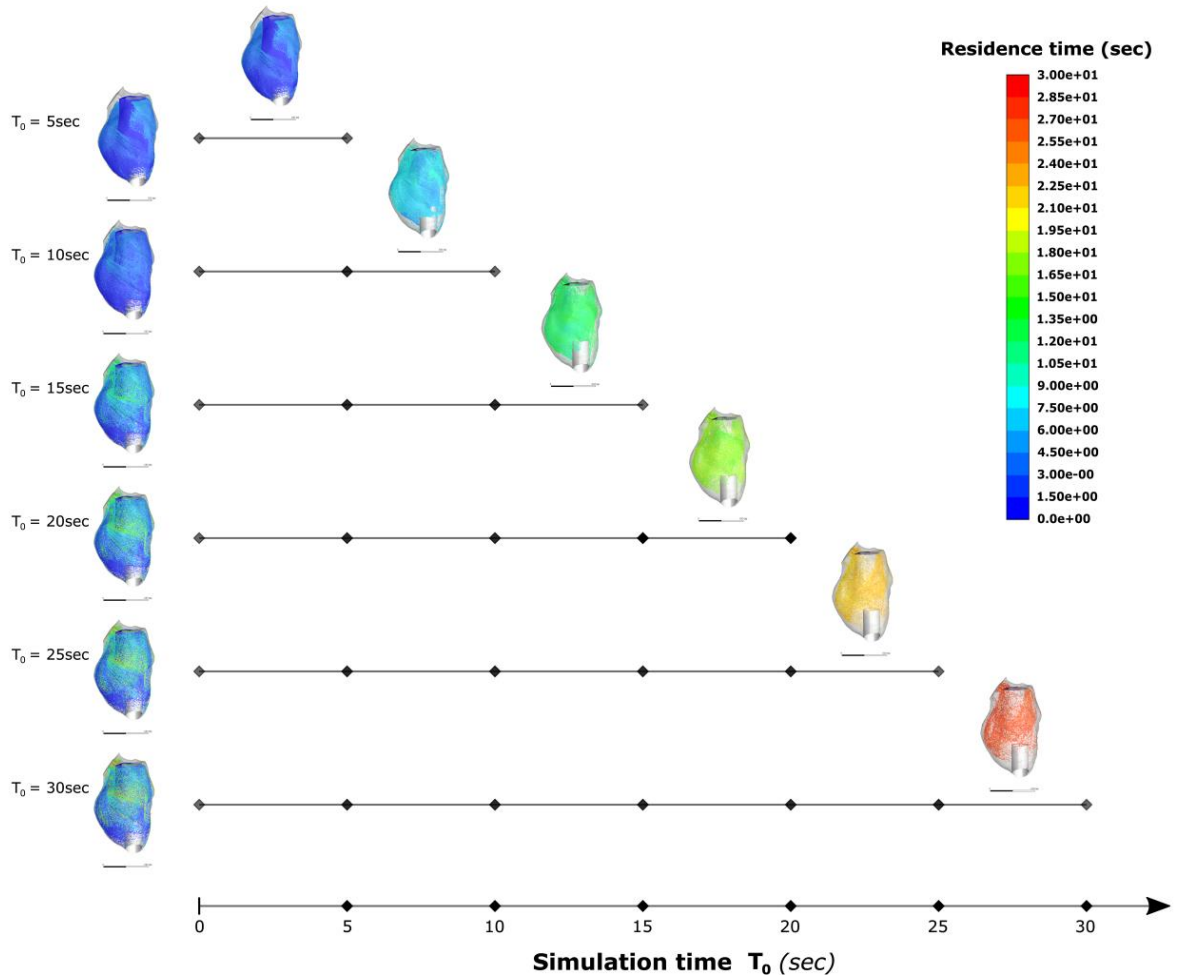

Figure 5.6 - Residence time with the laminar CFD model

T_0-5 seconds and T_0 seconds. Analysing left images, the cavity seems completely filled and repartition seems similar from T_0 equal to 15 seconds. This is confirmed by diagonal images that illustrates a decrease of particle density with a high residence time, and a similar distribution from 15 seconds. Analysing the particles' velocity magnitude distribution in space, same conclusions were obtained. Spatial distribution of the residence time and velocity magnitude may therefore be investigated with a simulation time of 15 seconds for the laminar model. Notice that same conclusion was obtained with the LES model.

In the same way, we evaluate the velocity magnitude distribution in the laminar and LES model on a 2D surface crossing lengthways the IC in its middle (Figure 5.7). For the laminar model the mean velocity is provided, while for the LES model the instantaneous velocity is illustrated at three different simulation time (T_0 = 15,16 and 17 seconds). Analysing the three illustrations from the LES model, variations of the blood flow velocity around the MV stream are visible. This difference overtime of velocity magnitude is explained by the swirling structures that are created outside the

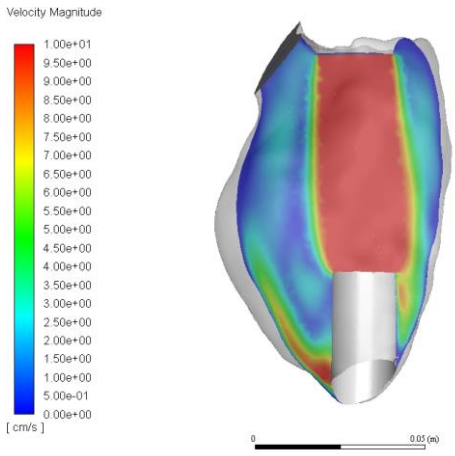

Laminar model

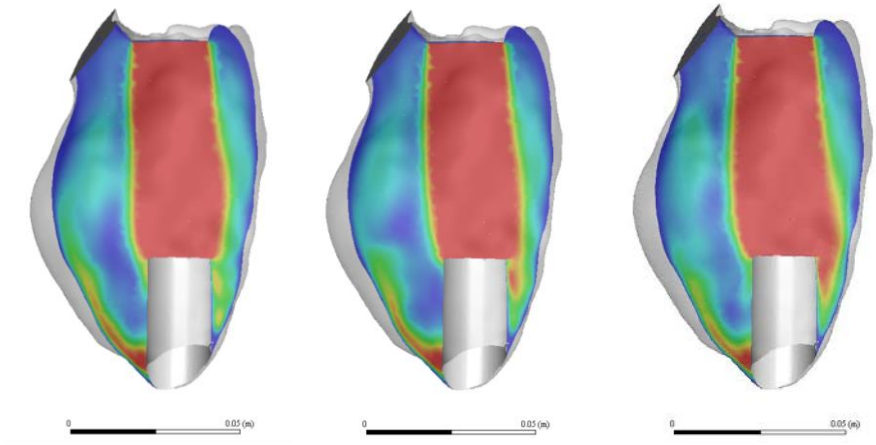

T_0 = 15s T_0 = 16s T_0 = 17s

LES model

Figure 5.7 - Comparison of the velocity magnitude from the laminar to the LES model

flow path with the LES model. These phenomena do not exist in laminar. Nevertheless, with both models the MV stream presents a high velocity as well as the apical region, while blood flow is slower in the lateral regions (areas that were not directly along the path).

3.1.2. Interpretation of the results

High residence time and low velocity are not necessarily interdependent. A low velocity generally involves a long residence time, but the reverse is not necessarily true. A particle may have a high velocity with a long residence time when this one is trapped in a vortex. We investigated thus both velocity and residence time, as well as the particles trajectories.

- Particles trajectories

Figure 5.8 illustrates particles movement during the first 3.0 seconds of simulation. At the cannula level, for both models some particles are drowned into the cannula whereas others are separated around the IC. Particles are pushed toward the basal region of the LV before going upstream. Only a relatively modest difference in trajectories may be noticed from 2.0 seconds. In the LES model, particles seems to slowly go upstream contrary to the laminar model. This is explained by the turbulences present in the LES model.

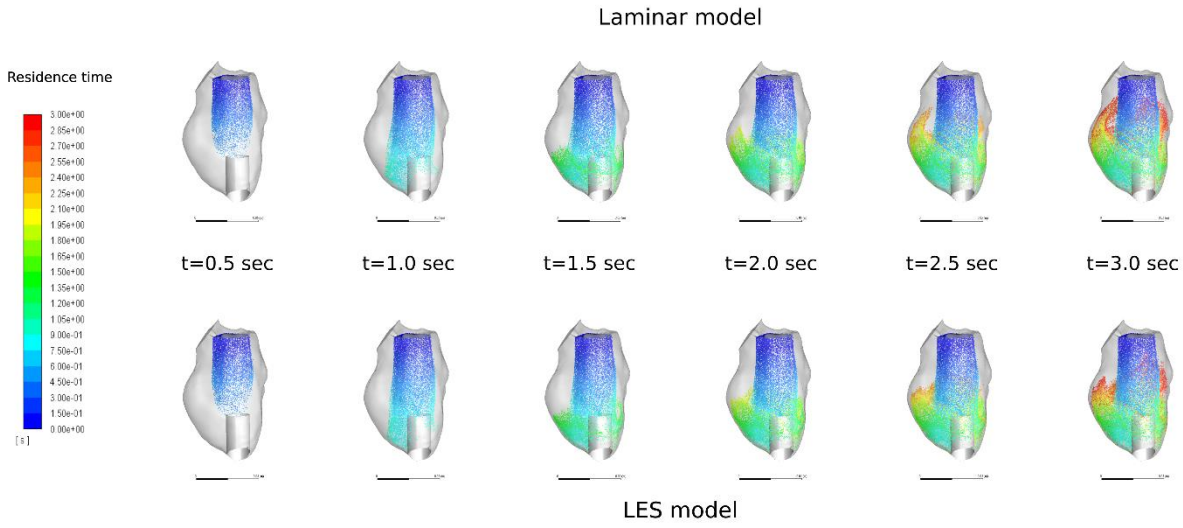

Figure 5.8 - Illustration of particles coloured by their residence time from 0.5sec to 3.0sec of simulation time – coaxial configuration

To analyse velocity magnitude and residence time for the determination of stagnation areas, we choose the LES model and considered 15 seconds of simulation time.

- Velocity magnitude

The velocity magnitude flow vectors (Figure 5.9) confirm that the blood flow is separated at the cannula level and LV remaining particles are pushed with a high velocity at the basal LV region before going upstream. Thus, the apical region does not present areas of low velocity potentially responsible for thrombus creation. When going at the top of the LV, particles lose speed before regaining the blood flow from the MV. This trajectory seems to be a repeatable pattern.

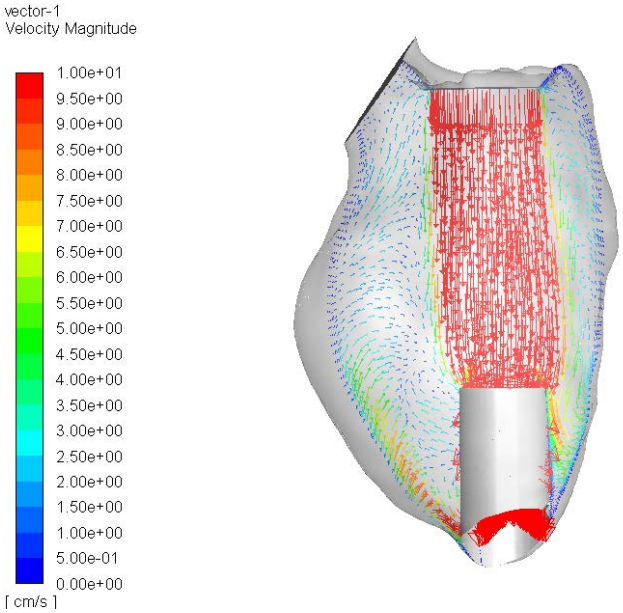

Figure 5.9 - Velocity magnitude flow vectors (LES)

Figure 5.10 represents the 3D distribution of the fluid velocity magnitude. Any particles with a velocity higher than 3.0 cm.s^{-1} are not represented in the figure. This value represents around 25%

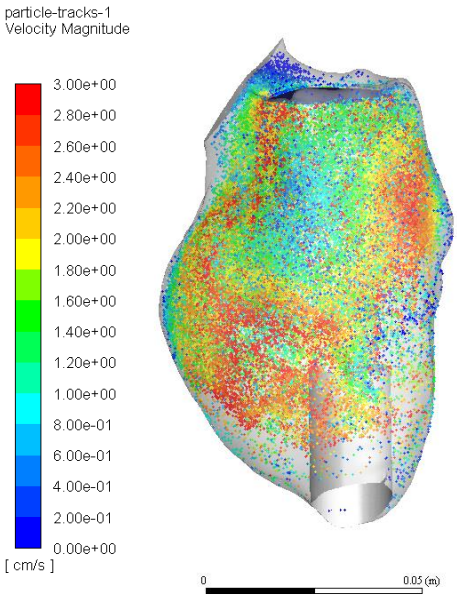

Figure 5.10 - Distribution of velocity magnitude within the left cavity (LES)

of blood cells velocity definition. Two main interpretations may be noticed with this figure. First, at the apical region no particles are present in the figure. This cavity area is thus associated to high velocity magnitude. Particles in this area come directly from the MV stream and present thus a high velocity. Secondly, particles with a low velocity are located above the apical region and all around the MV stream flow. After being pushed down, they lose their speed going upstream. A homogeneous distribution is visible.

- Residence time

Figure 5.11 represents the 3D distribution of particles with a residence time higher than 5 seconds. As for velocity magnitude distribution, this figure first illustrates that the apical region is not associated to high residence and thus stagnation. Then, particles with a high residence time present a homogeneous distribution.

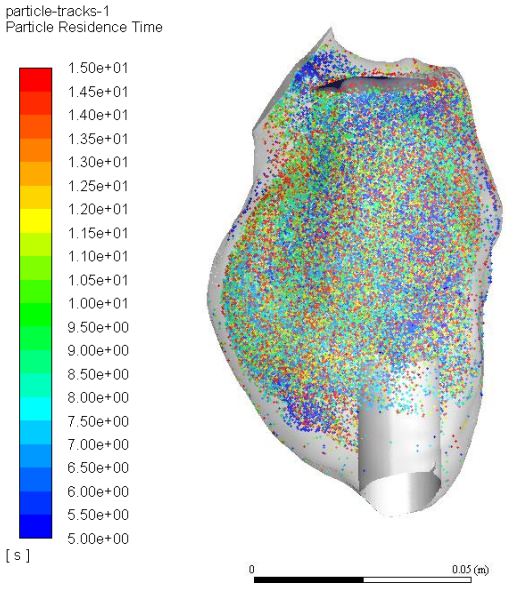

Figure 5.11 - Distribution of residence time within the left cavity with an inflow cannula oriented toward the mitral valve

Assessing hemodynamics within the LV with an IC coaxial to the normal to the MV highlights that there is a large number of particles with a low velocity and high residence time spread across the volume. No specific stagnation areas are brought to light.

3.2. Quantification of the residence time

3.2.1. Parametrization analyses

A statistical calculation may be performed with Fluent, in order to quantify the residence time. During a number n_{stat} of iterations performed after T_0, states (position, velocity, mass flow rate,

residence time, etc.) of each particle leaving the LV through the cannula were recorded. The time t_{stat} associated to n_{stat} is defined by $t_{stat} = n_{stat} * \Delta t$. Probability Density (PD) function of the residence times (denoted PD_{RT}) can thus be obtained with these data. This function represents the temporal distribution of blood particles leaving the LV cavity during t_{stat}. Both t_{stat} and T_0 may influence PD_{RT} results. We investigated these two parameters in order to determine the minimal number of iterations necessary to obtain a convergence of the PD_{RT} functions. In the following, parameters are defined in seconds, and both laminar and LES models are investigated. Figure 5.12 illustrates the graphs obtained with the laminar and LES model for six different values of t_{stat}. According to the results, a convergence is visible from t_{stat} = 0.30 sec. In the following, all statistics are therefore performed using t_{stat} = 0.35 sec.

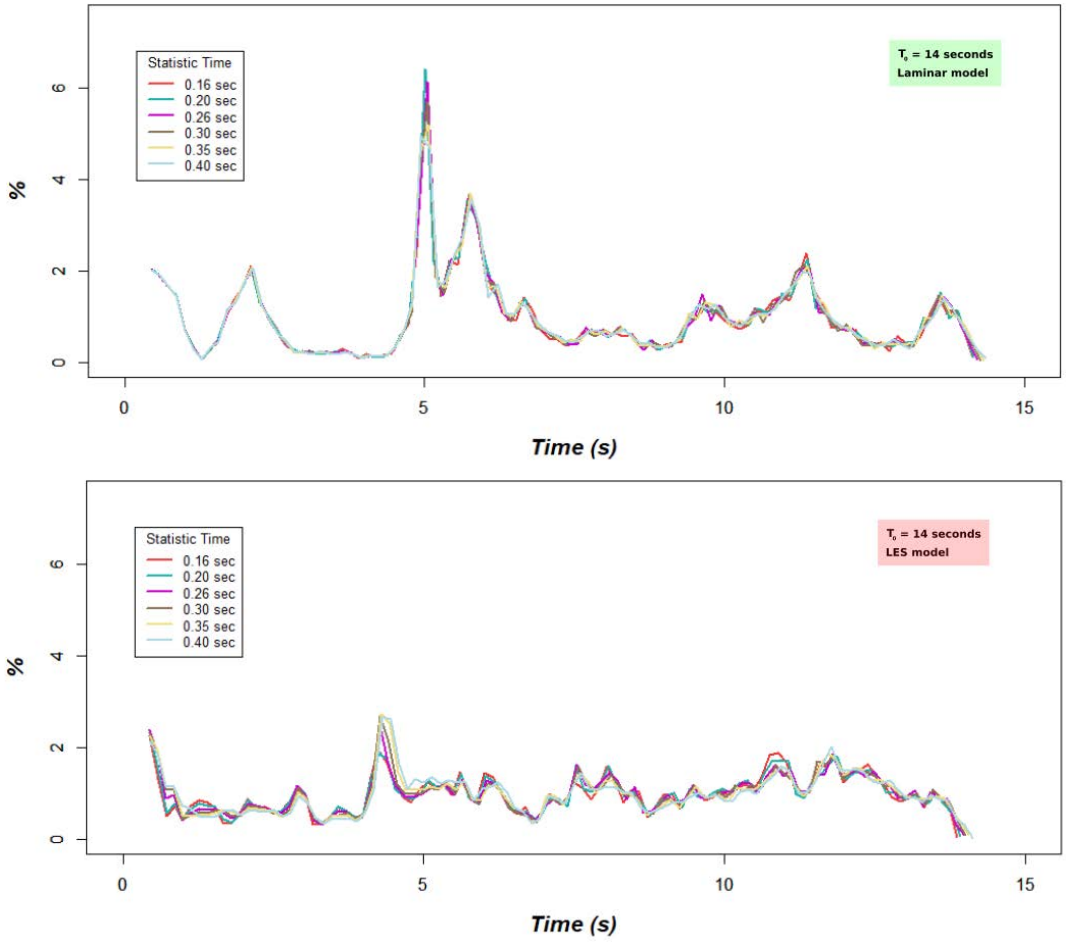

Figure 5.12 - Probability density of the laminar and LES model for several statistical time values (t_{stat})

In the same way, nine different values of T_0 were evaluated. Figure 5.13 illustrates results with the laminar model. Even though maxima are located at the same place, their intensity decreases with the increase of T_0. This is explained by the fact that for a specific T_0 all particles with a residence

time superior to T_0 are not considered. That is also why curves do not stop at the same time (abscissa value). Nevertheless, a trend curve is clearly distinctive and analysing the graph obtained with T_0 = 30seconds, the function can be considered as having converged. Same conclusions were obtained with the LES model. To ensure the convergence of the PD_{RT} functions, the simulation needs therefore to be calculated during at least 30 seconds, and statistical analysis performed with a minimum of 0.30 seconds.

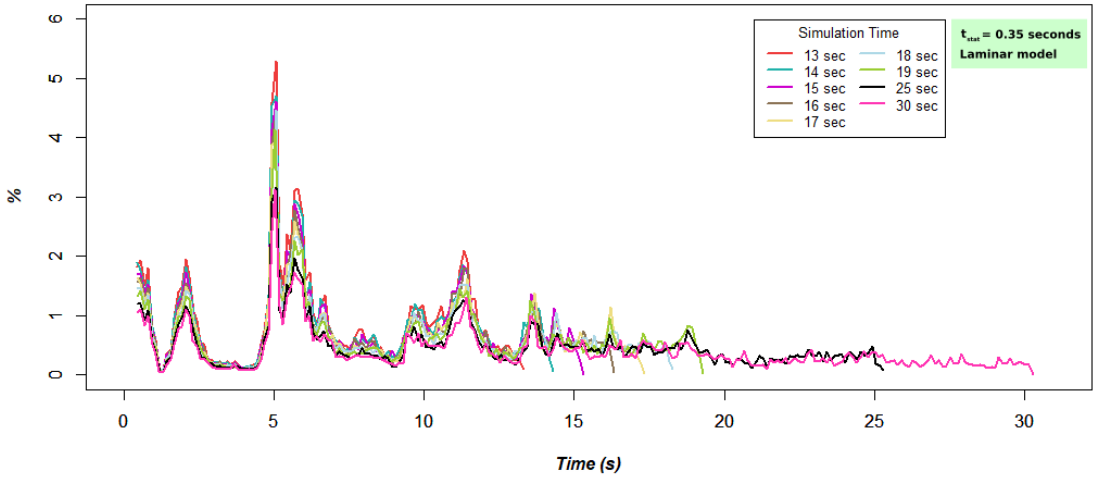

Figure 5.13 - Probability density of the laminar model for several simulation time values (T_0)

Comparing PD_{RT} functions obtained at 30 seconds with the two models (Figure 5.14), maxima are located at similar times. Both models can thus be used to determine ranges of time when a large number of particles leave the LV. The function associated to the LES model is quite more staggered than for the laminar model. Analysing the distribution of the residence time in Figure 5.15, the two functions present a difference of approximatively 10%. In the LES model, particles near the MV

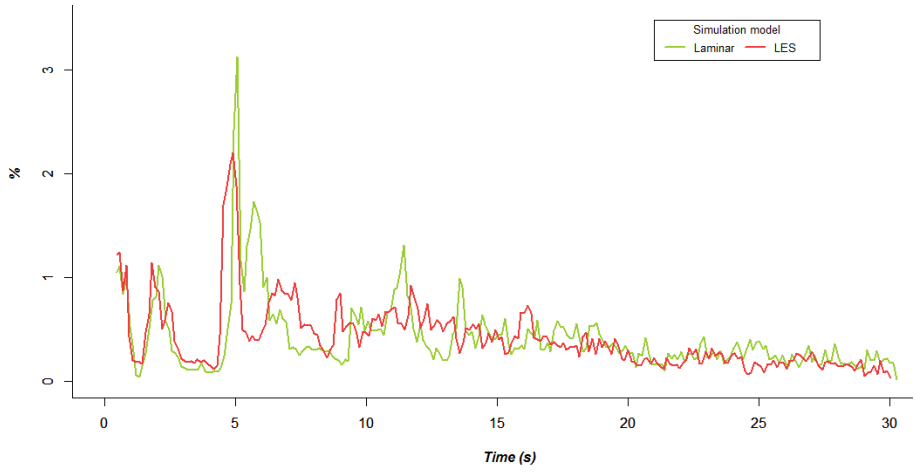

Figure 5.14 - Probability density of the residence time for laminar and LES models

stream are more likely to return in the stream because of the turbulent transport. In the laminar model particles present a linear trajectory by definition. Turbulences may therefore explain that particles from the LES model leave the cavity faster than in the laminar model. The laminar model overestimates the residence time.

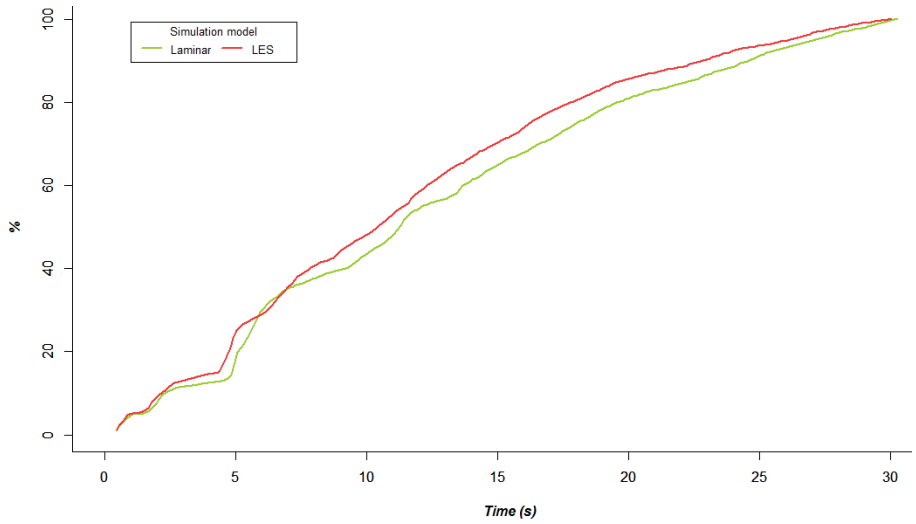

Figure 5.15 – Statistical distribution of the residence time for the laminar and LES models

Results demonstrated that considering an IC oriented coaxially to the normal to the MV, a mass of particles leaves the cavity at around 2.5 and 5 seconds of simulation, and approximatively 50% of the particles have left the cavity at 10 seconds. To conclude, valuable information such as time areas where a large number of particles goes out of the LV may be deduced from this post-processing approach.

4. LV hemodynamic with an IC oriented toward the septum

In this section, we analyse the blood flow involved by an IC oriented toward the Inter-Ventricular Septum (IVS). This configuration may be found postoperatively. Figure 5.16 illustrates this configuration. LV hemodynamic is investigated through flow fields and velocity vectors as well as spatial repartition and statistical analysis of the residence time. According to the results from the previous section, we use herein the LES model and 30 seconds of flow simulation was performed in order to make the statistical analyses.

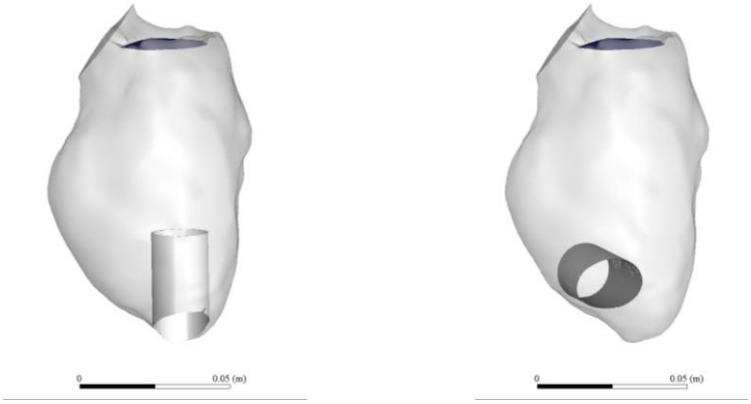

Figure 5.16 - Left ventricle geometry with a coaxial and IVS IC configuration

4.1. Particles trajectories

Figure 5.17 illustrates particles movement during the first 3.0 seconds of simulation for a LV with an IC oriented toward the septum. First, a large number of particles from the MV stream go down in the apex direction. A separation of the particles is clearly visible at 0.5 and 1.0 seconds and is characterized by particles going in a lateral direction, toward the IC (direction of the right ventricle) and in the opposite direction. A vortex is clearly formed above the IC and blood flow presents a circular circulation not in the lengthwise like the coaxial configuration, but transversally.

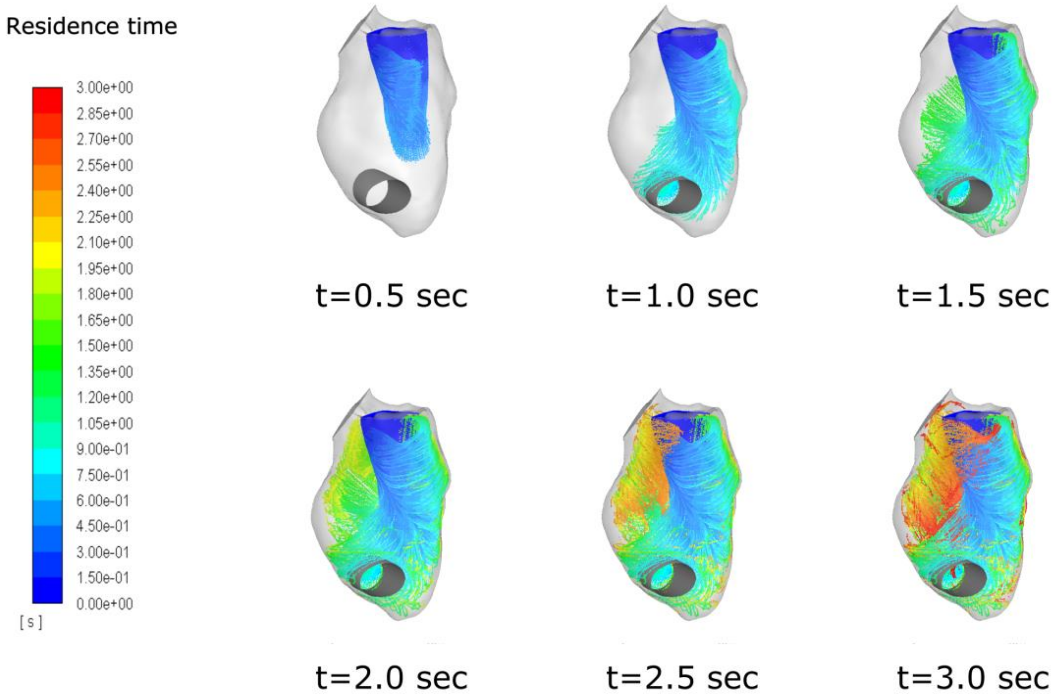

Figure 5.17 - Illustration of particles coloured by their residence time from 0.5sec to 3.0sec of simulation time – IVS configuration

4.2. Velocity magnitude and residence time

Figure 5.18 represents the 3D distribution within the left cavity of the velocity magnitude. Only particles with a velocity under 3.0 $cm.s^{-1}$ were conserved in the figure. Results put forward two areas of low velocity. The first one is located at the opposite side of the IC distal-end, while the second one is visible above the IC output. Vortex centres are characterized by particles with a low velocity. The group of particles above the IC represent thus the centre of the vortex. The second low velocity area is explained by the particles decreasing speed when going up toward the MV. However, most of the particles seem to get close to the 3.0 $cm.s^{-1}$ of velocity and no many particles have a very low velocity within the cavity.

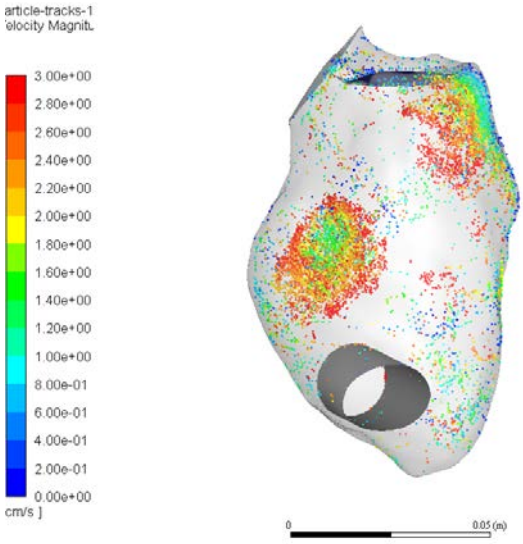

Figure 5.18 - 3D distribution of particles velocity magnitude with an inflow cannula toward the inter-ventricular septum

In the same way, Figure 5.19 represents particles with a residence time higher than 5seconds. Contrary to the velocity distribution, only one region with a high residence time is visible, above the IC. However, this region seems dilated with few particles. According to this figure, a very large majority of the particles leave the cavity before 5 seconds. This is confirmed by the PD and distribution functions of the residence time represented in Figure 5.20. In addition, approximatively 60% of particles have left the cavity at 5 seconds of the simulation (Figure 5.22).

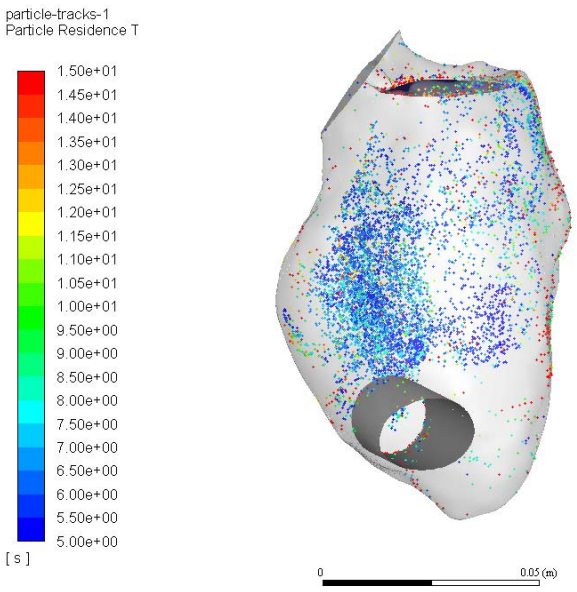

Figure 5.19 - Distribution of the residence time

Comparing results from the coaxial configuration analysis, the IVS configuration presents less particles with a high residence time and low velocity. In the IVS configuration, the LV volume is largely swept by the blood flow contrary to the coaxial configuration, and particles leave thus the cavity much faster. These results suggest that at this stage of the work, a coaxial configuration may not be the optimal option. Going against the current recommendation, these interpretations are more discussed in the next section.

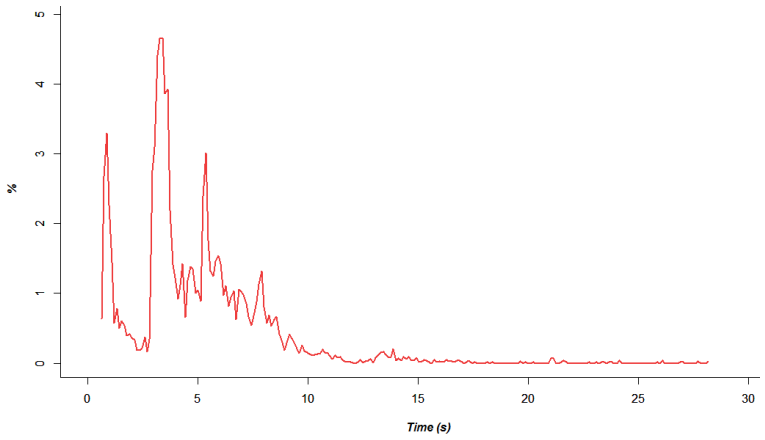

Figure 5.20 – Probability density of the residence time for the IVS configuration

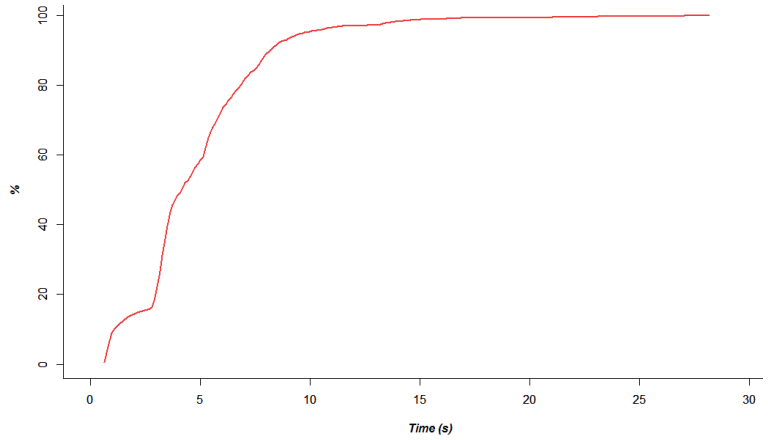

Figure 5.21 – Statistical distribution of the residence time for the IVS configuration

5. Conclusion and discussion

Computational modelling in cardiovascular becomes more reliable and presents several advantages. In the context of LVAD IC assessment, only few studies have been published. The purpose of this chapter was to elaborate a representative CFD model with the future aim of improving the clinical knowledge and define IC pose criteria for the decision support solution presented in chapter 4. It has been established that blood stagnation leads to thrombus events associated with chronic complications in VAD patients. We investigated thus blood stagnation for two IC configurations analysing the particles residence time and velocity magnitude.

To the best of our knowledge, only one article has investigated the influence of the IC orientation on LV hemodynamic (Prisco et al. 2017). A static LV geometry from a patient implanted with a LVAD and laminar flow were used in this article. Besides, both closed and intermittently opened boundary condition defined the aortic valve. Authors compared an apical and diaphragmatic (lateral wall) implantation of the IC. They demonstrated a relatively modest difference in stagnation between the two configurations; with a diaphragmatic configuration that even induces small areas of stagnation in the apex potentially inducing formation of thrombi. However, they quantify the stagnation with a virtual ink technique from (Rayz et al. 2010), which estimates the flow residence time based on a passive scalar distribution maps. Considering diffusion in this method, errors at low velocity are involved, particularly in a steady model.

In this chapter, we compared the LES and laminar model and analysed the residence time with a DPM method which minimizes errors at low velocity. Determining the optimal T_0, results demonstrated that statistical analysis required a long simulation time (30 seconds) involving a long computation time (around 7 days with an Inter Core i7 processor, 3.20 GHz, 16Go RAM, and

GPU NVIDIA Quadro 5000) compared to 3D spatial distribution (15 seconds – around 4 days). In addition, the quantitative analysis highlighted that the laminar model seems to overestimate the residence time compared to the LES model. Two IC configurations were thus analysed with the LES model and 30 seconds of simulation time.

Comparing the coaxial and IVS configuration, simulation results highlighted that an IVS configuration ensures a faster discharge of the cavity. An IC implanted out of alignment seems to promote the creation of vortices allowing a better sweep of the cavity. Indeed, as mentioned in chapter 2, vortices contribute to minimize cardiac work and facilitate the blood mass coming into and leaving the LV. However, vortices also contribute to suction events (Kheradvar, Milano, and Gharib 2007). Retrospective analyses presented in chapter 4 associated the IC deviation to postoperative complications (pump dysfunction and thrombosis). With an IC toward the septum, suction events are clearly promoted, altering thus the LV hemodynamics, the right ventricle function as well as the pump efficiency. Taking into account these myocardium mechanical reactions, current clinical recommendations prescribe to implant the IC toward the MV and away from the septum. This contradiction brings therefore our results to discussion.

The myocardium is considered as static in our simulations. Neglecting the LV mechanical reactions in our simulations, we neglect the suction events and the potential related alterations of the hemodynamics. Despite retrospective analyses associate the IC misalignment to the creation of thromboses, one can ask if the principal source of LV hemodynamic alteration leading to stagnation areas is not the suction events rather than a misalignment. The configurations presented in this work are very extreme but one can ask whether a small deviation not involving suction events might be hemodynamically preferable rather than a perfect coaxiality.

These conclusions show the major interest of the question related to the IC implantation configuration. In the one hand, even though the validation of this model was not performed, this CFD modelling methodology could be used to further investigate the influence of the cannula implantation configuration on the LV hemodynamic. Besides, further retrospective analyses should be performed considering IC orientation range of values and well distinguishing patients presenting thrombus creation with and without suction events. For this sort of analysis, a large number of studied patients is necessary, but results could be related to those obtained with simulations in order to validate CFD interpretations. On the other hand, from a methodological point of view, there is still room for improvement in the modelling of the LV hemodynamics under LVAD support. Although in our work the aortic valve was approximated as close as the majority of articles from the literature, it could be described as intermittently open and. The myocardium could also be defined as a hyperelastic wall and the mitral valve with a representative valve function. In

addition, heart motion could be considered. The perspectives of our works are related to the improvement of CFD simulations with the aim of enlarging knowledge on LVAD supported ventricle hemodynamic. Figure 5.22 illustrates through a flowchart a possible way for the elaboration of a heart beating model. Multi-atlas segmentation is used to extract left ventricle from preoperative multi-phase CTs. A mesh warping process is considered in the workflow in order to match the meshes describing the structure of interest at each cardiac phase, and thus to compute the motion vector field to apply to the CFD mesh. Radial basis function based mesh morphing (e.g. RBF-Morph, ANSYS) or iterative point matching based registration (Rigaud et al. 2017) could be used to this aim.

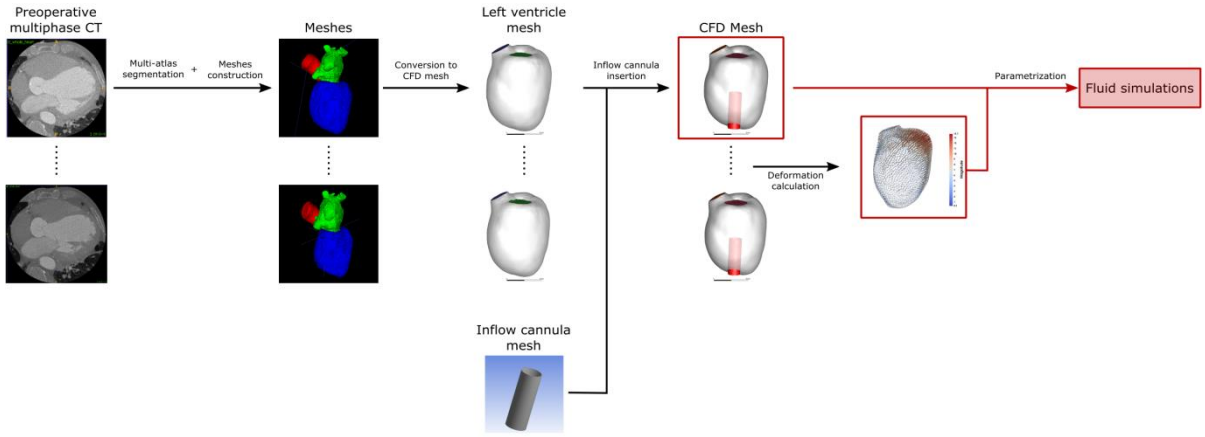

Figure 5.22 - Flowchart for the elaboration of heart beating simulation with a LVAD inflow cannula

References

Fluent, ANSYS. 2015. "Ansys Fluent." *Academic Research. Release* 14. http://www.ansys.com/fr-fr/products/fluids/ansys-fluent (January 14, 2018).

Fraser, John F., Shaun. Gregory, and Michael. Stevens. 2017. *Mechanical Circulatory and Respiratory Support*. Academic Press.

Fraser, Katharine H et al. 2011. "Computational Fluid Dynamics Analysis of Thrombosis Potential in Left Ventricular Assist Device Drainage Cannulae." *ASAIO journal (American Society for Artificial Internal Organs: 1992)* 56(3): 157–63.

Herman, Irving. 2007. Physics of the Human Body *Physics of the Human Body*.

Jhun, Choon-Sik, Kay Sun, and Joshua P. Cysyk. 2014. "Continuous Flow Left Ventricular Pump Support and Its Effect on Regional Left Ventricular Wall Stress: Finite Element Analysis Study." *Medical & Biological Engineering & Computing* 52(12): 1031–40.

Kheradvar, Arash, Michele Milano, and Morteza Gharib. 2007. "Correlation between Vortex Ring Formation and Mitral Annulus Dynamics during Ventricular Rapid Filling." *ASAIO journal (American Society for Artificial Internal Organs: 1992)* 53(1): 8–16.

Kirisli, H. A. et al. 2010. "Evaluation of a Multi-Atlas Based Method for Segmentation of Cardiac CTA Data: A Large-Scale, Multicenter, and Multivendor Study." *Medical physics* 37(12): 6279–91.

Lilly, D. K. 1992. "A Proposed Modification of the Germano Subgrid-Scale Closure Method." *Physics of Fluids A* 4(3): 633–35.

Liu, Guang Mao et al. 2012. "Numerical Simulation of LVAD Inflow Cannulas with Different Tip." *International Journal of Chemical Engineering* 2012.

McCormick, M., D. a. Nordsletten, D. Kay, and N. P. Smith. 2013. "Simulating Left Ventricular Fluid-Solid Mechanics through the Cardiac Cycle under LVAD Support." *Journal of Computational Physics* 244: 80–96.

McCormick, Matthew et al. 2009. "Fluid-Mechanics Simulations of Ventricular Function under LVAD Support." *IFMBE Proceedings* 25(4): 1572–75.

Menter, F. R. 1994. "Two-Equation Eddy-Viscosity Turbulence Models for Engineering Applications." *AIAA Journal* 32(8): 1598–1605. http://arc.aiaa.org/doi/10.2514/3.12149 (February 6, 2018).

Menter, F. R., and Y. Egorov. 2010. "The Scale-Adaptive Simulation Method for Unsteady Turbulent Flow Predictions. Part 1: Theory and Model Description." *Flow, Turbulence and Combustion* 85(1): 113–38.

Mittal, Rajat et al. 2015. "Computational Modeling of Cardiac Hemodynamics: Current Status and Future Outlook." *Journal of Computational Physics* 305: 1065–82.

Morris, Paul D et al. 2016. "Computational Fluid Dynamics Modelling in Cardiovascular Medicine." *Heart* 102(1): 18–28.

Ong, C et al. 2012. "Fluid Structure Interaction Simulation of Left Ventricular Flow Dynamics under Left Ventricular Assist Device Support." *IEEE EMBS*: 1–4.

Ong, ChiWei et al. 2013. "Numerical Investigation of the Effect of Cannula Placement on Thrombosis." *Theoretical biology & medical modelling* 10(1): 35.

Prisco, Anthony R et al. 2017. "Impact of LVAD Implantation Site on Ventricular Blood Stagnation." *ASAIO Journal* 63(4): 392–400.

Rayz, V L et al. 2010. "Flow Residence Time and Regions of Intraluminal Thrombus Deposition in Intracranial Aneurysms." *Annals of Biomedical Engineering* 38(10): 3058–69.

Rigaud, Bastien et al. 2017. "Treatment Plan Library Based on Population Shape Analysis for Cervical Adaptive Radiotherapy." In *SURGETICA, France*,.

Townsed, A A. 1976. *The Structure of Turbulent Shear Flow*. Cambridge University Press.

Tsukiya, Tomonori et al. 2011. "Computational Fluid Dynamic Analysis of the Flow Field in the Newly Developed Inflow Cannula for a Bridge-to-Decision Mechanical Circulatory Support." *Journal of artificial organs: the official journal of the Japanese Society for Artificial Organs* (June): 25–33.

de Vecchi, A. et al. 2016. "A Novel Methodology for Personalized Simulations of Ventricular Hemodynamics from Noninvasive Imaging Data." *Computerized Medical Imaging and Graphics* 51: 20–31.

Yushkevich, Paul a. et al. 2006. "User-Guided 3D Active Contour Segmentation of Anatomical Structures: Significantly Improved Efficiency and Reliability." *NeuroImage* 31(3): 1116–28.

Zuin, M et al. 2016. "Computational Fluid Dynamics as a Tool in the Development Process of Left Ventricular Assist Devices." *Journal of Advanced Therapies and Medical Innovation Sciences* 1: 52–53.

Conclusion

This thesis dealt with the issues of computer-aided planning for long term MCS implantation and the potential of CFD modelling for the assessment of LVAD inflow cannula configuration.

First, the approach was to analyse intraoperative complications the surgeons may face during the surgical procedure itself. Physiological, mechanical and hemodynamic changes caused by MCS implants and potentially leading to adverse events have been presented. We highlighted the large number of factors potentially altering several organs' functioning, as well as the significant amount of issues raised in this domain. Quite a few studies have been published in this field, but currently it seems difficult to anticipate the optimal MCS pose considering all factors potentially leading to adverse events.

Focusing on two main aspects: collision between the device and surrounding critical organs (the heart and thoracic wall), and quantification of the LVAD inflow cannula orientation, we assessed the feasibility of elaborating a computer-aided solution with the aim of anticipating the device choice and position according to the patient anatomy. A strategy for patient structures description was investigated, implementing and comparing several segmentation methods. We identified that segmentation of the lungs and thoracic wall and bones are still a challenge in the context of MCS implantation due to the variability of lungs pathology and the presence of contrast media and metal artefacts in CT images. On the contrary, segmentation of the aorta and heart are quite promising. Based on these results, we presented a novel planning approach that uses multi-atlas segmentation of the heart and density analyses. The potential of this pose planning has been shown as well, through the comparison of a preoperative virtual positioning of the device with the post-operative configuration. Current recommendations prescribe to orient the LVAD inflow cannula toward the mitral valve, but no more precise metrics are provided. In the proposed pose planning, criteria representing the LVAD inflow cannula configuration are used as indicators to improve decision support.

CFD simulation has been addressed in the perspective of determining more precise recommendations for the inflow cannula orientation. We first analysed the CFD implementation of a left ventricle with an inflow cannula implanted with the aim of assessing the impact of the cannula configuration on left ventricle hemodynamic. The literature presents a huge variability in CFD modelling. Comparing a laminar and a turbulent (LES) model, we highlighted that results for spatial distribution of the velocity magnitude and residence time were similar for both models. We

investigated thus the influence of the inflow cannula orientation with the LES model comparing two configurations: toward the mitral valve and toward the interventricular septum.

In this work we focused on device dislodgement due to thorax compression. Through a retrospective analysis, we highlighted that for most cases, LVAD dislodgement could be associated to chest wall compression. However, other factors may impact device position and orientation. More detailed investigations are necessary to further analyse factors of dislodgement. Besides, additional objective criteria must be defined and the importance of the different indices impact on postoperative complications determined.

A novel patient-specific pose planning with the aim of anticipating the device pose according to the intrathoracic space has been presented in this thesis. Although the solution may currently provide valuable information, the methodology has some limitations. First, results for the multi-atlas heart segmentation demonstrated that this approach still presents limitations. Image pre-processing could be considered, and an alternative should be sought for patient contra-indicated for contrast injection. Secondly, detection of collision is partly based on density analysis in order to overcome current limitations related to the segmentation of the thoracic wall. Even though only few works have been reported in this domain, it could be interesting to further investigate such an approach. Thirdly, only a static geometry was considered, neglecting breathing and cardiac motion. A preoperative multi-phase CT or CT images combined with echocardiography could be used to anticipate tissue movement over time. Finally, optimization of the device positioning is determined interactively by the user according to different parameters. An automatic positioning method could be considered.

Even though clinical recommendations preconize to orient the LVAD inflow cannula toward the mitral valve, results obtained with CFD simulations highlighted a faster discharge of the left ventricle with a configuration toward the septum. Our simulations only focused on hemodynamics and did not take into account the mechanical reaction of the myocardium. However, this work shows a real interest in revaluating the necessity of a perfect coaxiality of the inflow cannula with the normal to the mitral valve plane. In addition, our model still presents some limitations. Several boundary conditions could be refined especially for the mitral valve and aortic valve, for further investigations in this context. Finally, computational modelling of larger vessels hemodynamics is a relatively mature field and many factors related to the outflow cannula are supposed to impact the aortic blood flow (length, orientation and position). Quite a few articles have investigated this issue but from a clinical point of view optimization of the outflow cannula anastomosis according to the patient anatomy still needs to be solved. To patient specific planning, the perspectives of

our works are related to the improvement of knowledge concerning the aorta and ventricle hemodynamics exploiting CFD simulations.

List of publications

S. Collin, A. Anselmi, J. P. Verhoye, P. Haigron, and E. Flecher, "Virtual positioning of ventricular assist device for implantation planning," Irbm, vol. 1, no. 6, pp. 5–11, 2015.

Anselmi, S. Collin, P. Haigron, J. P. Verhoye, and E. Flecher, "Virtual implantation and patient-specific simulation for optimization of outcomes in ventricular assist device recipients," *Med. Hypotheses*, vol. 91, pp. 67–72, 2016.

A. Anselmi, S. Collin, J.-P. Verhoye, P. Haigron, and E. Flécher, "Association between intraventricular position of inflow cannula and clinical outcomes in lvad recipients," *J. Hear. Lung Transplant.*, vol. 35, no. 4, p. S320, 2016.

A. Anselmi, S. Collin, P. Haigron, J. P. Verhoye, and E. Flecher, "Virtual implantation of a novel LVAD: toward computer-assisted surgery for heart failure," *J. Surg. Res.*, vol. 205, no. 1, pp. 204–207, 2016.

A. Anselmi, S. Collin, P. Haigron, J.-P. Verhoye, and E. Flecher, "Device-specific evaluation of intraventricular left ventricular assist device position by quantitative coaxiality analysis," *J. Surg. Res.*, vol. 213, no. 0, pp. 110–114, 2017.

S. Collin, A. Anselmi, J. P. Verhoye, E. Flecher and P. Haigron, "Potential benefits of pose planning for LVAD implantation," SURGETICA 2017, Strasbourg, France, Nov 2017.

Annexes

Annex 1
Total Artificial Hearts -TAH

TAH without FDA approval

- Liotta heart (Dr. Denton A. Cooley & Dr. Domingo Liotta), the first TAH implanted in 1969 in the US (Houston).
- Akutsu III (Texas Heart Institute, US) implanted in 1981, a double-ventricle pump, pneumatically driven.
- Sarns-3M (3M Health Care Inc., St Paul, MN) a translating roller screw driven system
- Nimbus (Nimbus Inc., Rancho Cordova, CA) a hydraulic driven system.

The last two devices underwent animal implantation but were not considered adequate for human implantation.

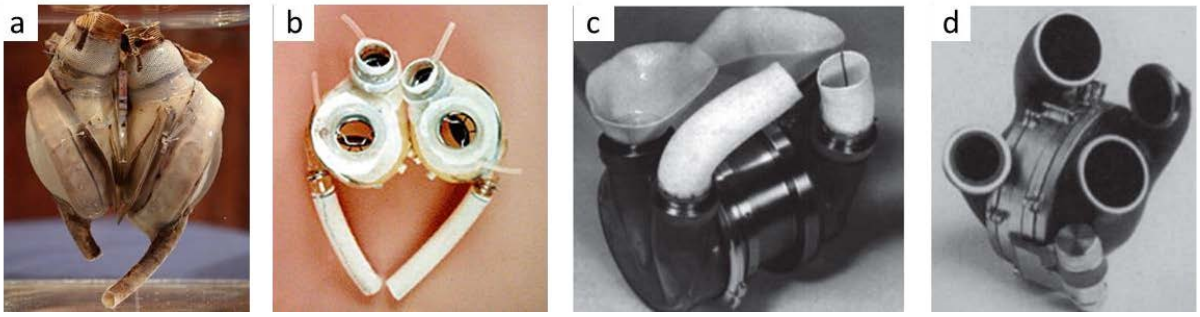

a. Liotta heart; b. Akutsu III heart; c. Sarns-3M heart; d. Nimbus heart

TAH with a FDA approval

- Jarvik-7 (Syncardia, Tucson, AZ), a double-ventricle pump, pneumatically driven, that was developed in 1982 and renamed Cardiowest 70cc in 1993. This device received the first full FDA approval in 2004.
- The Abiocor heart (Abiomed, Danvers, MA) is the first fully implantable device with a transcutaneous energy transfer system driving the hydraulic pump. It is also composed of an intracorporeal controller and battery having autonomy of 30-40 min. This device received a FDA approval in 2006.

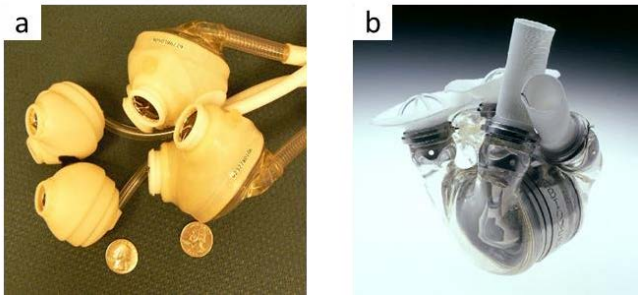

a. 50cc and 70cc Cardiowest heart (Syncardia - US); b. Abiocor heart (Abiomed - US)

TAH prototypes

- BiVACOR (BiVACOR, Inc., Houston, TX), a continuous flow magnetically powered device.
- ReinHeart (ReinHeart TAH GmbH, Gütersloh, Germany), an electromagnetic powered device composed of a linear motor displacing two pusher plates in an alternating way.
- Carmat (CARMAT, Velizy Villacoublay, France), that is more recent. This new TAH uses an electro-hydraulic driven system, aimed to mimic the shape of a natural heart. Instead of using mechanical valves, this device uses bioprosthetic materials in order to reduce the use of anticoagulant. The first human implantation was made in 2011, and Carmat received the CE marked in 2013.

a. BiVACOR (BiVACOR, Inc. - US); b. ReinHeart (ReinHeart TAH GmbH - Germany); c. Carmat (Carmat – France)

Annex 2
Ventricular Assist Devices - VAD

Example of first generation devices

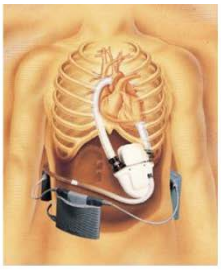

Novacor LVAD
1st human implantation: 1984
FDA approval for BTT: 1998
Stop production in 2008

Excor
1st human implantation:
1984 (adult) – 2000 (child)
FDA approval for pediatric: 2011

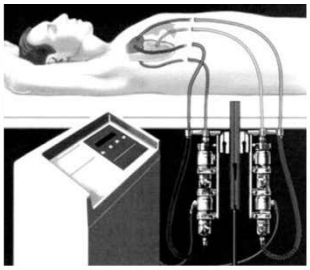

BVS 5000
1st human implantation: 1988
FDA approval for PCR: 1992

LionHeart LVAD
1st human implantation: 1999
No FDA approval
Stop production in 2005

Novacor (World Heart Corp., Oakland, CA); Excor (Berlin Heart Inc., Berlin, Germany); BVS-5000 (Abiomed, Danvers, MA); LionHeart (Arrox International Inc., Reading, PA)

Example of second generation devices

TandemHeart pVAD
1st human implantation: 2003
FDA approval for Short-term: 2003

HearteMate II
1st human implantation: 2003
FDA approval for BTT: 2008
FDA approval for DT: 2010

Jarvik 2000
1st human implantation: 1988
DA approval for BTT: 1994

TandemHeart ((CardiacAssist, Inc.; Pittsburgh, Pa); HeartMate II (St. Jude Medical, Inc, Saint Paul, MN, USA); Jarvik 2000 (Jarvik Heart, Inc., NY, USA)

Example of third generation devices

HearteWare - HVAD
1st human implantation: 2006
FDA approval for BTT: 2010
FDA approval for DT: 2012

EvaHeart
1st human implantation: 2007
FDA approval on going

DuraHeart
1st human implantation: 2004
FDA approval BTT start: 2008
FDA approval DT start: 2010

CentriMag
1st human implantation: 2003
FDA for humanitaria: 2008

HeartWare(HeartWare International Inc, Framingham, MA); EvaHeart (Evaheart, Houston, TX); DuraHeart (Terumo Heart, Ann Arbor, MI, USA) CentriMag (Thoratec Corp, Pleasanton CA, USA)

Annex 3
Four heart cavities and left myocardium segmentation approaches, a state of the art

Study	Database	Approach	Running time Processor (GHz) / RAM (GB)	Gold Standard	Performance
(Zhuang et al. 2015)	30 CTs	Multi-Atlas	13,2 min NM / NM	Manual delineation	AD_{wh} = 1,58 ± 0,92 mm DSC_{wh} = 0,918 ± 0,0212 AD_{LV} = 0,82 ± 0,55 mm DSC_{LV} = 0,967 ± 0,0125 AD_{LMy} = 1,10 ± 0,76 mm DSC_{LMy} = 0,901 ± 0,0242 AD_{RV} = 1,56 ± 1,03 mm DSC_{RV} = 0,918 ± 0,0308 AD_{LA} = 1,79 ± 1,08 mm DSC_{LA} = 0,920 ± 0,0413 AD_{RA} = 2,46 ± 1,64 mm DSC_{RA} = 0,872 ± 0,0481 AD_{Ao} = 0,84 ± 0,47 mm DSC_{Ao} = 0,955 ± 0,0153 AD_{PA} = 1,35 ± 0,79 mm DSC_{PA} = 0,789 ± 0,1294
(Zuluaga et al. 2013)	22 MRI 8 CTs	Multi-Atlas	30 min 2,13 GHz / NM	Manual delineation	DSC_{LV} = 0,93 ± 0,05 DSC_{LMy} = 0,86 ± 0,07 DSC_{RV} = 0,89 ± 0,03 DSC_{LA} = 0,90 ± 0,04 DSC_{RA} = 0,84 ± 0,05 DSC_{Ao} = 0,87 ± 0,06
(Zhuang et al. 2013)	15 CTs	Multi-Atlas	231 sec NM / NM	Manual delineation	AD_{wh} = 1,17 ± 1,39 mm DSC_{wh} = 0,89 ± 0,02 AD_{LV} = 0,90 ± 0,78 mm DSC_{LV} = 0,94 ± 0,03 AD_{LMy} = 1,09 ± 1,01 mm DSC_{LMy} = 0,83 ± 0,05 AD_{RV} = 1,12 ± 1,16 mm DSC_{RV} = 0,91 ± 0,03 AD_{LA} = 1,67 ± 1,96 mm DSC_{LA} = 0,87 ± 0,04 AD_{RA} = 1,70 ± 1,77 mm DSC_{RA} = 0,85 ± 0,05 AD_{Ao} = 0,73 ± 0,81 mm DSC_{Ao} = 0,91 ± 0,03 AD_{PA} = 1,14 ± 1,55 mm DSC_{PA} = 0,80 ± 0,11
(Ecabert et al. 2011)	37 CTs	Deformable Model	12 sec (SD = 1 sec) 2,33 GHz / 4 GB	Multi-step approach (heart model extended to the image and correction by a clinical expert)	AD_{wh} = 0,70 ± 1,03 mm AD_{LV} = 0,77 ± 1,14 mm AD_{LMy} = 0,68 ± 0,96 mm AD_{RV} = 0,63 ± 0,66 mm AD_{LA} = 0,70 ± 0,87 mm AD_{RA} = 0,82 ± 1,00 mm AD_{Ao} = 0,60 ± 1,14 mm AD_{PA} = 0,50 ± 0,49 mm

Note – NM = Note Mentioned; AD = mean Absolute surface Distance; DSC = Dice Score; wh = whole heart; LV = Left Ventricle; LMy = Left Myocardium; RV = Right Ventricle; LA = Left Atrium; RA = Right Atrium; Ao = Aorta; PA = Pulmonary Arteries

Note – NM = Note Mentioned; AD = mean Absolute surface Distance; DSC = Dice Score; wh = whole heart; LV = Left Ventricle; LMy = Left Myocardium; RV = Right Ventricle; LA = Left Atrium; RA = Right Atrium; Ao = Aorta; PA = Pulmonary Arteries

Study	Database	Approach	Running time Processor (GHz) / RAM (GB)	Gold Standard	Performance
(Kirisli et al. 2010) (Kirisli & Schaap 2010)	1380 CTs	Multi-Atlas	20 min 3,4 GHz / 24 GB	Manual delineation	AD_{wh} = 0,99 ± 1,25 mm DSC_{wh} = 0,89 ~ 0,95 AD_{LV} = 0,62 ± 0,63 mm DSC_{LV} = 0,95 AD_{LMy} = 1,04 ± 1,15 mm DSC_{LMy} = 0,95 AD_{RV} = 1,40 ± 1,47 mm DSC_{RV} = 0,90 AD_{LA} = 0,66 ± 0,84 mm DSC_{LA} = 0,94 AD_{RA} = 1,44 ± 1,88 mm DSC_{RA} = 0,89 AD_{Ao} = 0,44 ± 0,60 mm DSC_{Ao} = 0,94
(J. Peters et al. 2010)	28 CTs 42 MRI	Deformable Model	10 – 30 sec NM / NM	Semi-automatic segmentation with manual corrections	AD_{wh} = 0,82 ± 1,00 mm AD_{LV} = 0,98 ± 1,32 mm AD_{LMy} = 0,82 ± 1,07 mm AD_{RV} = 0,84 ± 0,94 mm AD_{LA} = 0,71 ± 0,88 mm AD_{RA} = 0,89 ± 0,96 mm AD_{Ao} = 0,74 ± 0,89 mm
(Ecabert et al. 2008)	28 CTs	Deformable Model	10-30 sec 1,7 GHz / 1 GB	Manual delineation	AD_{wh} = 0,82 ± 1,00 mm AD_{LV} = 0,77 ± 1,14 mm AD_{LMy} = 0,68 ± 0,96 mm AD_{RV} = 0,63 ± 0,66 mm AD_{LA} = 0,70 ± 0,87 mm AD_{RA} = 0,82 ± 1,00 mm AD_{Ao} = 0,74 ± 0,89 mm AD_{PA} = 0,83 ± 1,05 mm
(Zheng et al. 2008) (Zheng et al. 2007)	323 CTs	Active Shape Model	4 sec 3,2 GHz / 3 GB	Manual delineation	AD_{wh} = 1,13-1,57 ± 0,38-0,55m AD_{LV} = 1,13 ± 0,55 mm AD_{LMy} = 1,21 ± 0,42 mm AD_{RV} = 1,55 ± 0,38 mm AD_{LA} = 1,32 ± 0,42 mm AD_{RA} = 1,57 ± 0,48 mm
(Bajaj et al. 2006)	NM	Multi-seeded fast marching method	NM NM / NM	NM	NM
(Ecabert et al. 2005)	6 CTs	Deformable Model with statistical shape model	20 sec 2,4 GHz / 1 GB	NM	NM
(Von Berg & Lorenz 2005)	5 MSCTs	Deformable Model	2,6 GHz NM / NM	NM	NM
(Wierzbicki et al. 2004)	CT + MRI (canine CT / Human MRI)	Model based	NM NM / NM	Manual delineation	Euclidian distance = 2,4 ± 0,3 mm

Annex 4
Thoracic cavity and rib cage segmentation, a state of the art

Note – NM = Note Mentioned; DSC = Dice Score; ASASD = Average Symmetric Absolute Surface Distance; ASSSD = Average Symmetric Squared Surface Distance; MSSD = Maximum Symmetric Surface Distance; AO = Area Overlapped; RMSD = Root Mean Square distance

Thoracic cavity segmentation

Study	Database	Approach	Gold Standard	Performance	Contrast
(Cheirsilp et al. 2015)	37 CTs	Neighbouring anatomy-based	Semi-automatic corrected by 3 experts	DSC = 99,32% ± 1,28 Jaccard = 98,68% ± 2,43 Mean coverage = 99,2% ± 2,28	✓
(Bae et al. 2014)	50 CTs	Neighbouring anatomy-based	2 manual delineations	ASASD = 0.28±0.12 ASSSD = 1.28±0.53 MSSD = 23.91±7.64	×
(Huang et al. 2014)	6 CTs	Active Shape Model	Manual delineation	AO = 93,91 Average Distance = 1,2244 Maximum Distance =9,9016 RMSD = 1,7609	NM
(Vandemeulebroucke et al. 2012)	16 CTs	Feature extraction and Level set	Landmarks in lungs	Quantitative evaluation	×
(Choi & Kim 2010)	5 CTs	Active Contour Model (Gradient Vector Flow)	NM	No evaluation	NM
(Chittajallu et al. 2009)	20 CTs	Graph-based	Manual delineation	DSC = 99,1 ± 0,2%	×
(Zhou et al. 2005)	313 CTs	Region growing	Visual examination	Body cavity 88.8% success Thoracic cavity 95.2% success	✓

Rib cage segmentation

(Narkbuakaew et al. 2014)	1 CT	K-means clustering	Manual delineation	Visual	NM
(Zhou et al. 2004)	139 CTs	Thresholding and Region Growing	NM	Skeleton (93%) Skin (98%)	×

Annex 5
Segmentation of bones with high density and costal cartilages, a state of the art

Note – PSE = Point to Surface Errors; DSC = Dice Score; HD = Hausdorff Distance; FNPV = False Negative Volume Fractions; FPPV = False Positive Volume Fractions

High density bones segmentation

Study	Database	Approach	Gold Standard	Performance	Contrast
(Brahim et al. 2017)	30 CTs	Thresholding-based	NM	70% success 30% sternum removed	✓
(Xu et al. 2014)	400 CTs	Multi-scale Hessian analysis	Identification of errors	95% accuracy	NM
(Fu et al. 2017)	19 CTs	Single-atlas-based	Manual delineation	Spine: PSE = 0,92 mm / DSC = 0,88 Sternum: PSE = 0.89±0.30 (mm) DSC = 0.89±0.02	NM
(Yip et al. 2014)	16 CTs	Atlas-based	2 manual delineations	Articulated registration: DSCregister = 75 ± 2% HD = 0.37 ± 0.08 cm Deformable registration: DSCregister = 77 ± 3% HD = 0.34 ± 0.08 cm Rigid registration: DSCregsiter=59 ± 9% HD=0.69 ± 0.20 cm	✓
(Udupa et al. 2014)	50 CTs	Anatomy recognition and Fuzzy connectedness	Combination of methods supervised by human	FPVF mean = 0,19 ± 0,05 FNVF mean = 0,13 ± 0,07 HD = 10,6 mm ± 2,4 mm	✓

Costal cartilages segmentation

(Pazokifard et al. 2015)	15 CTs	Graph-cuts	Manual delineation	Different shape analysed, best = circle DSC = 77.5% Sensitivity = 84.8% Mean distance = 1.74 mm	✗
(Zhao et al. 2014)	5 CTs	Statistical shape model-based	Manual delineation	Average Distance = 2,89 mm	✗

Abstract

Mechanical Circulatory Support (MCS) therapy is increasingly considered for patients with advanced heart failure unresponsive to optimal medical treatments. In this context, we: *1)* presented an overview of clinical issues raised by MCS implantation, *2)* designed a novel computer-assisted approach for planning the implantation, *3)* implemented a CFD model to understand the ventricle hemodynamics induced by the inflow cannula pose. With the aim of decreasing complications and morbidity, quantitative criteria for optimizing ventricle unloading could be determined through CFD, and the planning approach may provide valuable information for choosing the device and adapting the clinical strategy.